

Turbulent transport in tokamak advanced scenarios

PROEFSCHRIFT

ter verkrijging van de graad van doctor aan de
Technische Universiteit Eindhoven, op gezag van
de rector magnificus, prof.dr.ir. C.J. van Duijn,
voor een commissie aangewezen door het College
voor Promoties in het openbaar te verdedigen op
donderdag 20 december 2012 om 14.00 uur

door

Jonathan Citrin

geboren te Hong Kong

Dit proefschrift is goedgekeurd door de promotoren:

prof.dr. W.J. Goedheer

en

prof.dr. N.J. Lopes Cardozo

Copromotor:

dr. G.M.D. Hogewei

A catalogue record is available from the Eindhoven University of Technology Library

Citrin, Jonathan

Turbulent transport in tokamak advanced scenarios

ISBN: 978-94-6191-533-7

NUR 928



The work described in this dissertation, supported by the European Communities under the Contract of Association between EURATOM/FOM, was carried out within the framework of the European Fusion Programme with financial support from the 'Nederlandse Organisatie voor Wetenschappelijk Onderzoek' (NWO). The views and opinions expressed herein do not necessarily reflect those of the European Commission. This work has also been supported by NWO-RFBR Centre-of-Excellence on Fusion Physics and Technology (Grant nr. 047.018.002). The research was carried out at 'FOM DIFFER - Dutch Institute for Fundamental Energy Research' in Nieuwegein, the Netherlands.

© Copyright 2012 Jonathan Citrin

Typeset in L^AT_EX 2 ϵ

Printed by: Ipskamp Drukkers B.V.

Cover graphics: 2D cross-sections of electrostatic potential fields calculated in GENE non-linear tokamak turbulence simulations presented in Chapter 6 of this thesis

Contents

1	Introduction	1
1.1	Motivation	1
1.2	The tokamak	1
1.3	Research Questions	2
1.4	Publications	6
2	Theoretical Background	11
2.1	Fusion basics	11
2.2	Basic tokamak physics	12
2.3	Tokamak transport	15
2.4	Transport modelling	22
3	Impact of heating and current drive mix on the ITER Hybrid Scenario	31
3.1	Introduction	32
3.2	Modelling techniques and methodology	33
3.3	Results	39
3.4	Sensitivity studies	51
3.5	Discussion and conclusions	54
4	Predictive analysis of q-profile influence on transport in JET and ASDEX Upgrade hybrid scenarios	59
4.1	Introduction	60
4.2	Experimental discharges	62
4.3	Modelling tools and techniques	69
4.4	Results: GLF23 q -profile substitution simulations	69
4.5	Additional contributions to core confinement differences	79
4.6	QualiKiz linear threshold analysis	83
4.7	Conclusions	86
5	Quasilinear transport modelling at low magnetic shear	91
5.1	Introduction	92
5.2	Review of the QualiKiz model	93
5.3	Magnetic shear impact on linear physics	94
5.4	Non-linear effects at low magnetic shear	98
5.5	Discussion and conclusions	116
5.A	Analytic fluid limit	117
5.B	Locality approximation at low magnetic shear	119
5.C	Analytical fluid eigenmode assumption	119

6	Ion temperature profile stiffness: non-linear gyrokinetic simulations and comparison with experiment	123
6.1	Introduction	124
6.2	GENE simulations	125
6.3	Low magnetic shear case	127
6.4	High magnetic shear case	138
6.5	Characteristics of linear simulations with flow shear	139
6.6	Conclusions	145
7	Evaluation and future prospects	151
7.1	Conclusions	151
7.2	Outlook	155
	Summary	161
	Acknowledgements	163
	Curriculum vitae	165

1 Introduction

1.1 Motivation

The quest for harnessing fusion power - the energy source of the stars - is one of paramount importance. Achieving terrestrial controlled fusion has the promise to solve one of the world's more pressing concerns: the provision of environmentally friendly, sustainable sources of energy [1]. In comparison to wind and solar energy, fusion offers the added benefits of high baseline loads and a lack of geographical constraints for reactor construction.

The fusion reaction is a nuclear process whereby light nuclei collide and form a heavier nucleus, releasing some of their mass as energy. This excess energy is manifested in the kinetic energy of the fusion products. In a reactor this energy can be recovered to drive electricity producing steam turbines. The temperatures required for the nuclei to overcome their electric repulsion and fuse at a high enough rate is enormous, on the order of 10^8 K (~ 10 keV). At such temperatures matter is in the plasma state.

However, confining plasmas at sufficiently high temperatures and densities for commercial fusion has proven to be a difficult task. The necessary high pressure gradients in fusion plasmas tend to lead to instabilities. Turbulent transport arises, leading to leakage of heat and particles at a rate higher than expected from collisional transport. Understanding and predicting the turbulence increases our confidence in extrapolating operational scenarios to future reactors, greatly aiding their design. The research carried out in this thesis is firmly with this goal in mind.

1.2 The tokamak

A leading approach for achieving controlled fusion is 'magnetic confinement fusion' (MCF). The most successful present-day application of MCF is the tokamak, where the plasma is contained in a toroidal magnetic chamber by a helical magnetic field [2]. This is illustrated in Fig. 1.1. The toroidal magnetic field is generated by external field coils. Toroidal current is then necessary for the formation of the poloidal component of the helical magnetic field. In standard operation this is induced by transformer action, where the plasma loop acts as the secondary circuit. This leads to an inherent limitation in the tokamak discharge pulse time since the primary coil current is limited. This is not ideal for a reactor due to the importance in maximising availability and minimising cyclic thermal loads on the plasma facing components. For more detailed background information on tokamak physics, the reader is referred to Chap.2.

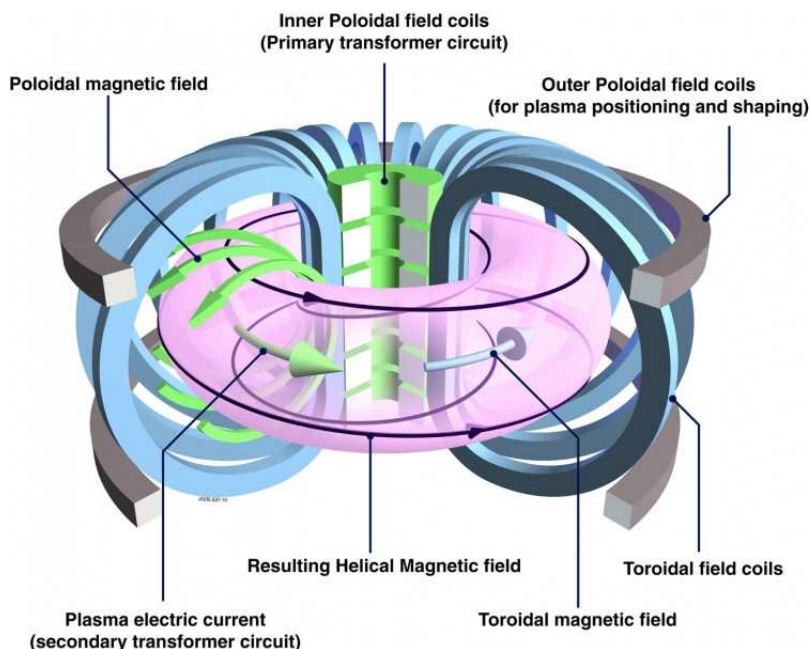


Figure 1.1: Principles of tokamak operation. An externally produced toroidal magnetic field is combined with a poloidal magnetic field generated by toroidal plasma current. Additional field coils are used for plasma shaping and positioning. (Source: EFDA-JET)

1.3 Research Questions

The aforementioned pulse time limitation issue brings us directly to the underlying question motivating this thesis:

How can a tokamak operational scenario be set-up which allows for significantly longer pulses than standard operation, compatible with both reactor fusion power and availability requirements?

By ‘operational scenario’ we mean the choices and timings of the various parameters and actuators for a tokamak discharge such as: transformer current, magnetic fields, plasma shaping currents, fueling, heating schemes, and external current drive schemes.

Fully steady-state scenarios have been developed on existing tokamaks, where 100% of the toroidal current is generated by non-inductive means. This is primarily done by increasing the plasma current internally produced by pressure gradients, by suppressing plasma turbulence in narrow regions of the plasma and creating regions of high pressure gradients called ‘internal transport barriers’ (ITBs). These ITBs are formed in addition to the edge transport barrier (pedestal) formed during standard high-power, high-confinement operation. However, the formation and maintenance of a stable ITB de-

mands the simultaneous control of plasma current and pressure profiles. This may not be possible in reactors, which have decreased scope for diagnostics due to the increased neutron and radiation flux compared with present-day experiments [3].

Additional scenarios have been developed on present-day tokamaks which allow for significantly increased pulse times while not being purely steady state. These are named ‘hybrid scenarios’. Many of the challenges associated with scenario control are alleviated by not demanding ITB formation. The discharge pulse time is increased by both reducing the total plasma current compared to standard high-confinement operational scenarios, and by increasing the fraction of externally driven current (compared to standard operation) by neutral beam injection (NBI) and coupling with radio-frequency (RF) waves.

Tokamak confinement empirical scaling laws [4] predict reduced confinement at lower current. Hybrid scenarios are thus expected to display reduced confinement compared to standard high-confinement operational scenarios. However, hybrid scenarios are characterised by better confinement than expected from the empirical scaling laws, resulting in confinement times comparable with standard high-confinement operation. This holds great promise for the extrapolation of this scenario to future devices, and the hybrid scenario may potentially form the basis of a viable long-pulse reactor scenario. There are numerous possibilities which can explain the improved confinement. Hybrid scenarios are characterised by broad radial profiles of toroidal current. Such current profiles reduce the extent of large-scale instabilities which can induce confinement decreasing magnetic field structures in the plasma. Broad current profiles may also reduce the impact of small-scale plasma instabilities which drive the outward turbulent transport of heat and particles, limiting plasma confinement. The relative height of the plasma edge transport barrier (pedestal) associated with high input power tokamak operation is often increased in hybrid scenarios compared to fully inductive scenarios. Finally, present-day hybrid scenarios are typically set-up with significant NBI, leading to significant plasma rotational flow shear. This is predicted to reduce plasma turbulence, and this effect is not taken into account in the empirical scaling laws. In future devices the rotation resulting from NBI will be significantly lower than in present-day devices, and the question arises whether high-performance hybrid scenarios can then be sustained.

To confidently extrapolate the hybrid scenario to future machines, the physics of each of the above factors must be fully understood and incorporated into the integrated modelling codes which simulate tokamak discharges. This thesis tackles one aspect of this task, and concentrates on the question:

What is the effect of the broad current profile which characterises hybrid scenarios on small-scale plasma instabilities which drive the turbulent transport?

The research has been split up into a number of sub-questions. Since the extrapolation of the hybrid scenario to reactors is the underlying goal, we first apply the question above to hybrid scenario extrapolation to ITER - the next-step tokamak currently under construction. ITER is designed for significant fusion power production, and the hybrid scenario target is a fusion gain of $Q > 5$, where $Q = \frac{P_{fus}}{P_{input}}$. Obtaining high performance of

the hybrid scenario in ITER may verify if the scenario is indeed suitable for long-pulse reactor operation. The more conservative goal of the hybrid scenario in ITER is for long-pulse operation, maximising the discharge neutron fluence for reactor relevant component testing [5]. Simulations of the ITER hybrid scenario have been carried out previously with integrated modelling codes, but no systematic optimisation of the scenario has been performed [6]. Since we are concerned with the current profile effect on the small-scale instabilities, we pose our first sub-question as follows:

What is the optimum application of external current drive in the ITER hybrid scenario for obtaining the current profile shape that minimises turbulent transport?

The tool used to examine this question is the integrated modelling code CRONOS [7], which simulates tokamak discharges, coupled to the quasi-linear transport model GLF23 [8]. An overview of these tools is given in Chap.2. The primary small-scale instability for this class of discharges is driven unstable by the ion-temperature-gradient (ITG). This instability is characterised by critical threshold behaviour, where above a critical ion temperature gradient the instability ignites. The value of the critical threshold is predicted to be parameterised in part by the current profile. This behaviour is captured by the GLF23 model. In Chap.3, ITER hybrid scenario simulations are performed with varying current drive inputs from actuators such as neutral beam injection (NBI) and electron cyclotron current drive (ECCD). The impact of the current drive choices on the fusion power is assessed, based on the ITG instability predictions inherent in the GLF23 model. This optimisation is carried out under a number of constraints (introduced below). A secondary question is thus asked in this work, also addressed in Chap.3.

What are the limits for defining an ITER hybrid scenario operational window given the scenario constraints?

By ‘operational window’ we mean the range of plasma parameters such as density and current within which a scenario can be set-up that satisfies its constraints. The constraints are as follows. Firstly, specific current profile shapes which can trigger large-scale magnetohydrodynamic (MHD) instabilities must be avoided. Secondly, a minimum fusion power is required for the scenario. The current profile constraint is easier to satisfy at low plasma current. The fusion power constraint is easier to satisfy at high plasma density. However, the plasma current and density are linked. In tokamak operation the plasma average density is typically constrained to remain below an empirically derived limit (Greenwald density limit [9]) to ensure stability. This limit is proportional to the total plasma current. Thus, even with optimum current profile shaping for the reduction of turbulent transport, it may transpire that the necessary density for sufficient fusion power is incompatible with the avoidance of large-scale MHD instabilities due to the value of the total current associated with the necessary average density. An important factor in determining this is the temperature at the top of the edge transport barrier (pedestal). The core plasma temperatures are closely linked to the pedestal temperatures. The current profile optimisation task is thus carried out for a number of different pedestal

assumptions. If the pedestal height is too low, satisfying the fusion power constraint (and thus the current profile constraint) is hampered. This work thus also predicts what the necessary pedestal height is such that an operational window for the ITER hybrid scenario can be defined.

Given the results in Chap.3, a natural question to ask is then:

Is the predicted impact of the current profile on the turbulent transport validated by present-day experimental discharges?

This question is addressed in Chap.4. A pair of hybrid scenario discharges from both the JET and ASDEX-Upgrade tokamaks were chosen for analysis. The discharges within each pair is characterised by similar pedestal heights but differences in both total confinement and current profile. The degree to which the differences in confinement can be attributed to the current profile is studied. CRONOS and GLF23 are used for predictive simulations of the discharges, as in the ITER case in Chap.3. These predictions are then compared to the actual experimental data. The effect of the current profile can be isolated in the simulations since all the various parameters and profiles in the simulations can be interchanged independently.

The analyses in Chap.3-4 are focused on the critical threshold variation of the ITG instability with the current profile shape. The degree that the temperature gradients can depart from the critical threshold at a given heat flux is called ‘stiffness’. GLF23 is a ‘stiff’ transport model, meaning that the predicted temperature gradients tend to be close to the critical gradient thresholds. However, in certain cases, the stiffness is reduced. This is seen in investigations with full non-linear turbulence simulations, where for flat current profiles (also known as low magnetic shear) typical in hybrid scenarios, the stiffness is reduced compared to the expectation of stiff transport models. This has been clearly observed in a comparison between a relatively new quasi-linear transport model - QuaLiKiz [10] - and full non-linear simulations using the GENE code [11]. QuaLiKiz predicted heat fluxes were significantly larger than the non-linear predictions at low magnetic shear, while for other parameter scans the agreement was satisfactory. The QuaLiKiz model is based on more realistic assumptions than GLF23, increasing the general confidence in its predictions and motivates its incorporation as a model routinely used for transport predictions. It was thus decided within the framework of this thesis to set out to improve the QuaLiKiz model in low magnetic shear parameter space, facilitating the future use of the model in hybrid scenario extrapolation. We then ask two questions:

What is the non-linear physics at low magnetic shear that leads to reduced stiffness in ITG turbulence?

How can the QuaLiKiz model be improved such that increased agreement with non-linear ITG turbulence predictions is obtained at low magnetic shear?

These questions are answered in Chap.5. The non-linear turbulence code GENE is used as the main investigation tool. The QuaLiKiz assumptions are systematically guided and validated by GENE calculations, which are based on a more complete physical model.

Experimental observation of reduced ion temperature profile stiffness at low magnetic shear has recently been reported at JET [12]. It is hypothesised that this is not purely due to the low magnetic shear, but rather due to the concomitant low magnetic shear and high rotational shear present in the specific discharges. The reduced stiffness has not been reproduced by transport models. In this thesis we set out on a more systematic investigation of this effect with non-linear modelling, and ask the question:

Can the observed reduced stiffness observed in JET discharges at low magnetic shear and high rotational flow shear be understood through non-linear simulations?

This is the subject of Chap.6, using the GENE non-linear code. This question is again deeply related to hybrid scenario extrapolation. If high rotational flow shear at low magnetic shear is indeed an important factor for improved hybrid scenario confinement, then this may pose concern for the extrapolation of the scenario to future machines where the flow shear is expected to be significantly reduced compared to current machines.

We can summarise the research questions as follows. Chap.3-4 deals with the prediction of the impact of hybrid-scenario relevant current profiles on ion-temperature-gradient instability critical thresholds. Chap.5-6 deals with the impact of the low magnetic shear inherent to hybrid-scenario relevant current profiles on the transport stiffness. We will evaluate the progress made in answering the research questions in Chap.7, where an outlook towards follow-up work and future potential research directions uncovered by the research within this thesis is also presented.

1.4 Publications

Chap.3-6 have all been published or submitted to peer reviewed journals. These are listed below, together with additional contributions related to this thesis.

Refereed journal papers (as main author)

- J. Citrin, C. Bourdelle, J.W. Haverkort, G.M.D. Hogeweij, F. Jenko, P. Mantica, D. Told, and JET-EFDA contributors. Ion temperature profile stiffness: non-linear gyrokinetic simulations and comparison with experiment. *To be submitted to Nucl. Fusion*, (2012)
- J. Citrin, C. Bourdelle, P. Cottier, D.F. Escande, Ö.D. Gürcan, D.R. Hatch, G.M.D. Hogeweij, F. Jenko, and M.J. Pueschel. Quasilinear modelling at low magnetic shear. *Phys. Plasmas* **19** 062305 (2012)
- J. Citrin, J. Hobirk, M. Schneider, J.F. Artaud, C. Bourdelle, K. Crombé, G.M.D. Hogeweij, F. Imbeaux, E. Joffrin, F. Koechl, J. Stober. Predictive analysis of q -profile influence on transport in JET and AUG hybrid scenarios. *Plasma Phys. Control. Fusion* **54** 065008 (2012)
- J. Citrin, J.F. Artaud, J. Garcia, G.M.D. Hogeweij, and F. Imbeaux. Impact of heating and current drive mix on the ITER hybrid scenario. *Nucl. Fusion*, **50** 115007 (2010)

Refereed journal papers (as co-author)

- G. Hommen, M. de Baar, J. Citrin, H.J. de Blank, R.J. Voorhoeve, M.F.M. De Bock, M. Steinbuch, and JET-EFDA contributors. A fast, non-iterative flux surface estimation and q-profile reconstruction algorithm for control of plasma profiles. *Submitted to Nucl. Fusion* (2012)
- G.M.D. Hogeweij, J.-F. Artaud, T.A. Casper, J. Citrin, F. Imbeaux, F. Köchl, X. Litaudon, I. Voitsekhovitch, and the ITM-TF ITER Scenario Modelling group. Optimizing the current ramp-up phase for the hybrid ITER scenario. *Submitted to Nucl. Fusion*, (2012)
- M.F.M. De Bock, J. Citrin, S. Saarelma, D. Temple, N.J. Conway, A. Kirk, H. Meyer, C.A. Michael and the MAST team. Measurements of the edge current evolution and comparison with neoclassical calculations during MAST H-modes using motional Stark effect. *Plasma Phys. Control. Fusion* **54** 025001 (2012)
- P. Mantica, C. Angioni, B. Baiocchi, M. Baruzzo, M.N.A. Beurskens, J.P.S. Bizarro, R.V. Budny, P. Buratti, A. Casati, C. Challis, J. Citrin, G. Colyer, F. Crisanti, A.C.A. Figueiredo, L. Frassinetti, C. Giroud, N. Hawkes, J. Hobirk, E. Joffrin, T. Johnson, E. Lerche, P. Migliano, V. Naulin, A.G. Peeters, G. Rewoldt, F. Ryter, A. Salmi, R. Sartori, C. Sozzi, G. Staebler, D. Strintzi, T. Tala, M. Tsalas, D. Van Eester, T. Versloot, P.C. deVries, J. Weiland, and JET EFDA Contributors. Ion heat transport studies in JET. *Plasma Phys. Control. Fusion* **53** 124033 (2011)
- F. Imbeaux, J. Citrin, J. Hobirk, G.M.D. Hogeweij, F. Köchl, V.M. Leonov, S. Miyamoto, Y. Nakamura, V. Parail, G. Pereverzev, A. Polevoi, I. Voitsekhovitch, *et al.* Current ramps in tokamaks: from present experiments to ITER scenarios. *Nucl. Fusion* **51** 083026 (2011)

Conference proceedings (as main author)

- J. Citrin, J. Hobirk, M. Schneider, J.F. Artaud, C. Bourdelle, K. Crombe, G.M.D. Hogeweij, F. Imbeaux, E. Joffrin, F. Köchl, J. Stober. Predictive transport analysis of JET and AUG hybrid scenarios, *38th EPS Conference on Plasma Physics, Strasbourg, France* (2011)
- J. Citrin, J.F. Artaud, J. Garcia, G.M.D. Hogeweij, F. Imbeaux. ITER Hybrid Scenario optimization by integrated modelling, *37th EPS Conference on Plasma Physics, Dublin, Ireland* (2010)

Conference proceedings (as co-author)

- X. Litaudon, I. Voitsekhovitch, J.F. Artaud, P. Belo, J. Bizarro, T. Casper, J. Citrin, E. Fable, J. Ferreira, J. Garcia, L. Garzotti, J. Hobirk, G.M.D. Hogeweij, F. Imbeaux, E. Joffrin, F. Koechl, J. Lönnroth, F. Liu, D. Moreau, V. Parail, P.B. Snyder, M. Schneider, ASDEX Upgrade Team, JET-EFDA contributors, and the EU-ITM ITER Scenario Modelling group. *24rd IAEA Fusion Energy Conference, San Diego, USA* (2012)
- F. Jenko, H. Doerk, T. Görler, D. Hatch, J. Hobirk, J. Schweinzer, G. Tardini, D. Told, A. Volk, E. Wolfrum, T. Dannert, T. Bird, P. Xanthopoulos, S. Brunner, O. Sauter, L. Villard, A. Bañón Navarro, D. Carati, P. Morel, C. Hegna, M.J. Pueschel, P.W. Terry, J. Citrin, P. Mantica, and M. Barnes. Global gyrokinetic simulations of high-performance discharges in view of ITER. *24rd IAEA Fusion Energy Conference, San Diego, USA* (2012)

- L. Garzotti, C. Bourdelle, J. Citrin, F. Köchl, J. Lönnroth, S. Moradi, V. Parail, I. Voitsekhovitch, P. Belo, J.P.S. Bizarro, G. Corrigan, the EU-ITM ITER Scenario Modelling group and EFDA-JET contributors. Simulations of density profiles in JET hybrid discharges, *39th EPS Conference on Plasma Physics, Stockholm, Sweden* (2012)
- I. Voitsekhovitch, X. Litaudon, E. Barbato, V. Basiuk, P. Belo, J.P.S. Bizarro, T. Casper, J. Citrin, E.Fable, J. Ferreira, J. Garcia, L. Garzotti, J. Hobirk, G.M.D. Hogeweij, I. Ivanova-Stanik, E. Joffrin, D. Kalupin, F. Köchl, F. Liu, J. Lönnroth, S. Moradi, D. Moreau, F. Nabais, V. Parail, A. Polevoi, M. Romanelli, M. Schneider, P. B. Snyder, ASDEX Upgrade Team, JET-EFDA contributors, and the EU-ITM ITER Scenario Modelling group. Integrated modelling for tokamak plasma: physics and scenario optimisation, *39th EPS Conference on Plasma Physics, Stockholm, Sweden* (2012)
- G.M.D. Hogeweij, J.-F.Artaud, T.A.Casper, J.Citrin, F.Imbeaux, F. Köchl, X. Litaudon and the ITM-TF ITER Scenario Modelling group. Optimization of the current ramp-up phase for hybrid ITER discharges, *38th EPS Conference on Plasma Physics, Strasbourg, France* (2011)
- S. Djordjevic, M.R. de Baar, M. Steinbuch, J. Citrin, G.M.D. Hogeweij. Controllability analysis for the magnetic flux in ITER, *38th EPS Conference on Plasma Physics, Strasbourg, France* (2011)
- S. Djordjevic, M.R. de Baar, M. Steinbuch, J. Citrin, G.M.D. Hogeweij. Controllability analysis for the magnetic flux in ITER, *Proc. 50th IEEE-CDC, Orlando, USA* (2011)
- E. Joffrin, J. Citrin, J.F. Artuad, C. Challis, F. Imbeaux *et al.* Extrapolation of JET hybrid scenario fusion performance to larger device, *37th EPS Conference on Plasma Physics, Dublin, Ireland* (2010)
- E. Joffrin, C. Challis, J. Citrin, J. Garcia, J. Hobirk *et al.* High confinement hybrid scenario in JET and its significance for ITER, *23rd IAEA Fusion Energy Conference, Daejeon, Republic of Korea* (2010)
- P. Mantica, C. Angioni, B. Baiocchi, C. Challis, J. Citrin, G. Colyer, A.C.A. Figueiredo, L. Frassinetti, E. Joffrin *et al.* A key to improved ion core confinement in the JET tokamak: Ion stiffness mitigation due to combined plasma rotation and low magnetic shear, *23rd IAEA Fusion Energy Conference, Daejeon, Republic of Korea* (2010)
- F. Imbeaux, V. Basiuk, R. Budny, T. Casper, J. Citrin, J. Ferreira, A. Fukuyama, J. Garcia *et al.* Current ramps in tokamaks: From present experiments to ITER scenarios, *23rd IAEA Fusion Energy Conference, Daejeon, Republic of Korea* (2010)
- T.C. Luce, C.D. Challis, S. Ide, E. Joffrin ... J. Citrin ... J. Hobirk, F. Imbeaux *et al.* Development of advanced inductive scenarios for ITER, *23rd IAEA Fusion Energy Conference, Daejeon, Republic of Korea* (2010)

Conference/workshop oral contributions

- J. Citrin, C. Bourdelle, J.W. Haverkort, G.M.D. Hogeweij, F. Jenko, P. Mantica, D. Told, and JET-EFDA contributors. Ion temperature profile stiffness: non-linear gyrokinetic simulations and comparison with experiment. *9th ITPA Transport & Confinement Topical Group Meeting, San Diego, USA* (2012)

- J. Citrin, J.F. Artaud, J. Garcia, G.M.D. Hogeweij, and F. Imbeaux. Fighting turbulence: modelling improved energy confinement in fusion reactors. *Physics@FOM, Veldhoven, The Netherlands* (2011)
- J. Citrin, J.F. Artaud, J. Garcia, G.M.D. Hogeweij, and F. Imbeaux. Optimization of ITER Hybrid Scenario performance with the CRONOS suite of codes. *3rd ITPA Integrated Operational Scenarios Topical Group Meeting, Frascati, Italy* (2009)

Seminars

- *Comparison between ion temperature profile stiffness observations and nonlinear gyrokinetic simulations.* Plasma Theory Group Seminars, Oxford University, Oxford, UK. July 2012
- *Quasilinear transport modeling at low magnetic shear.* CCFE Fusion Theory Meeting, Culham, UK. April 2012
- *Integrated modelling of tokamak turbulence.* Weizmann Institute, Rehovot, Israel. January 2011
- *Analyzing the role of the q -profile in JET hybrid improved confinement with current-overshoot.* CEA Cadarache, France. September 2010
- *Optimization of ITER Hybrid Scenario performance by integrated modelling.* CEA Cadarache, France. March 2010

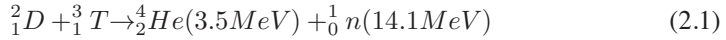
References

- [1] J. Ongena and G. Van Oost, 2010 *Trans. of Fusion Sci. and Technol.*, **57** 3.
- [2] J.A. Wesson and D.J. Campbell, 2004 *Tokamaks* 3rd edn. (Oxford: Oxford University Press).
- [3] A.J.H. Donné, A.E. Costley, and A.W. Morris, 2012 *Nucl. Fusion* **52** 074015.
- [4] ITER Physics Expert Group on Confinement *et al.*, ITER Physics Basis Chapter 2: Plasma confinement and transport, 1999 *Nucl. Fusion* **39** 2175.
- [5] M. Shimada *et al.*, Progress in the ITER Physics Basis Chapter 1: Overview and summary, 2007 *Nucl. Fusion* **47** S1.
- [6] C.E. Kessel *et al.*, 2007 *Nucl. Fusion* **47** 1274.
- [7] J.F. Artaud *et al.*, 2010 *Nucl. Fusion* **50** 043001.
- [8] R.E. Waltz *et al.*, 1997 *Phys. Plasmas* **7** 2482.
- [9] M. Greenwald *et al.*, 1988 *Nucl. Fusion* **28** 2199.
- [10] C. Bourdelle *et al.*, 2007 *Phys. Plasmas* **47** 14 112501.
- [11] F. Jenko, W. Dorland, M. Kotschenreuther and B.N. Rogers 2000 *Phys. Plasmas* **7** 1904, and <http://gene.rzg.mpg.de>.
- [12] P. Mantica *et al.*, 2011 *Phys. Rev. Lett.* **107** 135004.

2 Theoretical Background

2.1 Fusion basics

The most accessible nuclear fusion reaction combines the hydrogen isotopes deuterium and tritium into helium and a neutron:



Deuterium reserves in seawater are practically inexhaustible. Tritium must be produced within fusion reactors themselves, through the activation of lithium by the fusion neutrons in a blanket surrounding the fusion plasma, in conjunction with neutron multipliers such as beryllium [1]. Currently extractable world reserves of lithium are sufficient for centuries of tritium production for fusion, and the development of efficient lithium extraction from seawater could extent the reserves to be effectively limitless [2]. Radioactive waste issues are highly mitigated in fusion compared to nuclear fission. The tritium fuel itself is radioactive but has a short half-life of 12.3 years. The reactor wall components can be engineered such that neutron activation of wall materials leads only to short half-life byproducts [3]. Therefore no transport of nuclear waste for long-term storage would be necessary. Furthermore, no dangerous runaway nuclear reactions are possible in fusion reactors, as opposed to fission reactors.

The necessary conditions for maintaining a self-sustaining fusion burn is quantified by the “triple product” Lawson criterion [4], which for the DT reaction at fusion relevant temperatures can be approximated as a constant:

$$nT\tau_E \geq 5 \cdot 10^{21} \text{ keV s/m}^3 \quad (2.2)$$

n is the plasma density, T the temperature (in keV) and τ_E is the confinement time. This is defined in stationary-state as $\tau_E \equiv \frac{W}{P_{loss}}$, the ratio between the total stored thermal energy

$W = \frac{3}{2} \int P dV$ (where P is the plasma pressure), and the total power loss rate P_{loss} from the volume boundaries. In stars, the fusion plasma is confined by gravity. For terrestrial fusion plasmas, gravity is clearly insufficient. Two mainstream approaches exist for satisfying the Lawson criterion. ‘Inertial confinement fusion’ (ICF) purports to achieve pulsed fusion burn of dense plasmas at the cost of shortened confinement time. The leading ICF approach is the interaction of a high energy laser (MJ scale) with mm scale DT fuel pellets [5]. The second approach, which forms the physics framework in this thesis, is ‘magnetic confinement fusion’ (MCF). This consists of relatively long timescale (order of s) confinement of relatively diffuse ($10^{19} - 10^{20} \text{ m}^{-3}$) plasmas. The plasma is confined by magnetic fields which provides insulation from the surrounding walls.

2.2 Basic tokamak physics

Plasmas are ‘quasineutral’; at length scales above the Debye length $\lambda_D \equiv \sqrt{\epsilon_0 T_e / n_e e^2}$ and at frequencies below the plasma frequency $\omega_{pe} \equiv \sqrt{n_e e^2 / m_e \epsilon_0}$, the plasma effectively screens charge separation and the relation $\sum_s n_s q_s = 0$ holds. s is the species label (i.e. electrons, ions). All units are in MKS.

The charged particles in the plasma are susceptible to the Lorentz force, $\mathbf{F} = q(\mathbf{E} + \mathbf{v} \times \mathbf{B})$. When placed in a magnetic field, the particles are free to stream parallel to the magnetic field, while perpendicularly they rotate with a gyroradius $\rho_s = \frac{m_s v_\perp}{|q_s| B}$ and gyrofrequency (also called cyclotron frequency) $\omega_{cs} = \frac{q_s B}{m_s}$. This constraint of perpendicular motion is the primary confinement mechanism of MCF. A tokamak is such a magnetic confinement device, in which the plasma is contained in an axisymmetric toroidal magnetic chamber by strong helical magnetic fields with magnitudes on the order of several Tesla, as previously illustrated in Fig. 1.1.

The toroidal plasma current responsible for the poloidal magnetic field can be formed by: a toroidal electric field induced by transformer action, in which the plasma loops acts as the secondary circuit; so-called ‘bootstrap current’, which is self-generated by a combination of radial pressure gradients and collisions between particles in the plasma [6]; radio-frequency (RF) waves coupled to the plasma; beams of neutral particles injected into the plasma which are subsequently ionized and thermalized. Neutral beam injection (NBI) and RF coupling at electron cyclotron (EC), ion cyclotron (IC), and lower hybrid (LH) frequencies are used for plasma heating as well as current drive. This is necessary for raising plasma temperatures to the required magnitudes for fusion, due to the $T_e^{-3/2}$ dependence of plasma resistivity. Ohmic (resistive) heating becomes negligible at fusion relevant temperatures.

2.2.1 Particle drifts

Under external forces and/or due to field inhomogeneities, particles can drift across the magnetic field [7]. This provides a mechanism for confinement loss. The most important of these drifts are the $\mathbf{E} \times \mathbf{B}$ drift

$$\mathbf{v}_E = \frac{\mathbf{E} \times \mathbf{B}}{B^2} \quad (2.3)$$

which occurs for crossed electric and magnetic fields, and the combined ∇B and curvature drifts, brought about by inhomogeneous magnetic fields.

$$\mathbf{v}_{Bs} = \frac{m_s (T_{\perp s} + 2T_{\parallel s})}{2q_s} \frac{\mathbf{B} \times \nabla B}{B^3} \quad (2.4)$$

T_\perp and T_\parallel are the perpendicular and parallel velocities. The v_E drift is the same for all plasma species. v_B is of opposite sign for electrons and ions, and has a temperature dependence. This can give rise to charge separation and subsequent $\mathbf{E} \times \mathbf{B}$ drifts. This is the physical mechanism behind the most unstable branch of the ITG instability, discussed in section 2.3.

2.2.2 Tokamak geometry

Due to toroidicity the magnetic field is inhomogeneous, with a field magnitude dependence of $B \propto \frac{1}{R}$, where R is defined from the centre of the torus. The ‘high-field-side’ of the tokamak plasma is the inner side of the plasma ring closest to the centre (to the transformer in Fig. 1.1), and the ‘low-field side’ is the outer side of the torus. If the magnetic field were purely toroidal the combination of the aforementioned drifts would lead to outward radial bulk plasma motion. This is what necessitates a helical magnetic field for plasma confinement. The helical field lines connect the high and low-field-sides, and form nested flux surfaces, illustrated in Fig. 2.1. The radial component of the plasma drifts during motion along the helical field averages out such that confinement is attained. The equilibrium 2D flux surface geometry is set by the balance of pressure and magnetic forces: $\nabla p = \mathbf{j} \times \mathbf{B}$.

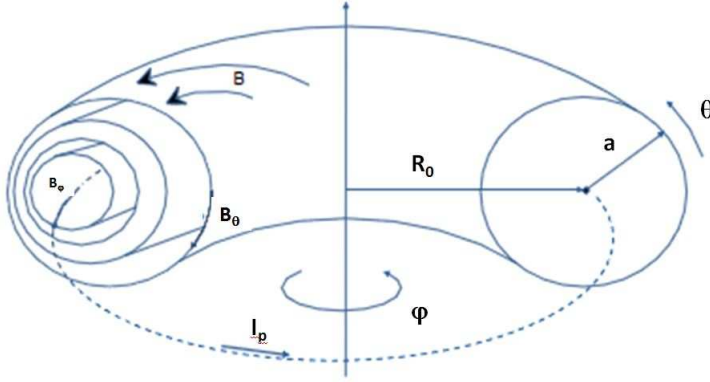


Figure 2.1: Illustration of tokamak geometry. The toroidal angle is ψ , the poloidal angle is θ . A flux surface is defined by its tangential helical magnetic field lines. A tokamak is comprised of nested flux surfaces. The major radius R_0 is defined as the length between the centre of the torus and the magnetic axis (where the poloidal field is zero). The minor radius a is defined from the magnetic axis to the plasma edge.

An important concept is the ‘q-profile’, which relates the relative magnitude of poloidal and toroidal magnetic fields. The q-profile is the ratio of toroidal rotations to one full poloidal rotation along the helical magnetic field on a given flux surface. For general flux surface geometries this is defined as:

$$q(\psi) = \frac{1}{2\pi} \int_0^{2\pi} d\theta \frac{\hat{\mathbf{b}} \cdot \nabla \varphi}{\hat{\mathbf{b}} \cdot \nabla \theta} \quad (2.5)$$

where ψ is a ‘radial’ coordinate that labels the flux surfaces. For circular flux surface geometries, the q-profile can be written as:

$$q(r) = \frac{r B_\psi}{R B_\theta} \quad (2.6)$$

where at a given flux surface, r is the radius from the magnetic axis. B_φ is the toroidal magnetic field, and B_θ the poloidal magnetic field. The normalized inverse gradient length of the q-profile is called the ‘magnetic shear’:

$$\hat{s} = \frac{r}{q} \frac{dq}{dr} \quad (2.7)$$

The q-profile and the magnetic shear play an important role in setting the onset and saturation level of the plasma instabilities which determine transport.

In modern tokamaks, the magnetic geometry towards the walls is tailored such that the majority of the plasma exhaust is confined to field lines that branch out from the last closed flux surface (the ‘separatrix’) at a prescribed location (the ‘x-point’), and strike plasma facing components designed to withstand the heat load. This is known as ‘divertor’ geometry, seen in Fig. 2.2, which serves to reduce the influx of impurities from the wall into the plasma. The study of plasma-wall interactions and divertor physics is critical for tokamak development. Reactor divertor concepts which can withstand the high reactor exhaust heat loads must be developed and validated. However, in the research presented in this thesis we concern ourselves with core plasma physics, and from henceforth limit our discussions to that realm.

2.2.3 Mirror forces

The parallel (to the magnetic field) trajectory of particles in the plasma leads to motion in the direction of the magnetic field gradient, which sets up a ‘mirror force’ opposite the direction of motion. This can be understood by considering the conservation of the magnetic moment $\mu = \frac{mv_\perp^2}{2B}$, which is the adiabatic invariant associated with the rapid (compared with the time variation of the magnetic field in the particle frame) periodic gyromotion of the particles, combined with conservation of energy [7]. As B changes in the particle frame, v_\perp must compensate to preserve μ . v_\parallel must then also change to conserve energy. This effect separates each plasma species into ‘passing’ and ‘trapped’ populations. The trapped population, set by the fraction of particles with insufficient parallel velocity to overcome the magnetic barrier, is confined to the low-field side and move with banana shaped orbits due to the v_B drift. This ‘bounce’ motion undergoes toroidal precession. This is illustrated in Fig. 2.2.

The passing particles traverse the poloidal angle with a transit frequency $\omega_{t(e,i)} = \frac{v_{th(e,i)}}{qR}$. qR is known as the ‘connection length’, since this is the length scale that connects the low-field-side and high-field-side of a given flux surface. $v_{ths} = \sqrt{T_s/m_s}$ is the thermal velocity of species s .

2.2.4 Diamagnetic drifts

The diamagnetic drifts arise from pressure inhomogeneities:

$$\mathbf{V}_{*s} = \frac{\mathbf{B} \times \nabla P_s}{n_s q_s B^2} \quad (2.8)$$

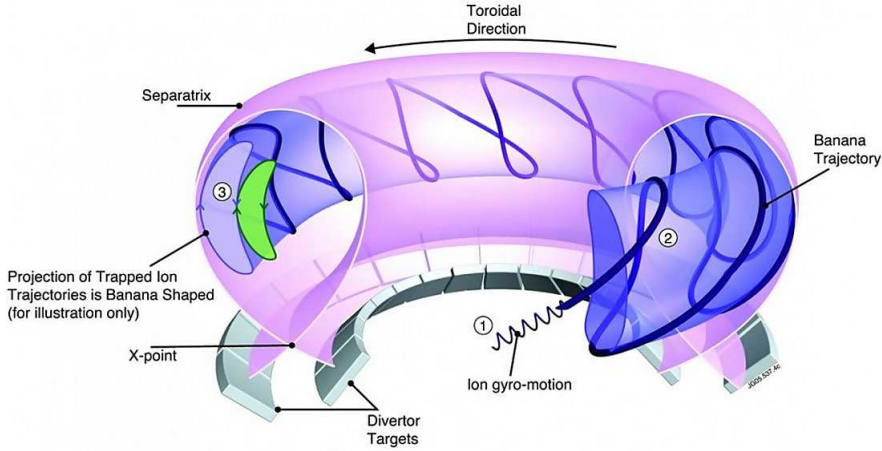


Figure 2.2: Trapped particles undergo a banana shaped motion on the low-field-side of the tokamak. This motion undergoes toroidal precession. The separatrix is also illustrated here, with open field lines diverging from the x-point onto dedicated divertor plates which absorb the bulk of the plasma exhaust. (Source: EFDA-JET)

These are not strictly single particle drifts but are rather fluid flows set up by the inhomogeneity of the gyrorotating particles [7]. Density perturbations propagating as a wave tangentially to the pressure gradient have phase velocities on the order of the diamagnetic drift velocities. These are collectively named ‘drift waves’. The drift wave frequency is $\omega_{*s} = \mathbf{k} \cdot \mathbf{V}_{*s}$. The various classes of unstable drift waves are the primary causes of tokamak turbulent transport [8]. For gyroradius scale fluctuations, ω_{*s} is approximately two or three orders of magnitude lower than the corresponding gyrofrequencies ω_{cs} . This temporal separation is of great practical use for reducing computational expense in drift wave calculations, as will be further explained in section 2.4.2.

2.3 Tokamak transport

On a flux surface the parallel particle diffusivity and heat conductivities are sufficiently high such that the densities and temperatures can be considered as flux functions, i.e. a function with a unique value over a flux surface. The plasma density and temperature profiles are thus ‘radial’. The transport across the flux surfaces, in conjunction with the core heat and particle sources, sets the value of the confinement time τ_E . This cross-field transport is observed to be orders of magnitude greater than the expectations from the theory of collisional transport in toroidal geometry - known as ‘neoclassical’ theory [9]. This ‘anomalous’ transport is due to turbulent transport driven by the high temperature and density gradients in the tokamak plasma [8]. The underlying instabilities which drive the transport are typically characterised by critical thresholds of temperature or density

gradients, above which the instability ignites. The values of the critical thresholds are calculated by analysing the dispersion relation derived by linearising (i.e. assuming small fluctuations) the system of equations governing the plasma behaviour. Above the critical threshold, the dispersion relation will support unstable modes. Such ‘linear’ instabilities arise at ion or electron gyroradii scales (depending on the underlying instability drive). These scales are much smaller than the system size, and these instabilities have thus been termed ‘microinstabilities’.

The plasma fluctuations saturate into a self-organized quasi-stationary state following mode-coupling in the non-linear regime. For electrostatic perturbations (when magnetic fluctuations are negligible), the transport can be intuitively understood as a $E \times B$ drift driven random walk through the saturated fluctuating electric potential field. An important regulating and saturation mechanism of the turbulence is through non-linear mode coupling to zonal flows [10]. These are linearly stable predominantly poloidally symmetric modes which provide radial plasma flow shear. They draw energy from the unstable drift waves and also reduce the radial extent of the turbulent eddies.

The frequency width of the microinstability fluctuations has been experimentally observed to be on the order of the frequency itself [11, 12]. For example, for ion scale turbulence, $\Delta\omega \sim \omega^{*i}$. Assuming random walk diffusivity, an estimate of the diffusion coefficient is $D_{turb} \sim \frac{(\Delta r)^2}{\Delta t}$. Δr is the random walk step size and Δt the time between steps. Taking $\Delta t \sim \frac{1}{\Delta\omega}$ and $(\Delta r) k_{\perp} \sim \rho_i$, we obtain an order of magnitude estimate for the ion heat diffusivity, $D_{turb} \sim \frac{\rho_i}{R} \frac{cT_i}{eB}$. This fundamental unit of diffusivity is named the ‘gyroBohm’ unit. Throughout this thesis, we normalise turbulent diffusivities by this quantity. GyroBohm scaling clearly points to the advantage of increasing the system size for reducing turbulent diffusivity, since the turbulent eddies scale with the normalised gyroradius.

Kinetic theory is necessary for an accurate description of the instabilities. This is due to the low collisionality in fusion plasmas, and due to wave-particle interactions. Resonances (Landau damping [7]) occur at the passing particle transit frequency, trapped particle precession frequency, and particle magnetic drift frequencies. The perpendicular scale length of the microinstabilities are on the order of several gyroradii: $k_{\perp} \rho_s \sim 0.1 - 1$. At higher k the instability is stabilised by finite Larmor radius effects, whereby the average magnitude of the field fluctuations ‘felt’ by a gyrating particle is reduced as the scale of the fluctuations decreases below the gyroradius. The parallel scale length of the fluctuations is ordered as $\frac{k_{\parallel}}{k_{\perp}} \ll 1$, since field line bending is energetically unfavourable. This anisotropy in the fluctuations simplifies calculations greatly, as will be shown in section 2.4.

The microinstabilities limit plasma confinement even in regimes where the plasma is stabilised against larger scale magnetohydrodynamic (MHD) instabilities - i.e. instabilities that can be adequately described by fluid plasma equations. However, even if the microinstabilities are quenched, MHD instabilities lead to practical limits of the achievable pressure in fusion plasmas, as characterised by experimentally observed limits in achievable $\beta = \frac{p}{B^2/2\mu_0}$, the ratio between the plasma kinetic and magnetic pressure [13]. An approximate empirical limit in the achievable plasma density is also observed, the ‘Gre-

enwald limit' [14]. This phenomenological limit is $n_G = I_p / \pi a^2$, with n_G in 10^{20} m^{-3} , I_p in MA , and a the minor radius in m . The Greenwald fraction is $f_G \equiv \bar{n}_e / n_G$, with \bar{n}_e the line averaged density. By controlling microinstabilities, the aim is to then operate tokamak scenarios in the vicinity of the MHD driven limits.

2.3.1 The ITG instability

An instability of particular relevance to fusion plasmas is that driven by the ion temperature gradient, the ITG instability [15–18]. This mode is thought to be the primary source of ion heat transport, which is critical in setting the eventual fusion power in a reactor. When not considering magnetic field curvature (the ‘slab limit’) the mode is a drift wave driven unstable by parallel compression due to ion acoustic waves [19]. When considering field curvature, the drift wave is also driven unstable due to curvature effects on the low-field-side of the tokamak, where the magnetic field gradient, curvature vector, and temperature gradient are all in the same direction. This ‘bad-curvature’ driven drive then dominates over the slab drive. The physical mechanism for the curvature drive - the Rosenbluth-Longmire picture [20] - is illustrated in Fig. 2.3. For simplification, the ion temperature has been split into two distinct regions, hot and cold. An initial fluctuation (drift wave) is set up on the boundary between the regions. The ∇B and curvature particle drifts are proportional to temperature. The ion velocity imbalance then sets up an electric field profile, which through the $E \times B$ drift then leads to an amplification of the original perturbation. On the high-field-side the $E \times B$ drift leads to a suppression of the original perturbation.

There exists a critical ion gradient threshold above which the instability ignites. The thresholds can be calculated from kinetic theory, invoking the quasineutrality constraint on the kinetic responses of the combined electron and ion density fluctuations, for example as in Ref. [21]. An often applied analytical parameterisation of the ITG critical gradient thresholds for circular flux surfaces in the limit of low r/R and low density

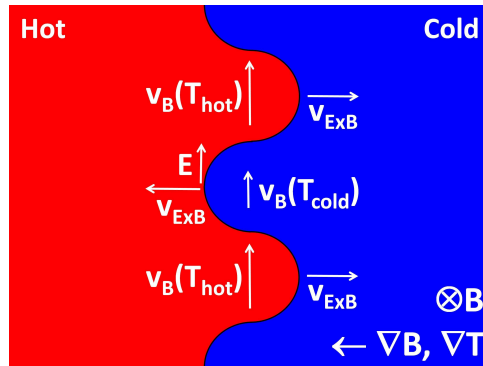


Figure 2.3: The Rosenbluth-Longmire picture of the physical mechanism behind the bad-curvature driven ITG instability

gradient is [18]:

$$\left(\frac{R}{L_{Ti}}\right)_{crit} = \frac{4}{3} \left(1 + \frac{T_i}{T_e}\right) \left(1 + 2\frac{\hat{s}}{q}\right) \quad (2.9)$$

where $L_{Ti} \equiv \frac{T_i}{\nabla T_i}$. The T_i/T_e dependence can be intuitively understood by considering that at lower relative electron temperatures, the electron density response is stronger for a given electrostatic perturbation. Thus, it is then ‘easier’ for the electrons to cancel out the ion density building up due to the magnetic drift velocity imbalance, which reduces the electric field and weakens the instability drive. The threshold is increased at low q due to the decreased connection length qR , increasing the transit frequency of the particles from the ‘bad-curvature’ low-field-side to the stabilising ‘good-curvature’ high-field-side. \hat{s}/q also stabilises the mode due to decorrelation.

A similar bad-curvature-drive instability can occur for the trapped electron species at similar spatial scales to ITG turbulence, since trapped particles are predominantly situated in the region of bad curvature. This trapped electron mode (TEM) can lead to significant outward ion and electron heat and particle transport at high R/L_n and/or R/L_{Te} . A very similar instability also exists at electron gyroradius scales, driven unstable by electron temperature gradients [22]. This is named the ETG mode, and can drive electron heat transport.

2.3.2 H-mode

A breakthrough in achieving increased tokamak confinement was the discovery of the so-called ‘H-mode’ (high-confinement-mode) in 1982 at the ASDEX tokamak [23]. In this regime, achieved when heating power above a certain threshold is introduced, the plasma self-organises into a state where turbulence is highly suppressed in a narrow region towards the plasma edge. This region is named the ‘edge transport barrier’, or the ‘pedestal’. In the region between the pedestal and the magnetic axis, the standard turbulent transport regime still holds. Tokamak temperature profiles tend to be constrained towards their critical inverse gradient thresholds, a property called ‘stiffness’. The core temperatures are thus often effectively proportional to the pedestal height. The increase in core plasma pressures, due to the H-mode pedestal and profile stiffness, approximately doubles the confinement time. Understanding the precise physics mechanisms which lead to pedestal formation is still an intense area of research. There is strong evidence that the formation of strong plasma rotation shear (flow shear) in the pedestal region plays a critical role in stabilizing the underlying turbulence [24].

The pedestal gradient is limited by MHD modes, thought to be peeling-ballooning modes [25]. These modes give rise to periodic violent outbursts of plasma from the pedestal, known as edge localised modes (ELMs). This poses a challenge to wall survivability and must be controlled in a reactor, a topic of ongoing research [26].

2.3.3 Tokamak operational scenarios

Worldwide progress in tokamak research has been steady since the concept was established as the leading MCF concept following the successful measurements of $\sim 1keV$ temperatures at the T3 tokamak in the Soviet Union in 1969 [27]. Progress is quantified by both the Lawson triple product $n_e T \tau_E$, as well as the fusion gain factor $Q \equiv \frac{P_{fus}}{P_{in}}$, the ratio of the fusion power produced to the tokamak input power. This is illustrated in figure 2.4. The world record for fusion power generation is $16MW$, set in 1997 at the Joint European Tokamak (JET) [28]. The next step in tokamak research is ITER (Latin for *the way*), presently under construction in Cadarache, France, which aims (at the time of writing) to produce first plasma by 2020. The goal of ITER is to produce 500 MW of fusion power with 50 MW power input, thus $Q = 10$, for a discharge time of 300 s [29]. The first fusion DT experiments are planned by 2027. ITER also plans to test necessary reactor technology, such as tritium breeding blankets. If ITER is successful, the construction of electricity producing demonstration fusion reactors can follow. From a wide database of tokamak discharges, a widely used empirical scaling law has been established that predicts the confinement time based on dimensional parameters such as total plasma current and magnetic fields [30]:

$$\tau_{IPB98(y,2)} = 5.62 \times 10^{-2} \cdot I^{0.93} B^{0.15} P^{-0.69} n^{0.41} M^{0.19} R_0^{1.97} \epsilon^{0.58} \kappa^{0.78} \quad (2.10)$$

where I is the total plasma current, B the magnetic field, P the input power, n the line averaged plasma density, M the average ion mass, R_0 the major radius, ϵ the separatrix aspect ratio $\epsilon \equiv a/R$, and κ the separatrix elongation $\kappa \equiv \frac{Z_{max} - Z_{min}}{R_{max} - R_{min}}$, where R and Z are separatrix coordinates. The ‘H-factor’ is a measure of plasma performance compared to the scaling law:

$$H_{98} \equiv \frac{\tau_E}{\tau_{IPB98(y,2)}} \quad (2.11)$$

where τ_E is the actual confinement time of the discharge.

Plasma discharges can be classified into a number of different scenarios, of which a few are listed below. They differ primarily in the heating power and in the q-profile. Schematics of the pressure profiles and q-profiles associated with the various scenarios are shown in figure 2.5.

L-mode A typically low power scenario without a edge transport barrier (pedestal). $H_{98} \sim 0.5$ in this case. Typically the initial and final phase of tokamak discharges, the current ramp-up and ramp-down phases, are in L-mode. Once sufficient power is applied to reach high plasma stored energy, the H-mode can form.

Inductive H-mode High current, high power discharges that typically provide the highest confinement times for a given machine. $H_{98} \sim 1$. The ITER $Q = 10$ target is planned with this scenario. The disadvantage of the scenario is the existence of periodic MHD instabilities which can reduce confinement. The high currents associated the scenario leads to a q-profile that dips below 1 in the inner core region. This instigates a periodic instability called the ‘sawtooth’ which reorganises the

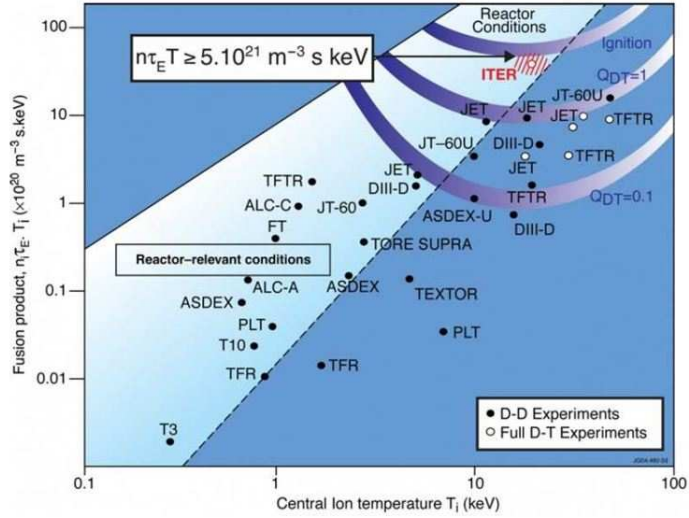


Figure 2.4: The steady progress achieved by tokamaks since 1969, as quantified by the central ion temperature and Lawson triple product. The points designated not reactor relevant correspond to transient periods in a discharge. ITER is currently under construction, and its performance is extrapolated. (Source: EFDA-JET)

plasma profiles, flattening the pressure profiles within the $q < 1$ region [31, 32]. If β is sufficiently high, the sawteeth can seed neoclassical tearing modes (NTMs) which lead to the formation of magnetic islands, reducing plasma confinement. In future devices such as ITER, it is crucial to control these NTMs by the dedicated injection of RF heating and current drive onto the magnetic islands [33], or by controlling the triggering sawtooth instability [34].

Steady State Scenario Another drawback of the standard H-mode scenario is need to draw inductive current from the central transformer, which limits the pulse time of the machine and reduces reactor relevance. Furthermore, thermal fatigue in a pulsed machine could increase the necessary machine maintenance. In the steady state scenario, the toroidal current is generated by non-inductive means. The external current drive is increased, and critically the internal bootstrap current is increased significantly. The necessary bootstrap current is created by inducing an internal transport barrier (ITB), where in a narrow region of the core plasma the microinstability transport is significantly reduced, similarly (and often in addition to) the H-mode edge barrier [35]. The high pressure gradients within the ITB significantly increases the bootstrap current fraction. The ITB is typically formed by setting up a region of negative magnetic shear, which is highly stabilising for the microinstabilities [36]. Plasma rotation has also been observed to be correlated with ITB formation [37]. The target q -profile of the steady state scenario demands

lower plasma current, and thus according to Eq.2.10 the confinement time is reduced. This is compensated by the ITB, which raises H_{98} to high values, up to $H_{98} \sim 2$. The drawback of the steady state scenarios is the need for combined control of the pressure profile and current profile. The scenarios are also susceptible to MHD instabilities.

Hybrid scenario The middle ground between the standard H-mode and steady state scenarios is named the ‘hybrid scenario’ [38]. Many of the problems associated with scenario control are abated by removing the need for an ITB. The discharge pulse time is significantly increased by both reducing the total plasma current (although not to the degree done by the steady state scenario), and increasing the external current drive fraction. Hybrid scenario q-profiles have a wide region of $q \sim 1$, and high magnetic shear towards the edge. Maintaining $q \sim 1$ reduces the risk of the deleterious MHD modes such as sawteeth and NTMs. High \hat{s}/q in the outer radii is also predicted to improve the stability of ITG turbulence, as according to Eq. 2.9. H_{98} factors reached in hybrid scenarios range from $H_{98} = 1 - 1.5$. The reasons for the improved confinement are still under debate. It is thought that low core \hat{s} at inner radii, high \hat{s}/q at outer radii, high rotation shear (which is typically associated with hybrid discharges), and the lack of deleterious MHD activity can all play a role in improved hybrid confinement. This question provides the motivation for the research carried out in this thesis, as laid out in Chap.1. The improved H_{98} in hybrid discharges holds great promise for the extrapolation of this scenario to ITER and beyond, and may pave a role towards a long-pulse reactor scenario.

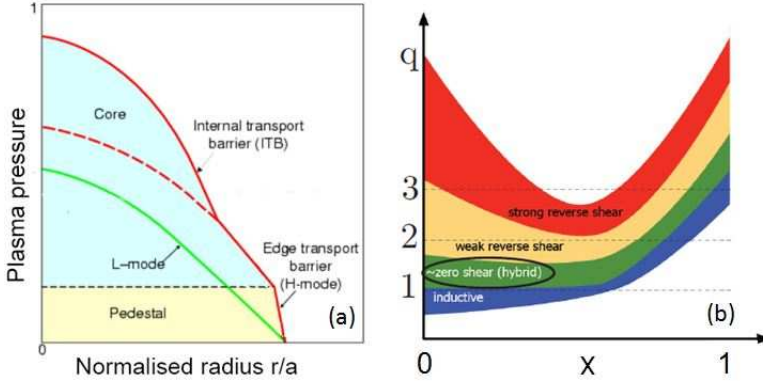


Figure 2.5: The schematic dependence of plasma pressure profiles on transport barriers is shown in (a). The range of (schematic) q-profiles corresponding to the various operational scenarios are illustrated in (b). Steady-state scenarios can correspond to both weakly and strongly reversed q-profiles with negative magnetic shear. ITG physics with hybrid-like q-profile is a recurring theme in this thesis. (Source: EFDA-JET)

2.4 Transport modelling

The ability to predict tokamak current, temperature, density, and rotation profiles (collectively known as kinetic profiles) is important for both the interpretation of current tokamak discharges and extrapolation to future machines. For brevity, we will exclude rotation (angular momentum) transport from the subsequent discussions, as no angular momentum transport calculations were carried out within the framework of this thesis.

The transport equations can be approximated as 1D diffusion equations, where the metric of the 1D grid is set by the self-consistently calculated 2D flux surface geometry. Codes which operate within this framework are thus known as 1.5D transport codes. ‘Integrated modelling’ codes also include calculations of the various sources in the equations, such as current drive and heating sources, and can simulate entire tokamak discharges. Much of the work in this thesis is carried out with the CRONOS integrated modelling code [39], introduced briefly in section 2.4.1. The calculation of the ‘anomalous’ heat and particle transport coefficients due to turbulence is a major aspect of such simulations. For speed and convenience empirical or semi-empirical transport coefficients can be used. The most accurate theoretical transport predictions are however provided by full non-linear simulations, as performed for example by the GENE [40] code introduced in section 2.4.2. Unfortunately, for integrated modelling applications such non-linear calculations are computationally prohibitively expensive since the transport time-scales are orders of magnitude greater than the fluctuation timescales of the underlying turbulence. More tractable theory based calculations, still based on first-principles, are thus commonly used. Two such ‘quasi-linear’ models used and studied in this thesis are introduced in section 2.4.3.

2.4.1 Integrated modelling - CRONOS

The heart of CRONOS is the 1D diffusion equation solver, to which multiple physics modules are attached which calculate the various terms in the equations. The 1D ‘radial’ coordinate is the toroidal flux coordinate $\rho = \sqrt{\frac{\phi}{\pi B_0}}$, where ϕ is the flux surface dependent toroidal magnetic flux, and B_0 is the vacuum magnetic field in the geometrical centre of the tokamak poloidal cross section. In CRONOS, this grid is normalized as $x = \frac{\rho}{\rho_m}$, where ρ_m is the value of ρ at the last closed flux surface, which may change in time if the volume and/or shape of the plasma itself changes.

The current diffusion equation is solved in terms of the poloidal flux ψ , where $\psi = \frac{1}{2\pi} \int \mathbf{B} \cdot d\mathbf{S}$, and the surface integral is carried out on the toroidal midplane up to the edge of a given flux surface. The current diffusion equation is as follows:

$$\begin{aligned} \frac{\partial \psi}{\partial t} = & \frac{\langle |\nabla \rho|^2 / R^2 \rangle}{\mu_0 \sigma_{\parallel} \rho_m^2 \langle 1/R^2 \rangle} \frac{\partial^2 \psi}{\partial x^2} + \left\{ \frac{\langle |\nabla \rho|^2 / R^2 \rangle}{\mu_0 \sigma_{\parallel} \rho_m^2 \langle 1/R^2 \rangle} \frac{\partial}{\partial x} \times \right. \\ & \left. \left[\ln \frac{V' \langle |\nabla \rho|^2 / R^2 \rangle}{F} \right] + \frac{x}{\rho_m} \frac{d\rho_m}{dt} \right\} \frac{\partial \psi}{\partial x} + \frac{B_0}{\sigma_{\parallel} F \langle 1/R^2 \rangle} j_{ni} \end{aligned} \quad (2.12)$$

The geometric quantity $\nabla\rho$, the volume enclosed by two neighbouring flux surfaces V' , and the flux surface averaging operator $\langle \rangle$, all depend on the solution of the flux surface geometry. This is typically carried out in CRONOS by the HELENA code [41], which solves the flux surface equilibrium for a prescribed separatrix boundary. σ_{\parallel} is the parallel conductivity, $F = RB_{\varphi}$ is the ‘diamagnetic function’, and j_{ni} is the noninductive current density at radius x set by the bootstrap current and external current sources such as NBI and RF wave injection. The conductivity and bootstrap current is calculated in a separate neoclassical transport module, such as NCLASS [42]. The external current sources are also calculated in dedicated modules for each of the separate current drive sources applied.

In CRONOS, the particle transport is formulated for the electron species only. The ability to separately model multiple ion species in CRONOS is currently in development. Presently, if multiple species are present, the quantity $Z_{eff} \equiv \sum_j q_j^2 \tilde{n}_j$ is prescribed (where j is an ion species index, q_j the ion charges, and \tilde{n}_j are the ion densities normalised to the electron density), relative ion density ratios are prescribed (when more than 2 ion species are present), and the ion densities are then calculated by invoking the quasineutrality constraint. The exception is helium transport in simulations that include fusion reactions, where a separate helium transport equation is solved. The particle transport equation is as follows:

$$\frac{\partial}{\partial t} (V' n_e) + \frac{\partial}{\partial \rho} \left(V' \langle |\nabla\rho|^2 \rangle \Gamma_e \right) = V' S_{ne} \quad (2.13)$$

Γ_e is the electron flux, and S_{ne} is the particle source due to NBI or gas puffing.

The electron and ion heat equations are as follows:

$$\frac{3}{2} \frac{\partial}{\partial t} \left(P_{e,i} V'^{\frac{5}{3}} \right) + V'^{\frac{2}{3}} \frac{\partial}{\partial \rho} \left[V' \langle |\nabla\rho|^2 \rangle q_{e,i} \right] = V'^{\frac{5}{3}} Q_{e,i} \quad (2.14)$$

$P_{e,i}$ are the electron and ion pressures. $q_{e,i}$ are the total electron and ion heat fluxes, and $Q_{e,i}$ are the heat sources. External heat sources are calculated in dedicated modules. Electron-ion heat exchange can also be an important heat source or sink if the collisionality is sufficiently high.

2.4.2 Gyrokinetic modelling - GENE

The most accurate calculations of the particle and heat fluxes are from direct numerical simulation of the kinetic equations. The ‘Eulerian’ approach solves the particle distribution functions directly. The starting point for this approach is the second lowest order truncation of the BBGKY hierarchy derived from the full N-particle Liouville equation, the collisional Vlasov equation [43]:

$$\frac{\partial f_s}{\partial t} + \mathbf{v} \cdot \nabla_x f_s + \frac{\mathbf{E} + \mathbf{v} \times \mathbf{B}}{m_s} \cdot \nabla_v f_s = C(f_j) \quad (2.15)$$

which describes the evolution of the single particle 6D distribution function, under the influence of the Lorentz force and purely binary collisions (i.e. ignoring 3 particle correlations or more - well justified for hot and diffuse fusion plasmas). This system is closed

by Maxwell's equations, where the charges and currents are self-consistently calculated from the distribution function.

$$\begin{aligned}\rho &= \sum_j q_j \int f_j d\mathbf{v} \\ j &= \sum_j q_j \int v f_j d\mathbf{v}\end{aligned}\tag{2.16}$$

The complexity of the system can be further reduced. The dynamics of interest (microinstabilities) are of low frequency compared to the gyrofrequencies. The particle trajectories can thus be spatially averaged over their gyromotion. The kinetic description is then reduced from a description of the gyrating particles to a description of rings of charge around the gyrocentre. This constitutes gyrokinetics [44]. The dimensionality of the system is reduced to 5D, and the minimum simulation timestep necessary to resolve the dynamics is significantly increased. This allows for tractable simulation of the system, albeit on massively parallel large-scale computing systems with typically $10^3 - 10^5$ CPU hours per run (depending on the additional approximations) to obtain the turbulent fluxes for a given input parameter set.

The anisotropy of the turbulent structures in tokamaks, with $k_{\parallel} \ll k_{\perp}$, allows the formulation of field line aligned coordinates with a reduced number of grid points in the parallel direction, further reducing the computational time. The distribution function f_s can also be split into a slowly evolving mean background distribution (typically Maxwellian) and a small, rapidly fluctuating part responsible for the transport: $f_s = F_{s0} + \delta f_s$. For a given background, the (now 5D) Vlasov equation can be recast for δf_s . The validity of these approximations is encapsulated by the gyrokinetic ordering with small parameters $\epsilon_B, \epsilon_{\omega}$ and ϵ_{δ} (from Ref. [44]):

$$\begin{aligned}\frac{\rho_i}{L_B} &\sim \epsilon_B \\ \frac{\omega}{\Omega_i} &\sim \epsilon_{\omega} \\ \frac{\delta f_s}{F_{s0}} \sim \frac{e\delta\phi}{T_e} \sim \frac{|\delta\mathbf{B}|}{|\mathbf{B}_0|} &\sim \epsilon_{\delta} \\ k_{\perp} \rho_i &\sim \epsilon_{\perp} \sim O(1) \\ \frac{k_{\parallel}}{k_{\perp}} &\sim \frac{\epsilon_{\omega}}{\epsilon_{\perp}}\end{aligned}\tag{2.17}$$

L_B is the magnetic field scale length, ω the instability frequency, Ω_i the ion gyrofrequency, $\delta\phi$ the electrostatic potential perturbation, and $\delta\mathbf{B}$ the magnetic field perturbation. Both ϵ_{ω} and ϵ_{δ} are of the order 10^{-3} for typical tokamak parameters. The last relation is motivated by the requirement that $\omega \sim k_{\parallel} v_{th}$ such that Landau damping in the parallel dynamics can be captured.

The GENE code (Gyrokinetic Electromagnetic Numerical Experiment) is one such Eulerian implementation for evolving the non-linear gyrokinetic system of equations [40].

In GENE, a linearized version of the equations can also be evaluated such that the growth rates and frequencies of the underlying instabilities can be studied. For a given set of input parameters (plasma gradient lengths, q -profile, flux surface geometry, etc.), δf is evolved, and the particle and heat diffusivities are calculated from the time averages of the eventual saturated state of the turbulence. More detailed information on the underlying structure of the turbulence, e.g. the frequency and k -space spectra of the fluctuations, can be calculated directly from the simulated distribution functions. The code can simulate multiple particle species simultaneously, important for a full kinetic description of electrons and impurity species. In the electrostatic limit for the study of ion heat fluxes, a reduction in computational complexity can be gained by evolving only the ion distribution function, and assuming an adiabatic response for the electrons - i.e. neglecting electron inertia, and assuming an instantaneous Boltzmann response to the electrostatic potential: $\frac{\delta n_e}{n_e} = \frac{e\delta\phi}{T_e}$. For the work carried out in this thesis, GENE has been used in its local version, where the turbulence around a single flux surface is calculated assuming that the background gradient scale lengths are larger than the turbulence scale lengths. For more complete descriptions of the underlying theory and numerical implementation in GENE, see Ref. [40] and references therein, as well as Ref. [45–48].

Given the computational expense for the simulations, it is impractical to routinely apply non-linear gyrokinetic simulations for Γ_e and $q_{e,i}$ calculations within an integrated modelling framework. Such a task demands multiple calculations for different radii and for time-evolving parameters. Gyrokinetic simulations are however vital for detailed study of the non-linear physics of tokamak turbulence, which can be compared to experimental results and also used to validate simplified transport models. GENE has been used in this thesis for both these purposes. The framework for simplified ‘quasi-linear’ transport models is introduced in the next section.

2.4.3 Quasi-linear transport models

Quasi-linear transport models assume that the non-linear saturated turbulent state can be described partly from linear characteristics calculated by linearising the underlying equations. Added assumptions guided by non-linear simulations then incorporate the unavoidable non-linear physics. To illustrate this, we write the general definition of the various fluxes for electrostatic turbulence at a given scale length denoted by wavenumber k . We assume harmonic fluctuations, $\delta n, \delta P_{e,i}, \delta\phi \propto e^{-i(\omega t - \mathbf{k} \cdot \mathbf{x})}$. For the particle flux we obtain:

$$\Gamma_e(k) = Re\langle \delta n_e \delta v_r \rangle = Re\langle \delta n_e \frac{ik\delta\phi}{B} \rangle \quad (2.18)$$

δv_r is from the fluctuating $E \times B$ drifts, hence $\delta v_r = \frac{\delta E_y}{B} = \frac{ik\delta\phi}{B}$, where y denotes the direction binormal to the magnetic field and the radial direction. The averaging is over time and the flux surface. The time averaging is carried out on a time-scale between the fluctuation and transport time-scales, such that the diffusivities are defined for static zeroth order parameters. Similarly for the heat fluxes:

$$Q_{e,i}(k) = Re\langle \frac{3}{2} \delta P_{e,i} \frac{ik\delta\phi}{B} \rangle \quad (2.19)$$

If the fluctuating quantities have the same phase, then the transport is equal to zero due to the averaging over $\cos(\omega t)$ $\sin(\omega t)$. Now comes the crux. δn , $\delta P_{e,i}$, and $\delta\phi$ can differ in phase and relative amplitude. The quasi-linear assumption is that these relations are taken from the solutions of the linearised equations describing the system. Summing over all unstable modes and frequencies (since due to non-linear broadening mechanisms more than one frequency may be present for a given k [43]), the quasilinear fluxes can be decomposed as:

$$(\Gamma_e, Q_e, Q_i) = \sum_{k,\omega} (Linear\ Response)_{k,\omega}^{(\Gamma_e, Q_e, Q_i)} \otimes |\delta\phi|_{k,\omega}^2 \quad (2.20)$$

The saturated electrostatic potential, $|\phi|_{k,\omega}^2$, is a quantity that is not possible to gauge from the linear physics. The choice for $|\phi|_{k,\omega}^2$ typically invokes a random walk argument where the random walk time-step at each spatial scale is assumed to be $\frac{1}{\gamma_k}$ (γ_k is the growth-rate for the mode with wavenumber k), and the step size is assumed to be $\frac{1}{k}$. Thus $D_k \sim |\delta\phi_k|^2 \sim \frac{\gamma_k}{k^2}$. The precise details of the mixing length rule [49], involving the assumptions on the k -space and frequency spectra of $\delta\phi$, as well as other factors which approximate additional non-linear phenomena such as zonal flows, depend on the precise model. These choices are guided by or fitted to the results of full non-linear simulations.

In summary, quasilinear theory assumes that the turbulence can be described by an ensemble of modes which retain their linear characteristics, but where the precise spectra and amplitudes of the modes are set by non-linear physics, which must then be incorporated in an ad-hoc manner into the model with the guidance of non-linear theory and simulations. The details of two specific quasilinear models applied in this thesis are now briefly presented.

GLF23

The system solved is the four-moment GLF (Gyro-Landau-Fluid) system of equations [50, 51]. Moments are taken of the Vlasov equation, which leads to a fluid description. The fluid closures involve terms which replicate the full kinetic response, taking into account effects such as Landau damping. The electrostatic potentials in the model are multiplied by factors that approximate the finite Larmor radius effects, where small-scale perturbations are zeroed out by the gyroaveraging. Solving a fluid system of equations provides a significant reduction in computational complexity compared with the gyrokinetic equation.

The GLF23 model [52] solves the eigenvalue problem of the linearised system of GLF equations. The mode structure (eigenmode) is not solved self-consistently, and is prescribed by trial functions with fitting parameters chosen such that the growth rates agree with full linear gyrokinetic calculations. The GLF23 mixing length rule is:

$$|\phi_k|^2 \propto \gamma_{net}^{1/2} \gamma_d^{1/2} / k_y^2 \quad (2.21)$$

The ‘net’ growth rate γ_{net} takes into account the stabilising effect of flow shear: $\gamma_{net} \equiv \gamma_k - \alpha_E \gamma_E$, where γ_k is the calculated growth rate at wavenumber k , and γ_E

is the flow shear. For pure toroidal rotation (as is often the case for NBI driven rotation) $\gamma_E = \frac{r}{q} \frac{d\Omega}{dr}$, where Ω is the angular velocity. The precise value and parameterisation for α_E is uncertain, and values ranging from 0.5 – 1.5 are typically used in simulations. $\gamma_d = 0.2 \frac{3}{2} \frac{T_i}{T_e} |\omega_d|$ approximates the damping effect of zonal flows, where $|\omega_d|$ is the magnetic drift frequency. No frequency broadening for the fluctuating potential is assumed in the GLF23 model.

QuaLiKiz

The QuaLiKiz transport model [53] is based on the linear electrostatic gyrokinetic eigenvalue solver Kinezero [54]. Solving the linear gyrokinetic equation directly is computationally more expensive than the fluid system, but simultaneously involves a minimum of fitting factors compared to the GLF models. The formalism in which both the growth rates and the quasi-linear fluxes are calculated is now very briefly expounded.

The starting point is again the Vlasov equation. The physical picture can be sufficiently elucidated by taking the electrostatic, collisionless case:

$$\frac{\partial f_s}{\partial t} + \mathbf{v} \cdot \nabla_x f_s + \frac{q}{m_s} \mathbf{E} \cdot \nabla_v f_j = 0 \quad (2.22)$$

where $\mathbf{E} = \nabla \phi$ is an $O(\epsilon)$ fluctuating quantity. Setting $f_s = F_{0s} + \delta f_s$, and linearising with a single harmonic fluctuation $\delta f = \delta f_{\mathbf{k}} e^{-i(\omega t - \mathbf{k} \cdot \mathbf{x})}$, we obtain the $O(\epsilon)$ linear response for $\delta f_{\mathbf{k}, \omega}$:

$$\delta f_{s, \mathbf{k}, \omega} = -\frac{q_s}{m_s} \frac{\mathbf{k} \cdot \nabla_v F_0}{\omega - \mathbf{v} \cdot \mathbf{k}} \delta \phi_{\mathbf{k}} \quad (2.23)$$

The quasineutrality constraint for a given mode is:

$$\sum_s q_s \delta n_{k, s} = \sum_s q_s \int d\mathbf{v} \delta f_{s, \mathbf{k}, \omega} = -\sum_s \frac{q_s^2}{m_s} \int d\mathbf{v} \frac{\mathbf{k} \cdot \nabla_v F_0}{\omega - \mathbf{v} \cdot \mathbf{k}} \delta \phi_{\mathbf{k}} = 0 \quad (2.24)$$

Where we have substituted the linear response for $\delta f_{\mathbf{k}, \omega}$ from Eq.2.23 in the last step above. The equation is reduced to solely depend on ω by integrating over space. This integrates over the radial mode structure of $\delta \phi_k$ and also over the space-dependent drift velocities in \mathbf{v} . We are then left with the dispersion equation for $\omega(\mathbf{k})$:

$$\sum_s \frac{q_s^2}{m_s} \int d\mathbf{x} d\mathbf{v} \frac{(\mathbf{k} \cdot \nabla_v F_0)}{\omega - \mathbf{v} \cdot \mathbf{k} + i0^+} \delta \phi_{\mathbf{k}} = 0 \quad (2.25)$$

The solution is $\omega = \omega_r + i\gamma$, obtained for a given wavenumber k . For positive γ , this constitutes an instability. The equation can be reduced to a 5D coordinate system by averaging over the gyroangle coordinate. In Fourier space this will simply result in Bessel functions $J_0(k_\perp \rho_s)$ multiplying the electrostatic potential, capturing the finite Larmor radius effects. To reduce computational complexity, the mode structure of $\delta \phi_{\mathbf{k}, \omega}(\mathbf{x})$ is not self-consistently calculated in QuaLiKiz. The mode structure is prescribed according

to a solution of the fluid limit of the gyrokinetic equation. The $i0^+$ term in the denominator of Eq.2.25 determines the position of the pole when carrying out the integration, and physically corresponds to a vanishing small growth rate such that the fluctuation disappears as $t \rightarrow -\infty$, necessary for causality.

To illustrate the calculation of the quasilinear fluxes we take the particle flux as an example. For a given mode, the definition of the particle flux is:

$$\Gamma_{sk} = Re \langle \delta n_s \frac{ik\delta\phi}{B} \rangle \quad (2.26)$$

δn_s is the first moment (velocity integration) of the linear response Eq.2.23. This is substituted into Eq.2.26, to obtain:

$$\Gamma_s = -Re \left(i \frac{q_s}{Bm_s} \sum_k \int d\omega \int d\mathbf{v} \frac{|k| (\mathbf{k} \cdot \nabla_v F_0) J_0(k_\perp \rho_s) |\delta\phi_{\mathbf{k}}|^2 \frac{\gamma_k}{(\omega - \omega_k)^2 + \gamma_k^2}}{\omega - \mathbf{v} \cdot \mathbf{k} + i0^+} \right) \quad (2.27)$$

where all unstable modes are summed over (practically speaking, a finite number of modes are summed over in the flux calculations), as well as the frequency spectrum for each mode. F_0 is taken as a Maxwellian function. A broadened frequency spectrum has been introduced here for $\delta\phi_{\mathbf{k},\omega}$, assumed to be a Lorentzian with a width equal to the growth rate. This assumption approximates stochastic non-linear effects which lead to the resonance broadening. The mixing length rule for $|\delta\phi_{\mathbf{k}}|^2$ is of the form γ_k/k_\perp^2 , with an assumed spectral shape that simulates the non-linear k-space flux spectrum. A single constant normalises the fluxes to equal the gyrokinetic non-linear prediction of a standard benchmark case, the ‘GA-standard case’. For deeper details of the specifics of the model, see Refs. [55, 56], as well as Chap. 5 in this thesis.

References

- [1] T. Ihli *et al.*, 2008 *Fusion Eng. Des.*, **83** 912.
- [2] D. Fasei and M.Q. Tran, 2005 *Fusion Eng. Des.*, **75-79** 1163.
- [3] H. Tanigawa *et al.*, 2011 *J. Nucl. Mater.*, **417** 9.
- [4] J.D. Lawson, 1957 *Proc. Phys. Soc. B*, **70**(1) 6.
- [5] M.G. Haines, 1997 *Astrophys Space Sci.* **256** 125.
- [6] A.G. Peeters, 2000 *Plasma Phys. Control. Fusion* **42** B231.
- [7] R.J. Goldston and P.H. Rutherford, 1995 *Introduction to Plasma Physics*. (Taylor & Francis).
- [8] W. Horton, 1999 *Rev. Mod. Phys.* **71** 735.
- [9] S.P. Hirshman and D.J. Sigmar, 1981 *Nucl. Fusion* **21** 1079.
- [10] P. Diamond, S-I. Itoh, K.Itoh and T.S. Hahm, 2005 *Plasma Phys. Control. Fusion* **47** R31.
- [11] C. Surko, 1983 *Science* **221** 817.
- [12] S.C. Cowley and R.M. Kulsrud, 1991 *Phys. Fluid B* **3** 10.
- [13] F. Troyon, A. Roy, W.A. Cooper, F. Yasseen and A. Turnbull, 2000 *Plasma Phys. Control. Fusion* **30** 1597.
- [14] M. Greenwald *et al.*, 1988 *Nucl. Fusion* **28** 2199.
- [15] F. Romanelli, 1989 *Phys. Fluids B* **1** 1018.
- [16] H. Biglari, P.H. Diamond and M.N. Rosenbluth, 1989 *Phys. Fluids B* **1** 109.
- [17] X. Garbet, 1992 *Phys. Fluids B* **1** 136.
- [18] S.C. Guo and F. Romanelli, 1993 *Physics of Fluids B* **5** 520.
- [19] B. Coppi and F. Pegoraro, 1977 *Nucl. Fusion* **17** 5.
- [20] M.N. Rosenbluth and C.L. Longmire, 1957 *Annals Phys.* **1** 120.
- [21] A. Casati *et al.*, 2008 *Phys. Plasmas* **15** 042310.
- [22] F. Jenko *et al.*, 2001 *Phys. Plasmas* **8** 4096.
- [23] F. Wagner, W. Dorland and G.W. Hammett 2007 *Plasma Phys. Control. Fusion* **49** B1.
- [24] K.H. Burrell, 1997 *Phys. Plasmas* **4** 1499.
- [25] P.B. Snyder, H.R. Wilson, and X.Q. Xu 2007 *Phys. Plasmas* **12** 056115.
- [26] T.E. Evans *et al.*, 2004 *Phys. Rev. Lett.* **92** 235003.
- [27] N.J. Peacock, D.C. Robinson, M.J. Forrest, P.D. Wilcock and V.V. Sannikov, 1969 *Nature* **224** 488.
- [28] A. Gibson, 1997 *Phys. Plasmas* **5** 1839.
- [29] M. Shimada *et al.*, Progress in the ITER Physics Basis Chapter 1: Overview and summary, 2007 *Nucl. Fusion* **47** S1.
- [30] ITER Physics Expert Group on Confinement *et al.*, ITER Physics Basis Chapter 2: Plasma confinement and transport, 1999 *Nucl. Fusion* **39** 2175.

- [31] S. von Goeler, W. Stodiek and N. Sauthoff, 1974 *Phys. Rev. Lett.* **33** 1201.
- [32] R.J. Hastie, 1997 *Astrophys Space Sci.* **256** 177.
- [33] R.J. La Haye, 2006 *Phys. Plasmas* **13** 055501.
- [34] O. Sauter et al., 2002 *Phys. Rev. Lett.* **88** 105001.
- [35] J.W. Connor et al., 2004 *Nucl. Fusion* **44** R1.
- [36] T.M. Antonsen 1996 *Phys. Plasmas* **3** 2221.
- [37] P.C. de Vries et al., 2009 *Nucl. Fusion* **49** 075007.
- [38] C. Gormezano et al., 2007, Progress in the ITER Physics Basis Chapter 6: Steady state operation *Nucl. Fusion* **47** S285.
- [39] J.F. Artaud et al., 2010 *Nucl. Fusion* **50** 043001.
- [40] F. Jenko, W. Dorland, M. Kotschenreuther and B.N. Rogers 2000 *Phys. Plasmas* **7** 1904, and <http://gene.rzg.mpg.de>.
- [41] G.T.A. Huysmans, J.P. Goedbloed and W. Kerner, 1991 *CP90 Conf. on Comp. Physics (Singapore: Word Scientific)* p 371.
- [42] W.A. Houlberg, K.C. Shaing, S.P. Hirshman and M.C. Zarnstroff, 1997 *Phys. Plasmas* **4** 3230.
- [43] J.A. Krommes, 2002 *Physics Reports* 360 1-352.
- [44] A.J. Brizard and T.S. Hahm, 2007 *Rev. Mod. Phys.* **79** 421–468.
- [45] T. Görler, 2009, PhD Thesis, Universität Ulm.
- [46] M.J. Pueschel, 2009, PhD Thesis, Universität Münster.
- [47] F. Merz, 2009, PhD Thesis, Universität Münster.
- [48] D. Told, 2012, PhD Thesis, Universität Ulm.
- [49] B.B. Kadomtsev., 1965. Plasma Turbulence. Academic Press, New York. (translated by L.C. Ronson from the 1964 Russian edition, in: Leontovich, M.A., Rusbridge, M.C. (Eds.), Problems in Plasma Theory Trans.).
- [50] R.E. Waltz, G.D. Kerbel and J. Milovich, 1994 *Phys. Plasmas* **1** 2229.
- [51] R.E. Waltz, G.D. Kerbel, J. Milovich and G.W. Hammett, 1995 *Phys. Plasmas* **2** 2408.
- [52] R.E. Waltz et al., 1997 *Phys. Plasmas* **7** 2482.
- [53] C. Bourdelle et al., 2007 *Phys. Plasmas* **47** 14 112501.
- [54] C. Bourdelle. et al., 2002 *Nucl. Fusion* **42** 892-902.
- [55] C. Bourdelle, 2000, PhD Thesis, Université Joseph Fourier-Grenoble 1.
- [56] A. Casati, 2009, PhD Thesis, Université de Provence (Aix-Marseille I).

3 Impact of heating and current drive mix on the ITER Hybrid Scenario

J. Citrin¹, J.F. Artaud², J. Garcia², G.M.D. Hogeweij¹ and F. Imbeaux²

¹FOM Institute for Plasma Physics Rijnhuizen, Association EURATOM-FOM, Nieuwegein, The Netherlands

²CEA, IRFM, F-13108 Saint Paul Lez Durance, France

Abstract

Hybrid scenario performance in ITER is studied with the CRONOS integrated modeling suite, using the GLF23 anomalous transport model for heat transport prediction. GLF23 predicted core confinement is optimized through tailoring the q -profile shape by a careful choice of current drive actuators, affecting the transport due to the predicted dependence of the turbulence level on the absolute q -profile values and magnetic shear. A range of various heating and current drive choices are examined, as are different assumptions on the pedestal height. The optimum q -profile shape is predicted to be one that maximizes the ratio of s/q throughout the bulk of the plasma volume. Optimizing the confinement allows a minimization of the plasma density required in order to achieve a defined target fusion power of 350 MW. A lower density then allows a lower total current (I_p) at the same Greenwald fraction (f_G), thus aiding in maintaining $q > 1$ as desired in a hybrid scenario, and in minimizing the flux consumption. The best performance is achieved with a combination of NBI and ECCD (e.g. 33/37 MW NBI/ECCD for a scenario with a pedestal height of 4 keV). The q -profile shape and plasma confinement properties are shown to be highly sensitive to the positioning of the ECCD deposition. Comparisons to the lower performing cases where some or all of the ECCD power is replaced with LHCD or ICRH are shown (e.g. 33/20/17 MW NBI/ECCD/LHCD or NBI/ECCD/ICRH). The inclusion of LHCD reduces confinement due to deleterious shaping of the q -profile, and the inclusion of ICRH, particularly in a stiff model, does not lead to significantly increased fusion power and furthermore does not contribute to the non-inductive current fraction. For the optimum NBI/ECCD current drive mix, the predictions show that a satisfactory ITER hybrid scenario ($P_{fus} \sim 350$ MW, $Q \geq 5$, q_{min} close to 1) may be achieved with $T_{ped} \geq 4$ keV. In addition, predicted performance sensitivity analysis was carried out for several assumed parameters, such as Z_{eff} and density peaking.

3.1 Introduction

The ITER “hybrid” advanced scenario aims to provide a discharge with an extended burn time ($> 1000\text{ s}$) while still maintaining a moderately high fusion power ($P_{fus} > 350\text{ MW}$) and significant α -particle heating ($Q > 5$), without the drawback of the stringent active control requirements which characterize steady-state scenario discharges [1]. The primary mission of this scenario is to maximize the neutron fluence per pulse, for effective testing of reactor-relevant components [2]. The extended burn time is achieved via reducing the flux consumption by operating at both reduced current ($I_p = 11 - 13\text{ MA}$) and a higher non-inductive current fraction ($\sim 50 - 60\%$) compared to the ELMy H-mode ITER reference scenario.

Scenarios that may extrapolate to the ITER hybrid scenario have been developed over this past decade at ASDEX-U [3, 4], DIII-D [5], JET [6], and JT-60U [7]. These discharges, particularly at ASDEX-U, DIII-D, and recent experiments at JET [8], have routinely displayed thermal energy confinement improvement beyond the IPB98(y,2) scaling expression [9]:

$$\tau_{IPB98(y,2)} = 5.62 \times 10^{-2} \cdot I^{0.93} B^{0.15} P^{-0.69} n^{0.41} M^{0.19} R^{1.97} \epsilon^{0.58} \kappa^{0.78} \quad (3.1)$$

Or, expressed in dimensionless parameters:

$$\omega_{ci} \cdot \tau_{IPB98(y,2)} \propto \rho^{*-2.70} \beta^{-0.90} \nu^{*-0.01} M^{0.96} q^{-3.0} \epsilon^{0.73} \kappa^{3.3} \quad (3.2)$$

Confinement enhancement factors of $H_{98(y,2)} \sim 1 - 1.4$ have been achieved, where $H_{98(y,2)}$ is defined as the ratio between the measured thermal energy confinement time and $\tau_{IPB98(y,2)}$. These enhanced confinement scenarios may extrapolate to ITER hybrid scenarios with Q significantly in excess of the defined minimum $Q = 5$ for the ITER hybrid scenario mission [10]. A key concept in these discharges is the maintenance of a broad safety factor profile above or close to unity throughout ($q > 1$), avoiding the instigation of sawteeth thus allowing operation at higher β_N (up to the no-wall limit), without triggering deleterious NTM's. Achievement in ITER of a high Q , long pulse discharge would widen the hybrid mission by assessing the potential of the pulsed tokamak for energy production [1].

The reasons for the reported confinement enhancement are not fully understood, complicating the extrapolation of the hybrid scenario to ITER. Microturbulence theory predicts that the typical shape of the hybrid scenario q -profile - a broad $q \sim 1$ volume with increased shear towards the edge - should lead to more favourable core confinement [11, 12]. This points to a potential over-simplification in using purely I_p in the $IPB(y, 2)$ scaling expression, due to the influence of the current profile shape itself on the confinement properties. Experimental support for the role of the current profile shape in improving core confinement has been seen at ASDEX-U [13], as well as in recent q -profile shaping experiments at JET [8], and at HL-2A [14]. Other analysis of ASDEX-U discharges has pointed to the role of pedestal confinement improvement at high power as being responsible for the global confinement enhancement [15, 16], pointing to the potential non-applicability of the $IPB98(y, 2)$ scaling expression at high β_N . However, in

[16], it was still suggested that a combination of pedestal *and* core confinement enhancement is present. With regard to the role of $E \times B$ flow shear, the influence of toroidal rotation on energy confinement was isolated in DIII-D [17], and it was found that at highly reduced rotation, $H_{98(y,2)}$ drops to 1.05.

A further complication for extrapolation of experimental hybrid scenarios to ITER is that the broad $q \sim 1$ volume observed in hybrid discharges cannot in some cases be explained by classical current diffusion. It has been suggested that MHD activity such as fishbones [4] and the $m/n = 3/2$ NTM [18, 19] leads to anomalous magnetic transport, broadening the q -profile to the observed level. While a potentially positive effect, the presently limited understanding of this phenomenon leads to difficulty in predicting its impact on the ITER hybrid scenario.

In this work, we utilize the CRONOS [20] integrated modelling code in order to make predictions on the ITER hybrid scenario, with particular emphasis on gauging the relative merit of various heating and current drive (H/CD) mixes, informing the choices of proposed ITER H/CD future upgrades. In light of the abovementioned difficulties in extrapolating each of the various phenomena which may potentially affect confinement, we choose to concentrate primarily on the impact of q -profile shaping on core-confinement improvement, and the influence of the various current drive mixes on the shaping. Towards this end, the GLF23 [21, 22] first-principles based transport model is applied for energy transport prediction, due to the q -profile dependence in the GLF23 predicted transport coefficients. Constant pedestal pressures are prescribed for these simulations, and no rotation is assumed, allowing for *relative* comparisons to be made between different current drive mixes and parameters at the same edge conditions and (zero) rotation profile. This assumed lack of fusion performance sensitivity to the NBI torque through $E \times B$ flow shear suppression is consistent with rotation predictions carried out with assumed Prandtl numbers $\chi_\phi/\chi_i > 0.5$ [23]. However, more optimistic assumptions of the momentum transport could lead to a significant improvement of the scenario performance [24, 25].

The outline of this paper is as follows: in section 2 we describe in further detail the modelling methodology, choices, and assumptions made, in section 3 results of the H/CD mix studies are presented, in section 4 we present sensitivity studies of the various assumptions made, and conclusions are given in section 5.

3.2 Modelling techniques and methodology

3.2.1 General philosophy of this work

The central point of this work is assessing and comparing the ability of various heating and current drive systems to provide a 'satisfactory' hybrid scenario for ITER. The target, 'satisfactory' hybrid scenario that we define here is one that provides a fusion power performance of $P_{fus} = 350 \text{ MW}$, $Q > 5$ in order to still maintain a significant degree of α -heating, $P_{loss} < \sim 110 \text{ MW}$ in order to avoid a heat flux to the divertor beyond the operational limit, and $t_{discharge} > 1000 \text{ s}$ in order to achieve high neutron fluence per

pulse. The target power of $P_{fus} = 350$ MW was specifically chosen to provide a neutron flux just above the minimum required value suitable for component testing [2], and serves as a baseline when comparing the results of simulations with varying pedestal and current drive mix prescriptions. In ITER, deleterious NTM's are predicted to be unstable even for β_N as low as 1.8, a significantly lower limit compared to present tokamaks [26]. Hence, if we are to assume a $\beta_N > 1.8$ scenario without transport reduction from NTM's, or alternatively to assume that no auxiliary power need be diverted to NTM control, we must avoid the initiation conditions of NTM triggering sawteeth. Towards this end, we aim for $q > 1$ throughout the simulations, or at least to maximize the time until a $q = 1$ surface forms and/or minimize the $q = 1$ radius at stationary state, i.e. following the relaxation of the current profile. Throughout this work we define the $q = 1$ radius as $x(q = 1)$. We will show in this work that devoting all auxiliary power to current drive and q -profile shaping is predicted to be vital for increasing both confinement and the non-inductive current fraction for pulse length optimization. We thus deem the $q > 1$ constraint as necessary for a satisfactory hybrid scenario as defined above.

For the various simulations involving different heating and current drive mixes, the plasma density is used as an actuator for controlling fusion power in order to approximately reach $P_{fus} = 350$ MW at stationary state. To maintain the same Greenwald fraction (f_G), the total current must then also be adjusted together with n_e . Therefore, we aim to determine the optimum heating and current drive mix that maximizes the core confinement and temperatures, such that a minimum n_e and thus Ohmic current is needed to achieve $P_{fus} = 350$ MW. Minimizing the Ohmic current would then raise the q -profile towards the goal outlined above. The maximum allowed f_G in the simulations is set at 0.95, slightly below the empirical Greenwald density limit [27]. If optimum simulations are achieved at $f_G < 0.95$, then the lower values are used. All radial profiles in this work are represented as a function of x , the normalized toroidal flux coordinate.

3.2.2 Models used

The core of CRONOS is a 1.5D transport solver, whereby 1D current diffusion, particle, energy, and momentum transport equations are solved up to the separatrix, self consistently with 2D magnetic equilibrium, which in these simulations is calculated by the HELENA [28] fixed boundary solver. The same fixed boundary was used for both the flat-top and ramp-up phases, and is described by $R = 6.2$ m (major radius), $a = 2$ m (minor radius), $\kappa = 1.89$ (elongation), $\delta_{upper} = 0.454$ (upper triangularity), $\delta_{lower} = 0.516$ (lower triangularity). Neoclassical transport, resistivity and bootstrap current is calculated by NCLASS [29]. Heating and current drive sources are determined as follows: NBI by NEMO, ECRH/ECCD by REMA [30] with an analytic approximation for the current drive efficiency [31], LHCD by either DELPHINE [32] or LUKE [33], and ICRH by PION [34]. Cyclotron radiation emission is calculated by EXACTEC [35]. Fusion reactions are determined by the Bosch-Hale formulation [36]. The contribution of supra-thermal fusion reactions is not considered. Anomalous transport is primarily calculated with the GLF23 model.

3.2.3 Assumptions made

The basic assumptions of these simulations are consistent with those made in the CRO-NOS simulations carried out for a recent hybrid scenario benchmarking study [37]. Maintaining these assumptions allows for a comparison to be made with the previous work. The assumptions are as follows: Equal ratios of D and T are assumed. Only electron and ion heat transport is predicted, whereas the density profile is prescribed flat (with $n_e(0)/\langle n_e \rangle = 1.03$). Rotation is set to zero - a conservative assumption. GLF23 is applied with α -stabilization off - equivalent to setting $\alpha \equiv -q^2 R_0 \mu_0 \frac{1}{B^2} \frac{dp}{dr} = 0$ within the GLF23 model. The sensitivity to this particular setting, which leads to more optimistic predictions compared with α -stabilization on, is mentioned in section 3.4.1. The pedestal temperature following the L-H transition is prescribed, and the top of the pedestal is set at $x = 0.92$. This same pedestal width is prescribed throughout all the simulations. This choice allows a comparison of the effect - at a constant pedestal height - of various heating and current drive combinations on the core confinement and q -profile evolution, while altering neither the temperature boundary conditions for GLF23 at the pedestal top nor the total value of the edge bootstrap current. The helium density profile is obtained in CRONOS by the solution of a 1D diffusion equation, where the helium diffusivity is chosen as $D_{He} = \max(\chi_e, \chi_i)$, with the anomalous component of χ_e, χ_i calculated by GLF23. The recycling source is adjusted such that we impose the He particle confinement time to global energy confinement time ratio as $\tau_{He}^*/\tau_E = 5$. Impurities are tied to the n_e profile, at assumed fractions of 2% Be and 0.12% Ar. This prescription leads to typical Z_{eff} values of ~ 1.7 . MHD effects are entirely ignored in these simulations, which excludes both the potential deleterious transport effects of NTM's and beneficial anomalous current transport effects which could in principle facilitate the maintenance of $q > 1$.

GLF23 calculates the anomalous transport in the core for radii inside the pedestal top, i.e. $x < 0.92$. However, at lower radii, within the approximate region of $x < 0.25$, no anomalous transport is predicted by GLF23, as the $T_{i,e}$ profiles retreat below the critical gradients due to the zero-derivative boundary condition on the magnetic axis. In order to correct this feature, which is not compatible with experimental observations, a moderate degree of anomalous transport is typically assumed, and in our case is set to $\chi_{ia,ea} = 0.5 \text{ m}^2 \text{ s}^{-1}$ throughout the simulations, to which the neoclassical transport is then also added. Sensitivity to this assumption is discussed in section 3.4.2, but in anticipation we note here that the volume within $x = 0.25$ corresponds to only $\sim 7.5\%$ of the total plasma volume, and a critical degree of fusion performance sensitivity is not found even if the transport is set to neoclassical levels within this region. However, the assumptions do have a significant effect on the inner q -profile.

Another factor which may affect the inner q -profile predictions is the breakdown, in the near region of the magnetic axis, of the thin banana orbit assumption intrinsic in the NCLASS resistivity and bootstrap current calculations. In this work, the NCLASS predicted resistivity and bootstrap current profiles are taken as calculated, without correction, in spite of the reduced validity of the assumptions in the magnetic axis region. On the magnetic axis itself the resistivity is calculated with a cubic spline extrapolation

of the NCLASS predicted profile. The bootstrap current on the magnetic axis is zero. In addition, we do not calculate the self-driven asymmetric current [38], which could further increase the current density in the magnetic axis region, lowering the inner q -profile.

The present study makes assumptions on the heating mix that are beyond what is projected for the ITER baseline, since one of the aims of the study is to indicate which realistic system upgrade could be applied in order to optimise the performance of the ITER hybrid scenario. The H/CD mixes assumed are comprised from the following components: 0-50 MW NBI (1 MeV, full off-axis injection [39]), 0-50 MW ECRH (equatorial launchers, angles varied between $20^\circ - 45^\circ$ [40]), 0-20 MW ICRH (53 MHz, 2nd T harmonic), and 0-40 MW LHCD (5 GHz, $n_{\parallel} = 2$). The LHCD directivity is set at 100% (i.e., the full LH power is contained in the co-current lobe of the injected spectrum at $n_{\parallel} = 2$). This optimistic assumption may lead to an overestimation of the LHCD driven current, as discussed in section 3.3.3.

3.2.4 Pedestal heights

In a stiff model such as GLF23, the fusion Q is typically a strong function of the pedestal temperature [24]. In light of the uncertainty in extrapolating the pedestal width and thus height to ITER [41], we carry out the optimization described above for a range of pedestal heights between 3-5 keV (set at $x = 0.92$). The sensitivity of the hybrid scenario to the pedestal height is twofold: lower core temperatures necessitate an increase of n_e and thus I_p in order to obtain $P_{fus} = 350$ MW; furthermore, at lower pedestals, the bootstrap current - primarily concentrated in the pedestal - would decrease, lowering the non-inductive current fraction and raising the Ohmic current further, with a deleterious consequence on our $q > 1$ goal.

3.2.5 L-mode treatment

The simulations presented in this work run between either 40-1200 s or 40-3000 s. The energy transport during the 40-100 s ramp-up phase is calculated by GLF23, in conjunction with a T_i and T_e boundary condition of typically ~ 700 eV set at $x = 0.92$, such that the H_{98} factor during the ramp-up ranges between 0.4 and 0.6. I_p is ramped linearly from 4-11.5 MA, with a ramped n_e maintaining $f_G \approx 0.5$. Different ramp-up scenarios with various H/CD mixes and waveforms were carried out, such that a scan of various initial q -profile conditions at the flat-top may be performed. An example of one such scenario is shown in Fig.3.1. The input powers in this scenario is comprised of a slow ramp of electron cyclotron injection up to a total of 17 MW at the L-H transition, with a quicker ramp to 37 MW at 140 s. 33 MW of neutral beams is initiated at the end of the ramp-up phase. In such a manner we obtain $P_{loss} \equiv P_{NBI} + P_{EC} - P_{Brem} - P_{cyclo} - 1/3 P_{rad} > P_{L-H}$ at 100 s. The $1/3$ factor preceding P_{rad} is an approximation to take into account only the radiative loss power (without Bremsstrahlung and cyclotron radiation loss terms) emitted at lower radii than the pedestal. The L-H transition is treated by initiating the full pedestal prescription at the ordained L-H transition time (usually 100 s), while simultaneously ensuring that $P_{loss} > P_{L-H}$ at the transition. P_{L-H} is taken from an empirical scaling

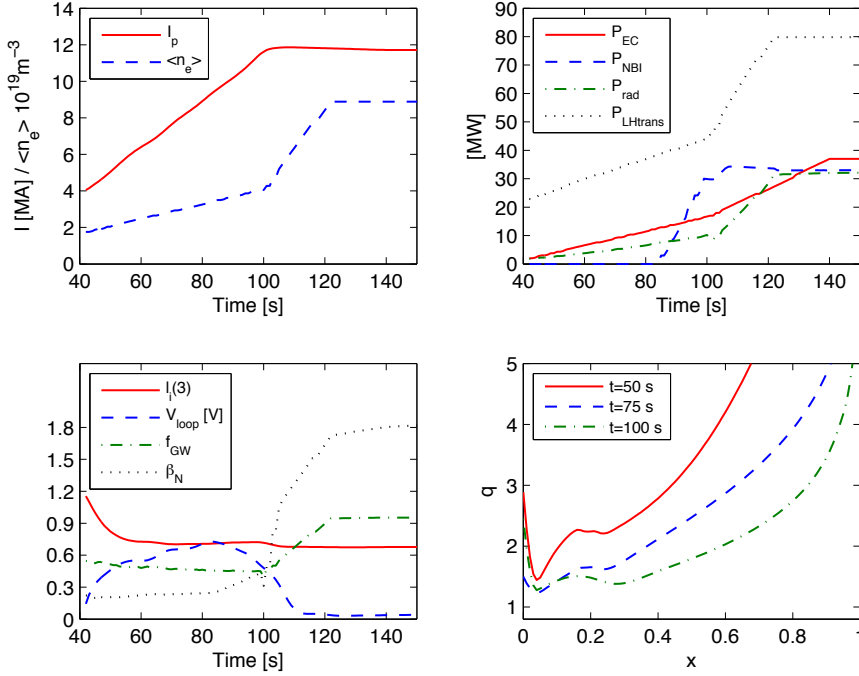


Figure 3.1: Plasma parameters and actuator waveforms for the ramp-up and L-H transition up to the flat-top, for the 'reference case' to be introduced in section 4.4. In the upper-left panel we observe the evolution of the total plasma current and the average electron density. The upper-right panel displays the powers sources and sinks (total radiation) as well as the necessary L-H transition power. The bottom-left panel displays the evolution of the loop voltage and the dimensionless parameters β_N , Greenwald fraction f_{GW} , and $l_i(3)$. The evolution of the q -profile during the rampup phase can be observed in the bottom-right panel.

law [42], and is typically ~ 45 MW at the transition. Following the L-H transition, n_e is rapidly ramped up to its flat-top value within 20 seconds. The H/CD sources are shifted to their flat-top values within 40 seconds. In some simulations the I_p values are also shifted to their final flat-top values within 40 seconds, if it is found that the necessary I_p for optimum flat-top parameters differs from the 11.5 MA value set at the L-H transition.

Self-consistency during the ramp-up with regard to the ITER $l_i(3)$ operational range of 0.65-1.2 [43] is also examined. It was found that an L-H transition before the conclusion of the I_p ramp may cause an l_i drop below the operational limit, as seen in Fig.3.2, due to an inordinate amount of current building up at high radii with slow inward diffusion due to the high temperatures.

This L-mode treatment is not intended as a definitive study of the ITER hybrid scen-

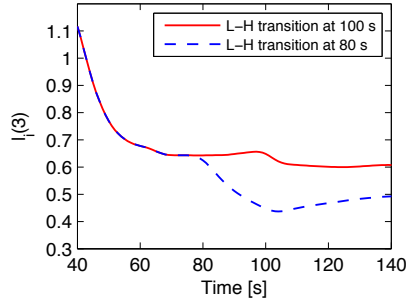


Figure 3.2: Comparison of the $l_i(3)$ evolution for 2 otherwise identical ramp-up scenarios, separated by the time prescribed for the L-H transition. The red (solid) curve, corresponding to $t_{L-H} = 100$ s, has a small kink at 100 s, due to the relatively quick redistribution of the edge current profile following the L-H transition. The blue (dashed) curve, corresponding to $t_{L-H} = 80$ s, drops to levels significantly below the l_i operational limit, peaking at 100 s, due to continued current ramp-up during the H-mode phase, during which the current diffusion time is higher.

ario ramp-up phase, which would be better served by applying a free-boundary equilibrium solver [44, 45] and starting from an early limited plasma phase, which would both assess the behaviour of the PF coil system and establish the flux-consumption during the early ramp-up phase. However, the treatment carried out here delivers a self-consistent q -profile at the beginning of the flat-top phase established through current-diffusion and the particular H/CD strategy employed, while not being dependent on the initial prescribed l_i condition and artificial q -profile set at the beginning of the simulation at $t = 40$ s. This can be seen in Fig.3.3, where by the end of the ramp-up, memory of the initial l_i condition has been mostly lost. The l_i values converge to within 5% of each other.

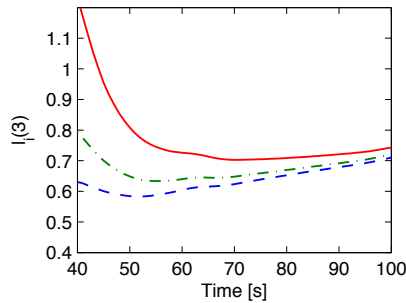


Figure 3.3: Otherwise identical ramp-up scenarios separated by the initial prescribed $l_i(3)$ condition, which sets the initial prescribed current profile at 40 s from which the current diffusion commences.

3.3 Results

Numerous simulations have been carried out in this study, systematically surveying the various H/CD mixes. For brevity, we will first present the optimum H/CD mix results for the various pedestal heights, and then outline the trends that have led to the optimum, by comparing a selected number of various H/CD mixes at the same pedestal height. Unless otherwise stated, the various simulations presented all share the same L-mode H/CD strategy: a gradual EC ramp up to 17 MW, and a rapid NBI ramp up to 33 MW just before the L-H transition at 100 s.

3.3.1 Optimum cases for various pedestal heights

The H/CD mix of NBI and EC was found to provide the best combination of a high degree of non-inductive current drive, due to the NBI, as well as q -profile shaping capability for core confinement maximization, through the deposition radius flexibility inherent in the EC system. This will be discussed more in detail in section 3.3.2. The simulation results for the optimum $T_{ped} = 4$ keV case are presented in detail in Figs.3.4-3.5. This case will henceforth be regarded as the 'reference case'. The $T_{ped} = 5$ keV case is outlined in Fig.3.6, and the q -profile evolution from the $T_{ped} = 3$ keV case in Fig.3.7. Each of the cases was designed to approximately reach the target of $P_{fus} = 350$ MW. The global parameters of these simulations are summarized in table 3.1. For comparison, results of a pedestal scan with all other parameters remaining identical to the $T_{ped} = 5$ keV case are also displayed in table 3.2.

In the $T_{ped} = 5$ keV optimum case, $q > 1$ at stationary state, and the lower amount of ECCD compared to the $T_{ped} = 4$ keV optimum case is deposited at a more inner radius to lock q_{min} towards 1. In the $T_{ped} = 4$ keV optimum case, $x(q = 1) = 0.03$ even at stationary state. There is also a local minimum in the q -profile at $x=0.35$, where $q=1.005$ at stationary state. In the $T_{ped} = 3$ keV case, $x(q = 1) = 0.44$ at 1200 s, which is unsatisfactory for our target ITER hybrid scenario as defined in section 3.2.1.

The $T_{ped} = 4$ keV case is marginal for the $P_{loss} < 110$ MW constraint. A high T , low n discharge with a high P_{aux} for current drive maximizes the non-inductive current fraction, and may be critical for the hybrid scenario, but may be at odds with the requirement of maintaining a sufficiently low P_{loss} . Increased margin in the operational space is obtained with more optimistic pedestal assumptions.

The flattop loop voltage of the $T_{ped} = 5/4/3$ keV cases is $\sim 21.5/31/49.8$ mV respectively, calculated as an average up to 1200 s. The increasing loop voltage is due to progressively lower T_e and higher n_e (and thus I_p), as well as reduced bootstrap current at the edge. For the 4 keV and 5 keV cases particularly, this loop-voltage may be sufficiently low to allow a flattop of up to 3000 s, provided that resistive flux consumption is saved during the ramp-up phase by application of early heating [44, 46].

Note that the differences in H_{98} in the cases outlined above are primarily due to the different prescribed pedestal heights. In the subsequent comparisons, we will observe the more interesting cases of comparing the H_{98} obtained with different H/CD mixes under the same pedestal assumption, where the differences in confinement result from first-

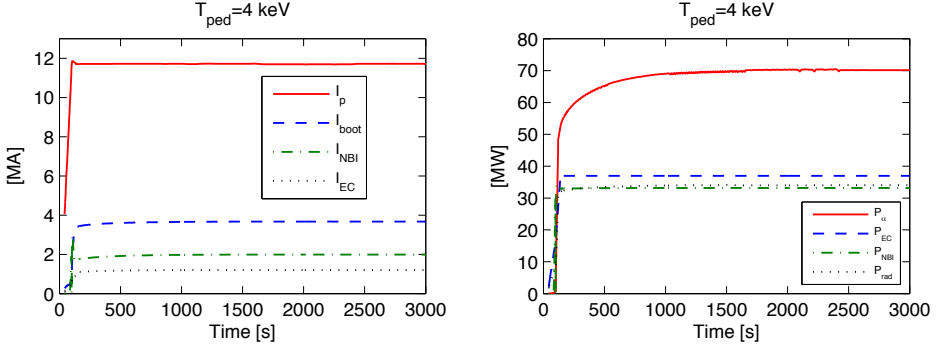


Figure 3.4: Total powers and currents of the optimized $T_{ped} = 4$ keV simulation (the reference case). In the left panel we can see the evolution of the total current, bootstrap current, neutral beam driven current, and electron cyclotron driven current. The right panel displays the evolution of the α -power, electron cyclotron injected power, neutral beam injected power, and the total emitted radiation power sink.

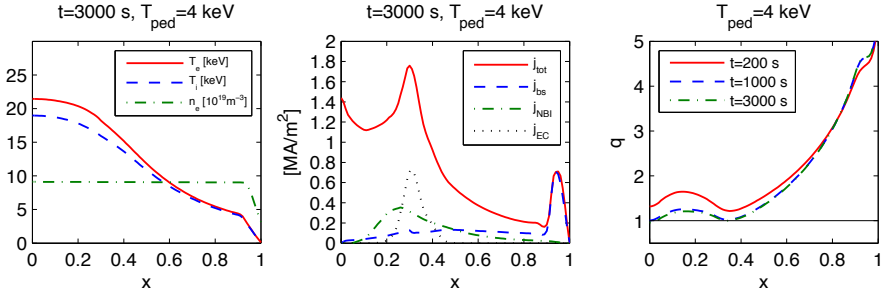


Figure 3.5: Various plasma profiles for the optimized $T_{ped} = 4$ keV simulation (the reference case) at $t = 3000$ s: electron temperature, ion temperature and the electron density profiles (left panel); total current, bootstrap current, current driven by 33 MW neutral beam injection, and current driven by 37 MW electron cyclotron wave injection (central panel); evolution of the q -profile (right panel).

principle based physics predictions of the anomalous transport q -profile dependence.

The absolute results, under our various assumptions and transport model applied, state that a satisfactory hybrid scenario may be achieved - where even at stationary state $x(q = 1) = 0.03$ - with a pedestal of 4 keV (assuming a EC upgrade to 37 MW). For a pedestal of 5 keV a $q > 1$ profile can be maintained at stationary state with the currently designed ITER H/CD mix. Note that for this $T_{ped} = 5$ keV case we retain some margin for achieving a scenario with both $q > 1$ and $P_{fus} > 350$ MW. In a further run carried out, increasing I_p and f_{GW} in the 5 keV simulation to 11.7 MA and 0.95 respectively, leads to a result of $q_{min} = 1.04$ and $P_{fus} = 412$ MW ($Q = 8.2$) at 1200s, at near

Table 3.1: Summary of results for optimum performance scenarios for various T_{ped} at the target $P_{fus} \sim 350$ MW. All evolving parameters such as Q and $x(q = 1)$ are quoted at 3000 s for the $T_{ped} = 4, 5$ keV cases, and at 1200 s for the $T_{ped} = 3$ keV case.

T_{ped}	I_p [MA]	f_G	NBI/EC [MW]	f_{boot}/f_{ni}	P_{fus} [MW]	Q	β_N	H_{98}	P_{loss} [MW]	$t(q = 1)$	$x(q = 1)$	$\langle s/q \rangle$
5	11.5	0.9	33/17	0.36/0.62	365	7.2	2.15	1.23	99	— —	0	0.74
4	11.8	0.95	33/37	0.31/0.59	351	5	2.02	1.08	114	1050	0.02	0.85
3	12.2	0.95	16.5/50	0.26/0.47	348	5.2	1.82	0.98	109	360	0.44	1.06

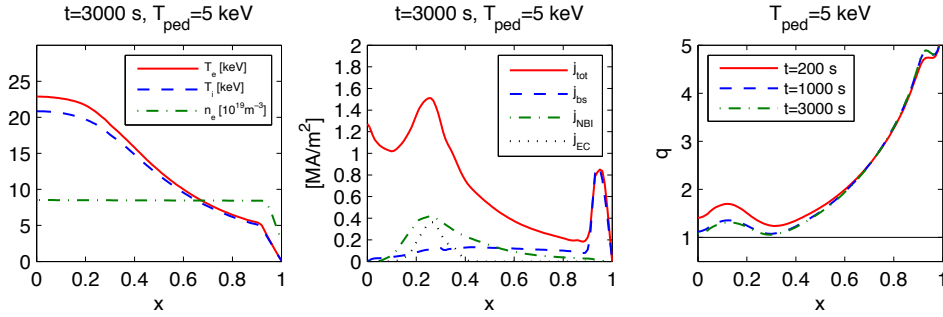


Figure 3.6: Various plasma profiles for the optimized $T_{ped} = 5$ keV simulation at $t = 3000$ s: electron temperature, ion temperature and the electron density profiles (left panel); total current, bootstrap current, current driven by 33 MW neutral beams injection, and current driven by 17 MW electron cyclotron wave injection (central panel); evolution of the q -profile (right panel).

stationary state conditions. For a 3 keV pedestal, no satisfactory hybrid scenario may be obtained: a $q=1$ surface appears rather early in the discharge from $t = 360$ s, and develops into a broad surface with $x(q = 1) = 0.44$ by $t = 1200$ s, as can be seen in the simulation displayed in Fig.3.7.

The observed evolution of P_α in the current diffusion timescale, as can be observed in Fig.3.4 and is present in all simulations carried out with GLF23, is a result of the q -profile evolving to a more favourable predicted confinement regime, as discussed in section 3.3.2. This effect was separated and can be clearly seen in Fig.3.8. There, the red (solid) curve corresponds to the P_{fus} of the reference case. The blue (dashed) curve corresponds to an identical case, apart from the poloidal flux profile (from which j and q are calculated), which is prescribed to a non-evolving state between 200-600 s and 620-1200 s, and evolves between the two states in the intermediate time. The prescribed poloidal flux profiles are that of the reference case at 200 s and 1200 s respectively. We see that the predicted time evolution of the fusion performance on the current diffusion timescale in the reference case is a consequence of the dependence of the predicted anomalous transport on the evolving q -profile. This observation has ramifications for the ramp-up H/CD strategy, and is discussed in section 3.3.6.

Table 3.2: T_{ped} sensitivity scan, with all other prescribed parameters remaining the same as an optimized $T_{ped} = 5$ keV, $f_G = 0.9$ case (first row) tailored for $P_{fus} = 350$ MW. All evolving parameters are quoted at 1200 s.

T_{ped}	I_p [MA]	f_G	NBI/EC [MW]	f_{boot}/f_{ni}	P_{fus} [MW]	Q	β_N	H_{98}	P_{loss} [MW]	$t(q=1)$	$x(q=1)$	$\langle s/q \rangle$
5	11.5	0.9	33/17	0.36/0.62	365	7.2	2.15	1.23	99	— —	0	0.74
4	11.5	0.9	33/17	0.30/0.53	285	5.6	1.86	1.10	82	520	0.06	0.81
3	11.5	0.9	33/17	0.24/0.44	214	4.2	1.58	0.96	73	280	0.38	0.89

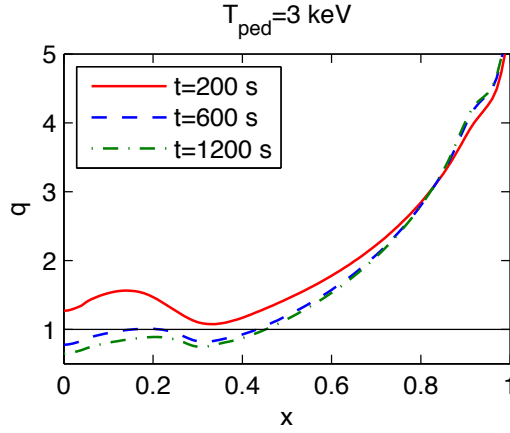


Figure 3.7: Evolution of the q -profile in the best achieved $T_{ped} = 3$ keV case.

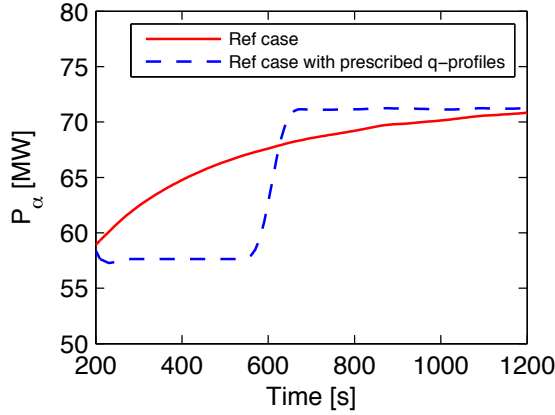


Figure 3.8: Illustration of the evolving q -profile affecting the confinement and thus Q . The red (solid) curve is the P_α of the reference case. The blue (dashed) curve is an identical case, apart from a prescribed poloidal flux profile which alternates between the states of the reference case at 200 s and 1200 s respectively.

3.3.2 Critical importance of q -profile shaping

The degree of ITG dominated turbulence is predicted to increase with increasing q but decrease with increasing s (for $s - \alpha > \sim 0.5$), as can be seen in Fig.6 of reference [12], and in [47]. This points to the advantage in maximizing the parameter s/q throughout the bulk of the plasma volume where $s > \sim 0.5$, and maintaining flat or weak inverse shear in the inner region where $q \sim 1$. This recipe would remain the same even with α -stabilization on, which only introduces a slight shift of the radial position from which $s - \alpha > \sim 0.5$. The s/q parameter can be considered as a figure of merit for the q -profile shape in the region corresponding to $s > \sim 0.5$, and appears explicitly in various approximate formulations of the ITG linear threshold [48, 49]. In the simulations considered here, the $s > \sim 0.5$ region typically corresponds to $x > \sim 0.4$. In the remainder of the region in which GLF23 is operational in our simulations, $x = 0.25 - 0.4$, it is more difficult to quantify the quality of the q -profile shape, but it is clear from the theoretical dependence that maintaining q as close to 1 as possible, and $s \sim 0$, is advantageous. Note that we are considering here only families of q -profiles without strongly reversed shear which may lead to an ITB, and where we constrain $q > 1$ for sawteeth avoidance.

The key to maximizing confinement is thus to maximize the extent of the inner $q \sim 1$ region, which then also leads to a maximization of s/q throughout the outer part of the plasma. This can be achieved with ECCD, whose position of localized deposition can be tailored to 'pin' down the q -profile towards 1 at a radius dependent on the EC power employed. The higher the EC power, the further out the q -profile can be pinned down to 1. A scan of EC deposition radius, with the same general parameters as the reference case apart from the EC launcher angles, can be seen in Fig.3.9, illustrating the sensitivity of the scenario performance to the q -profile shaping. The further out the ECCD deposition radius, the higher the q -profile is raised in the region of the deposition. The effect on fusion performance is significant, with a 20% difference between the extreme cases in the scan. The local changes of shape in the q -profile lead to a corresponding shift in the ion temperature gradient lengths. The volume averaged s/q parameter ($\langle s/q \rangle$), as displayed in the figures, is compared in the region $x = 0.4 - 0.9$, which corresponds to the region up to the pedestal in which $s > \sim 0.5$. Note that even though the EC power remains constant throughout this scan, the total EC driven current drops as the ECCD deposition radius moves outwards. This is due to both the increasing trapped electron fraction, and the fact that at lower temperatures (resulting in this case primarily from the less optimized q -profiles), the current drive efficiencies decrease.

Optimizing a scenario with an NBI/EC mix of 50/20 MW instead of the reference case of 33/37 MW leads to very similar results, as can be seen in Fig.3.10. The average s/q is reduced in the 50/20 MW case leading to a higher necessary n_e and thus I_p to achieve the same target fusion power. Furthermore, the average T_i/T_e parameter is higher in the 50/20 MW NBI/EC case by $\sim 2\%$ compared to the reference case, also aiding in reaching a similar degree of fusion power in spite of the lower average s/q . The higher NBI driven current leads to a similar value of I_{ohmic} , resulting in a similar stationary state q -profile, with $t(q = 1)$ increased by 23%. However, in terms of flexibility, it would be more advantageous to upgrade the EC system towards 40 MW. For the ITER steady

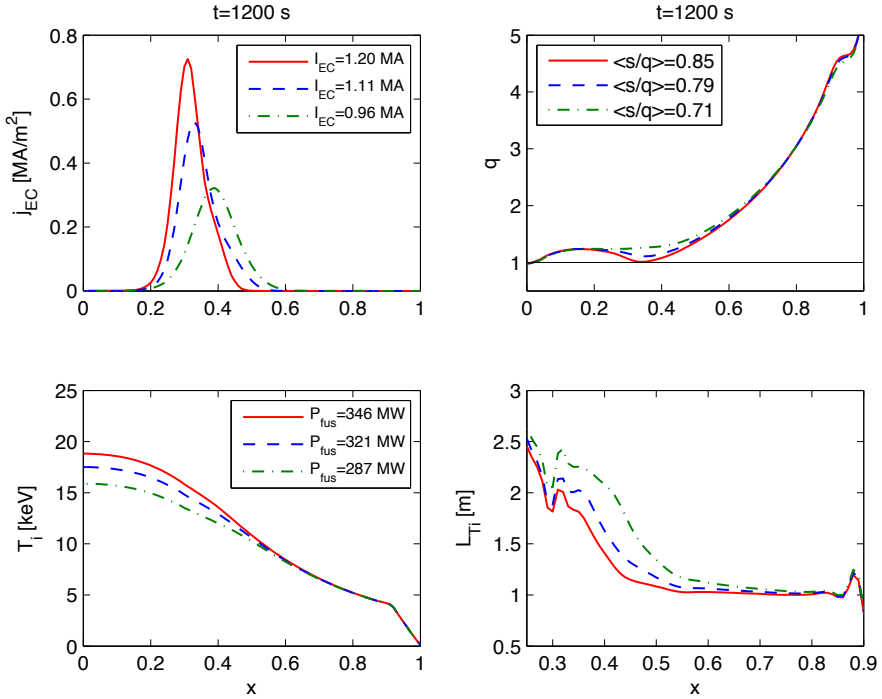


Figure 3.9: Scan of ECCD launcher angles from the equatorial ports. The red (solid) curve corresponds to the reference case, and the blue (dashed) and green (dash-dot) curves correspond to identical cases apart from the launcher angles and thus ECCD deposition radius, which is progressively increased, as seen in the upper-left panel. The q -profiles are displayed in the upper-right panel. The ion temperatures and corresponding fusion performances are shown the lower-left panel. Ion temperature gradient lengths are displayed in the lower-right panel.

state scenario for example, it has been shown that use of NBI may degrade the ITB [50], and a significant degree of ECCD power would be required for current profile shaping.

3.3.3 Inclusion of LHCD

Here we examine the effect of departing from our optimum NBI/EC mix. We take the parameters of the reference case, and carry out a scan replacing EC power with LHCD power, as calculated by DELPHINE. The results are seen in Fig.3.11. LHCD is effective in driving far off-axis non inductive current (at around $x = 0.7$), and this provides a significant broadening of the current profile. However, from the confinement point of view, this broadening leads to a significant decrease of $\langle s/q \rangle$ and thus to a degradation of the energy confinement properties of the discharge with respect to the reference case as pre-

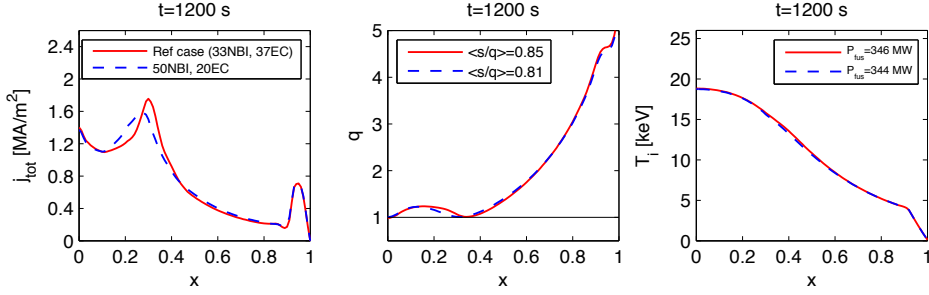


Figure 3.10: Comparison of the reference $T_{ped} = 4$ keV case (red solid curves) with an optimized 50/20MW NBI/EC case (blue dashed curves). The left panel displays the total currents. The central panel shows the q -profiles and volume averaged s/q values. The right panel displays the ion temperatures and corresponding fusion performances.

dicted by GLF23. This can be clearly seen by the reduction in T_i and the corresponding fusion performance, as well as the increase in L_{T_i} . The decrease in fusion power in the LHCD case is almost purely due to the now non-optimal q and s profiles, and not due to the reduction in heating at the more inner radii where the ECCD power is deposited. This is a typical consequence of the highly stiff GLF23 model, where pure heating has a minor influence on the temperature profiles, and the primary influence of the H/CD mix on the temperature gradient lengths is through the current drive q and s profile shaping, setting the degree of GLF23 predicted turbulence. This can be clearly seen in Fig.3.12, where we separate the effects of q -profile shaping and heating on fusion performance. Therein, the green (dash-dot) curve begins as the NBI/EC/LHCD case, and at 1160 s is prescribed the same poloidal flux profile (and thus q and s profiles) as the reference case, while maintaining the NBI/EC/LHCD heating deposition profiles. At 1180 s the poloidal flux profile is switched back to the NBI/EC/LHCD case. After each switch, the fusion performance relaxes to its new equilibrium within the thermal confinement timescale. The minor discrepancy between the green (dash-dot) and red (solid) curves between 1165-1180 s is thus the difference caused by the pure heating effect of switching 17 MW of power from $x \sim 0.3$ (the EC power) to $x \sim 0.7$ (the LHCD power), a small effect due to the stiffness of the GLF23 model. Thus, the respective impact of q -profile shaping and heating on the fusion performance, as predicted by GLF23, is clearly illustrated.

The time between the initial stage of the flat-top and $t(q = 1)$ is increased by $\sim 19\%$ in the 17 MW LHCD case compared to the reference case, due to the significantly broader current profile. This is in spite of the fact that I_{ohmic} has actually increased by 0.14 MA from 4.86 MA (reference case) to 5 MA (17 MW LHCD case), due to the slightly reduced bootstrap current and NBCD/ECCD efficiencies at lower electron temperatures. Although the total I_{ohmic} is larger, the T_e and thus conductivity profiles are slightly broader in the LHCD case and the resulting Ohmic current density is slightly lower near the magnetic axis, delaying the occurrence of the $q = 1$ surface. This higher

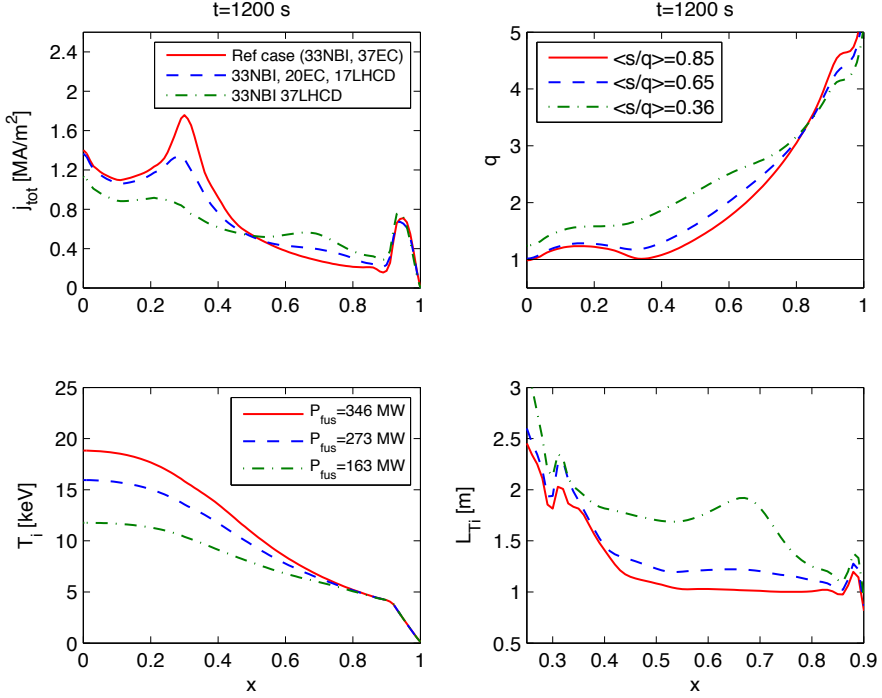


Figure 3.11: Effect on fusion performance of LHCD inclusion. The red (solid) curve corresponds to the reference case, the blue (dashed) curve an identical case apart from transferring 17 MW of ECCD to 17 MW of LHCD, and the green (dash-dot) curve an identical case apart from a H/CD mix of 33MW NBI and 37MW LHCD. We can observe the differences in total currents (upper-left panel), q -profile (upper-right panel), ion temperature and fusion performance (lower-left panel), and ion temperature gradient lengths (lower right panel).

$t(q = 1)$ would lead to a number of total emitted neutrons until $t(q = 1)$ lower by only 2% in the LHCD case compared to the reference case. However, for the 17 MW LHCD case at $t=1200$ s, P_{fus} is below the defined target by 21%. When setting the n_e and I_p parameters such that we reach towards the target $P_{fus} = 350$ MW, $t(q = 1)$ and $x(q = 1)$ in the 17 MW LHCD case is noticeably worse than in the reference case, as seen in row 5 in table 3.3. In the 37MW LHCD case, the q -profile would remain above unity even at stationary state, in spite of $I_{ohmic} = 5.07$ MA, an increase of 0.2 MA compared to the reference case. However, at $t = 1200$ s P_{fus} is only 47% of the target value.

The magnitude of LHCD driven current may have been overestimated due to the 100% directivity assumption. At lower assumed directivity the trends outlined above would still hold, but at a reduced sensitivity to the degree of LHCD power. At lower

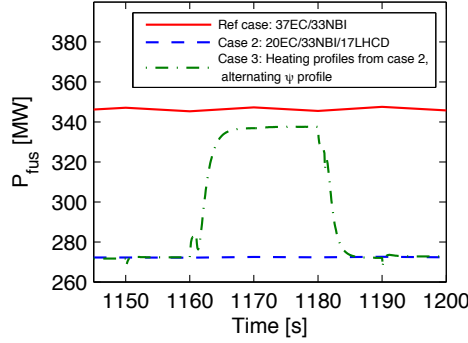


Figure 3.12: Separation of heating and q -profile shaping effects. The red (solid) curve corresponds to the reference case, the blue (dash) curve to the 33/20/17 MW NBI/EC/LHCD case. The green (dash-dot) curve corresponds to a case containing the NBI/EC/LHCD heating deposition profiles, and a prescribed poloidal flux profile alternating from the values in the NBI/EC/LHCD case, to the reference case, and back again to the NBI/EC/LHCD case.

LHCD current, the reduction of $\langle s/q \rangle$ and thus P_{fus} would be less severe. However, the increase of $t(q=1)$ would also be diminished.

We can compare the above results to simulations employing a transport model without q and s dependence, such as the 'kiauto' model [51]. The kiauto model is used here with a prescribed pedestal, and the core transport coefficients have a fixed profile shape renormalized such that the plasma energy follows the IPB98(y,2) scaling law. These results, together with all other simulations carried out at $T_{ped} = 4$ keV, are summarized in table 3.3. We can see that replacing 17 MW of ECCD with LHCD leads to marginally improved results due to the higher LHCD driven current - an improvement of $t(q=1)$ from 810 s to 860 s, and a reduction of $x(q=1)$ from 0.04 to 0.03. However, previous work on the validation of GLF23 on experimental hybrids has been reasonably successful in reproducing the average stiffness ratio $T(x=0.3)/T(x=0.8)$ [52], lending confidence to the trends predicted by the GLF23 model particularly given that the variation of the q -profile as seen above in the ECCD and LHCD scans is concentrated within this region. Further specific hybrid scenario experiments targeting the effect of q -profile shaping on core-confinement would be beneficial in assessing the trends predicted here with GLF23.

We note that even though the replacement of ECCD by LHCD is detrimental for energy confinement with respect to the optimised reference case, LHCD is effective in broadening the current profile. This capability may be needed for the development of some ITER scenarios, and LHCD would add a key feature to the ITER H&CD mix (namely efficient far off-axis current drive). In particular, LHCD may be a vital component for the ITER steady state scenario [50]. ECCD from the ITER upper launcher can also drive far off-axis current, but at total current drive efficiencies lower by a factor of ~ 7 [53], compared with the LHCD efficiency predicted by DELPHINE.

Table 3.3: Comparison of various scenarios all with $T_{ped} = 4$ keV, and $f_{GW} = 0.95$. All evolving parameters are quoted at 1200 s. The first row corresponds to the reference case to which the others are to be compared to. Run 235 is the 50/20 MW NBI/ECCD case. Runs 352 and 353 are the ECCD launcher angle scan, runs 255, 256, and 346 the cases with LHCD. Run 256 has slightly different parameters to the reference case in order to boost P_{fus} towards 350 MW (which leads to a worsened $t(q = 1)$ and $x(q = 1)$). Run 270 is the ICRH case. Runs 339 and 340 are the cases with the scaling transport model, where inclusion of LHCD leads to a marginal improvement of the scenario.

Index	Transport model	I_p [MA]	NBI [MW]	EC [MW]	EC launcher angles [deg]	LHCD [MW]	IC [MW]	P_{fus} [MW]	Q	β_N	H_{98}	$t(q = 1)$	$x(q = 1)$	$\langle s/q \rangle$
Ref	GLF23	11.8	33	37	34,36,37	0	0	346	4.9	2.00	1.069	1050	0.01	0.85
235	GLF23	11.9	50	20	32,33,36	0	0	342	4.9	2.00	1.04	1290	0	0.81
352	GLF23	11.8	33	37	38,38,38	0	0	323	4.6	1.94	1.044	940	0.01	0.79
353	GLF23	11.8	33	37	42,42,42	0	0	288	4.1	1.86	1.027	740	0.02	0.71
255	GLF23	11.8	33	20	34,36,37	17	0	273	3.9	1.81	1.003	1220	0	0.64
256	GLF23	12.3	33	20	32,33,36	17	0	331	4.7	1.88	1.004	490	0.06	0.66
346	GLF23	11.8	33	0	N/A	37	0	163	2.4	1.52	0.892	—	0	0.37
270	GLF23	11.8	33	20	34,36,37	0	17	362	5.2	2.00	1.053	420	0.13	0.81
339	Scaling	11.8	33	37	34,36,37	0	0	286	4.1	1.90	1.044	810	0.04	0.87
340	Scaling	11.8	33	20	34,36,37	17	0	295	4.2	1.90	1.048	860	0.03	0.66

3.3.4 Dependence of P_{fus} on $\langle s/q \rangle$

In Fig.3.13 we summarize the predicted dependence of P_{fus} on $\langle s/q \rangle$ in the ECCD and LHCD simulations described above, for the subset in which I_p , f_{GW} , and total P_{aux} are kept constant. This set is comprised of the reference run, and runs 352, 353, 255 and 346 as seen in table 3.3. Runs including ICRH in the H/CD mix, as to be described in section 3.3.5, are not included in this dataset, since with on-axis ICRH we heat the region of the plasma ($x < 0.25$) where the anomalous transport is prescribed as a constant value, which leads to raised temperatures since the temperature profiles are therefore not stiff in that region. By concentrating the dataset on the ECCD and LHCD scans, where the deposition is primarily in the region $x > 0.25$ where GLF23 is operational, we isolate the effect of the GLF23 predicted dependence of transport on the q -profile shape. On the left panel of the figure, the data points in the lower range of P_{fus} and $\langle s/q \rangle$, with $(\langle s/q \rangle, P_{fus}) = (0.64, 273 \text{ MW})$, and $(\langle s/q \rangle, P_{fus}) = (0.37, 163 \text{ MW})$, correspond to the runs with 17MW and 37MW of LHCD respectively, which underline the deleterious nature of LHCD on the q -profile and subsequent predicted transport. The strong correlation between $\langle s/q \rangle$ and P_{fus} is a consequence of the linear relationship between s/q and the normalized inverse ion temperature gradient scale length, R/L_{Ti} , which can be seen in the right panel of the figure. This linear relationship can be expected from ITG dominated turbulence in the flat density limit, particularly since in our case neither the T_i/T_e nor the Z_{eff} profiles vary by more than 5% between the various simulations in the dataset, further isolating the instability threshold dependence on the q -profile.

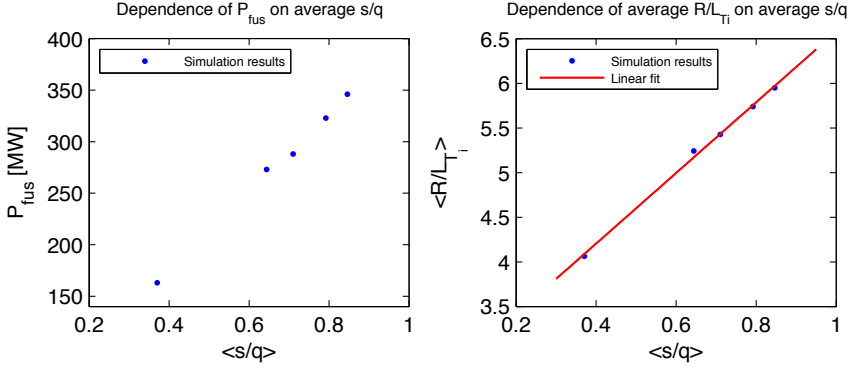


Figure 3.13: $\langle s/q \rangle$, the volume average of s/q , and $\langle R/L_{Ti} \rangle$, the volume average of R/L_{Ti} , are calculated at $t = 1200$ s between $x = 0.4 - 0.9$ (the region where GLF23 is operational and $s > \sim 0.5$).

3.3.5 Inclusion of ICRH

Here, we replace 17 MW of EC from the reference case with 17 MW of ICRH (2nd T harmonic). The results are shown in Fig.3.14, where we can see both a marked decrease in $t(q = 1)$ to 420 s, and an increase in $x(q = 1)$ at 1200 s to 0.13. The reason for this is twofold: (i) no current is being driven by the ICRH scheme assumed here, (ii) the central heating raises T_e such that the resistivity and thus current profile is sharper, decreasing q near the magnetic axis. Even though GLF23 is a highly stiff model, the temperatures are raised in the center with the on-axis ICRH due to the fact that GLF23 does not predict any anomalous transport within $x < \sim 0.25$, and a constant $\chi_{ia,ea}$ has been set in that region, as explained in section 3.2.3. At the constant transport coefficient, the added ICRH heating source indeed leads to a rise in temperatures and fusion Q (an increase of $\sim 6\%$), which compensates the loss of q -profile shaping from the missing ECCD, but also has the deleterious effect of sharpening the current profile. However, even if the transport would have been stiff throughout, the addition of ICRH would then only serve to remove the needed ECCD without any advantageous effect on performance.

An advantage which may be expected for on-axis ICRH in the hybrid scenario is direct ion heating (on top of the strong electron-ion collisional energy exchange), which would provide higher T_i and thus fusion reactivity. This effect would only be significant if the plasma temperature profiles were not strictly stiff, which can be expected [54, 55]. In addition, in a minority He^3 ICRH scheme, suprathermal fuel ion tails may develop, also boosting fusion reactivity [56]. It remains to be seen whether such performance improvements would compensate the lack of current drive that is vital in the hybrid scenario for both reducing the non-inductive current fraction and shaping the q -profile.

The differences in average flat-top loop-voltage between the reference case, the 33/20/17 NBI/EC/LHCD, and the 33/20/17 NBI/EC/IC cases is not significant, being 31/32.3/34.5 mV respectively.

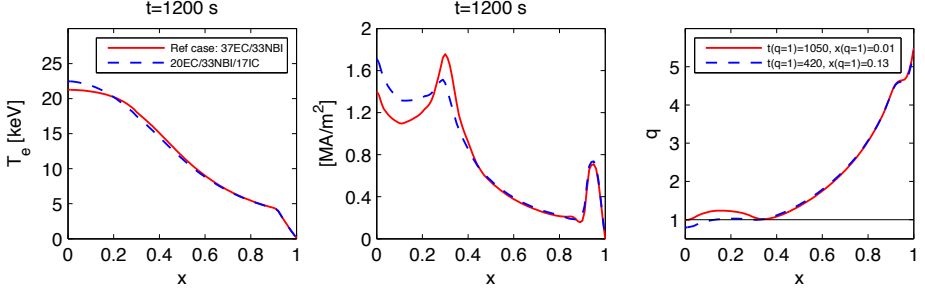


Figure 3.14: Effect on $t(q = 1)$ and $x(q = 1)$ of ICRH inclusion. The red (solid) curve corresponds to the reference case, and the blue (dashed) curve to the case where 17 MW of EC is replaced by 17 MW of ICRH. The T_e profiles are displayed in the left panel, the total current profiles in the central panel, and the q -profiles in the right panel.

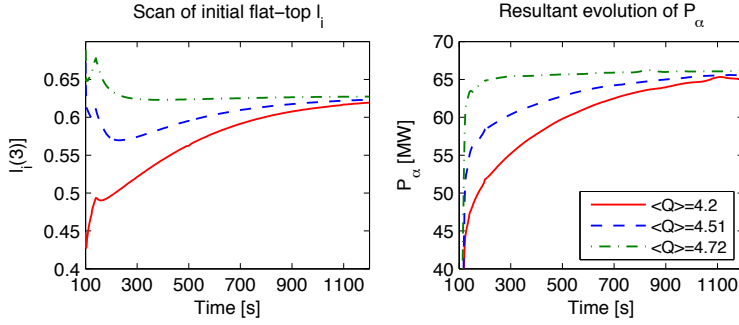


Figure 3.15: Effect of initial l_i on the P_{fus} evolution. The three cases outlined are all an H/CD mix of 33NBI/17EC/18.5LHCD, with $T_{ped} = 5$ keV. They differ only by the ramp-up strategy, which results in different initial q -profile conditions (affiliated with l_i) at the beginning of the flat-top. The various l_i evolutions are seen in the left panel, while the right panel displays the P_α evolution.

3.3.6 Initial l_i scan for q -profile matching

As mentioned in section 3.3.1, P_α evolves on the current diffusion timescale as the Ohmic current diffuses inwards and raises $\langle s/q \rangle$ throughout the bulk of the discharge, improving confinement and raising the temperatures. The average Q throughout the discharge is then dependent on the q -profile at the beginning of the flat-top phase, whereas the closer the initial q -profile to the optimised final relaxed state, the higher the average Q . This is illustrated in Fig.3.15, where a scan of initial q -profiles is carried out for simulations with otherwise identical parameters, with a H/CD mix of 33NBI/17EC/18.5LHCD (with LUKE). For an optimized hybrid scenario where the final relaxed q -profile is satisfactory

(i.e. either $q > 1$ or has a sufficiently small $x(q = 1)$), then maximizing the average Q demands a careful tailoring of the ramp-up H/CD strategy, both in terms of actuators used and timing, such that the optimised final relaxed q -profile is reached at the beginning of the flat-top.

3.4 Sensitivity studies

We have examined the sensitivity of the absolute predictions to the following assumptions: α -stabilization, value of prescribed centre $\chi_{ia,ea}$, and Z_{eff} . In addition, we have examined cases with a prescribed peaked density profile as opposed to the flat density profile. Sensitivity to the assumptions regarding the He ash diffusivity and recycling, and to the plasma rotation, were not carried out here, but have been well studied for ITER in other works [23, 24, 57].

3.4.1 α -stabilization

The reference case was rerun with α -stabilization set on in the GLF23 model, which led to a reduction in fusion performance by $\sim 15\%$. Including α leads approximately to the effective replacement of s with $s - \alpha$ within GLF23, increasing the degree of predicted anomalous transport. This is typical for monotonic q -profiles without an ITB, where $s > 0.5$ throughout the bulk of the plasma. Other H/CD mixes were also rerun with α -stabilization on, and the relative trends reported in the previous sections remain identical.

3.4.2 Sensitivity to inner prescribed $\chi_{ia,ea}$

In section 3.2.3 we discussed that GLF23 does not predict anomalous transport within $x < 0.25$, and that we assumed a constant value of $\chi_{ia,ea} = 0.5 \text{ m}^2 \text{ s}^{-1}$ within this region. The region between $x = 0.25$ and the pedestal contains the majority of the fusion power in ITER, as seen in Fig.3.16, thus the sensitivity of the assumptions in the $x < 0.25$ region is not expected to be critical with regard to the fusion performance. This was examined by carrying out a systematic scan of $\chi_{ia,ea}$ for the reference case. We display the results in Fig.3.17. We can see that indeed, the P_{fus} sensitivity to the assumptions is quite low. However, the q -profile in that region is highly sensitive to the assumption on χ_{ea} , particularly since electron neoclassical transport is more than an order of magnitude lower than ion neoclassical transport (whereas the total transport $\chi_{i,e} = \chi_{ineo,eneo} + \chi_{ia,ea}$). We can see that $t(q = 1)$ and $x(q = 1)$ are highly effected by T_e within the sensitive region, which sets the degree of current profile sharpness. The 'worst-case' scenario is run 5, that corresponds to a case with no prescribed anomalous transport in the sensitive region $x < 0.25$, which drops down to neoclassical levels towards the axis. In run 5, $t(q = 1)$ drops to 400 s, and $x(q = 1)$ increases to 0.19. Comparison of runs 2 and 3 show that the sensitivity of $t(q = 1)$ and $x(q = 1)$ to the χ_i assumption is low. For values of $\chi_{ea} > 0.5 \text{ m}^2 \text{ s}^{-1}$, the sensitivity is highly reduced as the T_e profile flattens.

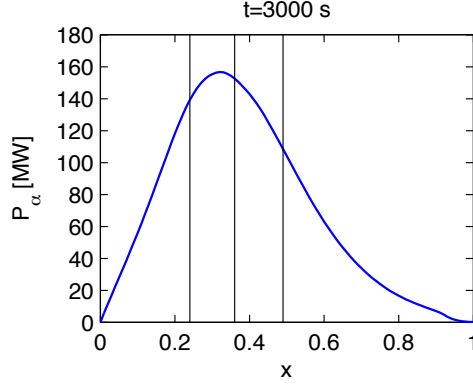


Figure 3.16: P_α per unit normalized toroidal flux coordinate (for the reference case at 3000 s), following multiplication by the Jacobian (volume element). We can see that the peak power is at $x = 0.36$. The vertical lines split the profile into four equal quarters of fusion power.

3.4.3 Sensitivity to Z_{eff}

A Z_{eff} scan was carried out by changing the assumptions of Ar and Be impurity concentrations (while maintaining the same assumed Ar/Be ratio). A Z_{eff} of 1.35 or 2.07 as opposed to the standard assumption of 1.67 leads to a P_{fus} enhancement of +20% or reduction of -20% respectively, due primarily to the degree of impurity dilution of the DT fuel. We have assumed that the Ar and Be impurity profile shapes are identical to the (flat) electron density profile shape. Therefore, no significant alteration to the bulk ion density gradients occurred during this particular Z_{eff} scan, which could in itself have affected the GLF23 predictions.

The ion and electron heat flux profiles differed throughout the Z_{eff} scan, due to variations in quantities such as P_{brem} , P_{rad} , and P_{fus} . However, this did not have an appreciable effect on the electron and ion temperature profiles, due to the high degree of stiffness inherent in GLF23. Application of a less stiff transport model would thus increase the sensitivity of the fusion power performance to Z_{eff} , due to the variation of the ion temperature profile, in addition to the DT fuel dilution.

3.4.4 Prescribed peaked density profile

Cases with a $\times 1.5$ prescribed peaked density profile were examined for the optimum NBI/ECCD mix. The $\times 1.5$ peaking factor is predicted by ν^* scaling experiments [58]. Both linear and quadratic n_e profile shapes were assumed, and the pedestal pressure was kept the same as the reference $T_{ped} = 4 \text{ keV}$ case, which resulted in $T_{ped} = 5 \text{ keV}$ for the peaked n_e cases. f_{GW} was kept at 0.95, and the EC powers and injection angles were varied such that the cases were optimized at the $P_{fus} = 350 \text{ MW}$ target with $Q > 5$.

The results are shown in Fig.3.18. We can see that even though transport is slightly increased by the finite density gradient, the higher pedestals more than compensates and improves the scenario performance. Only 17 MW of EC power is sufficient for a satisfactory scenario. However, for the quadratic profile shape, this improvement is marginal due to the larger density gradients, particularly towards the edge, leading to higher transport. For even higher gradients, for example with assumed x_2 density peaking, the scenario performance may even be eroded. This high degree of sensitivity of predicted heat transport to the inverse density gradient length above a certain threshold is typical of GLF23 predictions with prescribed density profiles. For regions with sufficiently high inverse density gradient lengths, completely flat temperature profiles may even be predicted. For the simulations carried out in this work, the density gradients are assumed to be flat or moderate already from directly within the pedestal region. Therefore, such overly pessimistic temperature profile predictions just inside the pedestal do not occur.

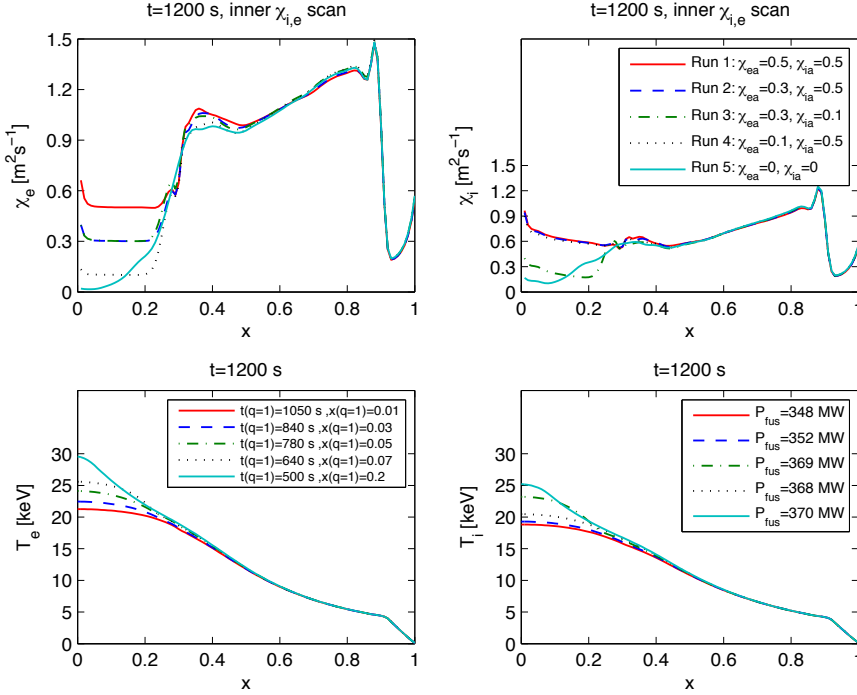


Figure 3.17: Sensitivity to prescribed inner $\chi_{ia,ea}$ (in units of $m^2 s^{-1}$). The upper-left and upper-right panels illustrate the various pairs of χ_{ia} and χ_{ea} assumptions, with the consequences on T_e and T_i shown on the bottom-left and bottom-right panels respectively.

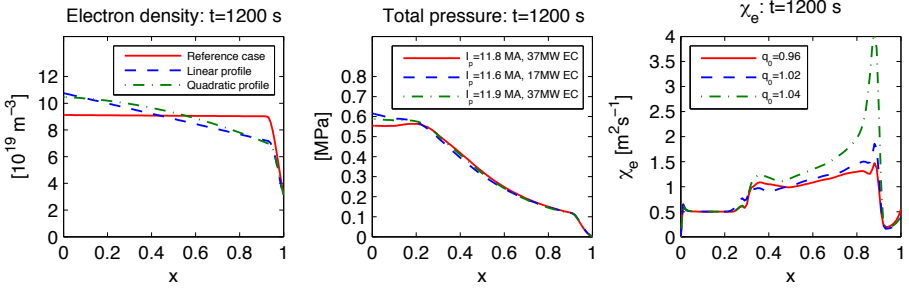


Figure 3.18: Effect of density peaking. The red (solid) curve is the reference case with a flat electron density profile, the blue (dashed) curve a case with a linear $\times 1.5$ peaked density profile, and the green (dash-dot) curve a quadratic $\times 1.5$ peaked density profile. The various density profiles are seen on the left panel. Total pressure profiles are displayed in the central panel. The electron heat diffusivity profiles are seen on the right panel.

3.5 Discussion and conclusions

An extensive study of the H/CD mix for the ITER hybrid scenario has been performed, with the GLF23 anomalous transport model predicting transport in the energy channel, and for a range of prescribed pedestals. According to GLF23, the key point for scenario optimization is tailoring the q -profile with a judicious choice of current drive, in order to minimize the predicted q and s dependent transport. This then allows a minimization of n_e and thus I_p needed for the scenario target $P_{fus} = 350$ MW, raising the q -profile towards 1 as desired in a hybrid scenario. Note that for a hybrid scenario with no ITB, we have excluded the examination of cases with highly reversed shear. The recipe for such optimization is to maximize the volume of the inner low shear $q \sim 1$ region, which both improves confinement in itself, and also maximizes the value of the s/q profile in the remaining bulk of the plasma where $s - \alpha > 0.5$, which further reduces transport. The optimum H/CD mix towards this end was found to be an NBI/EC mix. With respect to this optimal mix, the replacement of about half of the ECCD power by LHCD delays $t(q = 1)$ by 15%, but at a price of significantly worse confinement due to the far off-axis current deposition, which decreases the outer s/q values and raises the inner q values. The dependence of the total P_{fus} on the volume averaged $\langle s/q \rangle$ in the region $x = 0.4 - 0.9$ (where GLF23 is operational and $s > \sim 0.5$) was found to be highly correlated, due to the linear relationship between $\langle s/q \rangle$ and $\langle R/L_{Ti} \rangle$. Pure heating alone does not affect $T_{i,e}$ to a large degree, due to the extreme stiffness of the GLF23 model. Therefore, in the context of this transport model, 2nd T harmonic ICRH found not to be beneficial to the hybrid scenario, primarily due to the lack of current drive. For $T_{ped} = 5$ keV, $q > 1$ was predicted to be maintained at stationary state with a 33/17 MW NBI/ECCD mix, with $Q = 7$. For a more conservative $T_{ped} = 4$ keV, $x(q = 1) = 0.03$ was predicted at stationary state with a 33/37 MW NBI/ECCD mix, with $Q = 5$. This strongly informs

the choice of ITER H/CD upgrades towards increasing the power of the ECRH/ECCD system. Similar performance was achieved for a 50/20 MW NBI/ECCD mix. For $T_{ped} = 3 \text{ keV}$, no satisfactory hybrid scenario was predicted, with $x(q = 1) = 0.44$ at 1200 s. The q -profile dependence of the transport also points to the necessity of matching the q -profile at the beginning of the flat-top to the final relaxed q -profile, as long as the final q -profile is optimised for the hybrid scenario, in order to maximize the average Q throughout the discharge. Comparison with experimental data which specifically aims to test the effect of q -profile shaping on core confinement is needed, in order to gauge the veracity of the importance of this effect predicted by GLF23.

The GLF23 predictions reported here do not succeed in extrapolating the high β_N hybrid scenarios achieved in present-day tokamaks to ITER. In order to further increase β_N towards these values it would be necessary in these simulations to either increase n_e (and thus I_p) to values that would result in $q < 1$, or to increase T_{ped} by an unreasonably high degree. However, under the assumptions outlined in section 3.2.3, the hybrid scenarios predicted here are able to achieve the ITER hybrid scenario primary mission as defined in section 6.1, for $T_{ped} \geq 4 \text{ keV}$. Sensitivity scans of these various modelling assumptions were carried out, and numerous uncertainties exist which could each potentially alter the fusion performance by $\sim \pm 20\%$. In this light, it is clear that our absolute predictions are still heavily influenced by the assumptions. However, the strength of the approach taken in this work is that the significant performance differences between the various H/CD settings and mixes are dependent primarily on the physical ITG/TEM/ETG microturbulence picture and the predicted q and s dependence of the transport. The trends observed towards hybrid scenario core confinement optimization should hold regardless of the specific transport model, as long as these models are based upon these same first principle physics. The predicted relative core confinement improvement achieved by careful q -profile shaping, as illustrated for ITER in this work, should hold in spite of the high number of assumptions made which strongly affect the absolute predictions.

Acknowledgments

This work, supported by the European Communities under the contract of Association between EURATOM/FOM and EURATOM/CEA, was carried out within the framework of the European Fusion Programme with financial support from NWO. The views and opinions expressed herein do not necessarily reflect those of the European Commission. This work is supported by NWO-RFBR Centre-of-Excellence on Fusion Physics and Technology (Grant nr. 047.018.002). The authors wish to thank Wim Goedheer, Egbert Westerhof, George Sips, Marc Beurskens, and the ITER Scenario Modelling Working Group for fruitful discussions.

References

- [1] C. Gormezano *et al.*, 2007, Progress in the ITER Physics Basis Chapter 6: Steady state operation *Nucl. Fusion* **47** S285.
- [2] M. Shimada *et al.*, Progress in the ITER Physics Basis Chapter 1: Overview and summary, 2007 *Nucl. Fusion* **47** S1.
- [3] A.C.C. Sips *et al.*, 2002 *Plasma Phys. Control. Fusion* **44** B69.
- [4] A.C.C. Sips *et al.*, 2007 *Nucl. Fusion* **47** 1485.
- [5] T.C. Luce *et al.*, 2003 *Nucl. Fusion* **43** 321.
- [6] E. Joffrin *et al.*, 2005 *Nucl. Fusion* **45** 626.
- [7] A. Isayama *et al.*, 2003 *Nucl. Fusion* **43** 1272.
- [8] E. Joffrin *et al.*, 2008 22nd Int. Conf. on Fusion Energy 2008 (Geneva, Switzerland, 2008) (Vienna IAEA) CD-ROM file EX/1-4Ra, <http://www-naweb.iaea.org/napc/physics/FEC/FEC2008/html/index.htm>.
- [9] ITER Physics Expert Group on Confinement *et al.*, ITER Physics Basis Chapter 2: Plasma confinement and transport, 1999 *Nucl. Fusion* **39** 2175.
- [10] M.R. Wade *et al.*, 2005 *Nucl. Fusion* **45** 407.
- [11] C. Fourment *et al.*, 2003 *Plasma Phys. Control. Fusion* **45** 233.
- [12] J.E. Kinsey, R.E. Waltz and J. Candy, 2006 *Phys. Plasmas* **13** 022305.
- [13] J. Stober *et al.*, 2007 *Nucl. Fusion* **47** 728.
- [14] Q.D. Gao, R.V. Budny, Y.M. Jiao and K. Indireskumar, 2007 *Nucl. Fusion* **47** 1318.
- [15] Yong-Su Na *et al.*, 2006 *Nucl. Fusion* **46** 232.
- [16] C.F. Maggi *et al.*, 2007 *Nucl. Fusion* **47** 535.
- [17] P.A. Politzer *et al.*, 2008 *Nucl. Fusion* **48** 075001.
- [18] M.S. Chu *et al.*, 2007 *Nucl. Fusion* **47** 321.
- [19] C.C. Petty *et al.*, 2009 *Phys. Rev. Lett.* **102** 045005.
- [20] J.F. Artaud *et al.*, 2010 *Nucl. Fusion* **50** 043001.
- [21] R.E. Waltz *et al.*, 1997 *Phys. Plasmas* **7** 2482.
- [22] J.E. Kinsey, G.M. Staebler and R.E. Waltz, 2005 *Phys. Plasmas* **47** 052503.
- [23] R.V. Budny *et al.*, 2008 *Nucl. Fusion* **48** 075005.
- [24] F. Halpern *et al.*, 2008 *Phys. Plasmas* **15** 062505.
- [25] G.M. Staebler and H.E. St John, 2006 *Nucl. Fusion* **46** L6.
- [26] R.J. La Haye, 2006 *Phys. Plasmas* **13** 055501.
- [27] M. Greenwald *et al.*, 1988 *Nucl. Fusion* **28** 2199.
- [28] G.T.A. Huysmans, J.P. Goedbloed and W. Kerner, 1991 *CP90 Conf. on Comp. Physics (Singapore: Word Scientific)* p 371.
- [29] W.A. Houlberg, K.C. Shaing, S.P. Hirshman and M.C. Zarnstropp, 1997 *Phys. Plasmas* **4** 3230.

-
- [30] V. Krivenski, I. Fidone, G. Giruzzi and G. Granata, 1985 *Nucl. Fusion* **25** 127.
- [31] Y.R. Lin-Liu, V.S. Chan and R. Prater, 2003 *Phys. Plasmas* **10** 4064.
- [32] F. Imbeaux and Y. Peysson, 2005 *Plasma Phys. Control. Fusion* **47** 2041.
- [33] Y. Peysson and J. Decker, 2007 *EPS Conf. on Plasma Phys. (Warsaw)* vol 31F (ECA) P-4.164, <http://epsppd.epfl.ch/Warsaw/start.htm>.
- [34] L.-G. Eriksson, T. Hellsten and U. Willén, 1993 *Nucl. Fusion* **33** 1037.
- [35] J. García *et al.*, 2008 *Nucl. Fusion* **48** 075007.
- [36] H.-S. Bosch and G.M. Hale, 1992 *Nucl. Fusion* **32** 611.
- [37] C.E. Kessel *et al.*, 2007 *Nucl. Fusion* **47** 1274.
- [38] Yu. V. Gott and E.I. Yurchenko, 2009 *Phys. Plasmas* **16** 112502.
- [39] T. Oikawa *et al.*, 2008 22nd *Int. Conf. on Fusion Energy 2008 (Geneva, Switzerland, 2008)* (Vienna IAEA) CD-ROM file IT/P6-5, <http://www-naweb.iaea.org/naweb/physics/FEC/FEC2008/html/index.htm>.
- [40] G. Ramponi *et al.*, 2007 *Fus. Sci. Techn.* **52** 193.
- [41] P.B. Snyder and H.R. Wilson 2003 *Plasma Phys. Control. Fusion* **45** 1671.
- [42] E.J. Doyle *et al.*, Progress in the ITER Physics Basis Chapter 2: Plasma confinement and transport, 2007 *Nucl. Fusion* **47** S18.
- [43] N. Holtkamp, 2008 22nd *Int. Conf. on Fusion Energy 2008 (Geneva, Switzerland, 2008)* (Vienna IAEA) CD-ROM file OV/2-1, <http://www-naweb.iaea.org/naweb/physics/FEC/FEC2008/html/index.htm>.
- [44] S.H. Kim *et al.*, 2009 *Plasma Phys. Control. Fusion* **51** 065020.
- [45] C.E. Kessel *et al.*, 2009 *Nucl. Fusion* **49** 085034.
- [46] G.L. Jackson *et al.*, 2010 *Phys. Plasmas* **17** 056116.
- [47] J.E. Kinsey *et al.*, 2005 *Nucl. Fusion* **45** 250.
- [48] T.S. Hahm and W.M. Tang, 1989 *Phys. Fluids B* **1** 1185.
- [49] F. Romanelli, 1989 *Phys. Fluids B* **1** 1018.
- [50] J. García *et al.*, 2008 *Phys. Rev. Lett.* **100** 255004.
- [51] J.-F. Artaud *et al.*, 2005 *Proc. 32nd EPS Conf. on Plasma Physics (Tarragona, 2005)* vol 29C (ECA) P-1.035, <http://eps2005.ciemat.es/papers/start.htm>.
- [52] F. Imbeaux *et al.*, 2005 *Plasma Phys. Control. Fusion* **47** B179.
- [53] R. Prater *et al.*, 2008 *Nucl. Fusion* **48** 035006.
- [54] X. Garbet, P. Mantica, F. Ryter, G. Cordey, F. Imbeaux *et al.*, 2004 *Plasma Phys. Control. Fusion* **46** 1351.
- [55] X. Garbet *et al.*, 2005 *Plasma Phys. Control. Fusion* **47** (2005) 957.
- [56] E.F. Jaeger *et al.*, 2008 *Phys. Plasmas* **15** 072513.
- [57] R.V. Budny, 2009 *Nucl. Fusion* **49** 085008.
- [58] H. Weisen *et al.*, 2006 *Plasma Phys. Control. Fusion* **48** A457.

4 Predictive analysis of q -profile influence on transport in JET and ASDEX Upgrade hybrid scenarios

**J. Citrin¹, J. Hobirk², M. Schneider³, J.F. Artaud³,
C. Bourdelle³, K. Crombe⁴, G.M.D. Hogeweij¹, F. Imbeaux³,
E. Joffrin³, F. Koechl⁵, J. Stober², the ASDEX Upgrade team,
JET-EFDA contributors*, and the ITM-TF ITER Scenario
Modelling group**

¹FOM Institute DIFFER - Dutch Institute for Fundamental Energy Research,
Association EURATOM-FOM, Nieuwegein, The Netherlands

²MPI für Plasmaphysik, EURATOM Assoc., Boltzmannstr. 2, 85748 Garching,
Germany

³CEA, IRFM, F-13108 Saint Paul Lez Durance, France

⁴Department of Applied Physics, Ghent University, Rozier 44, 9000 Ghent, Belgium

⁵Association EURATOM-ÖAW/ATI, Atominstitut, TU Wien, 1020 Vienna, Austria

* See the Appendix of F. Romanelli et al., Proceedings of the 23rd IAEA Fusion Energy Conference 2010,
Daejeon, Korea

Abstract

Hybrid scenarios in present machines are often characterized by improved confinement compared to the IPB98(y,2) empirical scaling law expectations. This work concentrates on isolating the impact of increased s/q at outer radii (where s is the magnetic shear) on core confinement in low-triangularity JET and ASDEX Upgrade (AUG) experiments. This is carried out by predictive heat and particle transport modelling using the integrated modelling code CRONOS coupled to the GLF23 turbulent transport model. For both machines, discharge pairs were analyzed displaying similar pedestal confinement yet significant differences in core confinement. From these comparisons, it is found that s/q shaping at outer radii may be responsible for up to $\sim 50\%$ of the relative core confinement improvement observed in these specific discharges. This relative improvement is independent of the degree of rotational shear turbulence suppression assumed in the GLF23 model. However, employing the full GLF23 rotational shear model leads to an overprediction of the ion temperatures in all discharges analyzed. Additional mechanisms for core confinement improvement are discussed and estimated. Further linear threshold analysis with QuaLiKiz is carried out on both pairs of discharges. This work aims to validate recent predictions of the ITER hybrid scenario also employing CRONOS/GLF23, where a high level of confinement and resultant fusion power sensitivity to the s/q profile was found.

Published in:

Plasma Phys. Control. Fusion **54** 065008 (2012)

4.1 Introduction

Over the past decade, an attractive operating scenario for the ITER tokamak has emerged, combining long discharge times similar to the steady-state scenario, while maintaining the reliability of the reference H-mode scenario. This so-called 'hybrid' scenario aims to maximize neutron fluence per shot by achieving an extended burn time ($t > 1000$ s in ITER) together with significant α -particle heating ($Q > 5$) [1]. The extended burn time is achieved by operation at reduced current and at a higher non-inductive current fraction compared to the reference H-mode scenario. The basis for this scenario has been established at DIII-D [2], AUG ('improved H-modes') [3], JET [4], JT-60 [5], and NSTX [6].

In present tokamaks, the hybrid scenario is characterized by a q -profile tailored to form a broad region of low magnetic shear, with q_0 typically close to unity. Operation at a β_N higher than in standard H-mode discharges is allowed by either a total avoidance of deleterious NTM triggering sawteeth ($q > 1$ everywhere), or by having sawteeth small or frequent enough such that the β_N limit for NTM triggering is significantly raised compared to standard H-mode discharges. These discharges frequently display improved confinement compared to the IPB98(y,2) empirical scaling law expectations, with H_{98} in the range of $1 - 1.5$. $H_{98} \equiv \tau_{th}/\tau_{IPB98(y,2)}$, where τ_{th} is the thermal confinement time and $\tau_{IPB98(y,2)}$ the empirical scaling law confinement time introduced in [7]. Assuming the same H_{98} factor as in present experiments, this performance extrapolates favourably in ITER, beyond the minimum $Q = 5$ ITER hybrid scenario requirement [8–10]. It is clearly of great importance to understand the source of improved confinement in present machines, to reliably extrapolate the scenario to ITER.

A number of possibilities explaining the confinement improvement have been proposed. One possibility is that the confinement dependence on β is not as strong as suggested by the IPB98(y,2) $\beta^{-0.9}$ scaling. The IPB98(y,2) scaling law was developed with discharges primarily in the range $\beta_N = 1 - 2$, lower than most hybrid discharges. Thus, if the β dependence would be in reality weaker, then the high β_N hybrid scenarios would display significantly higher confinement than expected from the IPB98(y,2) scaling. Indeed, a weaker β scaling than IPB98(y,2) has been found in dedicated experiments in DIII-D and JET [11, 12]. Furthermore, pedestal confinement improvement due to an increase of pedestal width with β_N is reported in AUG improved H-modes [13, 14]. However, in more recent experiments at JET, the β_N confinement scaling has been observed to depend on triangularity [15]. Low triangularity discharges display a weak β_N dependence, while high triangularity discharges display a strong edge confinement degradation with β_N in accordance with the IPB98(y,2) scaling.

Improved core confinement is seen in DIII-D hybrids and 'late-heating' AUG improved H-mode discharges, with electromagnetic gyrokinetic calculations showing that β -stabilization may be responsible for the core confinement improvement [14]. Rotation is seen to play an important role in improved confinement. Variable torque experiments at DIII-D by simultaneous application of co and counter beams led to a decrease of H_{98} from 1.5 to 1.1 in the extreme low rotation case (central $M \approx 0.15$) [16]. However, this H_{98} factor is still as high as in high rotation conventional H-mode plasmas. This shows that further factors are also responsible for core confinement improvement in hybrid scen-

arios, since the hybrid scenario at low rotation should exhibit a higher H_{98} factor than standard H-mode scenarios at low rotation. The precise mechanism of rotational shear core confinement improvement is also currently under investigation. Observations at JET point to the combination of low magnetic shear and high rotational shear leading to significantly reduced ion temperature profile stiffness [17, 18]. This is in opposition to the instability threshold offset observed in non-linear simulations and reproduced in reduced models such as GLF23 [19], which describe well the effect of rotation particularly for DIII-D [16]. Finally, the characteristic hybrid scenario q -profile shape - a central broad region of low magnetic shear, and increased magnetic shear towards the edge - may further contribute to improved confinement through a relative increase in s/q at outer radii, leading to an increase in the ITG threshold. This can be seen from the ITG threshold linear gyrokinetic analytical expression, in the flat density limit [20]:

$$(R/L_{Ti})_{crit} = \frac{4}{3}(1 + T_i/T_e)(1 + 2\frac{s}{q}), \text{ with } R/L_n < 2(1 + T_i/T_e) \quad (4.1)$$

A similar dependency in the collisionless, flat density limit with both passing and trapped electrons was reported in modelling carried out with the Kinezero linear gyrokinetic code [21]. For $s > 0$ and for $T_i/T_e = 1$, the best fit of R/L_{Ti} following parameter scans in s and q was found as [22]:

$$(R/L_{Ti})_{crit} = 2(1.1 + 1.4s + 1.9\frac{s}{q}) \quad (4.2)$$

Similar s/q dependence has also been observed in electron heat transport experiments on Tore Supra [23, 24].

This work concentrates on isolating the impact of varying s/q at outer radii on core confinement in *low-triangularity* JET and AUG hybrid scenario experiments. For each machine, a pair of shots has been chosen which display a similar level of pedestal confinement yet a significant difference in core confinement. For each pair, the improved confinement case is correlated with a higher average s/q parameter. The aim of this work is to assess whether the predicted threshold improvement due to q -profile shaping is consistent with the observations. This is carried out by predictive heat and particle transport modelling using the integrated modelling code CRONOS [25] coupled to the GLF23 turbulent transport model [19, 26]. Successful validation of the GLF23 q -profile scaling has been carried out on DIII-D discharges at fixed magnetic shear [27]. The GLF23 modelling is supplemented by linear instability threshold calculations with the linear gyrokinetic code QuaLiKiz [28], based on the Kinezero code. One of the driving motivations of this work is to validate recent predictions of the ITER hybrid scenario also employing CRONOS/GLF23, where a high level of fusion power sensitivity to the s/q profile was found, even for relatively modest improvements in H_{98} [29].

This paper is organized as follows: the experimental discharges are described in section 4.2, the modelling tools and techniques in section 4.3, the GLF23 modelling results in section 4.4, additional mechanisms for core confinement improvement are discussed in section 4.5, the QuaLiKiz results in section 4.6, and the discussion and conclusions in section 6.6.

4.2 Experimental discharges

For both machines, discharge pairs were analyzed displaying similar pedestal confinement yet significant differences in core confinement. A variation in q -profile was experimentally achieved in each pair. For the JET pair (79626/79630), this variation was achieved via the 'current-overshoot' method [10, 30]. With this method, the current is ramped down to its flat-top value just prior to the main heating phase, resulting in a broader q -profile compared with a regular ramp-up scenario. For the AUG pair (20993/20995), the q -profile variation was achieved by varying the auxiliary heating timing, with the later heating case resulting in a broader q -profile [31]. Apart from the above-mentioned variations, all other control parameters (e.g. shaping, fueling, total heating power, PINI configuration) are kept the same between the discharges of each pair. The total flattop P_{aux} for the JET case is $\approx 17\text{ MW}$, all from NBI. For the ASDEX case, flattop $P_{aux} \approx 8\text{ MW}$, with 5 MW from NBI and 3 MW from ICRH to reduce central tungsten impurity concentration. Temporal evolution of the total plasma current, heating power, and confinement factor H_{98} for each pair can be seen in Fig.5.1.

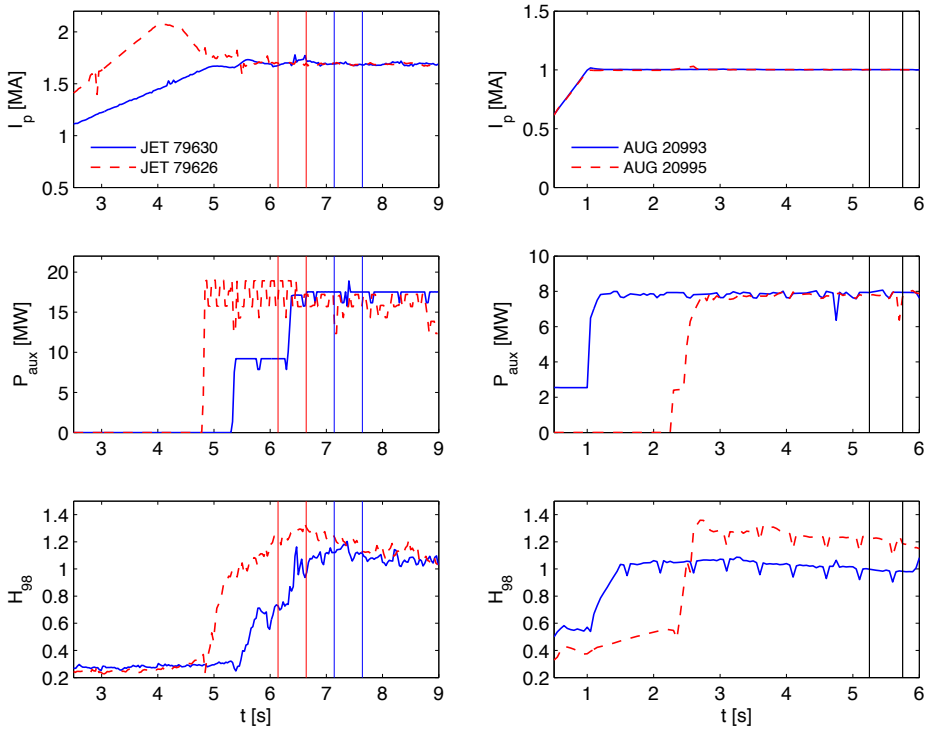


Figure 4.1: Temporal evolution of total plasma current (upper row), total auxiliary heating power $P_{aux} = P_{NBI} + P_{ICRH}$ (center row), and H_{98} confinement factor (lower row) for the JET pair 79626/79630 (left panels) and AUG pair 20993/20995 (right panels).

The vertical lines in the plots enclose the periods during which the kinetic profiles are averaged for analysis: 6.14-6.64 s for JET 79626, 7.14-7.64 for JET 79630, and 5.25-5.75 s for both ASDEX discharges. The periods differ for JET due to the different heating scheme timings. Furthermore, it is during these periods that the pedestal confinement is similar for the two discharges. Following this period, the pedestal confinement in 79626 decays in time, contributing significantly to the observed reduction in H_{98} on a timescale significantly shorter than the current diffusion timescale. This behaviour is not a regular feature of JET hybrids with current-overshoot at either low or high triangularity. For example, Fig.1 in [10] illustrates improved confinement maintained throughout the flattop phase of a JET hybrid scenario discharge. We reiterate that the main purpose of this work is to isolate and validate the expected s/q impact on core confinement by comparing discharges in periods where they display similar pedestal confinement yet observed differences in both q -profile and core confinement. This is what is achieved by comparing the averaged kinetic profiles of the discharges within the above-mentioned time windows.

The degree of similarity of the pedestal confinement can be assessed by comparing the thermal β_N at the location of the GLF23 boundary conditions: $x = 0.83$ for the JET pair and 0.76 for the AUG pair. The values are 0.99/0.94 for JET 79626/79630, and 1.11/0.98 for AUG 20995/20993. The impact that these differences have on the core confinement is discussed in section 4.5.4, where core profile stiffness is assumed. Note that while the boundary condition values are related to the height of the edge transport barrier (pedestal), the correlation is not direct since the boundary condition locations for the GLF23 modelling do not coincide with the pedestal top. Particularly for the AUG simulations, the boundary condition is limited by the outermost data point of the T_i diagnostic, and no data on the actual T_i pedestal height is available. In principle, there may be differences in core confinement between the actual pedestal top and the boundary condition taken for the GLF23 modelling. Thus we cannot relate with full certainty the differences in the GLF23 boundary condition values to differences in pedestal confinement.

All GLF23 analyses in this paper take background kinetic profiles and boundary conditions from the averaged periods defined above. Details of 0D quantities averaged over these periods can be found in table 1. $\langle s/q \rangle$ is defined as the volume averaged s/q between $x = 0.4 - 0.8$, where x is the normalized toroidal flux coordinate. The average is carried out from $x = 0.4$, since for $x < 0.4$ the magnetic shear is low ($s < 0.6$) and the short wavelength approximation within which Eq.5.2 is derived may no longer hold. The averaging procedure is up to $x=0.8$, the approximate location of the GLF23 boundary conditions. All discharges have fishbone activity, and are devoid of NTMs in the temporal periods studied, apart from AUG 20993, which has a 3/2 NTM in the vicinity of $x = 0.5$. The potential polluting effect of this mode on the isolation of the s/q impact on confinement for the AUG pair is examined in section 4.5.

The s/q and rotation profiles used throughout this analysis can be seen in Fig.5.2, and the q -profiles themselves in Fig.5.3. For each pair of discharges, the interpretative q -profiles are compared with the measured q -profiles obtained by MSE constrained equilibrium reconstruction. By interpretative q -profiles, we mean q -profiles predicted by CRONOS through solving the current diffusion equation with prescribed temperatures and densities (from measurement), and calculated current drive sources. For the JET case,

Table 4.1: OD quantities for all discharges analysed in this paper. Quantities are averaged over 7.14-7.64s and 6.14-6.64s for JET 79630 and 79626 respectively, and 5.25-5.75s for AUG 20993 and 20995.

Shot	B_T [T]	I_p [MA]	β_N (W_{th})	β_N (W_{dia}/W_{mhd})	$\langle s/q \rangle$	Z_{eff}	H_{98}	MHD activity
JET 79630	2	1.7	1.9	2.6	0.79	1.97	1.13	Fishbones
JET 79626	2	1.7	2.1	2.8	0.94	1.76	1.26	Fishbones
AUG 20993	2.4	1	1.4	1.9	0.69	2.42	0.98	Weak 3/2 NTM
AUG 20995	2.4	1	1.7	2.3	0.84	2.35	1.2	Fishbones

the experimental and interpretative q -profiles agree to within 10% for $x > \sim 0.35$. For $x < \sim 0.35$ the interpretative q -profiles have significantly lower values than the measured q -profiles. This discrepancy is limited to a region comprising only $\sim 10\%$ of the plasma volume, and thus plays a minor role in the determination of total core confinement, which is the central point of this work. It was thus decided to use the interpretative JET q -profiles for the GLF23 transport modelling in this work, since it was deemed that the current diffusion model could capture with higher fidelity than the measurements the subtle effect of current overshoot on the q -profile. The discrepancy for $x < \sim 0.35$ may be due to MHD activity redistributing the current, clamping the q -profile to 1, as reported in [32–35]. The discrepancy within $x = 0.35$ is consistent with the lack of observed sawteeth in the JET pair. However in principle $q < 1$ is a necessary but not sufficient condition for sawteeth. The sawtooth trigger can also depend on the magnetic shear at the inversion radius, the location of the inversion radius and the fast ion distribution function. Thus it is possible that no sawteeth are present in spite of $q < 1$ for these specific discharges. All JET interpretative simulations started at 2 s - early enough in the ramp-up phase such that the sensitivity of the q -profiles at the time of interest for the predictive simulations to the initial prescribed q -profiles is negligible. The initial prescribed q -profiles corresponded to a quadratic current profile constrained to satisfy l_i from EFIT reconstruction.

In the AUG pair, the interpretative q -profiles significantly departs from the measured q -profiles within a much greater bulk of the plasma volume compared to the JET pair. Such discrepancies between interpretative and measured q -profiles was also seen in previous AUG improved H-mode modelling [36]. This increased discrepancy may be due to a higher degree of current redistributed by MHD activity. It was thus decided to use the measured q -profiles for the GLF23 modelling for the AUG cases, since it is possible that neoclassical diffusion cannot account for the precise q -profile shape in the AUG case even at higher radii.

Regarding q -profile measurement errors, the MSE measurement error for the AUG q -profiles are $\sim 10\%$. For the JET q -profiles, the modelled values are sensitive to the measured $\langle Z_{eff} \rangle$, Z_{eff} profile shape, and bootstrap current calculations. A thorough assessment of the q -profile sensitivity to the modelling assumptions has not been carried out for this work, apart from a Z_{eff} sensitivity check shown in section 4.4. However, both for the AUG and JET cases, the proximity of the shots (each pair was carried out

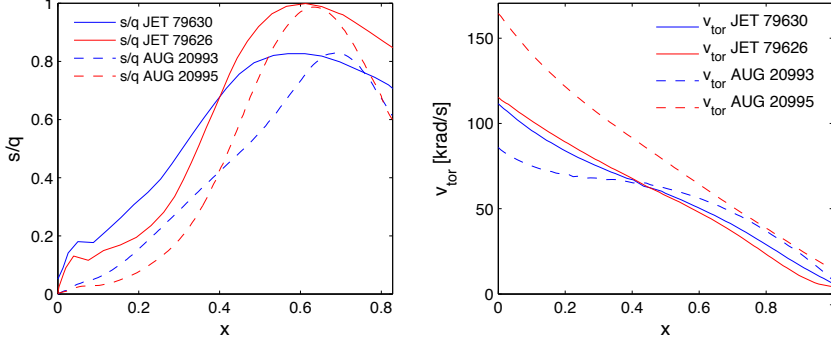


Figure 4.2: s/q profiles (left panel) and toroidal rotation profiles (right panel) for all discharges analysed in this paper.

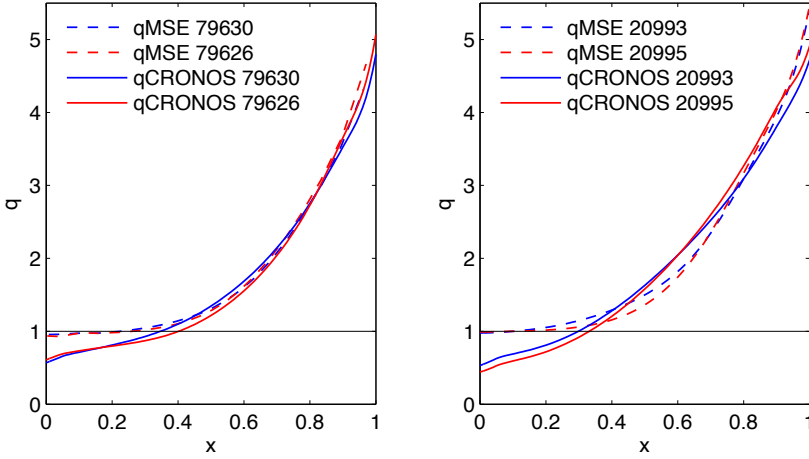


Figure 4.3: Comparison of interpretative and experimental q -profiles for the JET discharges (left panel) and for the AUG discharges (right panel).

in the same experimental session) means that it is likely that any systematic errors are the same for both discharges in each pair. Since we are concerned with *differences* in the q -profiles, this increases the reliability of the results. Nevertheless, it is indeed possible that the error in the difference between the q -profiles in each pair is of the order of the difference itself. This important caveat underlines this entire work.

The rotation profiles for the JET case are similar. For the AUG case, the 20993 (lower confinement) case has a significantly flatter rotation profile in the low magnetic shear region $x < 0.4$. It is possible that this flatter rotation profile is due to the magnetic braking induced by the 3/2 mode present in shot 20993.

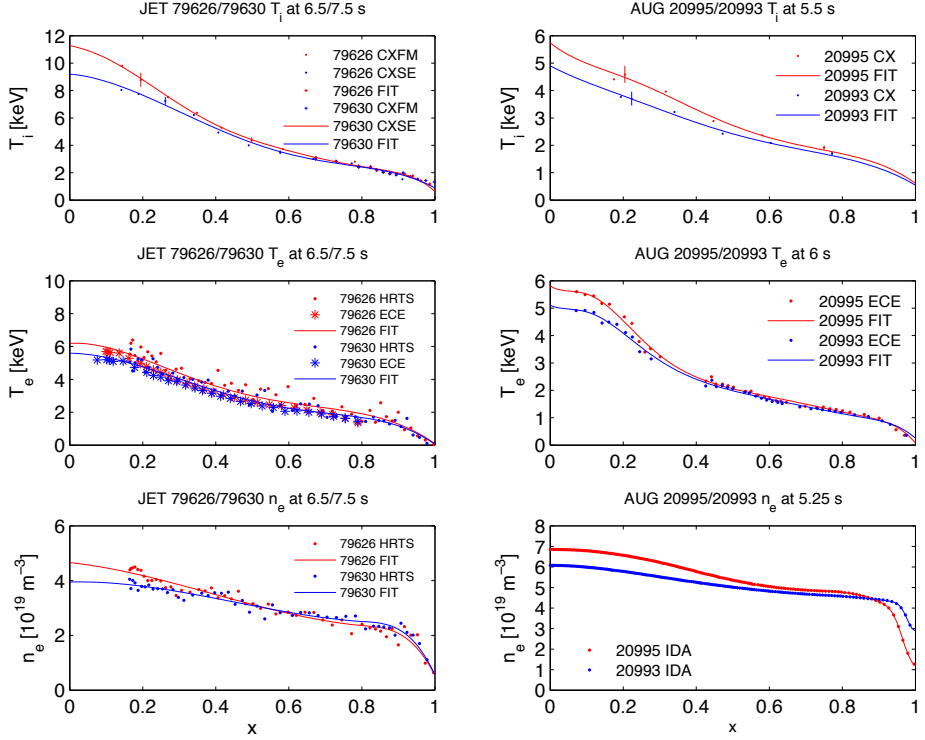


Figure 4.4: T_i (top row), T_e (center row) and n_e (bottom row) profiles for JET 79626/30 (left panels) and AUG 20993/95 (right panels)

A representative overview of the kinetic profile data and fit quality for all discharges analyzed in this paper can be seen in Fig.5.4 for *single timeslices*. Spline fits were carried out for each timeslice. The fit order (typically cubic or quartic) and break-points (typically near the pedestal if at all) varied between the different profiles. Note that the standard $\frac{d}{dx}|_{x=0}$ constraint on the profiles was not applied by the fitting routine used for this work. This constraint does not fundamentally change the profile shape in the region of interest for comparison with the GLF23 modelling ($x \sim 0.3 - 0.8$). JET T_i was measured by a combination of core and edge charge exchange (CXFM and CXSE) diagnostics. The CXSE is vital for determining the approximate equivalence of the T_i pedestal top values between the pair. However, the finite radial extension of the diagnostic does not allow the full resolution of the pedestal T_i profile. JET T_e was measured by both ECE and high resolution Thompson scattering (HRTS). The spline fit used both datasets on an equal footing. This is not ideal since the datasets are not fully mutually consistent. However, since the pedestal region (which will serve as the modelling boundary condition) is only resolved by HRTS, the choice of carrying out a combined data fit has no impact on the

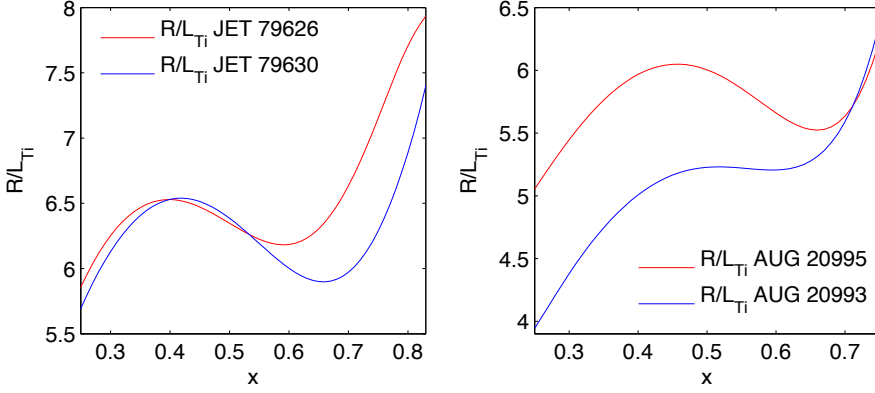


Figure 4.5: R/L_{T_i} profiles for JET 79626/30 (left panel) and AUG 20993/95 (right panel), for T_i profiles averaged over 0.5 s.

modelling results. Nevertheless, the lack of full agreement between the HRTS and ECE measurements should be maintained as a caveat when comparing the T_e modelling results to the fits from the experimental data. JET n_e was measured by HRTS.

For AUG, T_i was measured by CX. T_e was measured by ECE. n_e was measured by a combination of interferometry and lithium beam spectroscopy, and the data combined with the Integrated Data Analysis (IDA) approach [37].

For comparison of the kinetic profiles with the GLF23 predictions, the profiles were averaged for 0.5 s during the time windows displayed in Fig.5.1. This is more than an energy confinement time for both machines. This averaging also significantly reduces the RMS error of the data points, to below 2% for example for both the JET and AUG T_i and V_{tor} measurements. The boundary conditions for the GLF23 simulations were also taken from this averaging. From this averaging we can also analyze R/L_{T_i} , to determine the location and robustness of the R/L_{T_i} differences between the shots of each pair. This can be seen in Fig.5.5. These curves were made by time averaging the T_i spline fits made at each timeslice. R/L_{T_i} is calculated with respect to the average flux surface minor radius on the midplane, $r = (R_{out} - R_{in})/2$. The error from the scatter in these fits is 10% for the JET data, and 15% for the AUG data. We can see that the JET R/L_{T_i} differences are localized to the region $x = 0.6 - 0.8$, while the AUG R/L_{T_i} differences are localized from $x = 0.25 - 0.7$ (where $x=0.25$ is the approximate location of the innermost reliable T_i datapoint). While the error bars lead to overlap over much of the R/L_{T_i} profiles, the errors are not independent. The scattering of one specific data point creates an opposing change in R/L_{T_i} on either side of the position of that point. This fact increases the robustness of the observed R/L_{T_i} differences and locations.

Finally, we compare the ratios of these experimental R/L_{T_i} profiles to the predicted analytical R/L_{T_i} ratios from Eq.5.2, displayed in Fig.5.6. We note that the R/L_n ratios of all discharges are low enough to satisfy the flat density profile approximation -

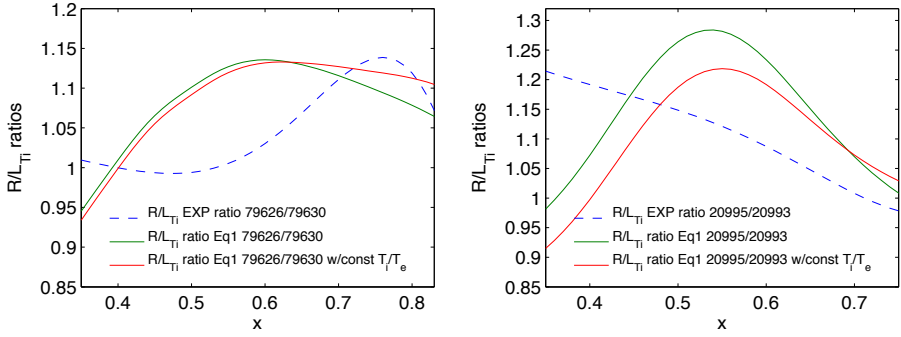


Figure 4.6: R/L_{Ti} experimental ratios compared with the analytical linear thresholds ratios (from Eq.5.2) for JET 79626/30 (left panel) and AUG 20993/95 (right panel)

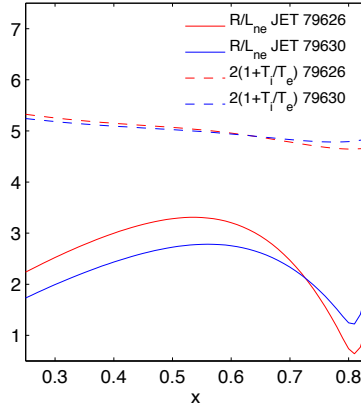


Figure 4.7: Comparison of R/L_{ne} and $2(1+T_i/T_e)$ in the JET pair of discharges for ascertaining the validity of the flat density limit applied in Eq.5.2

$R/L_n < 2(1 + T_i/T_e)$. This can be seen in Fig.5.7, where the R/L_n values of the JET discharges (calculated with respect to $r = R_{out} - R_{in}$) are compared with $2(1 + T_i/T_e)$. The constraint is satisfied to an even higher degree in the ASDEX pair, since the collisionality is higher and thus the density peaking reduced. In Fig.5.6 we also include analytical R/L_{Ti} ratios also assuming constant T_i/T_e , to separate the effect of s/q and T_i/T_e . Qualitatively the analytical and experimental ratios show the following similar features: in the JET case, the maximum observed difference for $x > 0.5$ is predicted by Eq.5.2, with no predicted difference (as in the observations) in the region of $x=0.4$; for AUG, the increasing difference from 0.75 in towards the core is also predicted by Eq.5.2. However, the observed difference in the AUG case for $x < 0.5$, the low magnetic shear region ($s < 0.6$), is not predicted. The T_i/T_e component has a minor influence

on the predicted R/L_{Ti} differences, as can be seen by comparing the curves with and without constant T_i/T_e . The differences between the analytical and experimental ratios can be either due to additional physics setting the transport, beyond ITG linear threshold physics, and/or due to the errors in the q -profiles identified with each discharge. Nevertheless, the correlations which are observed are encouraging with regard to isolating s/q as a significant factor in the observed core confinement differences within each pair of discharges. These analytical results are corroborated by numerical predictions by both GLF23 and QuaLiKiz, as outlined in the following sections.

4.3 Modelling tools and techniques

The core of CRONOS is a 1.5D transport solver, whereby 1D current diffusion, particle and energy equations are solved up to the separatrix, self consistently with 2D magnetic equilibrium [25]. In this work, the NBI heat and current sources are calculated by NEMO/SPOT [38, 39]. The ICRH heat sources for the AUG discharges are calculated with PION [40]. The magnetic equilibrium is calculated with HELENA [41]. The neoclassical transport, bootstrap current, and neoclassical resistivity is calculated with NCLASS [42]. Turbulent transport is calculated with the GLF23 model [19, 26]. The fast particle profiles calculated by NEMO/SPOT and PION for NBI and ICRH are subtracted from the ion density profiles entered into GLF23. The calculated fast particle fractions for both the JET/AUG simulations successfully account for the observed differences in $\beta_N(W_{dia}/W_{mhd})$ and $\beta_N(W_{th})$.

For the JET simulations, GLF23 is employed within the region $x=0-0.83$. For the AUG simulations, GLF23 is employed within the region $x=0-0.76$. The simulations are carried out on the energy confinement timescale until the kinetic profiles reach stationary conditions. The background profiles and scalar quantities for the simulations are averaged over the time periods displayed in Fig.5.1. Both *heat transport only* simulations (with prescribed density profiles for measurement) and *combined heat and particle transport* simulations are carried out. As mentioned in section 4.2, the JET input q -profiles are taken from CRONOS interpretative runs (current diffusion only simulations), and the AUG q -profile inputs from MSE measurements. For each discharge, comparison simulations were carried out substituting the q -profile input with the q -profile from the other member of each pair. The magnetic shear is then recalculated by CRONOS in a self-consistent manner. In such a manner GLF23 predicts the confinement difference solely due to the changed values of the q -profile and magnetic shear. Further linear threshold analysis examining the effect of s/q is also carried out with the quasilinear gyrokinetic transport model QuaLiKiz [28].

4.4 Results: GLF23 q -profile substitution simulations

In this section we isolate the degree of improved confinement which stems from the differences in q -profile between the two discharges in each pair, as according to the GLF23

model. A comparison of full simulations with GLF23 of each separate discharge shows a similar degree of improvement in core confinement as observed. This is particularly the case for the JET discharges, as seen in Fig.5.8, where the predicted total pressure is compared with the observations. Both with and without the GLF23 $E \times B$ turbulence suppression model (as specified by the $\alpha_{E \times B}$ parameter) the degree of predicted stored energy in 79626 is higher than that predicted for 79630 by a ratio comparable with the experimental observation. However, the main point of this work is to determine whether increased s/q in the outer radii of the improved confinement discharges is a significant factor responsible for the improved confinement through the increase of ITG linear thresholds. To this end, simulations for either JET 79630 or AUG 20995 were carried out substituting the q -profile of each simulation with the q -profile corresponding to the partner discharge in each pair. The comparison of simulations with differing q -profile inputs is the central point of this work. The details of these simulations are outlined in the following sections.

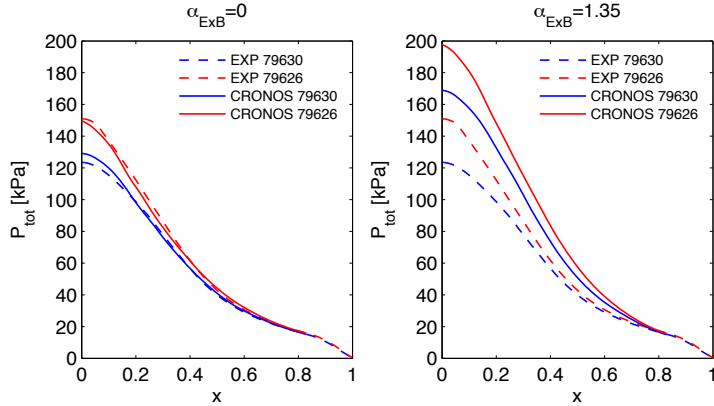


Figure 4.8: Results of combined heat and particle transport GLF23 simulations for JET 79630 and 79626. Predicted and observed P_{tot} profiles are compared with (right panel) and without (left panel) the inclusion of the full GLF23 $E \times B$ turbulence suppression model.

4.4.1 JET heat transport only

Fig.5.9 shows the T_i and T_e predictions for JET 79630. These simulations include *heat transport only*. Runs were carried out both with and without the GLF23 $E \times B$ turbulence suppression model. 79630 simulations with the substituted q -profile from 79626 (the improved confinement case) are also shown.

The inclusion of $E \times B$ suppression leads to overprediction of T_i . This overprediction is also seen in JETTO [43] simulations of the same discharge, verifying that this observation is not an artifact of the CRONOS/GLF23 methodology used in this work. However,

independently of the degree of prescribed $E \times B$ suppression, the q -profile substitution leads to a degree of T_i increase comparable to the experimentally observed difference between the two discharges. A more quantitative analysis of these differences, and of all subsequent simulations discussed below, can be found in the tables in section 4.4.5.

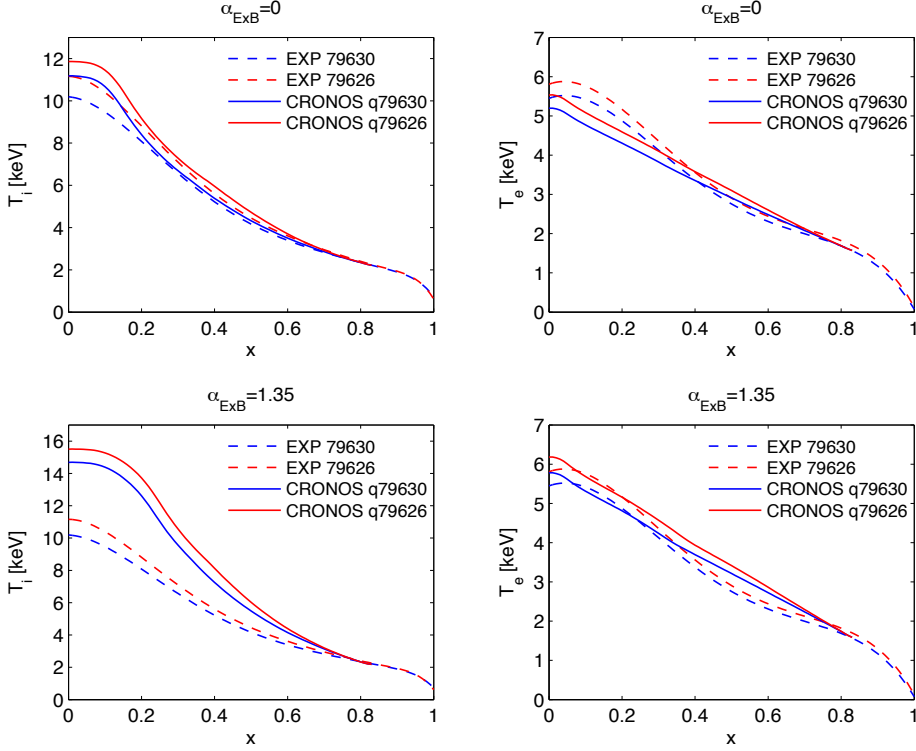


Figure 4.9: Results of heat transport only GLF23 simulations for JET 79630, comparing q -profile inputs from both 79630 and 79626. T_i profiles are on the left column. T_e profiles are on the right column. Results with both no $E \times B$ suppression (top row) and full $E \times B$ suppression (bottom row) are shown.

4.4.2 AUG heat transport only

The AUG simulations display a similar pattern to the JET simulations: simulations with the 20995 (improved confinement case) q -profile display improved ion confinement compared to a simulation which is identical apart from substituting in the 20993 q -profile. Inclusion of the $E \times B$ suppression model leads to T_i overprediction for both cases. This can be seen in Fig.5.10. In the AUG 20993 case the general degree of T_i overprediction is more severe. However, regardless of the $E \times B$ suppression assumption, the q -profile

substitution leads to a T_i difference qualitatively consistent with experimental observations.

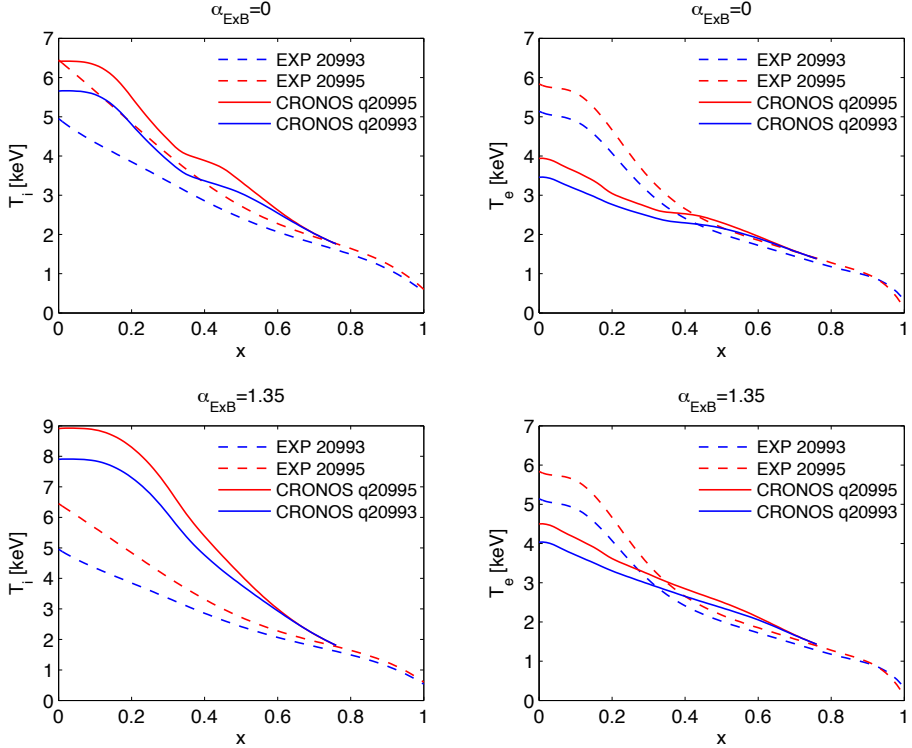


Figure 4.10: Results of heat transport only GLF23 simulations for AUG 20995, comparing q -profile inputs from both 20995 and 20993. T_i profiles are in the left column. T_e profiles are in the right column. Results with both no $E \times B$ suppression (top row) and full $E \times B$ suppression (bottom row) are shown.

4.4.3 JET combined heat and particle transport

In Fig.5.11, the results of *combined heat and particle transport* simulations for JET 79630 are shown. The pattern remains similar to the heat transport only cases, although the primary effect of global confinement improvement following the q -profile substitution is now in the particle channel. R/L_n is increased at $x > \sim 0.4$ up until the GLF23 boundary condition at $x = 0.83$, while R/L_n is decreased for $x < 0.4$. Compared to the heat transport only case, the T_i profile increase is reduced when switching to the 79626 q -profile. This is due to the increased transport predicted by GLF23 due to the increased density gradients at $x > 0.4$, interpreted as the destabilization of TEM modes due to the

propagation of the mode in the electron diamagnetic direction.

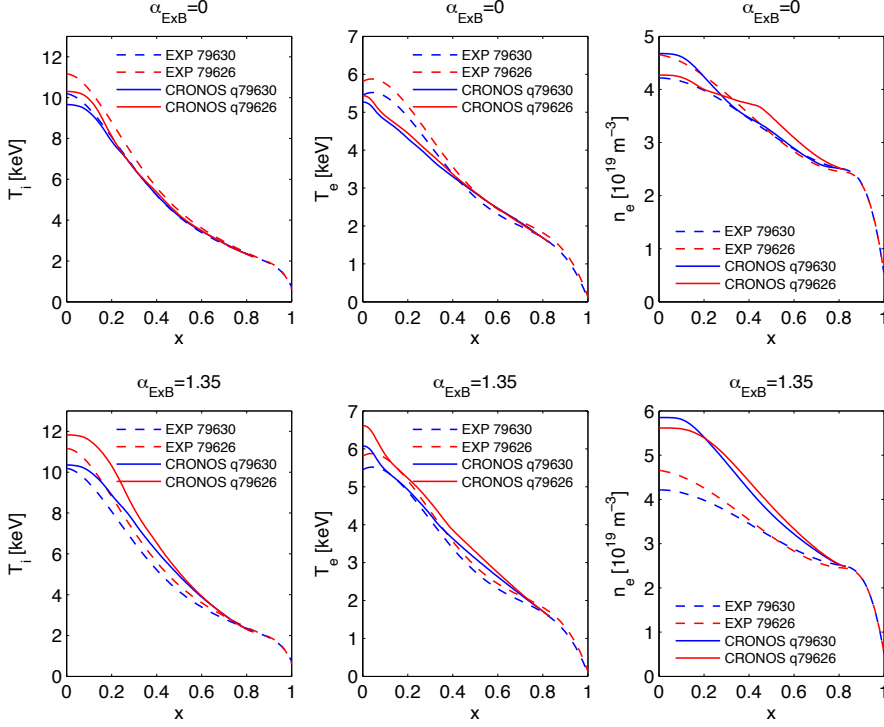


Figure 4.11: Results of combined heat and particle transport GLF23 simulations for JET 79630, comparing q -profile inputs from both 79630 and 79626. T_i profiles are in the left column. T_e profiles are in the center column. n_e profiles are in the right column. Results with both no $E \times B$ suppression (top row) and full $E \times B$ suppression (bottom row) are shown.

4.4.4 AUG combined heat and particle transport

The AUG heat and particle transport simulations show similar results to the JET heat and particle transport case. The AUG 20995 simulations are displayed in Fig.5.12. For the AUG case, the degree of improved particle transport is consistent with observation, although when $E \times B$ suppression is included the n_e profiles are significantly higher than the measured values.

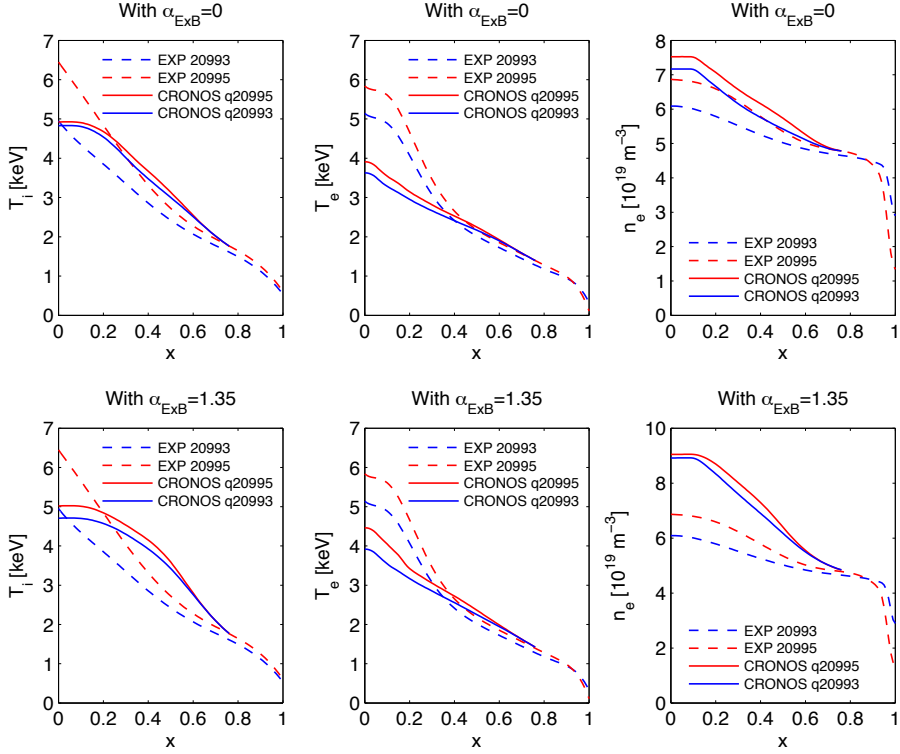


Figure 4.12: Results of combined heat and particle transport GLF23 simulations for AUG 20995, comparing q -profile inputs from both 20995 and 20993. T_i profiles are in the left column. T_e profiles are in the center column. n_e profiles are in the right column. Results with both no $E \times B$ suppression (top row) and full $E \times B$ suppression (bottom row) are shown.

4.4.5 Summary of GLF23 runs

In tables 2 and 3, the simulation results are summarized in terms of the predicted core thermal energy content: $W_{core} = \frac{3}{2} \int_0^{x_{bc}} (P_{th}(x) - P_{th}(x_{bc})) J dx$. P_{th} is the thermal pressure. x_{bc} is taken at the GLF23 operational zone boundary at $x = 0.83/0.76$ for JET/AUG. J is the Jacobian corresponding to the volume element. The tables summarize - according to GLF23 - the extent of the s/q effect *alone* in explaining the core confinement *differences* between each pair, both including and excluding $E \times B$ shear stabilization.

In spite of the absolute core energy content overprediction when including $E \times B$ shear stabilization, the degree of change when substituting the q -profile is maintained both with and without $E \times B$ shear stabilization. The degree of change also remains the

Table 4.2: Core thermal energy following GLF23 predictions for JET hybrids. Units are [MJ].

	EXP	Heat transport		Heat and particle	
		no $E \times B$	with $E \times B$	no $E \times B$	with $E \times B$
79630 (q30)	1.67	1.71	2.37	1.71	2.68
79630 (q26)	1.97	1.9	2.62	1.83	3.03
Ratio	1.17	1.11	1.11	1.07	1.13

Table 4.3: Core thermal energy following GLF23 predictions for AUG hybrids. Units are [MJ].

	EXP	Heat transport		Heat and particle	
		no $E \times B$	with $E \times B$	no $E \times B$	with $E \times B$
20995 (q93)	0.2	0.249	0.367	0.255	0.371
20995 (q95)	0.294	0.293	0.421	0.3	0.429
Ratio	1.47	1.18	1.15	1.18	1.16

same when including particle transport, due to the aforementioned increase in heat transport when increasing the density gradients. Taking the average of the GLF23 simulated core energy content for all runs, we obtain a ratio for 1.105 for the JET runs, and 1.17 for the AUG runs. This corresponds to the s/q effect *alone* contributing to 60% of the core confinement difference for the JET pair, and 35% of the core confinement difference in the AUG pair, according to GLF23. In section 4.5 we discuss other possible contributions to the core energy content differences.

4.4.6 Sensitivity of JET results to choice of Z_{eff} and $\alpha_{E \times B}$

The Z_{eff} taken for the JET simulations had an assumed form of $Z_{eff} \propto n_e^{-0.4}$, and was normalized such that the line average $\langle Z_{eff} \rangle$ agrees with Bremsstrahlung measurements. However, as seen in Fig.5.13, this assumption does not agree with Z_{eff} profiles calculated from carbon concentration measurements carried out by recombination charge exchange spectroscopy (CX). For $x > 0.8$, where no CX measurements were available, an assumed near constant CX Z_{eff} profile was prescribed.

The sensitivity of the calculated q -profile to Z_{eff} was examined by repeating the interpretative run for 79630 with alternative Z_{eff} profiles based on the discrepancy between the Bremsstrahlung and CX measurements. Since the CX measurements were only available following application of the neutral beam injection, neither precise information on the Z_{eff} profile shape in the early phase of the discharge, nor an alternative value of $\langle Z_{eff} \rangle$ was available. Therefore, we tested the sensitivity by simply assuming a Z_{eff} profile identical to the CX profile from Fig.5.13, and reducing $\langle Z_{eff} \rangle$ in the interpretative run by a constant factor ~ 1.3 , typical of the discrepancy between the Bremsstrahlung

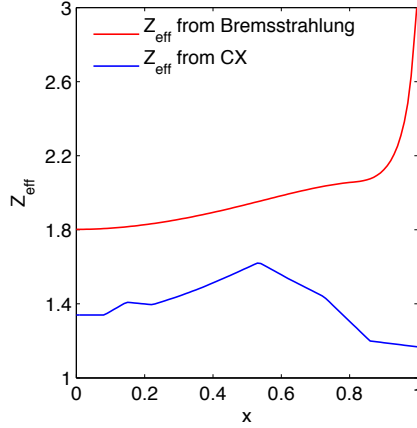


Figure 4.13: Comparison of Z_{eff} profiles for JET 79630 averaged between 7.14-7.64 s, both from line averaged Bremsstrahlung and an assumed profile, and from carbon concentration CX measurements.

and CX measurements.

The impact of using the CX Z_{eff} profile in the GLF23 simulations was also examined. Both the 79630 heat transport only and combined heat and particle transport simulations were repeated using CX Z_{eff} profiles averaged over the 7.14-7.64 s time window. Finally, the same simulations were repeated when reducing the GLF23 $\alpha_{E \times B}$ parameter to 1. The heat transport only results are seen in Fig.5.14, and the combined heat and particle transport results in Fig.5.15.

The q -profile sensitivity to the Z_{eff} profile, within the range studied, is small. However, the variation of the T_i predictions when switching to the CX measured Z_{eff} profile is not negligible, and is primarily due to reduced dilution. When combined with switching to $\alpha_{E \times B} = 1$, the ion temperature overprediction, while still apparent, is significantly diminished. This more minor level of T_i overprediction is consistent with GLF23 results reported in [44], where both CX Z_{eff} profiles and $\alpha_{E \times B} = 1$ were employed. Also in the combined heat and particle transport case, the degree of averaged n_e overprediction is reduced when switching to the CX Z_{eff} profile, although the profile peaking still remains well above the experimentally observed value. We reiterate that the relative differences due to the s/q effect - the central point of this work - are invariant to the choice of Z_{eff} and $\alpha_{E \times B}$.

4.4.7 Discussion of GLF23 $E \times B$ suppression model

The absolute W_{core} values are significantly overpredicted when including $E \times B$ shear suppression in the GLF23 model. It is difficult to determine whether this overprediction is due to a deficiency in the $E \times B$ suppression model, or due to an intrinsic overpredic-

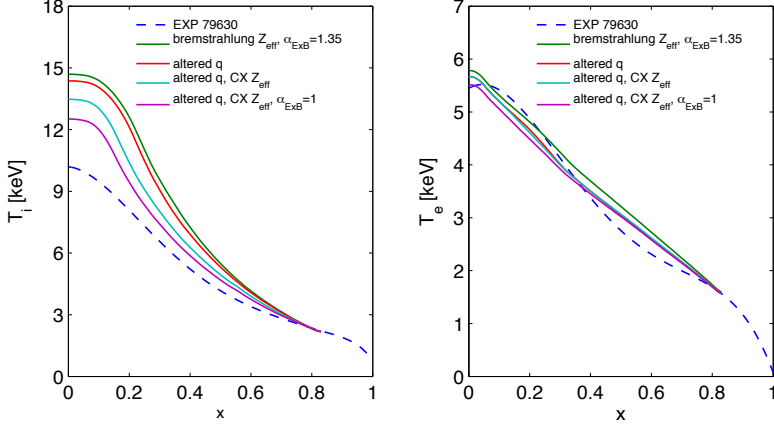


Figure 4.14: Results of heat transport GLF23 simulations for JET 79630, testing the sensitivity of the results to Z_{eff} and the $\alpha_{E \times B}$ parameter. Progressive results for T_i (left panel) and T_e (right panel) are shown where the experimental profile is compared to: the original 79630 simulation with Bremsstrahlung Z_{eff} and $\alpha_{E \times B} = 1.35$, a simulation where the q -profile is substituted with the q -profile obtained with lowered Z_{eff} profiles, additionally reducing Z_{eff} itself in the predictive simulation to the CX measured Z_{eff} profile, and finally additionally switching the $\alpha_{E \times B}$ parameter to 1.

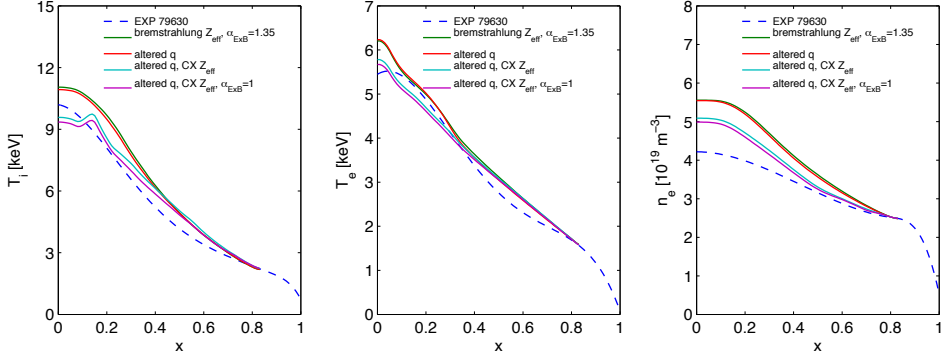


Figure 4.15: Results of combined heat and particle transport GLF23 simulations for JET 79630, testing the sensitivity of the results to Z_{eff} and the $\alpha_{E \times B}$ parameter. Progressive results for T_i (left panel), T_e (center panel), and n_e (right panel) are shown where the experimental profile is compared to: the original 79630 simulation with Bremsstrahlung Z_{eff} and $\alpha_{E \times B} = 1.35$, a simulation where the q -profile is substituted with the q -profile obtained with lowered Z_{eff} profiles, additionally reducing Z_{eff} itself in the predictive simulation to the CX measured Z_{eff} profile, and finally additionally switching the $\alpha_{E \times B}$ parameter to 1.

tion of the underlying instability thresholds. We note that GLF23 simulations for high triangularity JET hybrids also display a similar T_i overprediction as seen in this present work [45]. However, in previous work, the JET hybrid discharge 58323 was shown to be satisfactorily predicted by GLF23 [46], even when including $E \times B$ suppression. Similar satisfactory predictions of JET hybrid discharges have also previously been reported [47]. A simulation of discharge 58323 was repeated with the same CRONOS/GLF23 methodology performed in this work, and the previous result was indeed recovered. However, additional simulations taking into account the uncertainties in Z_{eff} , combined with the resultant differences in the modelled q -profile, also led to T_i overpredictions as seen here. For other JET discharges analyzed in [46], numerous examples of significant T_i deviations can be seen in figure 4. Also in this work, the degree of overprediction - while still significant - is reduced when using the Z_{eff} profile from charge-exchange measurements as shown in section 4.4.6.

These results highlight the modelling sensitivity to the input parameters, which helps explain the scatter in the literature with regard to the degree of predicted GLF23 T_i overprediction. We also note that in recent TGLF [48] modelling of DIII-D hybrid discharges [49], T_i was reported to be significantly underpredicted when not employing $E \times B$ suppression. However, the ion energy transport was reported to be reduced to neoclassical levels, while the neoclassical transport was taken from a modified Chang-Hinton model. This model yields diffusivities larger than that calculated by first-principle methods such as by the NCLASS [42] model employed in this work. This may lead to more pessimistic T_i predictions. Further validation of the various transport models on discharges from different machines, while employing using the same modelling methodology to reduce scatter induced by different modelling assumptions, would be highly beneficial.

With regard to potential explanations for a deficiency in the GLF23 $E \times B$ suppression model, we note that discharges considered here are highly NBI-driven discharges, with a relatively high degree of rotational shear. It has been shown that due to parallel velocity shear the efficiency of $E \times B$ shear in decreasing transport decreases at high rotation [50–52]. This may be relevant also for the increased q_{95} hybrid discharges. At higher q , the parallel (to the field line) component of the toroidal velocity is increased. While parallel velocity shear destabilization is included in GLF23, the destabilization effect is minor for the rotation velocities considered here. This is seen by comparing JET 79630 GLF23 T_i predictions (with heat transport only), for cases where the $E \times B$ suppression model is not included ($\alpha_{E \times B} = 0$), and where the toroidal velocity itself is set to zero ($V_{tor} = 0$). The difference between the predictions corresponds to the parallel velocity shear destabilization, which in this case only reduces the T_i profile by $\sim 2\%$. However, it would be worthwhile to reexamine the effect of parallel velocity gradient destabilization with gyrokinetic codes at experimentally relevant levels of turbulent fluxes for improved transport model verification.

Recent results at JET show that the effect of rotational shear in increasing R/L_{Ti} (due to decreased stiffness) is located only in the low magnetic shear region, in our case $x < 0.4$ [17, 18]. However, this is inconsistent with the main effect of including GLF23 $E \times B$ suppression in our simulations, which increases R/L_{Ti} primarily in the high mag-

netic shear region $x > 0.5$. Additionally, other recent JET results show that R/L_{Ti} in $x > 0.5$ does not vary with the NB/IC heating mix, at constant total power, even if the rotation profiles varies significantly [53]. This is corroborated by previous analysis of an AUG improved H-mode discharge [36], where core R/L_{Ti} was not observed to increase following a significant increase of NBI power during the discharge, which led to increased rotation. Furthermore, analysis of the same discharge with the Weiland model [54] predicted no significant improvement in core confinement due to rotation.

A further uncertainty in the modelling of the $E \times B$ shear is the contribution of the poloidal rotation. We have neglected the neoclassical poloidal rotation in our calculation of the radial electric field, as it is negligible compared with the NBI-driven toroidal rotation. However, measurements in DIII-D QH-mode discharges show a discrepancy in both magnitude and sign of impurity poloidal rotation velocities compared to the neoclassical expectation [55]. At JET, measurements have shown poloidal rotation velocities greater than the neoclassical expectation in the vicinity of internal transport barriers, while the measurements and neoclassical predictions agree outside of the ITB region [56]. In measurements at MAST, no significant disagreement between the poloidal rotation neoclassical prediction and measurements was found, although it has been suggested that at low aspect ratio the neoclassical damping of poloidal rotation may be stronger compared to at high aspect ratio [57]. There is still no clear consensus regarding the conditions necessary for the onset of non-neoclassical poloidal rotation and its degree of magnitude when existent. However, in light of these previous results it is possible that the discharges considered in this work may contain non-negligible anomalous poloidal rotation. No measurements are available in these specific discharges to shed light on this question. Nevertheless, anomalous poloidal rotation could reduce the magnitude of the radial electric field, reducing the degree of $E \times B$ turbulence suppression, partly explaining the discrepancy observed in the simulations.

The question of how to model and predict the effect of rotation on transport is thus still an open one. Nevertheless, the central point of this work is to verify the *relative* effect of the q -profile in leading to the difference in W_{core} between the two shots within each pair. This effect is independent of the $E \times B$ turbulence suppression model.

4.5 Additional contributions to core confinement differences

In this section we explore possibilities - other than the s/q effect - for explaining the observed differences in core confinement for both the JET and AUG pairs.

4.5.1 Density profiles

For the heat transport only simulations, the prescribed density profile may have an effect on the predicted core confinement. This may be due to both the inherent different stored energy content, and also the R/L_n parameterization of the predicted transport. In Fig.5.16 a comparison of AUG 20995 heat transport simulations prescribing both the

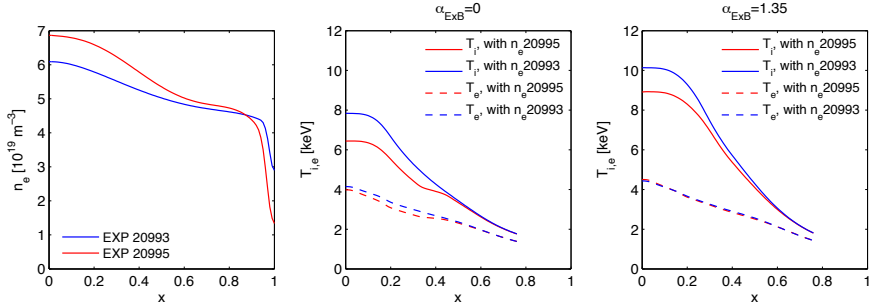


Figure 4.16: Comparison of AUG 20095 heat transport simulation with GLF23, with different prescribed n_e profiles. The dashed lines correspond to T_e , and the solid lines to T_i . The prescribed n_e profiles are seen in the left panel, the temperature profiles without $E \times B$ suppression in the center panel, and the temperature profiles with full $E \times B$ suppression in the right panel.

20995 and 20993 density profiles is displayed. This sensitivity test was carried out for AUG since the \bar{n} difference for the AUG pair is greater than the JET pair: 6% as opposed to 3%.

The resulting difference in W_{core} is a negligible $< 1\%$ increase when prescribing the 20993 n_e profile as opposed to the 20995 profile, for the no $E \times B$ suppression case. The increase in $T_{i,e}$ compensates for the decreased $n_{e,i}$ profiles. For the full $E \times B$ suppression case, prescribing the 20993 n_e profile led to a 6% decrease in W_{core} . The discrepancy between the two cases can be traced to the flat temperature profiles in the 20995 n_e case located at $x = 0.4$. This is an artifact of GLF23 modelling, where typically above a certain R/L_n threshold the sensitivity of the transport to R/L_n increases greatly. Evidently the 20995 R/L_n is at that threshold around $x = 0.4$. However, these TEM modes, which leads to a flat temperature profile in the region of $x = 0.4$ in the $\alpha_{E \times B} = 0$ case, are stabilized by the $E \times B$ suppression model when $\alpha_{E \times B} = 1.35$. Thus the flat temperature profile in the $x = 0.4$ region in the $\alpha_{E \times B} = 0$ case is not evident in the $\alpha_{E \times B} = 1.35$ case.

4.5.2 Z_{eff}

Sensitivity of the transport to Z_{eff} is examined for the JET pair, which displays a greater difference in measured $\langle Z_{eff} \rangle$ compared to the AUG case: 12% as opposed to 3%. The improved confinement discharge has lower $\langle Z_{eff} \rangle$ in both pairs. In Fig.4.17 two separate JET 79630 simulations are compared, with the differing Z_{eff} profiles. The simulations include both particle and heat transport, and no $E \times B$ suppression is included in these simulations. The results show that the sensitivity is small but not entirely negligible: the 79626 Z_{eff} case has an increased W_{core} by 4% compared to the 79630 Z_{eff} case, which is also in the correct direction of the experimentally observed improvement.

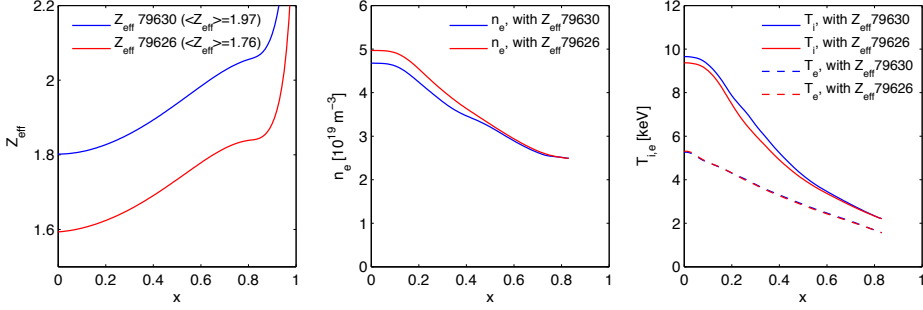


Figure 4.17: Comparison of JET 79630 combined particle and heat transport simulation with GLF23, without $E \times B$ suppression. The dashed lines correspond to simulations with Z_{eff} from 79630, and the solid lines to Z_{eff} from 79626. The prescribed Z_{eff} profiles are seen in the left panel, the density profiles in the center panel, and the temperature profiles in the right panel.

4.5.3 Heat and particle sources

Simulations which compare the effect of substituting only the heat and particle source profiles were carried out, to test the sensitivity of the predicted core energy content on the precise source profiles. This was done by re-running the combined heat and particle transport simulation of 79630 with the 79626 q -profile, and replacing the heat and particle sources in the simulation with those calculated in the 79626 interpretative simulation. However, due to the highly stiff nature of the GLF23 model, the predicted changes in W_{core} following such substitutions were completely negligible ($< 1\%$).

4.5.4 GLF23 boundary conditions

The largest part of the observed difference in confinement between each pair of discharges is from the core. However, the differences in the values of the kinetic profiles at the GLF23 boundary conditions - $x = 0.83$ for the JET pair and $x = 0.76$ for the AUG pair - can still play a significant role. To test the impact of the boundary condition on the core confinement, we first note that from the definition of the gradient length $1/L_T = \frac{dT/dr}{T}$, we can obtain $T(r) = T(r_{bc}) \exp(\int_{r_{bc}}^r 1/L_T(r) dr)$, where we have taken a temperature gradient length for this example, and r_{bc} is the boundary condition radius. If we then assume that the inverse gradient lengths of the kinetic profiles would be maintained following slight changes in the boundary condition values, then the modification of the kinetic profiles following a change in the boundary conditions can be calculated by a simple multiplication of each profile corresponding to the change in each respective boundary condition value. In such a case, the effect of these boundary conditions on the core confinement can be easily examined. We can recalculate the experimental W_{core} by simply multiplying the experimental kinetic profiles by factors corresponding to the ratios of the boundary conditions between the discharges in each

pair. This assumption was tested with GLF23 simulations, and was found to be adequate.

The 79630 experimental kinetic profiles were multiplied to match the 79626 boundary conditions, and W_{core} recalculated. The recalculated W_{core} was 5% higher than the original W_{core} . Thus, the boundary conditions alone may be responsible for $\sim 30\%$ of the perceived core confinement difference. For the AUG case, setting the 20993 experimental kinetic profiles to the 20995 boundary conditions showed that $\sim 25\%$ of the perceived core confinement difference may be due to the boundary conditions.

4.5.5 NTM effect

While the pair of JET discharges do not have any NTMs within the temporal period of analysis, AUG 20993 (the lowered confinement case) has a low amplitude 3/2 NTM located in the vicinity of $x = 0.5$, in accordance with the location of $q=1.5$ [31]. It is possible that the effect of this NTM on the kinetic profiles can explain part of the 40% difference in W_{core} for the AUG pair which remains after taking into account the s/q effect and the boundary condition effect. While it is difficult to precisely measure the impact of this NTM on confinement, we estimate the maximum possible impact of NTM as follows. The experimental T_e of the two AUG discharges are compared (Fig.4.18), where the 20995 profile is normalized to have the same boundary condition as 20993 at $x = 0.76$. We can see that the T_e differences following the normalization are indeed localized to the region $x < 0.5$, in line with a possible relation to the NTM activity. The ratio between the profiles is also seen in Fig.4.18. To estimate the effect of the NTM on the total W_{core} , we make a strong assumption that these T_e differences are fully due to the NTM, and not due to the differing q -profile and rotation profiles. We can then assess the potential impact of the NTM on W_{core} by multiplying all kinetic profiles ($T_{i,e}, n_{i,e}$) of discharge 20993 by the ratio seen in the right panel of Fig.4.18 for $x < 0.5$, and then recalculate W_{core} . This led to a W_{core} increase of 20993 of 17% of the total difference between 20993 and 20995. We can thus conclude that while the NTM may have a non-negligible impact on core confinement, the impact is not large enough to fully explain the remaining 40% difference.

4.5.6 Predictions in the low magnetic shear region

In Fig.4.19 we compare the predicted R/L_{Ti} profiles from the GLF23 simulations with the observed values, for both pairs of discharges. The results shown are from simulations including heat transport only, and the results both with and without $E \times B$ suppression are shown. The absolute predictions - particularly when including $E \times B$ suppression - deviate from the observations. However, the relative predictions - when substituting the q -profile - approximately agree with the observations in the region $x > 0.4$.

In the JET case, the location of the R/L_{Ti} differences when substituting the q -profile agrees with the location of the s/q differences, as seen in Fig.5.2. The location of these differences also fully agrees with the observations. For the AUG pair, this is also the case for $x > 0.4$, but the observed differences in R/L_{Ti} within the region $x < 0.4$ are not predicted by GLF23. This region corresponds to the low magnetic shear region

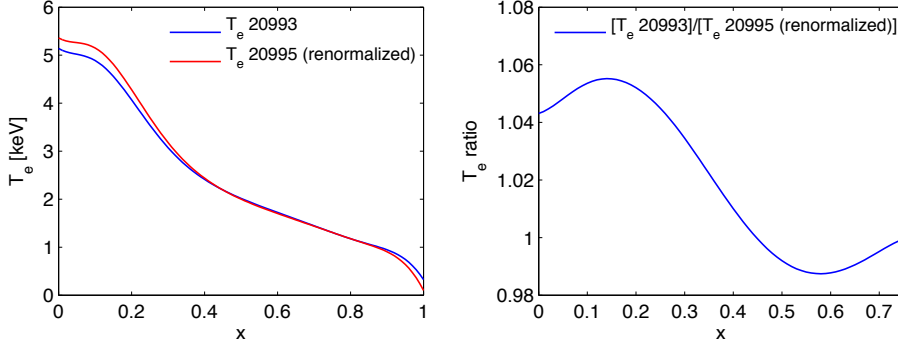


Figure 4.18: Comparison of AUG 20993 and 20995 T_e profiles, with the 20995 profile normalized to the 20993 GLF23 boundary condition at $x=0.76$. The T_e profiles themselves are seen in the left panel, and the ratio between the profiles in the right panel.

($s < 0.6$). Note that in the $\alpha_{E \times B} = 0$ AUG case, the dip of R/L_{Ti} at around $x = 0.4$ is due to the density gradient exceeding a threshold beyond which transport is greatly increased in GLF23. When replacing the density profiles with the 20993 profiles, this dip is not seen, but the relative differences in R/L_{Ti} when substituting the q -profile are maintained. When including $E \times B$ shear in the AUG case, the predicted R/L_{Ti} differences slightly increase in the $x = 0.4$ region. This is due to the difference in rotation profiles, also seen in Fig.5.2. However, this is still insufficient to explain the observed R/L_{Ti} differences for $x < 0.4$, which contributes to the observed W_{core} difference between AUG 20993/20995. A further proportion of the W_{core} difference in the AUG pair thus comes from the low magnetic shear region, a difference which is not predicted by GLF23.

4.6 QuaLiKiz linear threshold analysis

Additional analysis was carried out for both the JET and AUG cases with QuaLiKiz, where we assess the sensitivity of the instability linear thresholds to the q -profile, at the locations $x = 0.35, 0.45, 0.55, 0.65, 0.75$. This was carried out by a QuaLiKiz R/L_{Ti} scan, to identify the linear threshold. The QuaLiKiz calculations took as input the parameters for 79630 for the JET pair, and 20995 for the AUG pair. The simulation at each radial point was then repeated after replacing q and s with the values from 79626 and 20993 respectively. The results are seen in Fig.4.20. The QuaLiKiz results are compared to the experimental R/L_{Ti} calculated with respect to a radial coordinate defined as $(R_{in} + R_{out})/2$, where $R_{in,out}$ are the radii to the high field and low field side flux surfaces on the midplane. R/L_{Te} was kept at the observed ratio to R/L_{Ti} throughout the QuaLiKiz R/L_T scans.

While the predicted relative differences in R/L_{Ti} are recovered following the q -profile substitution - particularly for JET - the absolute values for $x > 0.5$ are over-predicted. However, both QuaLiKiz and GLF23 utilize $s - \alpha$ geometry, only correct in a

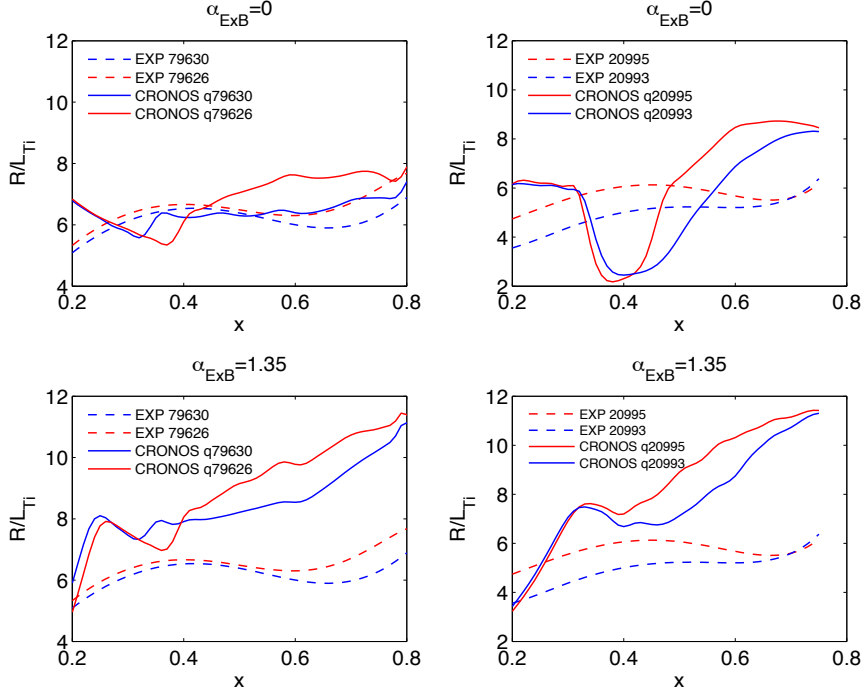


Figure 4.19: Comparison of R/L_{Ti} GLF23 predictions following q -profile substitution. Results are shown for the JET pair (left column) and the AUG pair (right column) both with (upper row) and without (lower row) the inclusion of $E \times B$ suppression.

circular small inverse aspect ratio limit. Shaped geometry can have a significant impact on the linear threshold calculation. A parameterization of this effect has been obtained from an extensive study of ETG linear thresholds from linear gyrokinetic calculations, which included shaping [58]. The study assumed adiabatic ions. The obtained (from fitting) ETG linear threshold formula is thus isomorphic to the ITG case assuming adiabatic electrons, which we rewrite as follows:

$$\left(\frac{R}{L_{Ti}}\right)_c = \max \left\{ \left(1 + \frac{T_i}{T_e}\right) \left(1.33 + 1.91 \frac{s}{q}\right) (1 - 1.5\epsilon) \left(1 + 0.3\epsilon \frac{d\kappa}{d\epsilon}\right), 0.8 \frac{R}{L_n} \right\} \quad (4.3)$$

where $\epsilon = r/R$ and κ is the elongation. Equation 4.3 is very similar to equation 5.2 apart from the increased weight of s/q , and the geometrical terms. These terms are of more importance at higher radii.

We estimate the effect of shaped geometry by multiplying the QuaLiKiz calculated R/L_{Ti} by the geometrical term $(1 - 1.5\epsilon) (1 + 0.3\epsilon(d\kappa/d\epsilon))$ from equation 4.3. The results are seen in Fig.4.21. The predicted and observed R/L_{Ti} are now reconciled for $x > 0.5$, particularly for the JET cases. The measured R/L_{Ti} at $x < 0.5$ remain far from threshold. However, this is consistent with observations in JET plasmas with high

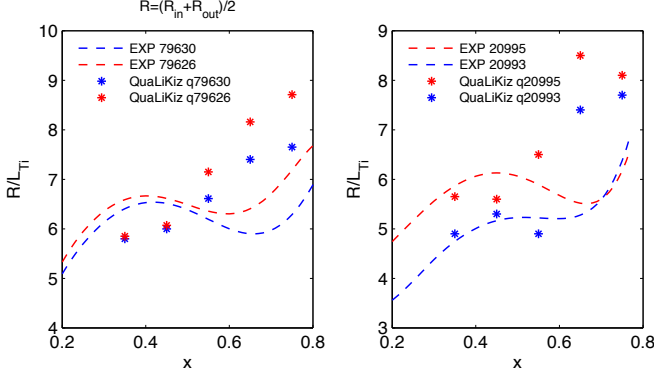


Figure 4.20: Comparison of R/L_{Ti} QuaLiKiz predictions following q -profile substitution. Results are shown for the JET pair (left panel) and the AUG pair (right panel).

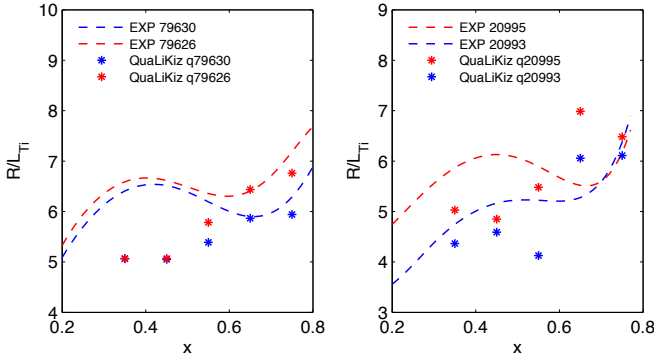


Figure 4.21: Comparison of R/L_{Ti} QuaLiKiz predictions following q -profile substitution. Results are shown for the JET pair (left panel) and the AUG pair (right panel). The QuaLiKiz predictions here have been multiplied by the geometrical factor from equation 4.3 to estimate the effect of shaping on the linear thresholds.

rotational shear, where R/L_{Ti} at greater radii have been measured to be tied close to the linear threshold, while at lower radii (low magnetic shear) the profile stiffness can be significantly reduced [17].

We note that agreement between the QuaLiKiz predictions and the measured R/L_{Ti} for $x > 0.5$ can be improved to the same degree as seen in Fig.4.21 by simply setting as input the experimental gradients with respect to R_{out} as opposed to $(R_{in} + R_{out})/2$. This may reflect the following physics: at high magnetic shear - characteristic of hybrid scenarios for $x > 0.5$ - the ITG modes are more strongly ballooned to the low field side due to the increased ion Landau damping. We speculate here that in such situations, it may thus be more appropriate to input experimental gradients defined with $R = R_{out}$

into the model, i.e. the gradient in the region where the mode is most unstable. This topic, as well as profile stiffness at low magnetic shear, is currently under investigation as part of the ongoing development of the QuaLiKiz transport model.

In summary, QuaLiKiz linear threshold calculations following q -profile substitution show that the s/q differences between each pair of discharges is responsible for a significant degree of the observed R/L_{Ti} differences. This is in corroboration with the GLF23 results. However, the significant overprediction of R/L_{Ti} for $x > 0.5$ may be a symptom of the well known limitation of applying $s - \alpha$ geometry in shaped plasmas. An estimation of the shaping effect, utilizing previous linear gyrokinetic calculations which included shaping, led to a reconciliation between the predicted and observed R/L_{Ti} values for $x > 0.5$, particularly in the JET case. This is consistent with the observation that even with no $E \times B$ shear included ($\alpha_{E \times B} = 0$), also the GLF23 model overpredicts R/L_{Ti} for $x > 0.5$ as seen in Fig.4.17.

4.7 Conclusions

4.7.1 JET 79630/79626 q -profile substitution

A significant proportion of the core confinement difference between the JET hybrid scenarios analysed here is due to an increase in the ITG threshold due to improved q -profile shaping in the high magnetic shear region, at $x > 0.4$, according to GLF23. A proportion of $\sim 60\%$ of the observed improvement in core is predicted through q -profile substitution alone. In the heat transport simulations, differences in R/L_{Ti} are in the JET case only observed in the high magnetic shear region ($x > 0.4$) and are correlated with differences in s/q . This relative difference in W_{core} is independent of the inclusion of the $E \times B$ suppression model in GLF23. In the combined heat and particle simulations, the primary channel of confinement improvement is n_e . The majority of the remaining 40% of core confinement difference can be linked to the differences in GLF23 boundary conditions at $x = 0.83$. Slight differences in n_e and Z_{eff} between the shots can account for the remaining proportion.

4.7.2 AUG 20995/20993 q -profile substitution

In the AUG hybrid scenarios analysed, approximately $\sim 60\%$ of the observed W_{core} difference can be accounted for by a combination of the s/q effect (35%) and the difference in boundary conditions ($\sim 25\%$). Again, this is independent of the $E \times B$ suppression model. It has been estimated that the NTM in 20933 may be responsible for up to a further $\sim 20\%$ of the difference. As in the JET case, the improvement due to the s/q effect is predicted to be primarily in the particle channel when including particle transport in GLF23. The observed R/L_{Ti} differences occur both in the low and high magnetic shear regions within $x = 0.2 - 0.6$. The R/L_{Ti} difference in the high shear region is correlated with a difference in s/q . However, the difference in the low shear region cannot be explained by s/q effects, according to GLF23. Due to the difference in rotational shear for

$x < 0.4$ between the two discharges in the AUG case (see Fig.5.2), it may be possible that reduced stiffness in the low shear region (not predicted by the stiff GLF23) may account for a further proportion of core confinement difference, as also observed in JET [17, 18]. It is possible that the low amplitude NTM present in 20993 at around $x = 0.5$ is responsible for a slight local difference in observed R/L_{Ti} in the $x=0.5$ region. However, the NTM cannot explain the observed differences in R/L_{Ti} for $x < 0.4$.

4.7.3 GLF23 $E \times B$ suppression model W_{core} overprediction

The overprediction of W_{core} in GLF23 when including the full $E \times B$ suppression model opens up questions regarding: the appropriate value of $\alpha_{E \times B}$ for use in GLF23, accuracy of Z_{eff} for modelling input, accuracy of the GLF23 parallel velocity shear destabilization model, the mechanism of $E \times B$ shear suppression (threshold shift vs stiffness reduction), and the possible role of anomalous poloidal rotation. However, in addition the intrinsic linear thresholds are overpredicted by the GLF23 $s - \alpha$ model. Finite aspect ratio and elongation effects reduce the predicted linear thresholds. This then would reduce the degree of apparent overprediction from the $E \times B$ model. However, the critical point is that the degree of core confinement improvement due to s/q is *independent* of both shaping effects and the value of $\alpha_{E \times B}$. Our conclusions that derive from q -profile shaping effects are thus independent of the abovementioned modelling uncertainties, while these results simultaneously underline the challenges raised by these same uncertainties.

4.7.4 Final conclusions

The majority of the W_{core} differences can be satisfactorily predicted regardless of the $E \times B$ model, and the s/q profile plays a significant role in these predictions. These GLF23 predictions are also corroborated by R/L_{Ti} threshold analysis using QuaLiKiz. A general caveat is that the relatively low magnitude of the experimentally observed and calculated differences in both R/L_{Ti} and the q -profile demands that these conclusions be treated with caution. The small magnitude of the effect - a H_{98} increase of up to ~ 0.1 due to s/q only - hinders the experimental isolation of the s/q impact which can be in general be easily masked by competing effects and experimental error. Nevertheless, the results obtained here are consistent with the theoretically expected impact of q -profile shaping on core-confinement through threshold increase at outer radii and provides an encouraging validation in this regard. In ITER operational scenario studies, such H_{98} improvements of up to ~ 0.1 due to q -profile shaping have in fact been shown to have a significant impact on the projected fusion power in the ITER hybrid scenario [29]. Validation of these ITER predictions made with GLF23 was the initial driving motivation for this work. Further q -profile shaping experiments aiming for larger differences would be extremely helpful for continued study of the q -profile impact on transport.

Acknowledgements

This work, supported by the European Communities under the contract of Association between EURATOM/FOM and EURATOM/CEA, was carried out within the framework of the European Fusion Programme with financial support from NWO. The views and opinions expressed herein do not necessarily reflect those of the European Commission. This work is supported by NWO-RFBR Centre-of-Excellence on Fusion Physics and Technology (Grant nr. 047.018.002). The authors are grateful to W. Goedheer, G. Sips, I. Voitsekhovitch, and E. Westerhof for fruitful discussions.

References

- [1] C. Gormezano *et al.*, 2007, Progress in the ITER Physics Basis Chapter 6: Steady state operation *Nucl. Fusion* **47** S285.
- [2] T.C. Luce *et al.*, 2003 *Nucl. Fusion* **43** 321.
- [3] A.C.C. Sips *et al.*, 2002 *Plasma Phys. Control. Fusion* **44** B69.
- [4] E. Joffrin *et al.*, 2005 *Nucl. Fusion* **45** 626.
- [5] A. Isayama *et al.*, 2003 *Nucl. Fusion* **43** 1272.
- [6] J.E. Menard *et al.*, 2007 *Nucl. Fusion* **39** S645.
- [7] ITER Physics Expert Group on Confinement *et al.*, ITER Physics Basis Chapter 2: Plasma confinement and transport, 1999 *Nucl. Fusion* **39** 2175.
- [8] M.R. Wade *et al.*, 2005 *Nucl. Fusion* **45** 407.
- [9] A.C.C. Sips *et al.*, 2007 *Nucl. Fusion* **47** 1485.
- [10] E. Joffrin *et al.*, in Fusion Energy 2010 (Proc. 23rd Int. Conf. Daejeon, 2010) (Vienna: IAEA).
- [11] C.C. Petty *et al.*, 2004 *Phys. Plasmas* **11** 2514.
- [12] D.C. McDonald *et al.*, 2004 *Plasma Phys. Control. Fusion* **46** A215.
- [13] C.F. Maggi *et al.*, 2007 *Nucl. Fusion* **47** 535.
- [14] C.F. Maggi *et al.*, 2010, *Nucl. Fusion* **50** 025023.
- [15] D.C. McDonald *et al.*, 2008 *Plasma Phys. Control. Fusion* **50** 124013.
- [16] P.A. Politzer *et al.*, 2008 *Nucl. Fusion* **48** 075001.
- [17] P. Mantica *et al.*, 2011 *Phys. Rev. Lett.* **107** 135004.
- [18] P. Mantica *et al.*, 2011 *Plasma Phys. Control. Fusion* **53** 124033.
- [19] R.E. Waltz *et al.*, 1997 *Phys. Plasmas* **7** 2482.
- [20] S.C. Guo and F. Romanelli, 1993 *Physics of Fluids B* **5** 520.
- [21] C. Bourdelle. *et al.*, 2002 *Nucl. Fusion* **42** 892-902.
- [22] C. Fourment *et al.*, 2003 *Plasma Phys. Control. Fusion* **45** 233.
- [23] G.T. Hoang *et al.*, 2003 *Phys. Plasmas* **10** 2 405.
- [24] G.T. Hoang *et al.*, 2001 *Phys. Rev. Lett.* **12** 87 125001.
- [25] J.F. Artaud *et al.*, 2010 *Nucl. Fusion* **50** 043001.
- [26] J.E. Kinsey, G.M. Staebler and R.E. Waltz, 2005 *Phys. Plasmas* **47** 052503.
- [27] C.C. Petty *et al.*, 2004 *Phys. Plasmas* **11** 3.
- [28] C. Bourdelle *et al.*, 2007 *Phys. Plasmas* **47** 14 112501.
- [29] J. Citrin *et al.*, 2010 *Nucl. Fusion* **50** 115007.
- [30] J. Hobirk *et al.*, submitted to Plasma Phys. Control. Fusion.
- [31] J. Stober *et al.*, 2007 *Nucl. Fusion* **47** 728.
- [32] S. Gunter *et al.*, 1999 *Nucl. Fusion* **39** 1535.
- [33] T.A. Casper *et al.*, 2007 *Nucl. Fusion* **47** 825.

- [34] C.C. Petty *et al.*, 2009 *Phys. Rev. Lett.* **102** 045005.
- [35] J.E. Menard *et al.*, 2006 *Phys. Rev. Lett.* **97** 095002.
- [36] Yong-Su Na *et al.*, 2006 *Nucl. Fusion* **46** 232.
- [37] R. Fischer *et al.*, 2010 *Fusion Sci. Technol.* **58** 675-84.
- [38] M. Schneider *et al.*, 2009 *Nucl. Fusion* **49** 125005.
- [39] M. Schneider *et al.*, 2011 *Nucl. Fusion* **51** 063019.
- [40] L.-G. Eriksson, T. Hellsten and U. Willén, 1993 *Nucl. Fusion* **33** 1037.
- [41] G.T.A. Huysmans, J.P. Goedbloed and W. Kerner, 1991 *CP90 Conf. on Comp. Physics (Singapore: Word Scientific)* p 371.
- [42] W.A. Houlberg, K.C. Shaing, S.P. Hirshman and M.C. Zarnstroff, 1997 *Phys. Plasmas* **4** 3230.
- [43] G. Cenacchi *et al* ENEA RT/TIB/88/5 (1988).
- [44] I. Voitsekhovitch *et al.*, 2009 *Nucl. Fusion* **49** 055026.
- [45] E. Joffrin *et al.*, 2010 *EPS Conf. on Plasma Phys. (Dublin)* P1.1047, <http://ocs.ciemat.es/EPS2010PAP/pdf/P1.1047.pdf>.
- [46] J.E. Kinsey *et al.*, 2005 *Nucl. Fusion* **45** 250.
- [47] F. Imbeaux *et al.*, 2005 *Plasma Phys. Control. Fusion* **47** B179.
- [48] J.E. Kinsey *et al.*, 2008 *Phys. Plasmas* **15** 055908.
- [49] J.E. Kinsey *et al.*, 2010 *Phys. Plasmas* **17** 122315.
- [50] J.E. Kinsey *et al.*, 2005 *Phys. Plasmas* **12** 062302.
- [51] E.G. Highcock *et al.*, 2010 *Phys. Rev. Lett.* **105** 215003.
- [52] M. Barnes *et al.*, 2010 *Phys. Rev. Lett.* **106** 175004.
- [53] T.W. Versloot *et al.*, 2011 *Nucl. Fusion* **51** 103033.
- [54] J. Weiland *et al.*, 1989 *Nucl. Fusion* **29** 1810.
- [55] W.M. Solomon *et al.*, 2006 *Phys. Plasmas* **13** 056116.
- [56] K. Crombé *et al.*, 2005 *Phys. Rev. Lett.* **95** 155003.
- [57] A.R. Field *et al.*, 2009 *Plasma Phys. Control. Fusion* **51** 105002.
- [58] F. Jenko *et al.*, 2001 *Phys. Plasmas* **8** 4096.

5 Quasilinear transport modelling at low magnetic shear

**J. Citrin¹, C. Bourdelle², P. Cottier², D.F. Escande³,
Ö.D. Gürcan⁴, D.R. Hatch⁵, G.M.D. Hogeweyj¹, F. Jenko⁵
and M.J. Pueschel⁵**

¹FOM Institute DIFFER - Dutch Institute for Fundamental Energy Research,
Association EURATOM-FOM, Nieuwegein, The Netherlands

²CEA, IRFM, F-13108 Saint Paul Lez Durance, France

³UMR 6633 CNRS-Université de Provence, Marseille, France

⁴Laboratoire de Physique des Plasmas, Ecole Polytechnique, CNRS, 91128
Palaiseau Cedex, France

⁵Max-Planck-Institut für Plasmaphysik, EURATOM Association, D-85748
Garching, Germany

Abstract

Accurate and computationally inexpensive transport models are vital for routine and robust predictions of tokamak turbulent transport. To this end, the QuaLiKiz [C. Bourdelle *et al.*, Phys. Plasmas **14**, 112501 (2007)] quasilinear gyrokinetic transport model has been recently developed. QuaLiKiz flux predictions have been validated by non-linear simulations over a wide range in parameter space. However, a discrepancy is found at low magnetic shear, where the quasilinear fluxes are significantly larger than the non-linear predictions. This discrepancy is found to stem from two distinct sources: the turbulence correlation length in the mixing length rule and an increase in the ratio between the quasilinear and non-linear transport weights, correlated with increased non-linear frequency broadening. Significantly closer agreement between the quasilinear and non-linear predictions is achieved through the development of an improved mixing length rule, whose assumptions are validated by non-linear simulations.

Published in:

Phys. Plasmas **19** 062305 (2012)

5.1 Introduction

The availability and accuracy of computationally inexpensive first-principle physics based transport codes is vital for both interpretation of tokamak experiments and extrapolation to future devices. With this goal in mind, the QuaLiKiz quasi-linear transport model has been developed [1]. Particle and heat flux calculation time in QuaLiKiz is ~ 50000 less than in local non-linear codes. Fluxes computed by QuaLiKiz have been validated by non-linear GYRO [2, 3] simulations over a wide range of parameter space [4]. However, significant discrepancies between QuaLiKiz and non-linear simulations have been observed at low magnetic shear.

The successful prediction of transport in the low magnetic shear regime is important for the interpretation of advanced tokamak scenarios, as has been recently seen in JET hybrid scenarios at combined low magnetic shear and high rotational shear [5]. Low magnetic shear regions are also expected during ramp-up and ramp-down phases. For extrapolation to ITER, transport at low magnetic shear is important for all scenarios. This is due to the fact that in ITER, the sawtooth period is expected to be an order of magnitude greater than the confinement time [6]. Therefore even in the ITER reference H-mode scenario, low magnetic shear transport within the inversion radius between sawtooth crashes will be critical for determining the average fusion power.

The primary motivation of this work is thus to understand the physics behind the low magnetic shear discrepancy between the QuaLiKiz model as formulated in Casati *et al* [4], and non-linear simulations. To this end, the assumptions made in the QuaLiKiz model are systematically examined at low magnetic shear. Both linear and non-linear simulations with the gyrokinetic code GENE [7] have been used extensively for comparisons and assumption validation.

The structure of the paper is as follows. In section 5.2 the QuaLiKiz model is reviewed and the discrepancy compared to non-linear simulations at low magnetic shear is introduced. In section 5.3, a review of basic understandings of the magnetic shear impact on linear modes is presented. QuaLiKiz and GENE linear growth rates are compared at low magnetic shear, and the differences between them are not sufficient to explain the flux discrepancy. In section 5.4, QuaLiKiz assumptions on non-linear effects are explored. The validity of the quasi-linear approximation itself with regard to the ordering of the non-linear characteristic times (Kubo numbers) is examined, and is found to still hold at low magnetic shear. The delicate choice of electrostatic potential saturation level, through the mixing length rule and frequency broadening, is reevaluated at low magnetic shear. The assumptions behind the saturated potential formulation have been reexamined in great detail with the aid of 16 non-linear GENE simulations at various values of magnetic shear, q -profile and driving gradient lengths. Partial isotropization of turbulent eddies, radial correlation length dependence on the magnetic shear, and increased resonance broadening at low magnetic shear are all observed. These observations are taken into account in the quasilinear model, and agreement with the non-linear magnetic shear scans is much improved. Conclusions are discussed in section 5.5.

A number of more technical aspects have been summarized in appendixes. In appendix 5.A the analytical fluid limit applied in the QuaLiKiz Gaussian eigenmode ansatz

is reviewed. In appendix 5.B the locality assumption is examined at low magnetic shear, and found to hold for $|s| > 0.1$. In appendix 5.C, the validity of the QuaLiKiz eigenmode ansatz is examined at low magnetic shear, through comparisons with self-consistent mode structure calculations from linear-GENE. This QuaLiKiz assumption was also found to hold for $|s| > 0.1$.

Many of the simulations carried out in this work refer to 'GA-standard case' parameters. For reference, we list these parameters here: $r/a = 0.5$, $R/L_{Ti,e} = 9$, $R/L_n = 3$, $q = 2$, $T_i/T_e = 1$, $s = 1$, $\beta = 0$, $\nu^* = 0$.

Finally, we clarify here the wavenumber notation used in this work. k_y is the wavenumber, normalized to $1/\rho_s$, corresponding to the binormal coordinate y in the GENE field-aligned coordinate system. In QuaLiKiz, k_θ is used, which corresponds to the wavenumber in the poloidal direction. For all parameters studied in this work, k_y differs from $k_\theta \rho_s$ by at most 2%. Thus for convenience we will not differentiate between the two, and henceforth always use k_y in reference to all simulation results.

5.2 Review of the QualiKiz model

QuaLiKiz is based on the electrostatic eigenvalue gyrokinetic code Kinezero [8], which includes two ion species and both passing and trapped electrons. For the minimization of computational expense - critical for integrated modelling applications - the electrostatic potential shape is not calculated self-consistently. Rather, an analytical solution obtained in the fluid limit is taken and the strong ballooning representation limit applied. A Krook-like collision operator accounting for the impact of collisions on the trapped electrons has also been included [9]. Shifted circle ($s - \alpha$) geometry is assumed for equilibrium.

The linear response calculated by Kinezero has been incorporated into the gyrokinetic quasilinear expressions for the particle and heat fluxes, resulting in the QuaLiKiz transport model [1]. From henceforth we will also refer to the eigenvalue solver as part of 'the QuaLiKiz model'. The fluxes can be schematically decomposed into contributions of the linear response and the saturated electrostatic potential:

$$\Gamma, Q_i, Q_e = \sum_{k_\theta, \omega, \omega_{kj}} \text{Im}(R_{lin}^{\Gamma, Q_i, Q_e}(k_\theta, \omega, \omega_{kj})) |\delta\phi(k_\theta, \omega, \omega_{kj})|^2 \quad (5.1)$$

Where $R_{lin}^{\Gamma, Q_i, Q_e}$ is the linear response for the density, ion temperature, and electron temperature fluctuations respectively, $\delta\phi$ the saturated electrostatic potential, ω the fluctuation frequency, and ω_{kj} the eigenfrequency of the unstable mode with poloidal wavenumber $k_\theta = nq/r$. Multiple instabilities may coexist with the same k_θ , and are discriminated by the index j . The contribution of each unstable mode (also named 'branches') to the fluxes are summed over. The linear response has been extensively validated by comparison with non-linear simulations [4, 10].

The model for the saturated electrostatic potential - a critical ingredient in evaluating the turbulent fluxes - consists of a mixing length rule weighted by a k-space spectral function validated against both non-linear simulations and experimental observations [4, 11].

The saturated potential frequency spectral shape is taken as a Lorentzian, with a width equal to the linear growth rate. This assumption has been shown to agree with non-linear simulations and experimental observations at transport relevant wavelengths [10]. Finally, the QuaLiKiz predicted fluxes are normalized by a single, constant, fitting coefficient, set such that the ion heat flux predicted by QuaLiKiz for the GA-standard case agrees with GYRO predictions.

The mixing length rule as previously applied in QuaLiKiz is now presented. We re-define for convenience the saturated electrostatic potential for each mode as $|\delta\phi_{k,j}|^2$, where k is the wavenumber index and j the branch index. We assume $|\delta\phi_{k,j}|^2 = S_{kj}L_j$, where S_{kj} is a branch dependent k -space spectral function shape, and L_j is the maximum mixing length amplitude for branch j : $L_j \equiv |\frac{\gamma_{k,j}}{\langle k_\perp^2 \rangle}|_{max}$. The maximum is taken over the k -spectrum. The k_θ corresponding to the maximum is denoted $k_\theta|_{max}$, and represents the peak of the flux spectrum defined by S_{kj} , designed to reproduce the downshifted non-linear flux spectrum [12]. S_{kj} is taken such that $S_{kj} \propto (k_\theta)^3$ for $k_\theta < k_\theta|_{max}$, and $S_{kj} \propto (k_\theta)^{-3}$ for $k_\theta > k_\theta|_{max}$. $\langle k_\perp^2 \rangle = k_\theta^2 (1 + (s - \alpha)^2 \langle \theta^2 \rangle)$, where $\langle \rangle$ denotes a poloidal average. This average over the ballooning structure, when integrating over the form imposed by the fluid Gaussian eigenmode assumption, is given by $\langle \theta^2 \rangle = \frac{2d^2\Gamma(3/4)}{w^2\Gamma(1/4)}$. d is the distance between rational surfaces and w is the mode Gaussian width. This choice of k -space spectrum is in agreement with nonlinear simulations, and observations [4, 11].

Fluxes computed by QuaLiKiz have been compared with GYRO non-linear simulations, and agreement for both heat and particle fluxes have been obtained in R/L_T , Z_{eff} , T_i/T_e and collisionality scans around GA-standard case parameters [4]. Extensive GYRO non-linear simulations consisting of q -profile and magnetic shear scans have previously been carried out [13]. In Fig.5.1, the R/L_T scan comparison is reproduced, and q -profile and magnetic shear scans around the GA standard case have been added. The q -profile scan also shows agreement between the predictions. However, significant discrepancies between QuaLiKiz and GYRO are evident in the magnetic shear scan, in the region $|s| < 0.5$. Note that $\alpha = 0$ in all these calculations. We now set out to uncover the sources of this discrepancy.

5.3 Magnetic shear impact on linear physics

In this section we review linear growth rate dependence on magnetic shear, and compare QuaLiKiz and linear-GENE growth rate calculations. Both the role of the magnetic shear on the R/L_{Ti} thresholds of ITG instabilities and on γ -stiffness is discussed. γ -stiffness is defined as the rate of change of the growth rate as a function of the driving gradient lengths. In section 5.3.1 analytical and computational results for the ITG instability threshold are briefly reviewed. While in the fluid limit we expect higher growth rates for higher s/q (see appendix 5.A), the linear thresholds of the ITG modes are in fact expected to decrease with s/q . This points to reduced γ -stiffness at low magnetic shear. Particularly, the toroidal ITG branch modes at low $k_y s$ are stabilized. The analytical linear results are corroborated by computations with both linear-GENE and QuaLiKiz. The agreement between dominant branch growth rate calculations in linear-GENE and Qua-

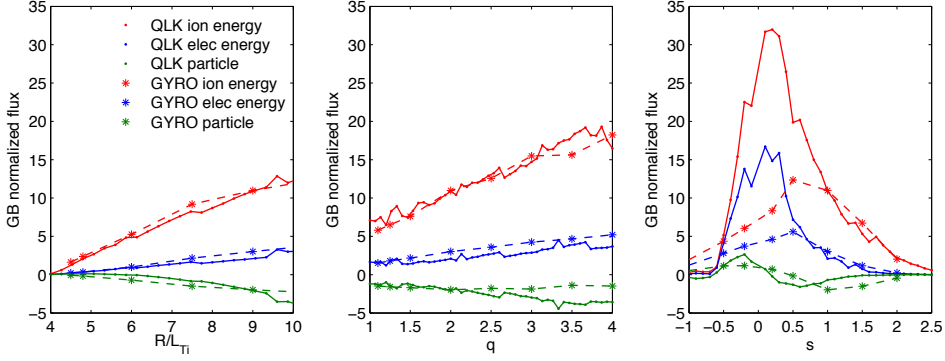


Figure 5.1: Ion and electron flux, compared between GYRO and QuaLiKiz for 3 scans around the GASTD case: R/L_T (left panel), q (central panel), and s (right panel). This comparison is with the previous mixing length formulation in QuaLiKiz as presented in Casati *et al* [4].

LiKiz is satisfactory at low magnetic shear. This leads to the conclusion that the reason for the discrepancy between the quasilinear and non-linear fluxes at low magnetic shear lies in the non-linear physics.

5.3.1 Linear thresholds from kinetic theory

In this section we briefly review previous results of kinetic theory regarding magnetic shear dependences on threshold, for ITG turbulence. For the η_i ITG mode ($\eta_i \equiv d\ln T_i / d\ln n$), the R/L_{Ti} threshold has been calculated in the short-wavelength, flat density limit ($k_\theta \rho_s s \approx (L_T/R)^{1/4}$, $R/L_n < 2(1 + T_i/T_e)$), as follows [14]:

$$(R/L_{Ti})_c \approx \frac{4}{3}(1 + T_i/T_e)(1 + 2\frac{s}{q}) \quad (5.2)$$

Increasing the density gradient is predicted to lead to an increased R/L_{Ti} threshold. However, when including trapped electrons the increased density gradient can destabilize the TEM branch, nullifying the turbulence stabilization [15].

A study of the (s, q) impact on the linear R/L_T threshold for ITG/TEM modes in Kinzero (and thus in QuaLiKiz) have previously been carried out with fixed $T_i/T_e = Z_{eff} = 1$, $\alpha = 0$. and in the flat density limit [16]. The parameterization of the critical temperature gradient lengths, $(R/L_T)_c$, was as follows for ITG-like modes: $1.1 + 1.4s + 1.9s/q$ for $s > 0$, and $0.9 + 1.6|s| + 9.9|s|/q$ for $s < 0$. This mixed s and s/q dependency share the same qualitative dependencies as in the analytical limits above. The asymmetry with the sign of s is due to the stabilization of the toroidal branch for negative shear. An extensive study of T_i/T_e dependence in QuaLiKiz was carried out by Casati *et al* [17].

Finally, comprehensive linear gyrokinetic simulations with GS2 have led to a parameterization of ETG linear thresholds, isomorphic with ITG linear thresholds (assuming adiabatic electrons), for which it can be written as follows [18]:

$$\left(\frac{R}{L_{Ti}}\right)_c = \max \left\{ \left(1 + \frac{T_i}{T_e}\right) \left(1.33 + 1.91 \frac{s}{q}\right) (1 - 1.5\epsilon) \left(1 + 0.3\epsilon \frac{d\kappa}{d\epsilon}\right), 0.8 \frac{R}{L_n} \right\} \quad (5.3)$$

where $\epsilon = r/R$ and κ is the elongation. In the circular cross-section limit, this formula is very similar to the analytical formula, equation 5.2.

Growth rate contour plots calculated by QuaLiKiz are shown in Fig.5.2. The growth rates correspond to the most unstable branch in GA-standard R/L_T and magnetic shear scans (where $R/L_{Ti} = R/L_{Te}$). In the left panel, the maximum growth rate for the spectrum $k_y < 0.8$ is displayed. In the right panel, the growth rates for $k_y = 0.2$ are displayed. In both plots, the increased instability threshold for high magnetic shear and negative magnetic shear is clearly visible. The residual modes at low R/L_T at low magnetic shear are modes in the electron diamagnetic direction due to the finite R/L_n in the GA-standard case.

An interesting detail to note in the low k_y case (right panel) of Fig.5.2 is reduced γ -stiffness at low magnetic shear. This is evidenced by the significantly decreased gradient with respect to R/L_T at $s < 0.2$. A possible explanation for this decreased γ -stiffness is that the long-wavelength limit is reached, defined by $k_y s \ll (L_{Ti}/R)^{1/4}$. In this limit, the toroidal branch is stabilized [19]. This is due to the growth of the eigenfunction envelope width along the magnetic field, given by $\theta \approx s^{-1/2} \epsilon_T^{1/4} (k_\theta \rho_i)^{-1}$. A broad envel-

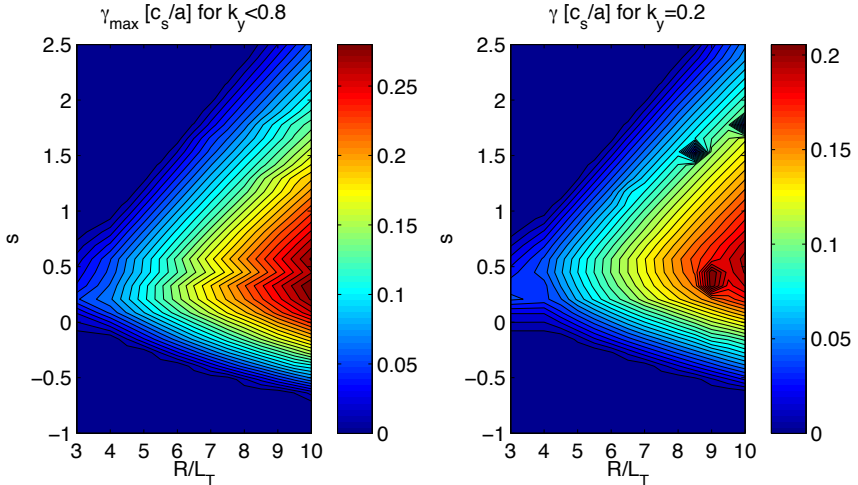


Figure 5.2: Linear growth rates for the most unstable branch calculated by QuaLiKiz in a GA-STD R/L_T scan, where $R/L_{Ti} = R/L_{Te}$. In the left panel the maximum growth rate for the spectrum $k_y < 0.8$ is shown. In the right panel, the growth rate for $k_y = 0.2$ is shown.

ope leads to decreased interaction with the bad curvature region, stabilizing the toroidal branch. In the QuaLiKiz Gaussian eigenmode approximation the envelope width is proportional to d/w , which increases at low k_y , and also increases at low magnetic shear as seen in figure 5 in Romanelli *et al* [9]. Decreased linear growth rates at low k_y s may lead to preferential quenching of long wavelength turbulence by zonal flows at low magnetic shear. Since these long wavelengths dominate the transport, this can play a major role in the determination of the fluxes.

5.3.2 Comparison of QuaLiKiz and linear-GENE growth rates

Growth rates of the dominant branch calculated by QuaLiKiz and GENE are compared in this section. In Fig.5.3 results of a R/L_T scan are displayed (where $R/L_{Ti} = R/L_{Te}$ throughout the scan), around the GA-standard case, at $k_y = 0.15, 0.3$ and $s = 0.1, 1$. We can see that even though the R/L_T thresholds are lower for the lower shear cases, the γ -stiffness is also lower for the lower shear case, leading to a crossover of the high-shear and low-shear γ curves at a R/L_T position dependent on k_y . At low k_y , this crossing point is much closer to the threshold, at experimentally relevant R/L_T . Note that this effect is predicted by both GENE and QuaLiKiz, in spite of the Gaussian eigenmode ansatz made in QuaLiKiz. Indeed, it is shown in Appendix 5.C that this ansatz is valid down to $s = 0.1, k_y = 0.15$.

We also show in Fig.5.4 a comparison between linear-GENE and QuaLiKiz of the

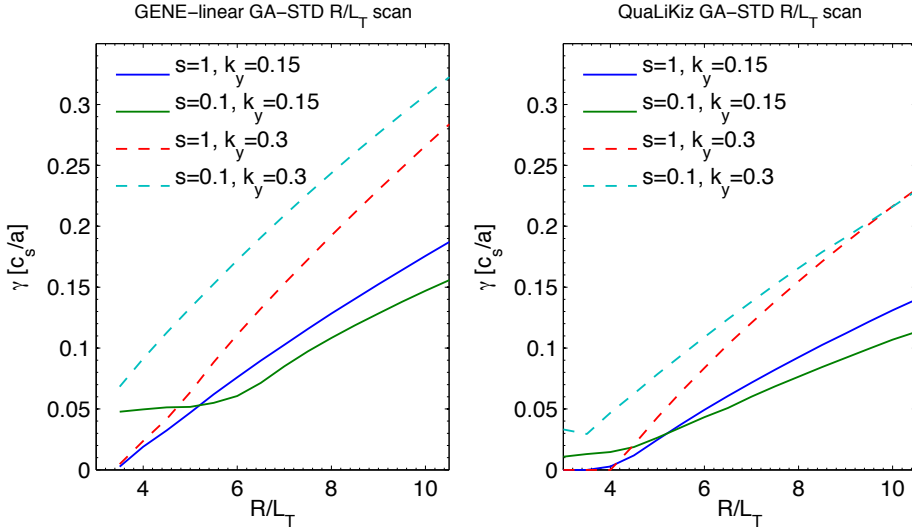


Figure 5.3: Linear growth rates calculated for the GA-STD kinetic electron case in a R/L_T scan at various k_y and magnetic shear values by both linear-GENE (left panel) and QuaLiKiz (right panel).

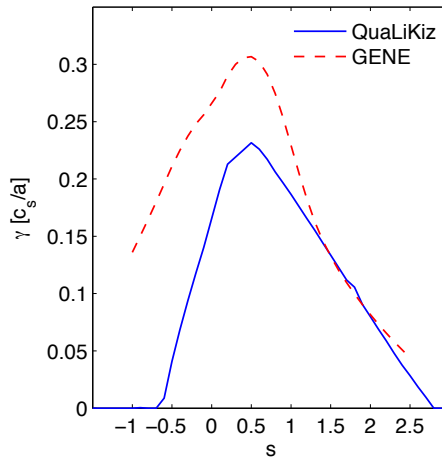


Figure 5.4: Linear growth rates calculated for a magnetic shear scan around the GA-standard case by both QuaLiKiz (solid lines) and linear-GENE (dashed lines) for $k_y = 0.3$.

growth rate calculation for a GA-standard magnetic shear scan at $k_y = 0.3$. The QuaLiKiz predictions agree with linear-GENE to within $\sim 30\%$ even at low magnetic shear. However, at negative magnetic shear QuaLiKiz severely underpredicts the growth rates, due to an underestimation of the slab ITG branch growth rate. This may be due to the strong ballooning representation and prescribed eigenmode assumptions. The resolution of this issue is left for future work.

In summary, while the ITG threshold decreases at low magnetic shear, the γ -stiffness is also reduced at lower magnetic shear. At low k_y this effect is increased. This is reproduced both by linear-GENE and QuaLiKiz. Furthermore, dominant branch linear-GENE and QuaLiKiz calculations agree to within $\sim 30\%$ in the parameter ranges studied, in spite of the QuaLiKiz Gaussian eigenmode ansatz. Therefore a miscalculation of the dominant branch growth rate cannot be responsible for the low magnetic shear flux discrepancy between QuaLiKiz and non-linear models, where the QuaLiKiz flux is significantly higher as seen in Fig.5.1. The reduced growth rates at combined low magnetic shear and low k_y is an important point, since this could have ramifications for setting the turbulence correlation length. This is explored further in the modification of the mixing length rule in section 5.4.3.

5.4 Non-linear effects at low magnetic shear

In this section we explore the non-linear physics which may lead to the lack of validity of the previous QuaLiKiz quasilinear computed fluxes at low magnetic shear. As described in section 6.1, the quasilinear flux can be decomposed into two parts: the linear response and the saturated electrostatic potential. This description is justified if the particles un-

dergo stochastic linearized trajectories. This assumption, central to quasilinear theory, can be verified by examining the ordering of the turbulence autocorrelation time compared to the eddy turnover time, as expressed through the Kubo number. This verification was done here for low magnetic shear. Furthermore, the QuaLiKiz mixing length model for the non-linear saturated potential was also reexamined at low magnetic shear. This includes the model for k_{\perp} , the evaluation of the k_y maximum of the non-linear flux spectrum, and the frequency broadening assumption. These assumptions were extensively validated previously for a wide range of parameters [4], but not for magnetic shear scans. We extend this validation towards low magnetic shear.

A set of dedicated GENE non-linear runs were carried out to test and validate the QuaLiKiz assumptions. These non-linear runs are introduced in section 5.4.1. In section 5.4.2 the evaluation of the Kubo numbers in the non-linear simulations are discussed. In section 5.4.3 the mixing length model for the saturated potential is reexamined, and modified following comparisons with the non-linear simulations. Finally, predicted fluxes from both the modified QuaLiKiz and the set of non-linear GENE simulations are compared in section 5.4.4.

5.4.1 Description of GENE runs

A total of 16 non-linear GENE runs were carried out. The runs are comprised of 4 sets of 4-point magnetic shear scans at $s = -0.4, 0.1, 0.6, 1$. The sets are comprised of the GA-standard case, and 3 further sets with lowered inverse gradient lengths and varying q -profile values, consistent with typical JET hybrid scenario parameters at mid-radius. This was done in order to widen the GENE-QuaLiKiz magnetic shear scan validation in q -profile parameter space, down towards $q = 1$ which often coincides with low magnetic shear in experiments. Furthermore, the added data sets allow GENE-QuaLiKiz validation at lower levels of flux than the GA-standard case. Since the eventual goal is to apply QuaLiKiz as a transport model within the integrated modelling framework, validation at more experimentally relevant fluxes is critical. The parameters for these sets are summarized in table 5.1. All GENE simulations carried out were electrostatic, local, collisionless, with periodic radial boundary conditions, kinetic electrons (and real mass ratio), and with $s - \alpha$ geometry. Throughout the sets, $\alpha = 0$, $r/a = 0.5$, and $R_0/a = 3$.

In all simulations, we used 16-point discretization in the parallel direction, 32 or 48-points in the parallel velocity directions (based on linear convergence studies), and 8 magnetic moments. For these parameters, non-linear convergence tests were carried out, and the heat flux sensitivities were negligible. For each simulation, extensive non-linear convergence studies were carried out in the number of toroidal modes, the perpendicular box sizes, and in the radial grid discretization. The box sizes in the perpendicular directions range from $[L_x/\rho_s, L_y/\rho_s] = [100, 126]$ for the set A, $s = 1$ case to up to $[L_x/\rho_s, L_y/\rho_s] = [333, 210]$ for the more challenging $s = 0.1$ cases. The number of toroidal modes (n_y) employed ranged from 16 for the set A, $s = 1$ case, to 32 for the $s = 0.1$ cases. The $n_y = 32$ cases correspond to $k_y(max) = 1.55$ or $k_y(max) = 0.93$, depending on the perpendicular box size. In general, the $s = 0.1$ cases were more computationally intensive due to the higher radial box size needed to satisfy the parallel

Table 5.1: Input parameters for the GENE magnetic shear scans.

Set name	R/L_{Ti}	R/L_{Te}	R/L_n	T_i/T_e	q
A (GASTD)	9	9	3	1	2
B	7.6	6.7	4	1.4	1.4
C	6.3	5.5	3.3	1.4	1.4
D	7.6	6.7	4	1.4	1

boundary condition, and also due to the higher number of toroidal modes necessary for convergence.

Low heat flux sensitivity was also found to the inclusion of collisions. However, it was found that the particle transport was highly sensitive to the velocity and parallel space resolutions, particularly when a particle inward flux dominates (as in the set A, $s = 1$ case). This particle transport sensitivity was greatly decreased when including collisions. In general, verification of the QuaLiKiz particle transport predictions is also of great importance. However, it is preferable to carry out this verification vs non-linear runs when including collisionality. This is due both to the increased experimental relevance, and also the seemingly improved non-linear convergence properties of particle diffusivity in collisional runs. Due to the increased computational expense of collisional runs, a more rigorous validation of the particle fluxes when including collisionality is deferred to future work. Here we concentrate on the heat transport validation of the collisionless QuaLiKiz model at low magnetic shear, and maintain a caveat on the convergence of the non-linearly calculated particle fluxes in this work, particularly the inward fluxes. The discretization and box size choices, as well as the transport predictions of all 16 runs, are shown in table 5.2.

5.4.2 Kubo numbers

The validity of the quasilinear assumption depends on whether test particles in the turbulent fields undergo stochastic linearized trajectories, allowing a diffusive random-walk process to be considered as opposed to field trapping. This can be quantified by the Kubo number K [20, 21], the ratio between the Eulerian autocorrelation time, τ_{ac} , of the fluctuating potential and the particle flight time, τ_f . τ_f is defined as $\lambda_x / \langle v_x \rangle$, where λ_x is the radial correlation decay length, and $\langle v_x \rangle$ the root mean square radial velocity of a test particle in the turbulent field. For $K < 1$, the autocorrelation time of the turbulent field is shorter than the transit time of a test particle around a turbulent eddy, justifying the use of a random-walk diffusive model. This condition is however necessary but not sufficient. In addition, there must be enough randomness in the Hamiltonian described in the dynamics, e.g. when it includes many waves with random phases [22]. This condition though is well satisfied in the strong turbulence cases studied here. For a R/L_T scan based on the GA-standard case, computed using GYRO, it was seen that $K < 1$ [4]. This was done calculating the autocorrelation time as $\tau_{ac} = 2D / \langle |v_x|^2 \rangle$, where D is the

Table 5.2: Grid settings and results of converged GENE non-linear runs.

Run	n_x	n_y	$k_y min$	n_z	n_v	n_w	L_x	Sim time[R/c_s]	$\chi_i/\chi_e/D$ [GB units]
A: s=1	140	16	0.05	16	32	8	100	950	39.64/9/-0.75
A: s=0.6	140	16	0.05	16	48	8	140	960	39.94/13.21/0.26
A: s=0.1	256	24	0.05	16	48	8	200	560	21.84/11.51/2.57
A: s=-0.4	256	25	0.03	16	32	8	166	630	23.66/11.67/5.36
B: s=1	140	16	0.05	16	48	8	140	800	18.33/5.7/0.9
B: s=0.6	160	32	0.03	16	48	8	160	750	25.58/11.64/3.32
B: s=0.1	300	32	0.03	16	48	8	333	720	11.63/7.88/2.84
B: s=-0.4	160	32	0.03	16	48	8	160	640	13.37/9.62/3.86
C: s=1	140	16	0.05	16	48	8	140	1570	9.54/1.77/-0.01
C: s=0.6	210	24	0.05	16	48	8	140	600	17.65/5.22/0.95
C: s=0.1	300	32	0.03	16	48	8	200	600	7.74/4.01/1.29
C: s=-0.4	240	24	0.05	16	48	8	160	610	7.32/4.89/1.9
D: s=1	200	32	0.05	16	48	8	200	610	8.94/2.25/0.05
D: s=0.6	240	32	0.05	16	48	8	160	385	15.69/6.08/1.46
D: s=0.1	300	32	0.05	16	48	8	200	560	9.18/5.42/1.87
D: s=-0.4	240	32	0.05	16	48	8	160	380	7.87/5.61/2.2

particle diffusivity, as carried out in [23]. This assumes a priori that the particle transport is due to a random-walk process in the oscillating field. In this work we calculate the Kubo number by a more direct method, by calculating the τ_{ac} directly from the fluctuating potential field from GENE non-linear simulations. The time correlation function is $C(\Delta t) = \langle \phi(x, y, t) \phi(x, y, t + \Delta t) \rangle / \langle |\phi^2| \rangle$, averaging over the x and y directions. The parallel coordinate is kept fixed at the low-field side. The correlation time is taken as the $1/e$ time of this function. All $n = 0$ modes are not included in the calculation, which thus considers only the flux inducing $n > 0$ background drift-wave population. λ_x is calculated as the $1/e$ length of the function $C(\Delta x) = \langle \phi(x, 0, t) \phi(x + \Delta x, 0, t) \rangle / \langle |\phi^2| \rangle$. $\langle v_x \rangle = \sqrt{\langle E_y^2 \rangle} / B_{ref}$, with the same averaging procedure as τ_{ac} for consistency. B_{ref} is the reference magnetic field used to normalize the GENE equations and variables.

We have calculated the Kubo numbers for the full set of GENE non-linear runs. The calculated correlation lengths, times and Kubo numbers can be found in table 5.3. For all cases, $K < 1$. We thus conclude that the quasilinear approximation indeed holds. Note furthermore that $K < 1$ but still of order unity supports the application of the mixing length rule for setting the level of the saturated potential, where the implicit assumption is that the step length of the random walk process is the eddy size. While the quasilinear approximation itself may hold, the value of the saturated electrostatic potential cannot be determined by linear theory. This value is determined by a mixing length rule, whose validation at low magnetic shear is evaluated in the next section.

Table 5.3: Correlation times, lengths and Kubo numbers for the GENE non-linear runs. Units are Larmor radii for the lengths, and R/c_s for the times.

Run	$\sqrt{\langle E_y^2 \rangle}$	λ_x	t_{ac}	K
A: s=1	8.6	12.60	1.85	0.42
A: s=0.6	11.78	11.2	2.05	0.72
A: s=0.1	12.23	7.12	0.58	0.33
A: s=-0.4	9.66	6.94	1.85	0.86
B: s=1	8.7	12.70	2.14	0.49
B: s=0.6	10.8	10.50	1.74	0.60
B: s=0.1	8.59	6.90	1.09	0.45
B: s=-0.4	7.93	6.87	2.14	0.82
C: s=1	5.37	13.67	1.90	0.27
C: s=0.6	8.48	10.92	3.44	0.89
C: s=0.1	6.69	7.30	1.44	0.44
C: s=-0.4	5.5	6.08	2.01	0.61
D: s=1	7.38	9.76	0.96	0.24
D: s=0.6	9.23	8.41	1.38	0.50
D: s=0.1	7.67	5.88	1.20	0.52
D: s=-0.4	6.9	5.93	1.96	0.76

5.4.3 Reevaluation of the QuaLiKiz saturated potential model

The model for the saturated potential is comprised of three parts: the model for k_\perp , setting the maximum and spectral shape of the non-linear flux spectrum, and frequency broadening. We briefly recall here the previous model. The k_y maximum of the flux spectrum is designated $k_y|_{max}$, and corresponds to the maximum of the mixing-length flux spectrum $\frac{\gamma_k}{\langle k_\perp^2 \rangle}$ [12, 24], where:

$$\langle k_\perp^2 \rangle = k_y^2 (1 + (s - \alpha)^2 \langle \theta^2 \rangle) \quad (5.4)$$

This formulation of k_\perp calculates only the effective k_x due to the shearing of the mode along the field line, and assumes that the dominant instability has intrinsic $k_x = 0$.

The k-spectrum is k_y^{-3} and k_y^3 above and below the flux spectrum maximum respectively. The frequency spectrum of the saturated potential is broadened by the linear growth rate as follows: $\phi_k(\omega) \propto \frac{\gamma_k}{(\omega - \omega_k)^2 + \gamma_k^2}$. This model has been shown to lead to discrepancies both in the k_y of the saturated potential peak and in the frequency spectrum width when compared to GENE non-linear results at low magnetic shear. The k-spectrum model is reviewed and an improved formulation for k_\perp is proposed. The frequency spectrum broadening comparison and consequences of the discrepancy are then addressed.

Choice of k_\perp and the model for calculating the flux spectrum peak

The correlation length of the turbulence is set both by the k_x inherent in the k_\perp formulation and also by $k_y|_{max}$. The magnetic shear dependence in equation 5.4 suggests (with $\alpha = 0$) that the effective k_x is lower at $s = 0.1$ than at $s = 1$ (for the same $k_y|_{max}$). This would correspond to increased correlation lengths as the magnetic shear is reduced. The k_x and k_y components of k_\perp from equation 5.4 are plotted in Fig.5.5, for the GA-standard $s = 1$ and $s = 0.1$ case, where $\langle\theta^2\rangle$ is calculated from the QuaLiKiz eigenmode ansatz. At $s = 1$ the assumed structures are approximately isotropic, particularly at lower, transport relevant k_y . At $s = 0.1$, $k_x < k_y$. Even though $\langle\theta^2\rangle$ increases as the magnetic shear decreases, this does not compensate the decreasing s^2 , at least down to $s = 0.1$. This was corroborated by linear GENE analysis, where the eigenmodes were self-consistently calculated.

However, the magnetic shear dependence in equation 5.4 is not consistent with the non-linear results, where the correlation length decreases with decreasing shear, as seen in table 5.3. The eddy structure for both the $s = 0.1$ and $s = 1$ non-linear GA-standard cases are shown in Fig.5.6. The structures are roughly isotropic. The decreased correlation length at low magnetic shear is a result of the increased $k_y|_{max}$ at $s = 0.1$.

Therefore the $k_y|_{max}$ calculation is also critical for setting correlation length and flux values. However, it was found that due to the large weight of $1/k_y^2$ at low k_y , $k_y|_{max}$ typically corresponds to the lowest (in k_y) unstable mode, in spite of the relatively low growth rates. For QuaLiKiz this is typically in the range of $k_y = 0.05 - 0.1$. This is in disagreement with the non-linear flux spectra maxima from the magnetic shear scans, only agreeing approximately at $s = 1$. Thus both the k_\perp and $k_y|_{max}$ formulations must be rectified to correctly account for the magnetic shear dependencies on the flux in the

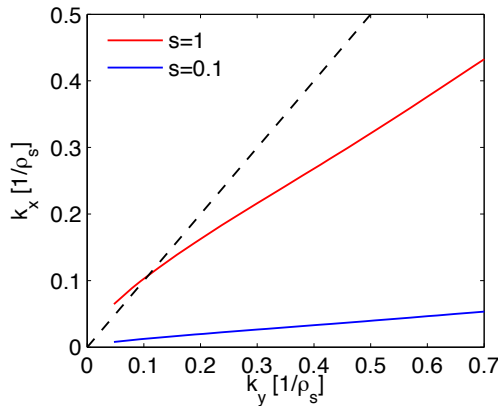


Figure 5.5: k_x as a function of k_y , as calculated in QuaLiKiz for $s = 1$ and $s = 0.1$, from the k_\perp formulation given in equation 5.4. The dashed curve represents $k_x = k_y$, as a measure for the degree of isotropy.

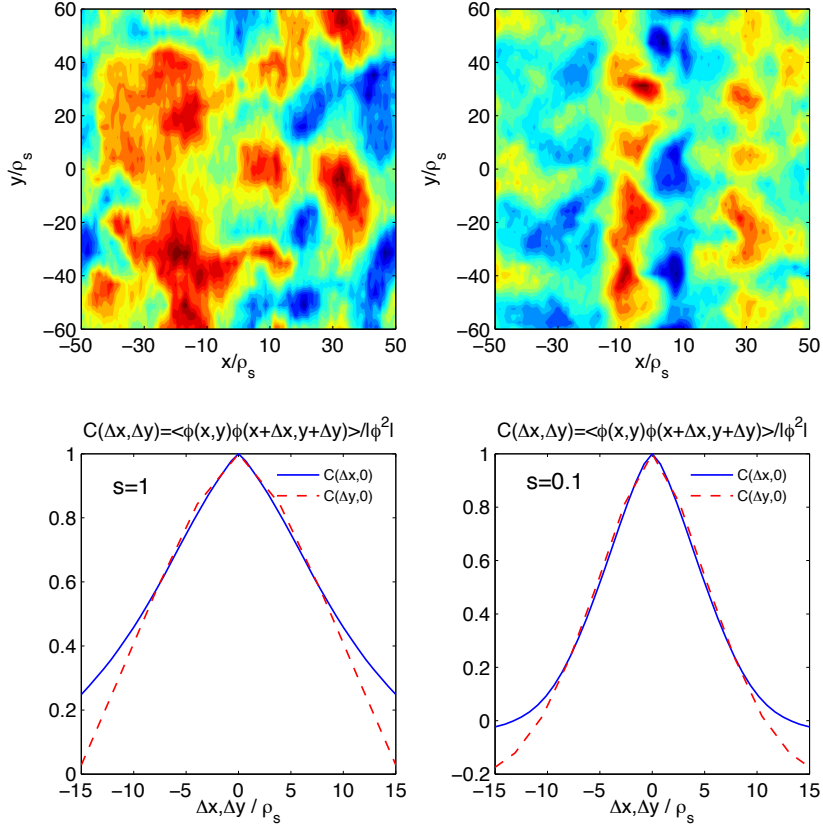


Figure 5.6: Contours of the electrostatic potential (top row) and the x and y length correlation functions (bottom row) for a typical timeslice in GENE $s = 1$ (left column) and $s = 0.1$ (right column) GA-standard case simulations.

mixing length model.

The non-linear flux spectra maxima, $k_y|_{max}$, were reproduced by replacing the effective k_x in k_\perp with the actual k_x values from the non-linear simulations. Thus $k_\perp^2(nl) = k_y^2 + \langle k_x \rangle_{nl}^2(k_y)$, where $\langle k_x \rangle_{nl}(k_y)$ is the averaged value of k_x for each k_y mode in the non-linear simulation. $\langle k_x \rangle(k_y)$ is defined as $\sum k_x |\phi(k_x, k_y)|^2 / \sum |\phi(k_x, k_y)|^2$, where the summation is over $k_x \geq 0$ for a given k_y . The values of $|\phi(k_x, k_y)|^2$ are pairwise averaged over negative and positive k_x , as well as over the parallel coordinate and for the times corresponding to the saturated state of the simulation. In the non-rotating, up-down symmetric plasmas considered in our simulations, k_x is symmetric around 0. In Fig.5.7 these $\langle k_x \rangle$ values are plotted versus k_y for the GENE non-linear GA-standard case magnetic shear scan. At low k_y , the eddies are not isotropic. $\langle k_x \rangle$ does not continue to drop

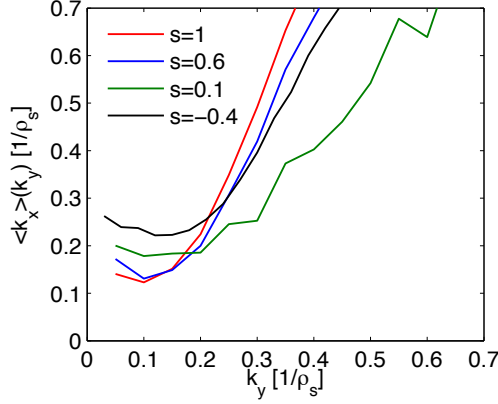


Figure 5.7: $\langle k_x \rangle(k_y)$ for the k_y points from a GENE non-linear GA-standard magnetic shear scan.

at low k_y , and saturates at a value which increases as the magnetic shear decreases. This corresponds to reduced correlation lengths at low magnetic shear.

The $k_y|_{max}$ corresponding to the maximum $\gamma_k/k_\perp^2(nl)$ corresponds well with the non-linear flux spectra k_y maximum, as seen in Fig.5.8 for the entire range of non-linear simulations carried out. γ_k was taken from GENE linear simulations and $k_\perp^2(nl)$ from GENE non-linear simulations. The considerations raised in sections 5.3.1 - the stabilization of the toroidal branch at low sk_y - also plays a role in setting $k_y|_{max}$. Not only is $\langle k_x \rangle$ increased at low magnetic shear, but the growth rates themselves are reduced at low sk_y , further increasing the obtained $k_y|_{max}$, leading to reduced correlation lengths at low magnetic shear.

In light of these observations from the non-linear simulations, we have improved the k_\perp^2 formulation in QuaLikiz by taking into account the non-linear contribution to $\langle k_x \rangle$. This simultaneously recovers the non-linear flux spectra k_y maximum, and provides the magnetic shear and q -profile dependence on the precise relation between k_y and $\langle k_x \rangle$ at $k_y|_{max}$. We have found that the following relation successfully reproduces the non-linear $\langle k_x \rangle(k_y)$ for the magnetic shear and q -profile scans carried out in this work:

$$\langle k_x \rangle(k_y) = k_y s \sqrt{\langle \theta^2 \rangle} + 0.4 \frac{e^{-2|s|}}{\sqrt{q}} + \frac{3}{2} (k_y - 0.2) H(k_y - 0.2) \quad (5.5)$$

Where H is a Heavyside function. The first term on the RHS is the effective k_x due to the magnetic shear, which also appears in the previous k_\perp^2 formulation. The second term approximates the value of the non-linear contribution to $\langle k_x \rangle$ in the long wavelength, transport relevant region. The third term on the RHS was set to fit the non-linear $\langle k_x \rangle$ at higher k_y , and only plays a minor role at transport relevant k_y . The first term dominates at high magnetic shear, while the second term dominates at low magnetic shear. The QuaLikiz mixing length rule formulation for k_\perp^2 was thus set in accordance with equation 5.5. The results for $k_y|_{max}$, using the QuaLikiz γ_k and the new $k_\perp^2 = k_y^2 + \langle k_x \rangle^2$,

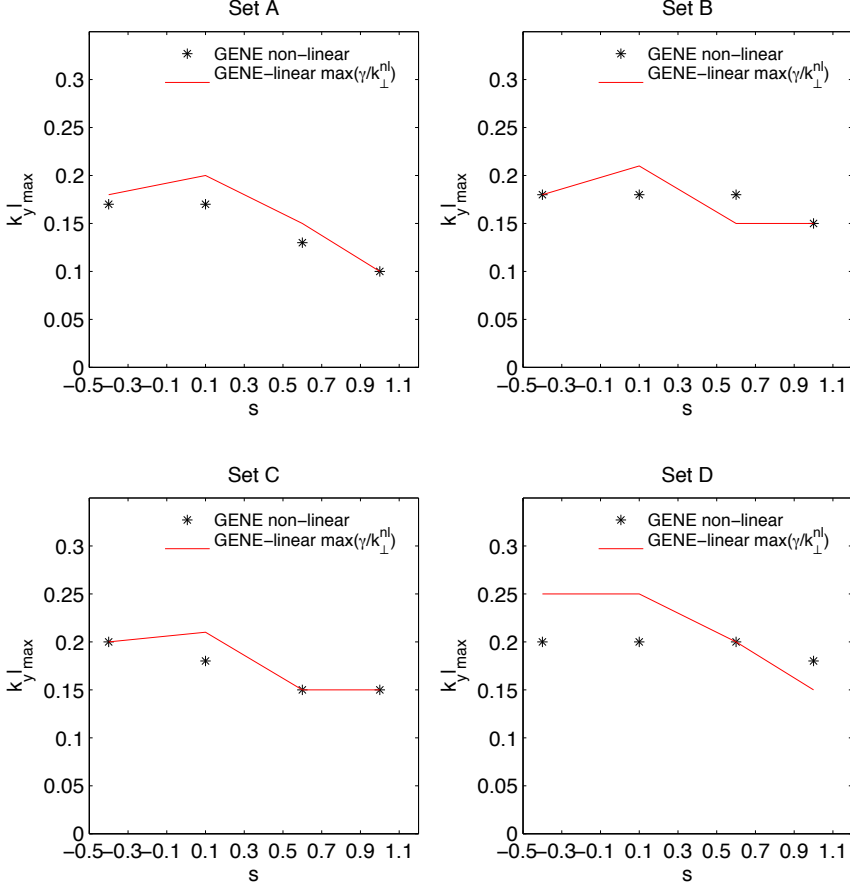


Figure 5.8: Comparison of $k_y|_{\max}$ from non-linear simulations, and from the maximum of the $\gamma_k/k_{\perp}^2(nl)$ spectrum, where γ_k is from GENE-linear calculations, and $k_{\perp}^2(nl) = k_y^2 + \langle k_x \rangle^2(k_y)$ is taken from the non-linear simulations.

are seen in Fig.5.9, where the results for the newly formulated k_{\perp}^2 are compared with the previously formulated k_{\perp}^2 . The new formulation leads to a much improved reproduction of the non-linear $k_y|_{\max}$. The absolute value $|s|$ in the exponent in the $\langle k_x \rangle$ formulation was set to avoid a non-physical exponential increase of $\langle k_x \rangle$ at large absolute values of negative magnetic shear. While the continuing decrease of the correlation length at negative magnetic shear is then not captured, we note that in general the QuaLiKiz predictions at negative magnetic shear deviate from the non-linear predictions due to an underprediction of the slab ITG branch. This is seen in Fig.5.9, for $s < \sim -0.3$, where the high values predicted for $k_y|_{\max}$ is due to mode stabilization at lower k_y , and not due to k_{\perp}^2 . The present formulation is thus relevant for low magnetic shear, while improved

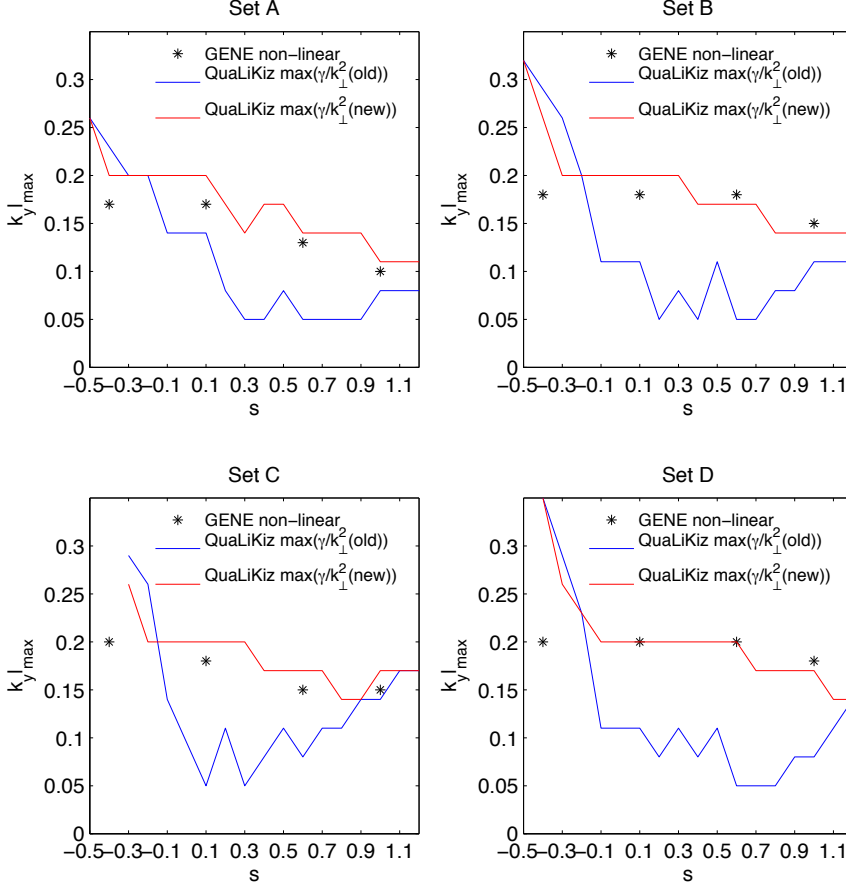


Figure 5.9: Reproduction of the non-linear flux spectra maximum from the maximum of the $\gamma_k/k_{\perp}^2(nl)$ spectrum, where γ_k is from QuaLiKiz, and $\langle k_x \rangle^2$ is taken from a formula found to reproduce GENE non-linear simulations.

agreement between QuaLiKiz and non-linear flux predictions at negative magnetic shear is left for future work.

In addition to improving the k_{\perp} formulation, we can consider also introducing a shearing effect of zonal flows on large wavelength turbulence [25]. This can be done by a ExB quench rule similar to that employed in the quasilinear models GLF23 [26, 27] and TGLF [28] for external toroidal velocity. Indeed, the non-linear $k_y|_{\max}$ was also recovered by calculating $\max(\gamma_{eff}/k_y^2)$, where γ_{eff} is a quenched growth rate taken as $\gamma_{eff} = \max(0, \gamma_k - 0.3\omega_{ExB})$. ω_{ExB} is the effective zonal flow ExB shear rate taken from the GENE non-linear simulations, including the effect of the autocorrelation time on the effective shearing time [29]. 0.3 is a tuned coefficient which provided a best fit to the

non-linear flux spectra maxima throughout the set of simulations. k_\perp was replaced by k_y due to the approximate k_x and k_y isotropy. However, the simultaneous inclusion of γ_{eff} and the improved k_\perp formulation does not change the calculation of $k_y|_{max}$ compared to the sole inclusion of the improved k_\perp formulation. This is because the role played by the zonal flow shearing - the quenching of long wavelength modes - is effectively played by the non-isotropy of k_y and k_x at low k_y . Due to the challenge in parameterizing the zonal flow shear rate ω_{ExB} throughout parameter space within QuaLiKiz, and given the minor effect the zonal flow shearing of low k_y modes has on determining $k_y|_{max}$ if the non-linear $\langle k_x \rangle$ is included in the model, it was decided not to include a zonal flow growth rate quench model in QuaLiKiz.

A possible mechanism for the dependence of magnetic shear on the zonal flow impact on $\langle k_x \rangle$ is now discussed. In non-linear mode coupling, the amount of energy that is injected into the primary mode is balanced by the coupling to other modes at the same scale or nearby scales. In general this coupling must satisfy a frequency matching condition as well as a wavenumber matching condition ($\omega_p + \omega_q - \omega_k = 0$, $\mathbf{p} + \mathbf{q} - \mathbf{k} = 0$). At high magnetic shear, the modes are more strongly ballooned (more localized around $\theta = 0$), and in addition the effective local radial wavenumber varies poloidally, since $k_x^{eff} \sim k_y \hat{s} \theta + k_x$. This makes it rather difficult for the dominant ballooning eigenmode to couple effectively to a zonal mode, which is poloidally symmetric, with a direct interaction. However, in the case of low shear, the ballooning structure of the primary mode is much less pronounced, and in addition the local k_x^{eff} is a much weaker function of θ . This makes it easier for the primary mode to couple directly to a zonal mode. This dependency of magnetic shear on zonal flows is well known and has been observed in a number of different contexts, for example in ETG gyrofluid simulations [30]. In the direct simulations carried out in this work, the relative amplitude of zonal flows is indeed found to be greater at low magnetic shear, as seen in Fig.5.10 for the set A (GA-standard case) $s = 1$ and $s = 0.1$ cases. The saturated electrostatic potential amplitudes are normalized, thus the lower normalized amplitude of the $s = 0.1$ $k_y > 0$ spectrum compared to the $s = 1$ case reflects the higher relative amplitude of the $s = 0.1$ $k_y = 0$ modes (zonal flows) compared with the $s = 1$ case.

Since in the case of wave interactions it takes at least three waves to interact, when the direct interaction with the zonal flow is allowed, another drift mode with non-zero k_x also extracts energy from this interaction (in fact enstrophy and not energy is exchanged, but for the sake of current argument this is not of essential importance). This has two effects on turbulence. First, the zonal flows isotropize turbulence, since they can shear streamers apart. They also reduce the degree of ballooning in the mode structure. This isotropization can make the non-linearly formed k_x important in the computation of the flux or the mixing length saturation level. At high magnetic shear, the 'non-linear' k_x is less important, since the zonal flow drive is lessened due to effective k_x being a function of θ . But at low magnetic shear, the turbulence is isotropized due to zonal flows, so a substantial amount of the energy is found in $k_x \neq 0$ fluctuations.

In summary, the previous k_\perp^2 formulation in QuaLiKiz led both to an incorrect estimate of the non-linear flux spectrum maximum, and to the wrong dependency on magnetic shear in the k_\perp^2 description itself at low magnetic shear. From analysis with non-linear

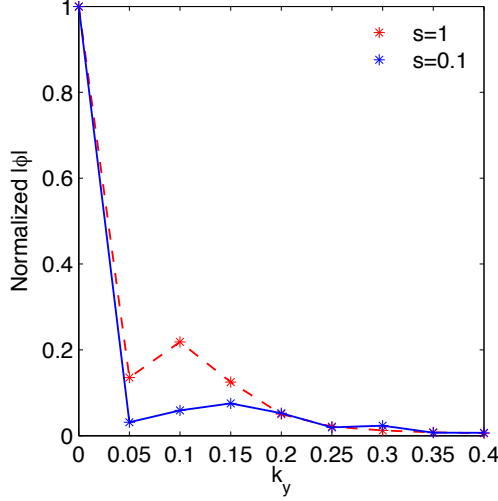


Figure 5.10: Relative amplitude of zonal flow modes ($k_y = 0$) compared with the $k_y > 0$ modes for the GA-standard $s = 1$ and $s = 0.1$ cases. k_x has been averaged over at each k_y .

and linear GENE simulations, it was found that improving the k_\perp^2 formulation in the QuaLiKiz mixing length rule, taking into account the $\langle k_x \rangle(k_y)$ found from non-linear simulations, leads to an improved estimate of $k_y|_{max}$ and the magnetic shear and q -profile dependence of k_\perp^2 . The increased values of $\langle k_x \rangle(k_y)$ at low magnetic shear at low, transport relevant, k_y values may be related to the observed greater relative amplitude of zonal flow modes. This may rise due to the less pronounced ballooning structure of the low magnetic shear eigenmodes. It is also possible that linearly unstable modes with k_x -center $\neq 0$ - which are more prevalent at low magnetic shear - further contribute to the k_x spectrum.

Frequency broadening

In the QuaLiKiz model the width of the broadened electrostatic field frequency function due to stochastic scattering is taken as the linear growth-rate, γ_k . This assumption can be checked by comparison to the non-linear frequency spectra from GENE. The width of the non-linear frequency spectra, calculated for each k_y , is compared to the linear growth rate from linear GENE. In Fig.5.11 we see the examples of the frequency broadening data and Lorentzian fit from set A (GA-standard case) $s = 1$ and $s = 0.1$ cases for $k_y = 0.2$. The GENE calculated linear frequency (ω_{lin}) and growth rate (γ_{lin}) are compared with the non-linear frequency spectrum center (ω_{fit}) and width ($\Delta\omega_{fit}$) as defined by the Lorentzian fit. We note that in analysis of GYRO frequency spectra, both Lorentzian and Gaussian fits to the frequency spectra were satisfactory in recovering the FWHM, while

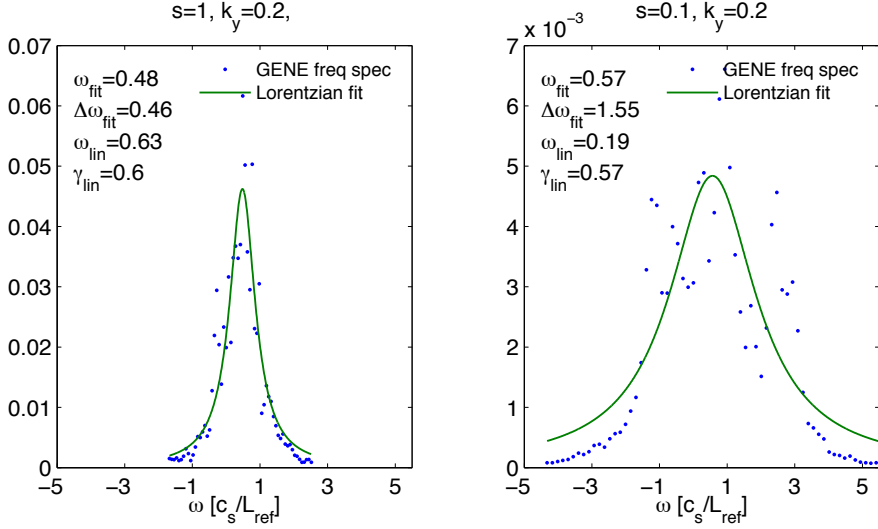


Figure 5.11: Frequency spectra for $k_y = 0.2$, averaged over saturated periods of GENE non-linear simulations from set A with $s = 1$ (left panel) and $s = 0.1$ (right panel).

a T-model was in fact the best fit to the data [10]. In Fig.5.12 the comparison between the non-linear frequency spectra width (from the Lorentzian fit) and the linear growth rate is shown for all the sets at $s = 1$, $s = 0.6$, and $s = 0.1$. The assumption generally holds for $s = 1$ and $s = 0.6$ in the transport-relevant range of $k_y < 0.3$. However, it is very interesting to note that for $s = 0.1$, the frequency width does not equal the linear growth rate for any value of k_y . In the transport relevant range $0.15 < k_y < 0.5$, the non-linear frequency width is significantly higher than the linear growth rate estimation. This is consistent with the generally lower autocorrelation times observed at low magnetic shear, as seen in table 5.3. This must be taken into consideration in the quasi-linear model.

This increased frequency broadening at low magnetic shear may be a result of non-linear decorrelation mechanisms, such as zonal flows, which play a stronger role at low magnetic shear as seen in the previous correlation length discussion. Also in the set with lowest flux, set D, where the impact of zonal flows is also expected to be stronger due to the vicinity to the instability threshold, the frequency broadening is greater than the linear growth rate estimation even at $s = 0.6$ and $s = 1$. The existence of zonal flows affects the response function. This can be seen via a renormalization of the wave-kinetic equation. In the presence of zonal flows, the basic wave-kinetic response function takes the form:

$$R = \frac{R_0}{\left[1 + R_0^2 \left(\frac{\partial}{\partial r} [V_E(r) k_y] \right)^2 \frac{1}{N} \frac{\partial^2 N}{\partial k_x^2} \right]}$$

where N is the wave action. Using this form instead of the linear response function, we

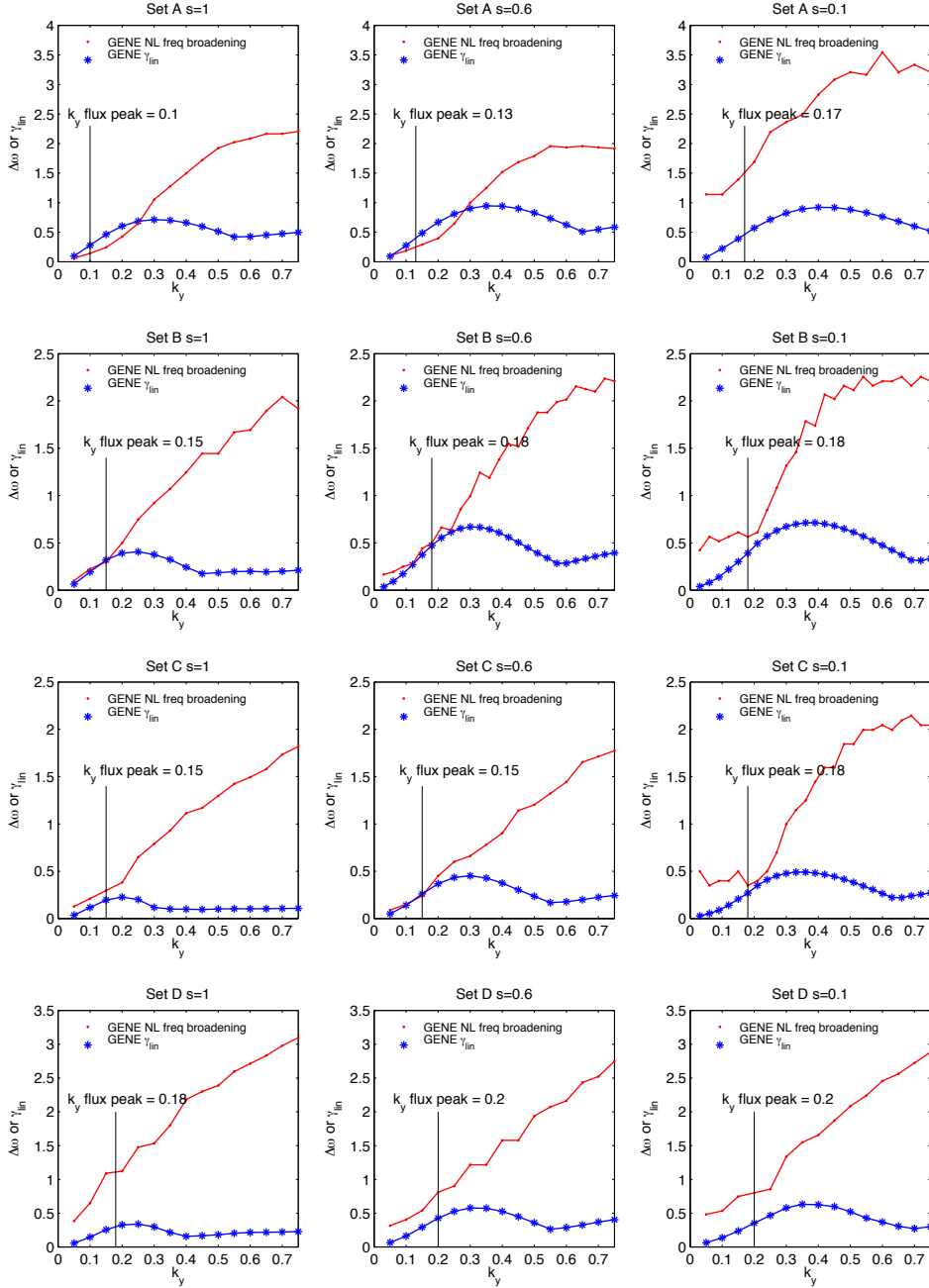


Figure 5.12: Non-linear frequency spectra fitted Lorentzian width and linear growth rates are compared for a range of k_y , for all 4 sets studied, for $s = 1$ (left column), $s = 0.6$ (middle column), and $s = 0.1$ (right column).

obtain:

$$|\Phi_{k,\omega}|^2 \propto \frac{|\Phi_k|^2}{(\omega - \omega_k)^2 + \gamma_k^2 + \alpha \left(\frac{\partial}{\partial r} V_E(r) \right)^2}$$

where $V_E(r)$ is the zonal flow velocity, and $\alpha \equiv \frac{k_y^2}{|\Phi_k|^2} \frac{\partial^2 |\Phi_k|^2}{\partial k_x^2}$. This equates to increased frequency broadening, beyond the linear growth rate assumption. Such a reduction of the fluxes due to perpendicular flow shear was also employed in a transport model by Hinton and Staebler [31].

We define the ratio between the frequency broadening from the non-linear simulations and the linear growth rate, at each magnetic shear value, as the weighted average $\langle \Delta\omega_k / \gamma_k \rangle$, with the weight set by the $\phi(k_y)$ amplitude spectrum. For the entire collection of simulations, $\langle \Delta\omega_k / \gamma_k \rangle_{s=0.1} / (\frac{1}{2} \langle \Delta\omega_k / \gamma_k \rangle_{s=1} + \frac{1}{2} \langle \Delta\omega_k / \gamma_k \rangle_{s=0.6}) = 2.5$, averaging over all four sets. This reflects the increased frequency broadening at low magnetic shear, which is highest for set A (GA-standard case) and lowest for set D. In the absence of more rigorous theory, we have simply included an additional shear dependent normalization factor to the fluxes calculated by QuaLiKiz, in the form of $2.5(1 - |s|)$ for $|s| < 0.6$. This normalization factor roughly captures the effect of the decreased autocorrelation time due to increased frequency broadening (possibly due to zonal flows) at low magnetic shear.

The increase in the frequency broadening is also correlated with a reduction in the effective non-linear transport weight. This is seen by comparing the ratio of the quasilinear transport weight (flux over spectral intensity as a function of k) with the non-linear transport weight, defined as an *overage* [32]. These overages were found to be ~ 1.4 - at transport relevant k values - for a variety of different cases. When calculating this overage for the $s = 0.1$ GA-standard case, as seen in Fig.5.13, we however obtain an increased overage compared to the ~ 1.4 value found for the $s = 1$ case. This overage increase, corresponding to the deviation of the quasilinear flux from the non-linear flux due to the non-constancy of the transport weight, corresponds well with our ad-hoc correction factor from the frequency broadening.

An additional possible explanation for the non-unity overage could be the non-linear transfer of energy from unstable eigenmodes to stable eigenmodes. This is proposed to lead to a similar factor ~ 1.4 between quasilinear and non-linear fluxes [33]. This is because the construction of the quasilinear flux assumes that the unstable mode contributes fully to the electrostatic potential amplitude. However, in the non-linear case, linearly damped modes take up a given proportion of the total electrostatic potential amplitude. The net contribution of these linearly damped modes to the flux is typically much reduced compared with the dominant unstable mode. Thus, since the transport weight (following a k_y decomposition) is defined as the flux divided by the electrostatic potential, the non-linear weight is expected to be lower than the quasilinear weight due to the existence of the low-flux-contributing linearly damped modes which do contribute to the saturated electrostatic potential amplitude. An increased proportion of linearly damped modes in the low magnetic shear system would then be consistent with increased transport weight overage. A broadened frequency spectrum could also be a signature of an increased spec-

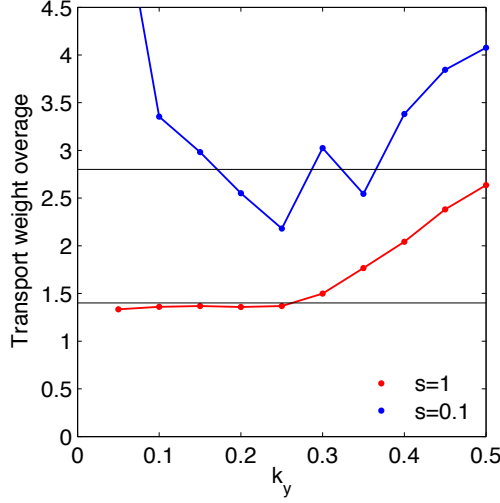


Figure 5.13: Ratio of quasilinear to non-linear transport weights for the GA-standard $s = 1$ and $s = 0.1$ cases.

trum of modes in the system. The increase of zonal modes - as observed at low magnetic shear - is expected to lead to increased coupling to $n > 0$ linearly damped modes. Indeed, as seen in Fig. 5.14, singular value decompositions of the saturated electrostatic potential of the GA-standard $s = 1$ and $s = 0.1$ cases show that the $s = 0.1$ case has a much broader spectrum of linearly stable modes beyond the dominant unstable mode. This method of analysis is outlined in Hatch et al [34]. The existence of a broader spectrum of linearly damped modes is consistent with a higher transport weight overage. However, we also note that at the current level of analysis it is not possible to separate in the singular value decomposition linearly damped modes from linearly unstable modes with midplane $k_{x0} \neq 0$ (related to the conventional ballooning angle through $k_{x0} = k_y \theta_0 s$). While the $k_{x0} = 0$ modes are dominant for both $s = 0.1$ and $s = 1$, the k_{x0} growth rate spectrum is broader for $s = 0.1$, when compared with $s = 1$. These modes could in principle also contribute to the frequency broadening. More analysis is necessary in this respect.

In summary, at low magnetic shear the non-linear frequency broadening is observed to be larger than the linear growth rate width assumption. This broadening is correlated with an increase in the quasilinear to non-linear transport weight overage. An ad-hoc magnetic shear dependent normalization factor, based on the degree of increased non-linear frequency broadening at low magnetic shear, has been introduced into QuaLiKiz. The physical explanation of the frequency broadening and associated transport weight overage increase may be related to the relative increase in the zonal flow amplitude at low magnetic shear. A direct renormalization of the linear response function due to zonal flows is suggested. An additional explanation may be the increased non-linear coup-

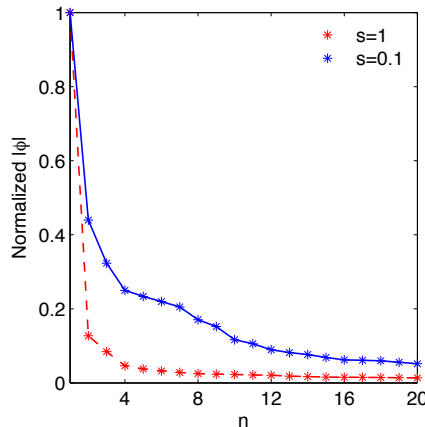


Figure 5.14: Singular value spectrum of mode amplitudes calculated from the GA-standard $s = 1$ and $s = 0.1$ saturated electrostatic potentials.

ling (via zonal flows) to linearly damped modes. More theoretical work is necessary to more fully uncover the mechanism of the increased frequency broadening and transport weight overage increase at low magnetic shear. However, on a more pragmatic level, the QuaLiKiz and non-linear flux prediction comparison is much improved through the combination of the k_{\perp} formulation improvement and the ad-hoc magnetic shear dependent normalization. This is shown in the following section.

5.4.4 Comparison of QuaLiKiz and non-linear flux predictions

Having taken into account both modifications discussed above, the k_{\perp}^2 alteration and frequency broadening renormalization, we now compare the particle and heat flux predictions from the modified QuaLiKiz and the non-linear simulations, for all GENE runs carried out, as well as GYRO for the GA-standard magnetic shear, q -profile, and R/L_T scans. The results are displayed in Fig.5.15. The agreement with the GA-standard case s -scan is much improved compared to the previous mixing length formulation shown in Fig.5.1. Simultaneously, the agreement with the q -scan and R/L_T scan is maintained. When exploring additional areas in parameter space, i.e. the B, C, and D sets, reasonable agreement is also observed. These results are summarized in table 5.4, where the RMS error between the particle and heat fluxes between QuaLiKiz and the non-linear GENE and GYRO simulations are listed. The RMS error is defined as $\sigma = \sqrt{\sum_i \epsilon_i^2 / \sum_j \chi_{j(NL)}^2}$, where ϵ_i is the diffusivity or flux difference between QuaLiKiz and the non-linear prediction for a given simulation, and $\chi_{j(NL)}$ the diffusivity or flux from the non-linear simulation. The RMS errors obtained using the previous QuaLiKiz version, correcting only k_{\perp}^2 , and both correcting k_{\perp}^2 and including the frequency broadening renormalization are all compared. Both modifications are of comparable importance.

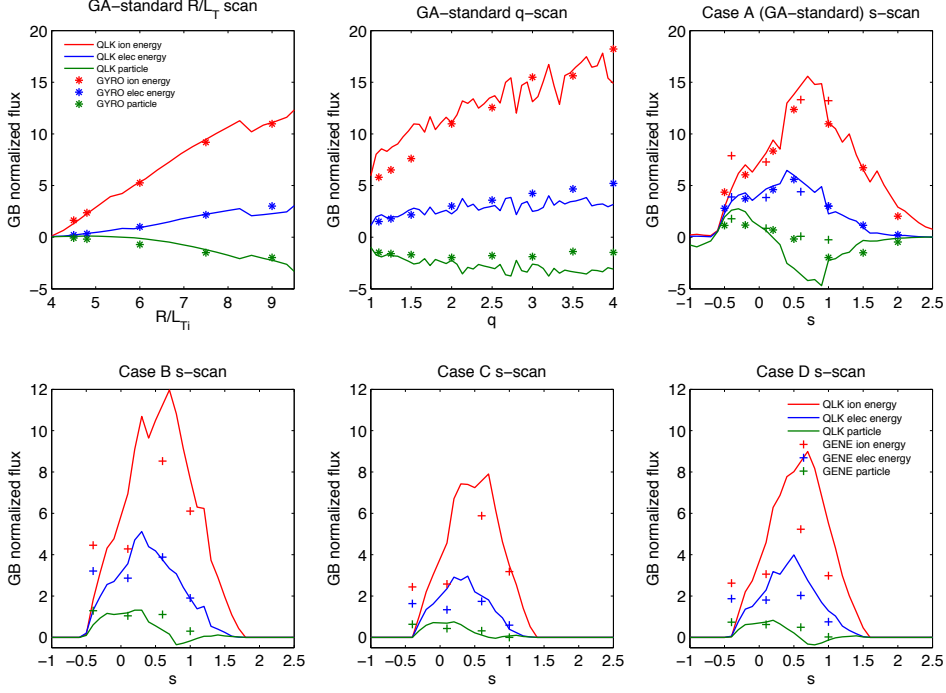


Figure 5.15: Comparison of the altered QuaLiKiz model with the 4 sets of GENE runs, and with the GYRO GA-standard case s-scan, q-scan, and R/L_T scan.

Table 5.4: RMS errors between QuaLiKiz and non-linear simulation predicted fluxes, for all GENE and GYRO runs shown in Fig.5.15.

	σ_{χ_i}	σ_{χ_e}	σ_D
QuaLiKiz09	1.13	1.53	1.84
With new k_{\perp}^2 only	0.52	0.77	1.24
With new k_{\perp}^2 and frequency broadening renormalization	0.26	0.33	1

5.5 Discussion and conclusions

Quasilinear flux predictions in the previous version of QuaLiKiz did not agree with GYRO non-linear flux predictions at low magnetic shear. This work has systemically examined the assumptions underlying the QuaLiKiz model, to uncover the physics behind this discrepancy. Improvements in the model were implemented, guided and validated by a further set of non-linear simulations carried out with GENE. This led to a significant improvement in the comparison between QuaLiKiz and non-linear simulations.

It was found that the previous formulation of k_{\perp}^2 in the QuaLiKiz mixing length rule for the saturated potential did not reproduce the magnetic shear dependence observed in non-linear simulations, neither in the $k_y|_{max}$ of the flux spectrum, nor in the relation between $\langle k_x \rangle$ and k_y . Furthermore, the frequency broadening at low magnetic shear was observed in the non-linear simulations to be greater than the linear growth rate broadening assumption. This is correlated with a increase in the ratio between the quasilinear and non-linear transport weights (transport weight overage), which must be taken into account in the model.

The QuaLiKiz mixing length rule was thus improved by introducing a formula for $\langle k_x \rangle(k_y)$ in the k_{\perp} formulation, which captures the magnetic shear and q -profile dependence from the non-linear simulations. This successfully reproduces the non-linear $k_y|_{max}$ from the maximum of the γ_k/k_{\perp}^2 mixing length spectrum, and also captures the degree of isotropy between $\langle k_x \rangle$ and k_y , setting the precise value of the correlation length. Furthermore, a renormalization based on the weighted average of the increased frequency broadening was implemented, which was consistent with the observed degree of increase in the transport weight overage. These modifications led to a much improved agreement between the new version of QuaLiKiz, and non-linear GYRO and GENE magnetic shear scans for various values of R/L_T , q , and T_i/T_e .

We note that the reproduction of $k_y|_{max}$ can also be achieved by invoking zonal flow quenching of large wavelength turbulence in the mixing length rule. This results in reduced correlation lengths at low magnetic shear due to the stabilization of the toroidal ITG branch at combined low s and k_y , which leads to reduced growth rates at low sk_y . This stabilization was discussed when summarizing linear analytical and numerical results at low magnetic shear. In spite of the lower ITG threshold at low magnetic shear, the γ -stiffness is also lower at low magnetic shear. At low k_y this is particularly the case, due to toroidal ITG branch stabilization at low sk_y . Since the $\langle k_x \rangle$ dependence on k_y also depends on zonal flows, these two approaches for altering the mixing length rule stem from the same physics.

As detailed in Appendix 5.B and Appendix 5.C, the intrinsic assumptions in the QuaLiKiz model were also examined. It was found that locality holds down to $s = 0.1$. The lowest order ballooning representation is also valid down to $s = 0.1$, following comparisons of the QuaLiKiz fluid eigenmode assumption and GENE linear eigenfunction solutions. The quasilinear approximation also holds at low magnetic shear. This was verified by calculating the Kubo numbers from the entire set of non-linear GENE simulations. It was found the $K < 1$ also at low magnetic shear. This strengthens the claim that the quasilinear/non-linear discrepancy at low magnetic shear is purely due to the formula-

tion of the saturated potential intensity and frequency spectrum - which is outside of the scope of the quasilinear model itself - while the fundamental formulation of quasilinear diffusivities is still valid.

Future work on QuaLiKiz will be directed on reproducing the effect of external ExB shear and introducing a parameterization for shape effects beyond the $s - \alpha$ model. Furthermore, from the magnetic shear scans, we can see that ITG-TEM modes are fully stabilized at high magnetic shear. These correspond to experimentally relevant values towards the edges of tokamak plasmas. This is not consistent with density fluctuation measurements which increase strongly with r/a . Present quasilinear models based purely on ITG-TEM-ETG modes tend thus to underpredict the level of transport towards the edge, compared to experimental measurements, if not constrained to a typical range of $r/a < \sim 0.8$. Resolving this issue is critical for fully predictive modeling of L-modes up to the separatrix, or for the region close to an H-mode pedestal.

Finally, the improved agreement in predicted fluxes between the present version of QuaLiKiz and the non-linear simulation magnetic shear scans were not only seen in the high flux GA-standard case, but also in lower flux cases closer to experimental parameters. This is encouraging for the future experimental validation of the QuaLiKiz model and for extrapolation to ITER. Transport in ITER at low magnetic shear will be important for all scenarios, due to the predicted ITER sawtooth period being significantly higher than the energy confinement time.

Acknowledgments

This work, supported by the European Communities under the contract of Association between EURATOM/FOM and EURATOM/CEA, was carried out within the framework of the European Fusion Programme with financial support from NWO. The views and opinions expressed herein do not necessarily reflect those of the European Commission. This work is supported by NWO-RFBR Centre-of-Excellence on Fusion Physics and Technology (Grant nr. 047.018.002). The authors would like to thank: T. Görler, F. Merz, D. Told and H. Doerk for their support in using GENE; R. Waltz, J. Candy, P. Mantica, G. Staebler and C. McDavitt for fruitful discussions; J. Kinsey for having providing access to GYRO simulation results. This research used resources of the National Research Scientific Computing Center, which is supported by the Office of Science of the U.S. Department of Energy under Contract No. DE-AC02-05CH11231. The authors are extremely grateful to D. Mikkelsen for having provided computational resources.

5.A Analytic fluid limit

The analytic fluid limit is obtained by considering mode frequencies far above the resonance, i.e. $\omega \gg \omega_d, k_{\parallel} V_{\parallel i}$. This corresponds to driving gradients far above the linear thresholds. We assume an ordering $k_{\perp} \rho_e \ll k_{\perp} \rho_i \ll 1$, and $k_{\perp} \delta_e \ll k_{\perp} \delta_i \ll 1$, as well as adiabatic passing electrons, large-aspect-ratio, $\alpha = 0$, and strongly ballooned eigen-

functions centered around the equatorial midplane. The fundamental linear gyrokinetic dispersion equation can then be simplified to the following [35]:

$$\left[1 + \frac{n^2 \omega_{pe}^* \omega_d (f_t + \frac{\tau}{Z})}{f_p \omega^2} - \frac{n \omega_{ne}^*}{\omega} + \frac{n \omega_d}{\omega} + \left(-\frac{k_{\parallel}^2 c_{eff}^2}{2 \omega^2} + \frac{k_{\perp}^2 d_{eff}^2}{2}\right) \left(1 + \frac{\tau}{Z} \frac{n \omega_{pe}^*}{\omega}\right)\right] \tilde{\phi} = 0 \quad (5.6)$$

Where $\rho_{i,e}$ and $\delta_{i,e}$ are the particle Larmor radii and banana widths, n is the toroidal wave number, $\omega_d = -\frac{k_{\theta} T_s}{e_s B} (\cos \theta + s \theta \sin \theta)$ is the vertical drift frequency, $\omega_{ne}^* = -\frac{k_{\theta} T_s}{e_s B} \frac{1}{L_n}$ and $\omega_{pe}^* = -\frac{k_{\theta} T_s}{e_s B} \frac{1}{L_p}$ are the diamagnetic frequencies associated with the density and pressure gradient lengths respectively, $V_{\parallel i}$ is the ion parallel velocity, $\tau = \frac{T_i}{T_e}$, Z is the effective ion charge, $f_{t,p}$ are the trapped and passing particle fractions respectively, $c_{eff}^2 \equiv \frac{T_e}{m_p}$, and $d_{eff}^2 \equiv \frac{f_p}{f_c} \frac{T_e}{n_e} \sum_i \frac{n_i Z_i^2}{T_i} \delta_i + \frac{4 T_e m_p}{e^2 B^2}$. In the limit where $q(r) \approx q(r_0) + q'(r_0)x$, we can write $k_{\parallel} = k'_{\parallel} x = k_{\theta} x / L_s$, where $x \equiv (r - r_0)$ (the distance from the rational surface) and $L_s \equiv Rq/s$. Transforming the radial coordinate from Fourier space to real space, we can also write $k_{\perp}^2 = k_{\theta}^2 - d^2/dx^2$. Equation 5.6 is then a second order differential equation for $\tilde{\phi}(x)$. A Gaussian solution, $\tilde{\phi} = \phi_0 e^{-\frac{x^2}{2w^2}}$, with $w^2 = -\frac{i \omega d_{eff} L_s}{k_{\theta} c_{eff}}$, implies that $\tilde{\phi}'' = -\left(\frac{1}{w^2} + \frac{1}{w^4} x^2\right) \tilde{\phi}$, and thus imposes a quadratic equation for the solution of the growth rate $\gamma = n \text{Im}(\Omega)$, with $\Omega = \omega/n$:

$$\begin{aligned} \Omega^2 \left(1 + \frac{k_{\theta}^2 d_{eff}^2}{2}\right) + \Omega \left(-\omega_{ne}^* + \omega_d + i \frac{k_{\theta}}{n L_s} \frac{c_{eff} f_d d_{eff}}{2} + \frac{k_{\theta}^2 d_{eff}^2}{2} \frac{\tau}{Z} \omega_{pe}^*\right) \\ + \frac{\omega_{pe}^* \omega_d}{f_p} \left(f_t + \frac{\tau}{Z}\right) + \frac{\tau}{Z} \omega_{pe}^* i \frac{k_{\theta} c_{eff} d_{eff}}{2 n L_s} = 0 \end{aligned} \quad (5.7)$$

To recover the interchange limit, where curvature dominates, we take the ordering $f_p, f_t, \frac{\tau}{Z}, \sim O(1)$, $k_{\theta} d_{eff}, L_p/R, \frac{(qR/\epsilon^{0.5})}{L_s} \sim O(\delta)$, $L_p/L_n \sim O(\delta^2)$, where ϵ is the inverse-aspect-ratio. In this limit, we obtain for the growth rate:

$$\gamma^2 = \frac{(f_t + \frac{\tau}{Z}) n^2 \omega_{pe}^* \omega_d}{f_p} \quad (5.8)$$

While for the slab limit, the relevant ordering is $f_p, f_t, \frac{\tau}{Z}, \sim O(1)$, $k_{\theta} d_{eff}, L_p/R, \frac{L_s}{(qR/\epsilon^{0.5})} \sim O(\delta)$, $L_p/L_n \sim O(\delta^2)$, which leads to the following expression for the growth rate:

$$\gamma^2 = \frac{\tau}{Z} \frac{n \omega_{pe}^* k_{\theta} d_{eff} c_{eff}}{2 L_s} \quad (5.9)$$

Let us examine the magnetic shear dependence in each of the above limits. For the interchange limit, the s -dependence can be found in ω_d , where $\omega_d \propto \cos \theta + s \theta \sin \theta \Rightarrow \gamma^2 \propto \cos \theta + s \theta \sin \theta$. In the slab limit, since $L_s \equiv Rq/|s|$, we have $\gamma^2 \propto |s|$. In both cases, the growth rates increase with magnetic shear. The fact that the growth rates increase with s in the limit far above the linear instability threshold, while simultaneously the ITG instability threshold also increases with s , points towards reduced growth rate stiffness at lower magnetic shear.

5.B Locality approximation at low magnetic shear

The QuaLiKiz model is a local code (as are the versions of non-linear GYRO and GENE used here in this work), and thus assumes constant profile gradient lengths. This can be formulated as $\max(w, d) < \min(L_{n(e,i)}, L_{T(e,i)})$, where w is the mode width, d the distance between rational surfaces, and L_n, L_T the electron or ion density and temperature gradient lengths respectively. This assumption must fail at a sufficiently low value of s as the distance between rational surfaces grows further and further apart, since $d = 1/sk_\theta$. At low shear d and w are comparable in the QuaLiKiz model (see Appendix A in [9]). We can estimate this s value as follows: firstly since d and w are comparable at low shear, we find the s for which $d = L_T$. $\frac{R}{d} = \frac{R}{L_T} \Rightarrow sk_\theta R = \frac{R}{L_T} \Rightarrow s(k_\theta \rho_s) \frac{R}{\rho_s} = \frac{R}{L_T}$. Taking $k_\theta \rho_s = 0.1$, which is approximately the value above which unstable modes are predicted to contribute significantly to the fluxes, and taking a typical R/L_T value of 9, we obtain: $s = 90 \frac{\rho_s}{R}$. For mid-sized tokamaks, a typical value of $\frac{\rho_s}{R}$ is 0.001, thus a typical s for which the locality assumption fails is 0.1, higher for smaller tokamaks and lower for larger tokamaks.

5.C Analytical fluid eigenmode assumption

In this appendix we show, in comparisons with linear-GENE, that the analytical fluid Gaussian eigenmode approximation made in QuaLiKiz, and the strong ballooning representation inherent therein, are valid for $|s| > 0.1$.

The scale separation of the microinstabilities, where $k_\parallel \ll k_\perp$, is captured in the eikonal representation for the electrostatic potential perturbation: $\Phi_n(r, \theta, \varphi) = e^{-in(\varphi - q(r)\theta)} \phi_n(r, \theta)$, where ϕ_n has slow varying θ -dependence along the field line. To first order $q(r) \approx q(r_0) + xq'|_{r_0}$, with r_0 corresponding to the resonating surface where $q(r_0) = m_0/n$, and $x \equiv r - r_0$, the radial distance from the resonating surface. The poloidal harmonic of Φ_n is thus:

$$\tilde{\phi}_{mn}(r) = \frac{1}{2\pi} \int_{-\pi}^{\pi} \phi_n(\theta) e^{i\theta(\frac{x}{d} - \nu)} d\theta \quad (5.10)$$

With $\nu = m - m_0$, $d = 1/nq'$, and where we have assumed radial dependence only through $q(r)$. In the QuaLiKiz model, $\tilde{\phi}(r)$ is not solved, but prescribed from the fluid limit solution, which is a Gaussian: $\tilde{\phi}(r) = \phi_0 e^{-r^2/2w^2}$, with w the Gaussian width [8]. The fluid limit solution is outlined in appendix 5.A. If $\phi_n(\theta)$ vanishes sufficiently quickly at $\pm\pi$, then equation 5.10 describes a Fourier transform. $\phi_n(\theta)$ is then the conjugate of $\phi_n(r)$, with $\theta = k_r d$. However, for low shear and long wavelengths, this assumption may fail since the prescribed $\phi(k_r)$ solution may not be compatible with $\phi(\theta)$ periodicity since then $\phi(\theta)$ may not necessarily vanish at $\pm\pi$. Indeed, it is known that as $s \rightarrow 0$ the full ballooning representation solution of $\phi(\theta)$ tends to a Mathieu function [36], which is not localized in the vicinity $\theta = 0$. Therefore we expect that below a particular value of s , the QuaLiKiz Gaussian eigenmode assumption must break down.

The validity of the QuaLiKiz assumption that the eigenmode is a Gaussian and vanishing at $\pm\pi$, i.e. $\phi_n(\theta = \pm\pi) \rightarrow 0$, is examined versus the solution of $\phi_n(\theta)$ from linear GENE, displayed in the ballooning representation [37]. The QuaLiKiz/GENE comparison is seen in Fig.5.16 for the GA standard case at both $s=0.1$ and $s=1$. We examine the cases with the transport relevant $k_y = 0.1, 0.15, 0.2$. The GENE calculated modes tend to be more extended in the ballooning angle for the combination of low s and low k_y . The QuaLiKiz assumption holds for all cases apart from $s = 0.1, k_y = 0.1$. However, since the peak of the non-linear flux spectrum for the GA-standard $s = 0.1$ case falls between $k_y = 0.15 - 0.2$, the linear calculations for $k_y = 0.1$ are less critical in the low shear case (see section 5.4.3). We can conclude that the lowest order ballooning representation assumption made in QuaLiKiz holds down to $s = 0.1$.

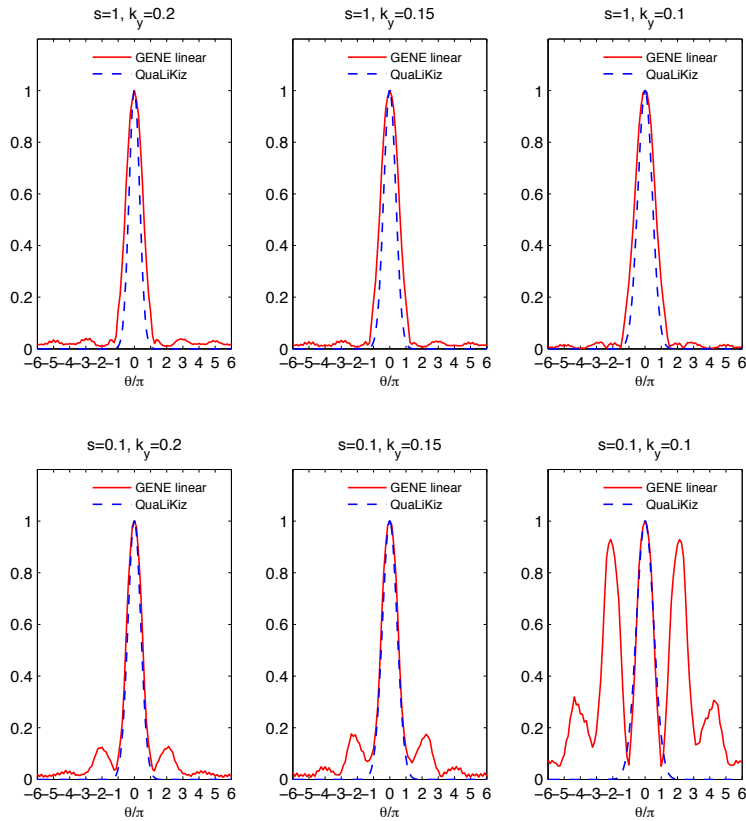


Figure 5.16: Calculated GENE linear eigenfunctions compared with the QuaLiKiz strong ballooning assumption for the mode envelope, for $s=1$ (upper panels) and $s=0.1$ (lower panels) GASTD case parameters.

References

- [1] C. Bourdelle *et al.*, 2007 *Phys. Plasmas* **47** 14 112501.
- [2] J. Candy and R.E. Waltz, 2003 *J. Comp. Phys.* **186** 545.
- [3] J. Candy and R.E. Waltz, 2003 *Phys. Rev. Lett.* **91** 045001.
- [4] A. Casati *et al.*, 2009 *Nucl. Fusion* **49** 085012.
- [5] P. Mantica *et al.*, 2011 *Phys. Rev. Lett.* **107** 135004.
- [6] F. Porcelli, D. Boucher and M.N. Rosenbluth, 1996 *Plasma Phys. Control. Fusion* **38** 2163.
- [7] F. Jenko, W. Dorland, M. Kotschenreuther and B.N. Rogers 2000 *Phys. Plasmas* **7** 1904, and <http://gene.rzg.mpg.de>.
- [8] C. Bourdelle. *et al.*, 2002 *Nucl. Fusion* **42** 892-902.
- [9] M. Romanelli, G. Regnoli and C. Bourdelle, 2007 *Phys. Plasmas* **14** 082305.
- [10] A. Casati, 2009, PhD Thesis, Université de Provence (Aix-Marseille I).
- [11] A. Casati *et al.*, 2009 *Phys. Rev. Lett.* **102** 165005.
- [12] F. Jenko, T. Dannert and C. Angioni, 2005 *Plasma Phys. Control. Fusion* **47** B195.
- [13] J.E. Kinsey, R.E. Waltz and J. Candy, 2006 *Phys. Plasmas* **13** 022305.
- [14] S.C. Guo and F. Romanelli, 1993 *Physics of Fluids B* **5** 520.
- [15] M. Romanelli, C. Bourdelle and W. Dorland, 2004 *Phys. Plasmas* **11** 3845.
- [16] C. Fourment *et al.*, 2003 *Plasma Phys. Control. Fusion* **45** 233.
- [17] A. Casati *et al.*, 2008 *Phys. Plasmas* **15** 042310.
- [18] F. Jenko *et al.*, 2001 *Phys. Plasmas* **8** 4096.
- [19] F. Romanelli, Liu Chen and S. Briguglio, 1991 *Phys. Fluid B* **3** 2496.
- [20] R. Kubo, 1963 *J. Math. Phys.* **4** 174.
- [21] J.A. Krommes, 2002 *Physics Reports* 360 1-352.
- [22] D.F. Escande and F. Sattin 2007 *Phys. Rev. Lett.* **99** 185005.
- [23] Z. Lin *et al.*, 2008 *Phys. Rev. Lett.* **99** 265003.
- [24] T. Dannert and F. Jenko 2005 *Phys. Plasmas* **12** 072309.
- [25] P. Diamond, S-I. Itoh, K. Itoh and T.S. Hahm, 2005 *Plasma Phys. Control. Fusion* **47** R31.
- [26] R.E. Waltz *et al.*, 1997 *Phys. Plasmas* **7** 2482.
- [27] J.E. Kinsey, G.M. Staebler and R.E. Waltz, 2005 *Phys. Plasmas* **47** 052503.
- [28] J.E. Kinsey *et al.*, 2008 *Phys. Plasmas* **15** 055908.
- [29] T.S. Hahm *et al.*, 1999 *Phys. Plasmas* **6** 922.
- [30] L. Jiquan and Y. Kishimoto, 2005 *Phys. Plasmas* **12** 054505.
- [31] F.L. Hinton and G.M. Staebler, 1993 *Phys. Fluid B* **5** 1281.
- [32] R.E. Waltz, A. Casati and G.M. Staebler, 2009 *Phys. Plasmas* **16** 072303.
- [33] D.R. Hatch, P.W. Terry, W.M. Nevins and W. Dorland, 2009 *Phys. Plasmas* **16**

022311.

- [34] D.R. Hatch, P.W. Terry, F. Jenko, F. Merz and W.M. Nevins, 2011 *Phys. Rev. Lett.* **106** 115003.
- [35] C. Bourdelle, 2000, PhD Thesis, Université Joseph Fourier-Grenoble 1.
- [36] J. Candy, R.E. Waltz and M.N. Rosenbluth, 2004 *Phys. Plasmas* **11** 1879.
- [37] J.W. Connor, R.K. Hastie and J.B. Taylor, 1978 *Phys. Rev. Lett.* **40** 396.

6 Ion temperature profile stiffness: non-linear gyrokinetic simulations and comparison with experiment

**J. Citrin¹, C. Bourdelle², J.W. Haverkort^{1,3},
G.M.D. Hogewij¹, F. Jenko⁴, P. Mantica⁵, D. Told⁴,
and JET-EFDA contributors***

JET-EFDA, Culham Science Centre, Abingdon, OX14 3DB, UK

¹FOM Institute DIFFER – Dutch Institute for Fundamental Energy Research -
Association EURATOM-FOM, Nieuwegein, The Netherlands

²CEA, IRFM, F-13108 Saint Paul Lez Durance, France

³Centrum Wiskunde & Informatica (CWI), PO Box 94079, Amsterdam,
The Netherlands

⁴Max Planck Institute for Plasma Physics, EURATOM Association,
Boltzmannstr. 2, 85748 Garching, Germany

⁵Istituto di Fisica del Plasma ‘P. Caldirola’, Associazione Euratom-ENEA-CNR,
Milano, Italy

*See the Appendix of F. Romanelli et al., Proceedings of the 23rd IAEA Fusion
Energy Conference 2010, Daejeon, Korea

Abstract

Recent experimental observations at JET show evidence of reduced ion temperature profile stiffness at low magnetic shear (\hat{s}) in the presence of flow shear. Non-linear gyrokinetic simulations are performed, aiming to reproduce the experimental results and discover the physical mechanism behind the observations. The sensitivity of profile stiffness to various parameters are assessed. It is found that non-linear electromagnetic effects, even at low β_e , can significantly reduce the profile stiffness, although not by a degree sufficient to explain the experimental observations. The effect of flow shear itself is not predicted by the simulations to lead to a significant reduction in flux. Agreement between the simulations and experiment is only attained when ignoring parallel velocity gradient destabilisation and assuming a degree of perpendicular flow shear above the experimental values. Finally, a new method of calculating linear growth-rates in the presence of rotation is proposed, where the growth-rates are calculated over an assumed non-linear correlation time.

6.1 Introduction

It is well established that one of the primary limitations of tokamak energy confinement is ion-Larmor-radius scale turbulent transport driven by background pressure gradients [1]. The ion-temperature-gradient (ITG) instability in particular has been long identified as an ubiquitous unstable mode in tokamak plasmas [2–5], and is primarily responsible for ion heat losses. The instability saturates in a non-linear state in conjunction with non-linearly excited zonal-flows, forming a self-organised turbulent system which sets the transport fluxes [6].

In addition to self-organised zonal-flows, the application of external flow shear is predicted to suppress turbulence through two broad mechanisms: decorrelation of the turbulent structures in the non-linear phase once the shearing rate is comparable with or exceeds the inverse non-linear autocorrelation time; suppression of the driving linear modes by coupling the mode at the most unstable spatial scale to nearby, more stable spatial scales [7, 8]. Flow shear has been observed experimentally to be correlated with tokamak transport barriers [9, 10], and with improved confinement in hybrid scenarios [11]. Non-linear gyrofluid simulations have predicted turbulence quenching above $\gamma_E/\gamma_{max} = 1 \pm 0.3$ [12, 13], where for purely toroidal rotation the normalised $E \times B$ shear rate $\gamma_E \equiv \frac{r}{q} \frac{d\Omega}{dr} / (\frac{v_{th}}{R})$, and γ_{max} is the maximum linear growth rate in the absence of rotation. Later gyrokinetic simulations predicted that quenching occurs at somewhat higher, but similar flow shear compared to the gyrofluid simulations, at $\gamma_E/\gamma_{max} = 2 \pm 0.5$ [14–16]. The seeming robustness of the transport quench has motivated formulations of effective growth rate reduction due to the flow shear in the mixing length rule of quasilinear transport models such as GLF23 and TGLF [17, 18]. When including parallel velocity gradient (PVG) destabilisation [19, 20] in the system, simulations have shown that they can limit the transport quench [12, 15, 21]. For pure toroidal rotation, the degree of the PVG destabilisation depends on the magnetic geometry since then $\gamma_p = \frac{q}{\epsilon} \gamma_E$, where γ_p is the PVG shear rate, and $\epsilon \equiv r/R$.

It has been recently observed in dedicated experiments at JET that ion temperature profile stiffness can be reduced at low normalised radii ($r/a < 0.5$), to a level significantly below the expectation from ITG turbulence [22, 23]. This has been hypothesised to be related to the correlation between low magnetic shear (\hat{s}) and increased flow shear in the low stiffness discharges. The term ‘stiffness’ refers to the sensitivity of gyro-Bohm normalised ion heat flux to the driving R/L_{Ti} (normalised inverse gradient length). The observations concentrated on $x = 0.33$ and $x = 0.64$ (where x is the normalised toroidal flux coordinate). While stiffness was observed to be low at $x = 0.33$ when the flow shear was increased, no significant difference in R/L_{Ti} was observed at $x = 0.64$. A previous non-linear gyrokinetic study based on the recent JET discharges, as detailed in Ref. [23], has reported only a ITG threshold shift with rotation, as opposed to a decrease in stiffness as observed.

In this paper, we extend this previous work and perform systematic and extensive linear and non-linear simulations with the GENE [24] non-linear gyrokinetic code to determine whether the experimental observation can be reproduced by gyrokinetic simulations. Three JET discharges have been selected: 70084, 66130, and 66404. Discharges 66130

and 66404 are situated on the ‘low-stiffness curve’ at $x = 0.33$ seen in Fig.1 in Ref. [23]. Discharge 70084 is a low flux, low rotation discharge selected to provide a data point near the turbulence threshold. These discharges have been reanalysed with the CRONOS suite of integrated modelling codes [25] to identify any differences in parameters apart from rotation within the chosen discharge set - such as R/L_n , β_e , and fast particle content - which may lead to decreased stiffness. The sensitivity to the ion heat flux and stiffness to each of these parameters was tested with GENE in dedicated R/L_{Ti} scans. Finally, complete simulations - i.e. collisional, electromagnetic, multi-species, and with rotation - were carried out at both $x = 0.33$ and $x = 0.64$ to determine whether the gyrokinetic simulations can reproduce the experimental fluxes.

The rest of the paper is organised as follows. In section 6.2 the GENE gyrokinetic code is briefly reviewed, as are the base parameters of the simulated discharges. In section 6.3 the results at $x = 0.33$ are reviewed. In section 6.4 the results at $x = 0.64$ are reviewed. In section 6.5 we present a comparison of sub-critical turbulence predictions for adiabatic and kinetic electrons, and also introduce a novel method of growth rate calculation in the presence of flow shear. In section 6.6 the conclusions are presented.

6.2 GENE simulations

GENE solves the gyrokinetic Vlasov equation, coupled self-consistently to Maxwell’s equations, within a δf formulation [26]. Computational efficiency is gained by solving in field line coordinates. x is the radial coordinate, z is the (poloidal) coordinate along the field line, and y is the binormal coordinate. Both an analytical circular geometry model (derived in Ref. [27]) as well as numerical geometry are used in this work. The analytical model differs from the often applied $s - \alpha$ model, which has inconsistencies of order $\epsilon = a/R$. For the numerical geometry, the FINESSE code was used to solve the extended Grad-Shafranov equation including toroidal rotation [28]. All simulations are local. Both linear and non-linear simulations are performed. In the linear mode, an eigenvalue solver may be used to compute multiple modes for each point in parameter space [29]. In the presence of rotation, when no time-independent eigenmodes can form, a complementary initial value solver is used.

Three discharges from the data-set presented in Ref. [23] were analyzed in more detail at $x = 0.33$ and $x = 0.64$, where x is the normalised toroidal flux coordinate. The discharges are 70084, 66130, and 66404. 70084 corresponds to a representative low rotation, low flux discharge and 66130 and 66404 are discharges further up on the ‘high rotation, decreased stiffness’ curve as seen in Fig.1 in Ref. [23]. The kinetic profiles were spline fitted and interpretative runs were carried out with the CRONOS integrated modelling suite of codes [25] for the equilibrium calculations and q-profile calculations. The kinetic profiles were then averaged over 1 s centered around 50/50/47 s respectively for calculations of the gradient lengths and other quantities such as β_e . The parameters are shown in table 6.1. In the table, the two quoted $\langle Z_{eff} \rangle$ values correspond to the charge-exchange (CX) and Bremsstrahlung measurements respectively, which are not consistent with each other. The CX measurements provide the lower quoted values. The CX $\langle Z_{eff} \rangle$

Table 6.1: Discharge parameters.

Shot no.@location	B [T]	I_p [MA]	T_i [keV]	T_e [keV]	n_e [$10^{19}m^{-3}$]	\hat{s}	q	T_e/T_i	R/L_{Ti}	R/L_{Te}	R/L_{ne}	β_e [%]	ν^*	$\langle Z_{eff} \rangle$	$M[v_{tor}/c_s]$
70084@ $x = 0.33$	3.5	1.8	2.01 ± 0.02	2.16 ± 0.1	2.6 ± 0.2	0.7	1.7	1.08 ± 0.04	4.2 ± 0.6	3.8 ± 0.6	1.4 ± 0.4	0.19 ± 0.01	0.07	1.4/2.2	0.09
66130@ $x = 0.33$	3.1	1.5	2.58 ± 0.04	3.3 ± 0.3	3.37 ± 0.24	0.7	1.8	1.25 ± 0.13	7.2 ± 0.6	6.5 ± 1	2.4 ± 1	0.46 ± 0.09	0.04	1.3/1.8	0.31
66404@ $x = 0.33$	3.5	1.8	3.1 ± 0.13	3.61 ± 0.08	2.3 ± 0.1	0.4	1.8	1.14 ± 0.06	9 ± 1.2	5.5 ± 0.8	3.8 ± 0.4	0.35 ± 0.07	0.02	NA/2.2	0.19
70084@ $x = 0.64$	3.5	1.8	1.08 ± 0.02	1.27 ± 0.05	2.3 ± 0.3	1.3	3	1.18 ± 0.05	8.3 ± 0.2	6.4 ± 1	1.8 ± 0.8	0.096 ± 0.01	0.16	1.4/2.2	0.03
66130@ $x = 0.64$	3.1	1.5	1.38 ± 0.03	1.5 ± 0.24	2.8 ± 0.3	1.5	3.5	1.1 ± 0.2	7.6 ± 0.3	8.5 ± 3	1.8 ± 1.4	0.18 ± 0.04	0.1	1.3/1.8	0.23
66404@ $x = 0.64$	3.5	1.8	1.34 ± 0.08	1.66 ± 0.14	1.51 ± 0.07	1.4	2.9	1.23 ± 0.13	8.2 ± 0.4	10 ± 1.6	2.1 ± 0.9	0.08 ± 0.01	0.05	NA/2.2	0.15

measurements for discharge 66404 were not available. The sensitivity of the transport to the range of $\langle Z_{eff} \rangle$ spanned by the diagnostics is explored in section 6.3.7. ν^* is the normalised collisionality: $\nu^* \equiv \nu_{ei} \frac{qR}{\epsilon^{1.5} v_{Te}}$, with $\epsilon = a/R$ and $v_{Te} = \sqrt{\frac{T_e}{m_e}}$. In previous gyrokinetic simulations based on 70084 parameters, the values for \hat{s}/q were taken as 0.57/1.3 [23]. This is not fully consistent with the q values from the CRONOS modelling shown here. However, uncertainty still exists regarding the validity of neoclassical current diffusion in setting the values of the q -profile, particularly at inner radii [30]. Therefore, to be consistent with the previous works, we assume $q = 1.3$. As seen in section 6.3, we also carry out most of the parameter scans at $x = 0.33$ with $\hat{s} = 0.2$, to ascertain that we are in a ‘low- \hat{s} regime’, in spite of the contradiction with the CRONOS current diffusion modelling predictions.

In the GENE simulations, typical grid parameters were as follows: perpendicular box sizes $[L_x, L_y] = [170, 125]$ (in units of ρ_s), perpendicular grid discretisations $[n_x, n_y] = [192, 48]$, 24 point discretisation in the parallel direction, 32 points in the parallel velocity direction, and 8 magnetic moments. Extensive convergence tests were carried out for representative simulations throughout the parameter space spanned in this work. The lack of convergence of the heat fluxes with increasing n_y as reported for GYRO [31] simulations of discharge 70084 in Ref. [23] - associated with increasing zonal flows - was not encountered here. In our cases the convergence with n_y is well behaved. The difference may stem from the different treatment of the radial boundary conditions in the GENE and GYRO simulations. Further investigation is necessary to ascertain this. The heat fluxes shown in the following sections are in gyroBohm normalised units, $T_i^{2.5} n_i m_i^{0.5} / e^2 B^2 R^2$. k_y is in units of $1/\rho_s$. These heat fluxes correspond to time averaged values over the saturated state of the GENE simulations. The statistical flux variations due to intermittency are for clarity not explicitly shown as error bars. This variation is typically 5 – 10% for our parameters. γ and γ_E are in units of c_s/R where $c_s \equiv \sqrt{T_i/m_i}$. All rotation is considered to be purely toroidal unless specifically mentioned. For the low/high rotation discharges, $\gamma_E = 0.1/0.3$ was assumed for both $x = 0.33$ and $x = 0.64$, which are representative values for the low and high stiffness discharges from the dataset in Ref. [23].

6.3 Low magnetic shear case

In this section, we first isolate the effect of various parameters on ion profile stiffness, at $x = 0.33$ (the low shear region). These parameters are: \hat{s} , rotation, effect of rotation on the magnetohydrodynamic (MHD) equilibrium, R/L_n , β_e , and fast particle content. We then proceed to realistic simulations of 70084, 66130, and 66404 for a full comparison between the gyrokinetic predictions and the experimental heat fluxes. These simulations simultaneously include: numerical geometry, collisions, electromagnetic effects, Z_{eff} (by including a carbon species), and realistic T_e/T_i .

6.3.1 Stiffness sensitivity to \hat{s}

While the ITG turbulence threshold increases with \hat{s}/q [32], the stiffness decreases with both decreasing \hat{s} and decreasing q . For decreasing \hat{s} , the reduced stiffness has been shown to be correlated with increased coupling to zonal flows [33]. For decreasing q , this is due to an increased downshift in the peak wavenumber of the turbulence spectrum, indicating increased correlation lengths [34]. These sensitivities are seen in Fig.6.1. For example, we can see that for both the $\hat{s}/q = 0.6/1.3$ and $\hat{s}/q = 1/2$ cases the turbulent threshold is similar while the stiffness is lower for the $\hat{s}/q = 0.6/1.3$ case.

The precise value of \hat{s} from the integrated modelling is uncertain, in light of inconsistent results regarding agreement between q -profile motional Stark effect (MSE) measurements and q -profile interpretative modelling [30]. Thus, for the remainder of this work, we assume a 'reference' \hat{s} of 0.2 instead of 0.57 at $x = 0.33$, to ascertain that we are studying a low- \hat{s} regime. For the numerical geometry cases, the current profile input into CRONOS was modified such that at $x = 0.33$ values of $\hat{s}/q = 0.2/1.3$ were obtained following the solution of the Grad-Shafranov equation.

6.3.2 Stiffness sensitivity to rotation

In this section we isolate the effect of rotation on stiffness, assuming pure toroidal rotation. Collisionless, electrostatic simulations based on 70084 parameters (with $\hat{s}/q = 0.2/1.3$) are carried out, applying analytical circular geometry [27]. The predicted gyroBohm normalised ion heat fluxes from the R/L_{Ti} scans are shown in Fig.6.2. The sensitivity to γ_E is examined. Even for $\gamma_E = 0.6$, double the highest level of flow shear achieved in the reference data set from Ref. [23], the simulated level of reduced stiffness is significantly less than the experimental observation. However, interesting effects related to the competition between stabilising $E \times B$ shear and destabilising parallel velocity gradient (PVG) modes - particularly in the vicinity of the threshold - are observed. At low R/L_{Ti} , the PVG destabilisation can dominate over the ITG turbulence, reducing stiffness in that region of parameter space. Due to the PVG destabilisation, the fluxes do not continue to decrease towards the ITG instability thresholds. This is seen in Fig.6.2a by examining the various curves at fixed R/L_{Ti} . At low R/L_{Ti} , the fluxes rise with γ_E due to PVG drive. However at higher R/L_{Ti} , the fluxes decrease with R/L_{Ti} due to the ITG stabilisation by perpendicular ExB flow shear dominating over the PVG destabilisation.

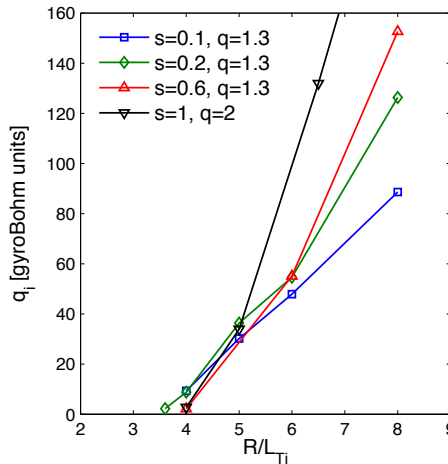


Figure 6.1: Non-linear electrostatic collisionless GENE R/L_{Ti} scans for various levels of \hat{s} and q -profile with circular geometry at $x = 0.33$. $R/L_{Te} = 5$, and $R/L_n = 1.1$.

In Fig.6.2b the parallel velocity gradients were artificially removed from the system, and the picture reverts to a threshold shift. Note that particularly for the (red) $\gamma_E = 0.3$ and (black) $\gamma_E = 0.6$ curves the apparent reduced slope near threshold is not necessarily indicative of reduced stiffness in that regime, since the actual effective non-linear threshold may lie between the precise values of the R/L_{Ti} values chosen for the simulations.

For pure toroidal rotation, the relative importance of PVG destabilisation versus $E \times B$ stabilisation is sensitive to the geometric parameter q/ϵ (where $\epsilon \equiv r/R$) [35]. As q/ϵ increases, the field lines are increasingly projected onto the toroidal direction. In Fig.6.3 a q/ϵ scan is carried out by varying ϵ in the various R/L_{Ti} scans. Simulations with $\epsilon = 0.11, 0.15$ assuming circular geometry were performed, as well as an $\langle \epsilon \rangle \equiv \langle r \rangle / R = 0.13$ case from the flux surface averaged minor radius at $x = 0.33$ using numerical geometry (in this case from the HELENA [36] equilibrium in the CRONOS simulations). The R/L_{Ti} values in the plots corresponding to numerical geometry are defined here with respect to the averaged midplane minor radius. The relative strength of the PVG destabilisation is seen to weaken as expected with decreasing q/ϵ , until an almost pure threshold shift case is reached with $q/\epsilon = 8.7$. While this qualitative PVG dependence on q/ϵ is well known, we here make quantitative predictions with kinetic electrons for R/L_{Ti} values in the vicinity of the turbulence threshold. For our particular case, the 70084 $x = 0.33$ parameters are very close to the boundary of a ‘zero-turbulence-manifold’ as defined in Ref. [37]. That study was carried out with adiabatic electrons, may decrease the predicted γ_E necessary for turbulence quenching compared with the kinetic electron case due to the reduced trapped electron drive.

The interplay between PVG destabilisation and $E \times B$ stabilisation demands that PVG modes are correctly accounted for in reduced transport models - such as in gyrokin-

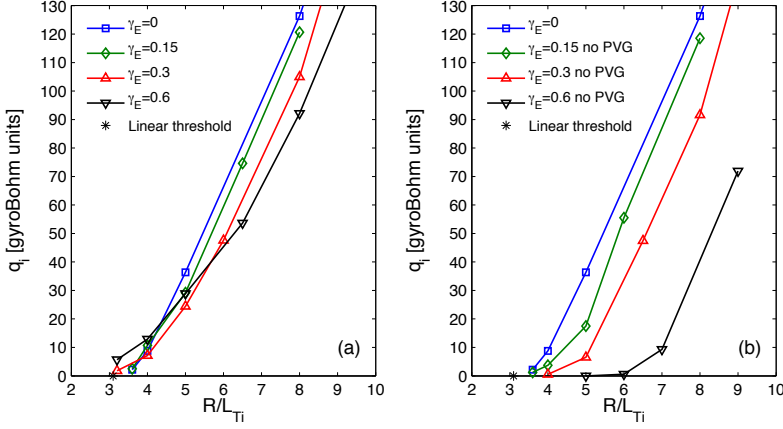


Figure 6.2: Non-linear GENE R/L_{Ti} scans based on 70084 parameters at $x = 0.33$ ($q/\epsilon = 11.8$) and various levels of γ_E [c_s/R]. Runs including PVG destabilisation are seen in (a). Runs ignoring PVG destabilisation are seen in (b). All runs were electrostatic, collisionless, and with circular geometry.

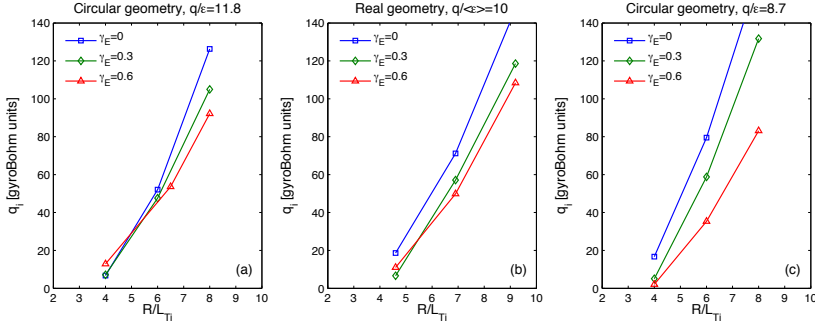


Figure 6.3: q/ϵ sensitivity of the PVG destabilisation as seen in R/L_{Ti} scans of ion heat flux. As q/ϵ is progressively raised, the γ_E induced stabilisation can not only be reduced but can even be reversed in the region of the instability threshold. Runs were electrostatic, collisionless, and with circular geometry.

etic or gyrofluid based quasilinear models. It is insufficient in such formulations to include a growth rate quench model due to $E \times B$ stabilisation without simultaneous self-consistent and validated modelling of the PVG modes. Correct modelling near the turbulent thresholds is particularly critical for high temperature tokamaks, such as ITER. This is because the normalised fluxes are expected to be in the vicinity of the turbulence thresholds due to the $T_i^{5/2}$ normalisation dependence.

Finally, we note that the observed Dimits shift [38] in these cases is only $\Delta R/L_{Ti} \approx$

0.5, or alternatively $\frac{\Delta(R/L_{Ti})}{R/L_{Tcrit}} \approx 15\%$. These values are similar to the $\frac{\Delta(R/L_{Ti})}{R/L_{Tcrit}} \approx 20\%$ shifts observed in previous realistic simulations [39]. The linear threshold was calculated by extrapolation to zero-growth-rate of linear R/L_{Ti} scans with GENE. The linear threshold in the numerical geometry case is nearly identical to the circular geometry case. Thus we can conclude that a significant departure from the Dimits shift paradigm is so far not experimentally observable with great certainty due to the experimental error in extrapolating to the instability thresholds.

6.3.3 Effect of rotation on the equilibrium

The effect of rotation on stiffness through its influence on the equilibrium was examined. An extended Grad-Shafranov equation including toroidal rotation was solved with the FINESSE code, using the 70084 pressure and F profiles as input, where $F \equiv B_{tor} R$. For the rotation profiles, scaled profiles from 66404 were used such that static ($\gamma_E = 0$), $\gamma_E = 0.3$ and $\gamma_E = 0.6$ cases were studied. All values correspond to $x = 0.33$. The different equilibria are seen in Fig.6.4. The sensitivity of the equilibria to these levels of rotation are found to be small, as expected due to the Mach number squared scaling of the ‘rotation pressure’. Only a 10% increase in the Shafranov shift was observed between the static and $\gamma_E = 0.6$ case. The non-linear predicted flux sensitivity to this different Shafranov shift is also minimal, with only a 6% decrease in ion heat flux when the $\gamma_E = 0.3$ equilibrium is used compared with the static equilibrium for a run with $R/L_{Ti} = 6.9$. We can thus conclude that the effect of rotation on the equilibrium itself does not play a role in setting the profile stiffness.

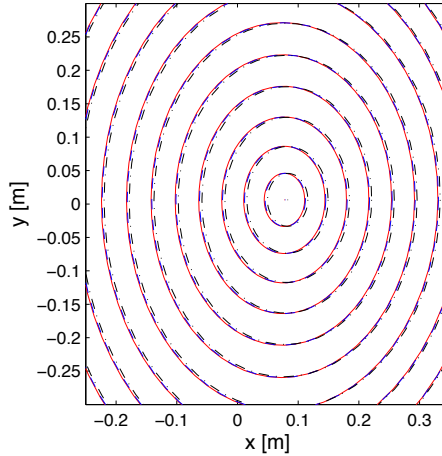


Figure 6.4: Flux surfaces in the vicinity of the magnetic axis from a solution of the generalised Grad-Shafranov equation using the kinetic profiles of 70084 and scaled rotation profiles from 66404. Three cases are shown: static (red solid curves), $\gamma_E = 0.3$ (blue dashed curves) and $\gamma_E = 0.6$ (black dashed-dotted curves).

6.3.4 Effect of R/L_n

In the limited experimental data set studied, there is a wide variation in R/L_n , from 1.4 in the 70084 case to 3.8 in the 66404 case (which corresponds to the highest R/L_{Ti} in the data set). The sensitivity of the turbulence to the R/L_n value was examined. In particular, the possibility that non-linear ITG-TEM (trapped electron mode) interplay takes place which can reduce the level of turbulence and thus the stiffness, as reported in Ref. [40], was examined. In Fig.6.5 these linear scans are shown. For $R/L_n = 1$, the dominant mode propagates in the ion diamagnetic direction (ITG mode). However, for $R/L_n = 3.8$ the mode at low R/L_{Ti} propagates in the electron diamagnetic direction. This is most probably a density gradient driven TEM mode, which is stabilised by R/L_{Ti} (which would correspond to low stiffness) until it switches to an ITG mode at $R/L_{Ti} \approx 5$. At that point we would expect turbulence stabilisation according to Ref. [40]. However, for higher R/L_{Ti} the growth-rate stiffness is similar to the $R/L_n = 1$ case, as a pure ITG regime is reached. For $R/L_n = 5$ the TEM-dominated regime is maintained for much higher R/L_{Ti} . However, the highest experimental R/L_n in the data set of Ref. [23] is $R/L_n \approx 4$. Furthermore, at the experimental high R/L_{Ti} values the transport is ITG dominated and stiff even for $R/L_n = 5$. Thus it is unlikely that R/L_n is responsible for reduced profile stiffness. Furthermore, even if the stiffness is low, the actual growth rates themselves are high, and we may expect a high degree of transport.

These results are maintained in the non-linear scans, seen in Fig.6.6. While at lower R/L_{Ti} stiffness is indeed reduced in the TEM regime for the high R/L_n case, at higher

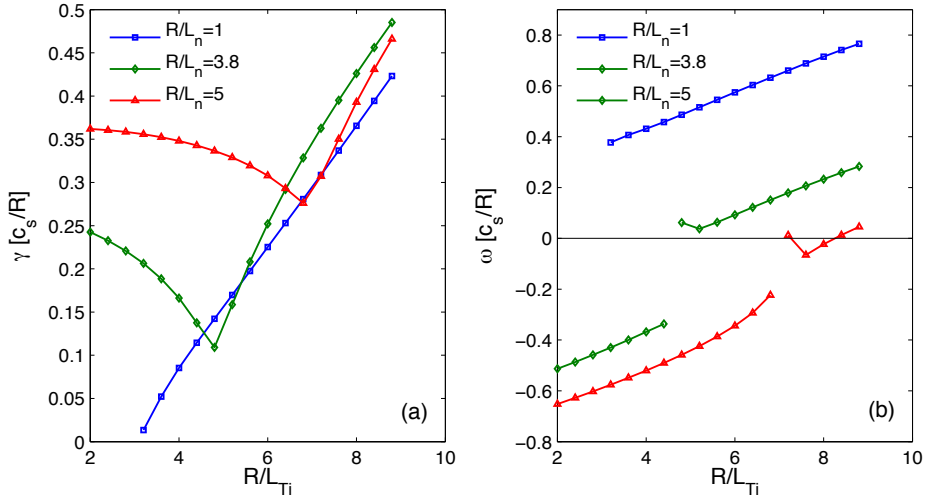


Figure 6.5: Linear R/L_{Ti} scans based on 66404 parameters at $x = 0.33$ with varying R/L_n . Growth rates are shown in (a), and frequencies in (b). Runs were electrostatic, with collisions, and with circular geometry.

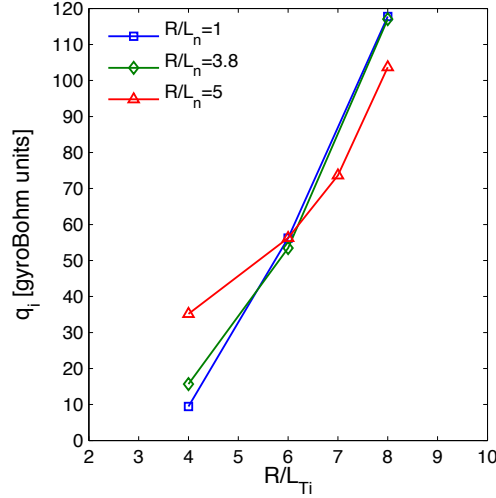


Figure 6.6: Non-linear R/L_{Ti} scans based on 66404 parameters at $x = 0.33$ with varying R/L_n . Runs were electrostatic, with collisions, and with circular geometry.

R/L_{Ti} values the difference in stiffness between the $R/L_n = 1$ and $R/L_n = 3.8$ cases becomes negligible. We can conclude that the variance of R/L_n in the data set is not responsible for the observed difference in stiffness.

6.3.5 Effect of β_e

In this section the sensitivity of the stiffness on β_e is examined. The simulations carried out take discharge 66404 parameters as a reference. Linear (at $k_y = 0.4$) and non-linear β_e scans are shown in Fig.6.7. From the linear scans, it is clear that the range of experimental β_e values ($0 - 0.5\%$) are significantly below the kinetic ballooning mode (KBM) thresholds, characterised in the plot by the sharp upturn in growth rates at $\beta_e \approx 1.5 - 2.4$. Below the KBM threshold, β_e stabilises the ITG mode [41, 42]. For our parameters, this leads to a growth rate reduction of $\approx 25\%$ at $\beta_e = 0.5\%$. This is at the upper range of our experimental β_e values. The KBM threshold varies with R/L_{Ti} , since the threshold is determined by the total pressure gradient through α_{MHD} . This 25% growth rate stabilisation factor is not exceeded when repeating the linear simulations for $k_y = 0.1 - 0.3$. However, a striking observation is that the *non-linear* β_e ITG stabilisation significantly exceeds the linear stabilisation. A decrease in ion heat flux by a factor of 65% is seen in Fig.6.7b for the $\gamma_E = 0$, $R/L_{Ti} = 9.2$ case between $\beta_e = 0 - 0.48\%$. Simultaneously, while the ion heat flux is reduced by β_e in the $\gamma_E = 0$, $R/L_{Ti} = 4.6$ case, it is not totally quenched. This is indicative of a decrease in stiffness as opposed to a threshold shift. We can thus conclude that electromagnetic effects play a significant role in stiffness reduction for our parameters, even at relatively low values of β_e . While this

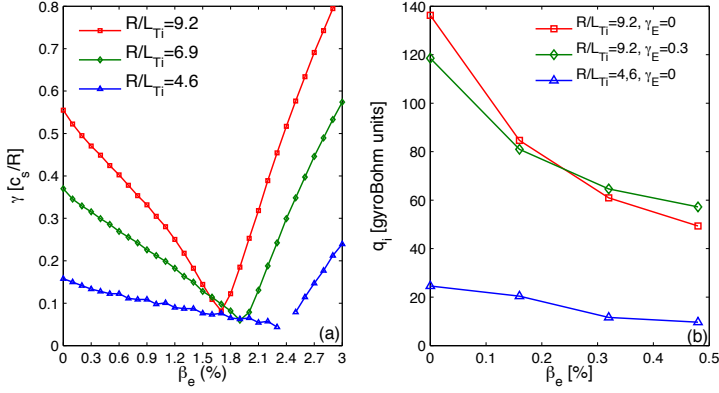


Figure 6.7: Linear (a) and non-linear (b) β_e scans with 66404 parameters at $x = 0.33$. R/L_{Ti} and γ_E are varied. Runs were with collisions and numerical geometry.

stiffness reduction is not sufficient to fully explain the experimentally observed stiffness reduction, it is a factor which must be taken into consideration. Additionally, from linear gyrokinetic analysis, β_e stabilisation of ITG modes has been invoked as a possible factor in improved hybrid scenario confinement at ASDEX Upgrade and DIII-D, particularly at outer radii [43]. The increased non-linear β_e stabilisation reported here may point to an even greater importance of this effect than previously recognised.

Simulations in which significant non-linear stabilisation of ITG modes at β_e values below the KBM limit have been previously reported [44]. There, an increase of the ratio between the zonal flow shearing rate to unstable mode growth rates (ω_{ZF}/γ_k) was observed with β_e . A possible physical mechanism for this relative increase in zonal flow activity, based on increased coupling between Alfvénic modes and drift waves, has been suggested [45]. In Fig.6.8 we plot the mode amplitude spectra for the $\gamma_E = 0$, $R/L_{Ti} = 9.2$ β_e -scan shown in Fig.6.7. The amplitude spectra have been normalised to the zonal flow ($k_y = 0$) amplitudes. Indeed a relative increase in the $k_y = 0$ modes is seen for the electromagnetic cases, which may be related to the ITG β_e stabilisation. We note that in Ref. [44] a significant instability threshold shift was observed for $\beta_e > \sim 0.4\%$. With our parameters, no such shift is seen across our spanned range of $\beta_e = 0 - 0.48\%$.

It is interesting to note that the PVG drive seems to be strengthened by finite β_e , and at higher β_e no stabilisation at all with rotation is seen. The deduction that the PVG drive is increased is from spot checks where the parallel velocity gradients were artificially suppressed. In those cases, $E \times B$ stabilisation remains strong at finite β_e .

In Fig.6.9 we can see, from the entire data set in Fig.1 of Ref. [23] the correlations between R/L_{Ti} and β_e for $x = 0.33$ and $x = 0.64$. There is a generally positive correlation between β_e and R/L_{Ti} at $x = 0.33$, consistent with the reduced stiffness. At $x = 0.64$, β_e is generally much lower than at $x = 0.33$. This is expected to further increase the stiffness at $x = 0.64$, beyond the increase due to the higher \hat{s} and q values.

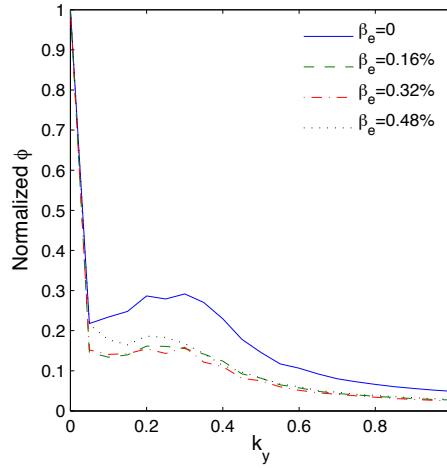


Figure 6.8: Amplitude spectra from the $\gamma_E = 0$, $R/L_{Ti} = 9.2$, non-linear β_e scan displayed in Fig.6.7b.

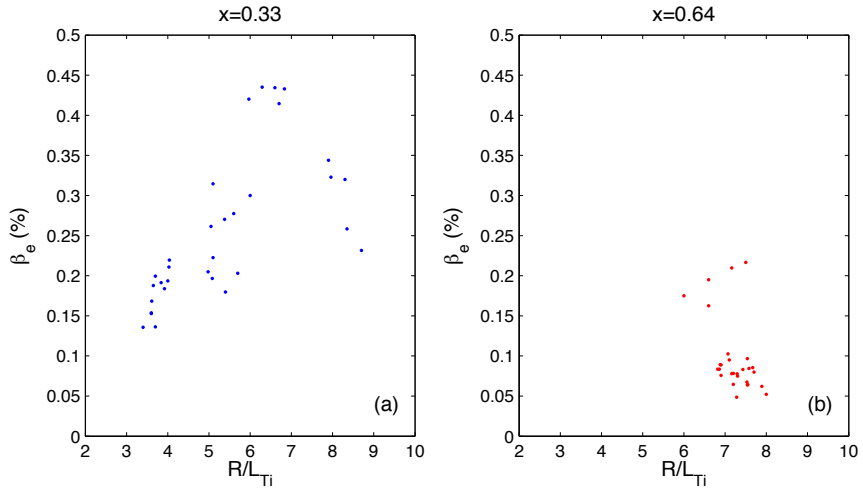


Figure 6.9: Correlation between R/L_{Ti} and β_e at $x = 0.33$ (a) and at $x = 0.64$ (b) from the entire data-set presented in Ref. [23].

6.3.6 Inclusion of fast particles

The discharges studied have relatively low density, and thus for the higher rotation cases where significant NBI is employed, it is possible that a large fast ion fraction is present. This is predicted to reduce the turbulent drive, since the fast ion species behaves mostly adiabatically due to the higher temperatures, and the density of the main ion species is reduced through dilution. In ASDEX Upgrade strong evidence has pointed to a fast ion dilution mechanism for ITB formation [46]. Monte Carlo simulations of the NBI injection and subsequent fast ion slowing down were carried out for discharge 66404 with NEMO/SPOT [47] within the CRONOS integrated modelling framework. The average fast particle temperature ($\approx 35\text{keV}$) at $x = 0.33$ was calculated. A linear GENE scan of fast particle densities (relative to n_e) can be seen in Fig.6.10. The scan is carried out for various k_y values in Fig.6.10a, assuming $R/L_{Tfast} = 0$. The R/L_{Tfast} sensitivity is examined in Fig.6.10b at $k_y = 0.4$. A suppression of the growth rates is observed with increasing n_{fast}/n_e . However, for our parameters the fast ion fraction is predicted by NEMO/SPOT to be only $\sim 10\%$, and thus insufficient to strongly affect the growth rates. While a fast ion fraction has been proposed to be responsible for some mismatch between gyrokinetic simulations and experiments [48], in our case it seems that the fast ion fraction may be too low to play a significant role.

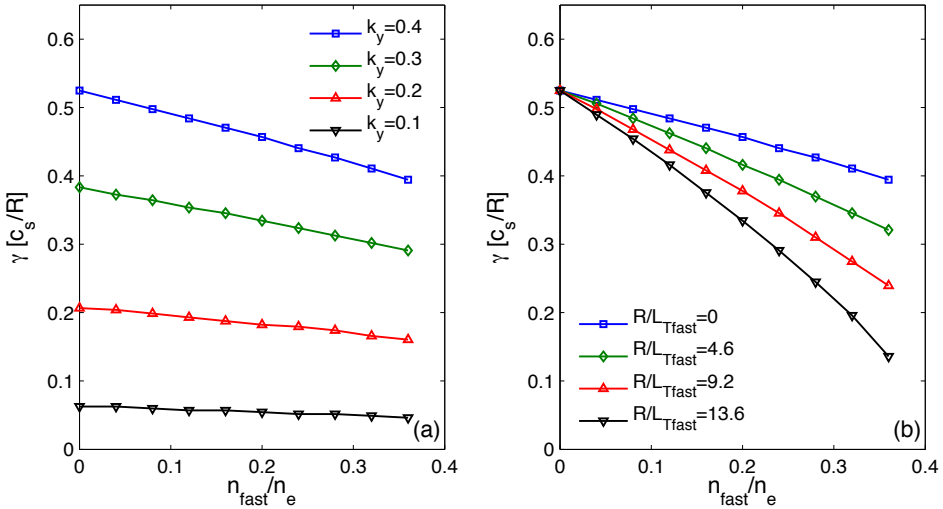


Figure 6.10: Linear fast particle density scans on 66404 parameters at $x = 0.33$ at various values of k_y . Runs were electromagnetic, with collisions, and with numerical geometry.

6.3.7 Full simulations including all effects

Simulations of all three discharges in the data set at $x = 0.33$ were carried out. These simulations assumed $\hat{s} = 0.2$, included rotation, the effect of rotation on equilibrium, experimental R/L_n , finite β , collisions, experimental Z_{eff} , and T_e/T_i . The effect of Z_{eff} - which is stabilizing for ITG turbulence - was modelled by lumping all impurities into a kinetic fully stripped carbon ion species. The carbon temperature and R/L_T were taken as identical to the main ion species. Simulations with Z_{eff} at values corresponding to both the CX and Bremsstrahlung values were carried out to test the sensitivity. The growth rate sensitivity to Z_{eff} and T_e/T_i for linear GENE runs based on discharge 66404 can be seen in Fig.6.11. For our cases, the Z_{eff} stabilisation is more than offset by the $T_e/T_i > 1$ destabilisation. From spot checks the error in simulated fluxes due to the statistical T_e/T_i error is less than 10%. Assuming $R/L_{Tc} = 0$ for the carbon species instead of $R/L_{Tc} = R/L_{Ti}$ altered the bulk ion heat flux by less than 2%.

The comparison between the GENE non-linear simulations and the experimental heat fluxes from power balance is shown in Fig.6.12. In (a), the GENE simulations with both $Z_{eff} = 1.4$ and $Z_{eff} = 1.9$ are shown. In (b), the $T_e/T_i = Z_{eff} = 1$ simulations are shown. The predicted reduced degree of stiffness is still significantly higher than the experimental observation. Only by not including PVG destabilisation and simultaneously assuming a γ_E value significantly higher than the experimental value (as seen in Fig.6.12b), can simulated heat fluxes comparable to the experimental fluxes be obtained for high R/L_{Ti} . However, the simulation for the low rotation, low flux case - discharge 70084 - does agree with the experiment.

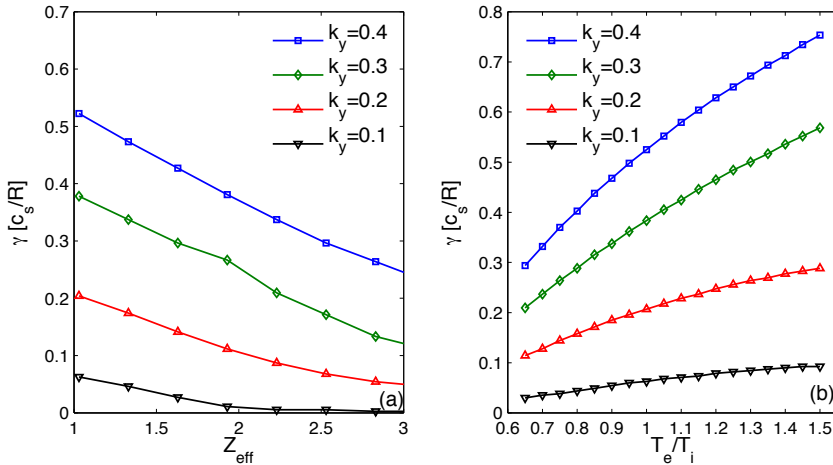


Figure 6.11: Sensitivity of growth rates to Z_{eff} (a) and T_e/T_i (b) from linear GENE runs based on 66404 parameters at $x = 0.33$. Runs were electromagnetic, with collisions, and with numerical geometry.

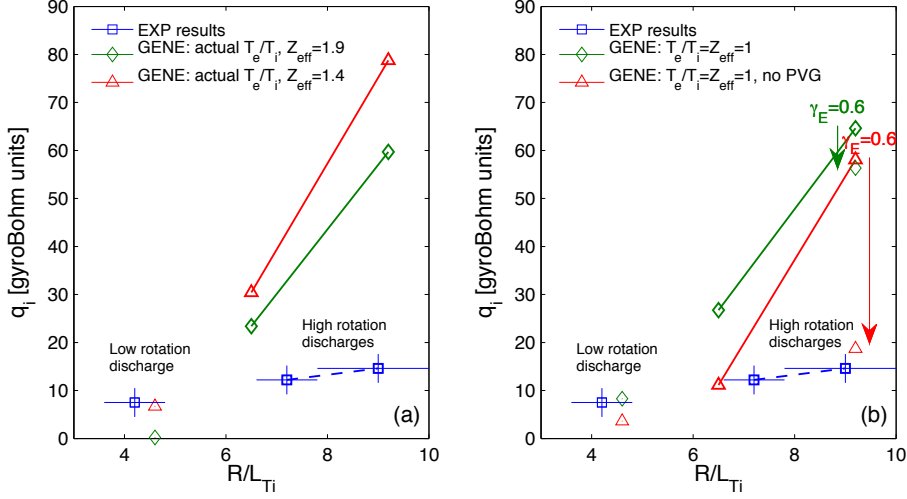


Figure 6.12: Comparison of non-linear simulations and experimental results for the three separate discharges at $x = 0.33$. The comparison with the experimental range of Z_{eff} and actual T_e/T_i (1.08/1.25/1.14 for 70084/66130/66404 respectively) is seen in (a), while in (b) the $T_e/T_i = Z_{eff} = 1$ case is shown, both with and without the inclusion of PVG modes and for various values of γ_E . Runs were electromagnetic, with collisions, and with numerical geometry.

The dramatic decrease in flux seen in the 66404 case when transitioning from $\gamma_E = 0.3$ to $\gamma_E = 0.6$ in the no-PVG case in Fig.6.12b can be understood as a consequence of suppression of lower k_y modes. In Fig.6.13, a 2D linear R/L_{Ti} and k_y scan of growth rates for discharge 70084 (including realistic parameters) is shown. 70084 is shown instead of 66404 for this illustration since the ITG behaviour is similar but the TEM driven modes at low R/L_{Ti} in the 66404 case complicates the picture without changing the qualitative message. No rotation was included in the scan. The contours for $\gamma = 0$ (linear threshold), $\gamma = 0.15$ and $\gamma = 0.3$ are highlighted in white. Modes with growth rates up to $\gamma = 0.15, 0.3$ can be expected to be suppressed by $\gamma_E \approx 0.3, 0.6$ respectively. Low k_y modes drive a significant amount of flux, as represented by the γ/k^2 mixing length argument. In Fig.6.13, the estimated low k_y cutoff due to a flow shear of $\gamma_E = 0.6$ is thus $k_y \sim 0.3$. In that regime, the flux should be significantly reduced since the high-flux-inducing low k_y modes are sheared out of the system. Indeed, when comparing the flux spectra maxima for the $\gamma_E = 0.3$ and $\gamma_E = 0.6$ no-PVG non-linear cases, the maxima are at $k_y = 0.25$ and $k_y = 0.35$ respectively, in line with the intuition gained from the linear runs.

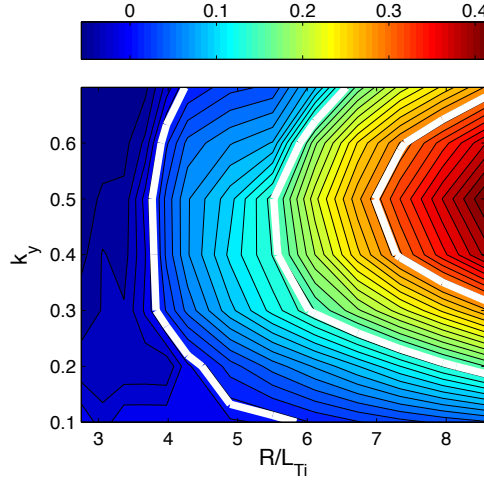


Figure 6.13: 2D plot of growth rates as a function of R/L_{Ti} (x-axis) and k_y (y-axis) for discharge 70084 with realistic parameters - identical to the non-linear case in Fig.6.12. The growth rates are in units of $[c_s/R]$. The three white contours correspond to $\gamma = 0, 0.15, 0.3$ from left to right respectively.

6.4 High magnetic shear case

In this section we compare the gyrokinetic simulations to the experimental results for the three discharges at $x = 0.64$. The experimental observations were that the transport was much stiffer at $x = 0.64$ compared with $x = 0.33$, and that no significant departures from high stiffness were observed at higher rotation. In Fig.6.14 a non-linear R/L_{Ti} scan with various levels of γ_E is shown. The scan is based on discharge 70084 parameters, but applies circular geometry, $\hat{s}/q = 3/2$, and is collisionless and electrostatic. The simulated stiffness is indeed greater than the $x = 0.33$ case as can be seen by comparison with the $\gamma_E = 0$ curve in Fig.6.2a. Moreover, the degree of experimental γ_E variation between the discharges (between $\gamma_E = 0.1 - 0.3$) is also not sufficient to lead to a significant difference in R/L_{Ti} for the same level of flux.

In Fig.6.15, the full comparison between the simulations and the experiments is shown. As in the $x = 0.33$ case, these gyrokinetic simulations are electromagnetic, collisional, with numerical geometry, include a carbon species at a density consistent with $Z_{eff} = 1.4$, and include the experimental T_e/T_i . The red curve in Fig.6.15 corresponds to a R/L_{Ti} scan with the 70084 parameters to gauge the stiffness level. For the high rotation cases 66130 and 66404, the experiment and the predictions differ by approximately a factor of 2. This difference can be explained within the uncertainties of the input modelling parameters. For example, an additional 66404 simulation carried out with $Z_{eff} = 2.4$, $T_e/T_i = 1.1$ and $R/L_{Ti} = 7.8$ led to agreement with the experimental flux within the experimental error-bars. However, the discrepancy between the model-

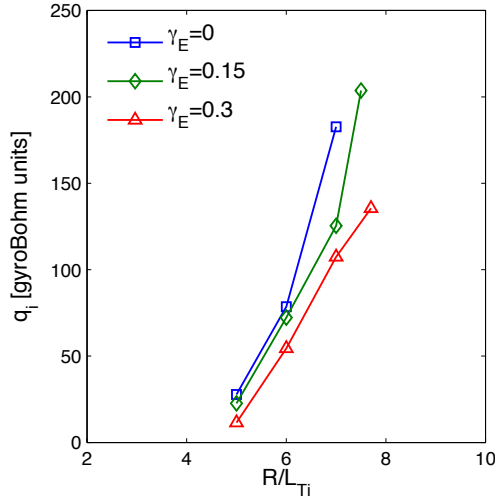


Figure 6.14: Non-linear R/L_{Ti} scan for various levels of γ_E , based on the 70084 parameters at $x = 0.64$.

ling and simulation for the low rotation 70084 discharge cannot be easily explained by the possible variation in the input parameters.

An R/L_{Te} sensitivity check for discharge 66130 was carried out, due to the large R/L_{Te} error bar. It was found from the dedicated non-linear simulations that within the possible R/L_{Te} range the impact on ion transport is minimal.

Examining the differences in experimental parameters for all 3 discharges between $x = 0.33$ and $x = 0.64$ in table 6.1, we can see that both \hat{s} and q are higher at $x = 0.64$, and β_e is lower. All of these differences are expected to lead to higher stiffness. These qualitative differences in q -profile and β_e between low and high radii are generic (apart from special cases such as in ITB discharges), and should hold in general in tokamak discharges.

6.5 Characteristics of linear simulations with flow shear

In this section we discuss some fundamental characteristics of local linear simulations when including flow shear. This includes: the differences between predictions of sub-critical turbulence when assuming either adiabatic or kinetic electrons; the presentation of a novel growth rate calculation method in the presence of rotation, which inhibits the formation of stationary eigenmodes. The second point is of particular relevance for the validation of effective growth rate models applied in the mixing length rule of quasilinear transport models in the presence of flow shear.

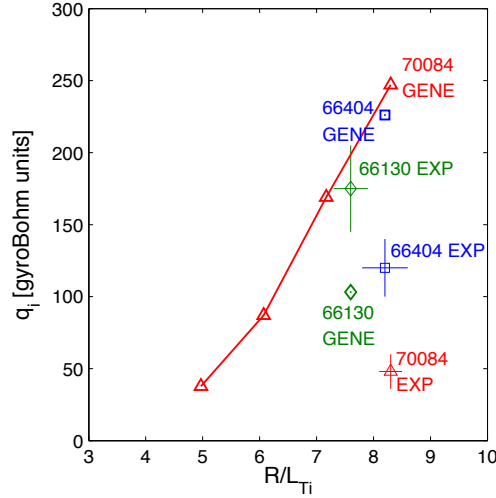


Figure 6.15: Comparison between gyrokinetic simulations and experiment at $x = 0.64$ for all three discharges. The experimental values (with the error bars) are shown for 70084 (red marker), 66130 (green marker) and 66404 (blue marker). The simulated values are shown with the same colour coding and marker style for all three discharges. In addition, simulations identical to the 70084 simulation but with reduced R/L_{Ti} were also carried out to gain a measure of the stiffness at realistic parameters. Runs were electromagnetic, with collisions, and with numerical geometry.

6.5.1 Sub-critical turbulence with kinetic vs adiabatic electrons

In Ref. [49], the analysis of sub-critical turbulence for Cyclone Base Case (CBC) parameters (circular geometry, $\hat{s}/q = 0.8/1.4$, $\epsilon = 0.18$, $R/L_n = 2.2$) assumed adiabatic electrons. This has motivated an examination of whether the qualitative behaviour of the system changes when studied with kinetic electrons. In Fig.6.16, γ_E scans performed by linear-GENE with CBC parameters taking $R/L_T = 6.9$ and $R/L_T = 8.75$ with kinetic and adiabatic electrons are shown. $R/L_{Ti} = R/L_{Te}$ for the kinetic electron cases. The growth rates were calculated by a time average, as in Ref. [49], for comparison. The methodology of growth rate calculation in a rotating system is further discussed in section 6.5.2. The simulations were performed with the initial value solver and thus calculate only the fastest growing mode. When including kinetic electrons, the static (i.e. without rotation) growth rates are significantly increased. This corresponds to the well known effect of added trapped electron drive to the ITG mode. A striking additional observation is that with the inclusion of kinetic electrons the modes are not quenched even at high γ_E , seemingly undermining the sub-critical turbulence paradigm.

This lack of mode quench turns out to be the result of a secondary mode in the system: an electron temperature gradient driven trapped electron mode. This influence of trapped electrons is evident from collisional simulations, shown in Fig.6.17. As colli-

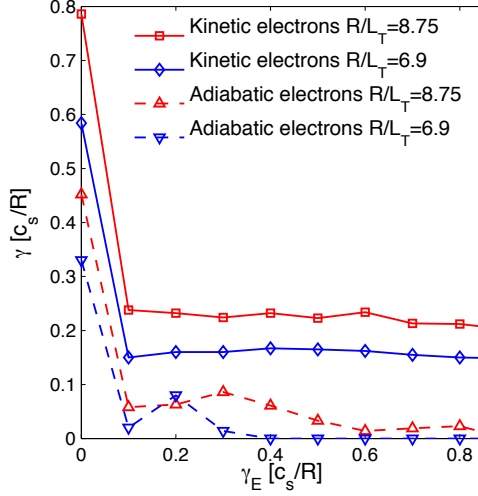


Figure 6.16: Comparison of Cyclone Base Case linear-GENE simulations with $R/L_T = 8.75$ (red curves) and $R/L_T = 6.9$ (blue curves) with kinetic (solid curves) and adiabatic (dashed curves) electrons. $R/L_{Ti} = R/L_{Te}$ for the kinetic electron cases.

sionality increases, the kinetic electron curve converges to the adiabatic electron curve, as the trapped electrons are progressively detrapped. The mode structure of the two leading modes as found by the eigenvalue solver for the kinetic electron $R/L_T = 8.75$, $\gamma_E = 0$ case is shown in Fig.6.18. The leading mode (propagating in the ion diamagnetic direction) is narrow in ballooning space, typical of ITG modes. However, the secondary mode (propagating in the electron diamagnetic direction) is extremely extended in ballooning space. This explains the relative lack of sensitivity of this mode to rotation, which induces a linearly time-dependent k_x shift. Quenching occurs when the mode structure is shifted to stable k_x values faster than the growth rate in the unstable region. If the unstable region is extended in k_x space, then rotation is less effective to quench the mode.

The onset of this mode for CBC parameters is at $R/L_{Te} \approx 5$, as seen in a R/L_{Te} scan shown in Fig.6.19. The growth-rates and frequencies for the two dominant modes are plotted (as calculated by the eigenvalue solver). The subdominant mode switches from an ion mode to an electron mode at $R/L_{Te} \approx 5$, following which the secondary mode growth rate rises sharply with R/L_{Te} .

However, in spite of the non-negligible growth-rate, we note that the secondary electron mode does not induce significant ion fluxes, as established by the low value of the T_i - ϕ crossphase. Additionally, non-linearly the effect of the mode also seems to be negligible and does not drive significant electron flux. This was established by non-linear CBC simulations with $\gamma_E = 1.6$ and $R/L_{Ti} = 8.75$, comparing the cases with $R/L_{Te} = 4$ and $R/L_{Te} = 8.75$. In the linearly stable $R/L_{Te} = 4$ case sub-critical turbulence is ignited in the non-linear simulation, as in Ref. [49]. The $R/L_{Te} = 8.75$ case, which

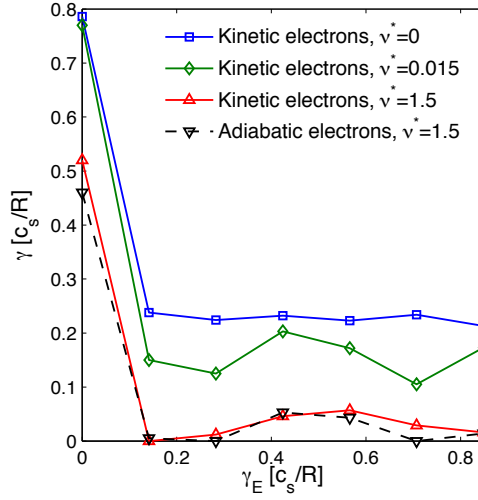


Figure 6.17: Comparison of adiabatic electron linear γ_E scans (CBC parameters with $R/L_T = 8.75$) with kinetic electron scans with various levels of normalised collisionality.

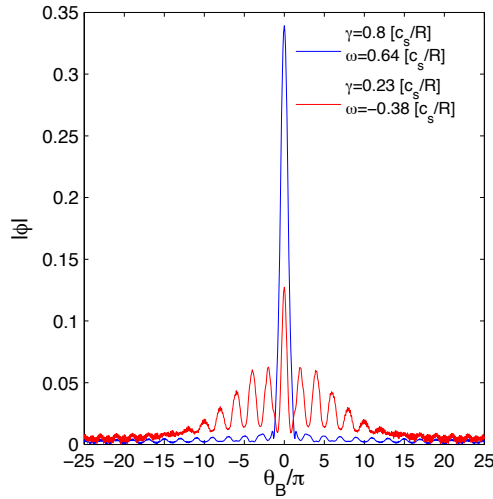


Figure 6.18: Mode structure for the two leading modes in the kinetic electron $R/L_T = 8.75$ case. The dominant mode (blue curve) propagates in the ion diamagnetic direction (note the positive mode frequency), while the subdominant mode (red curve) propagates in the electron diamagnetic direction.

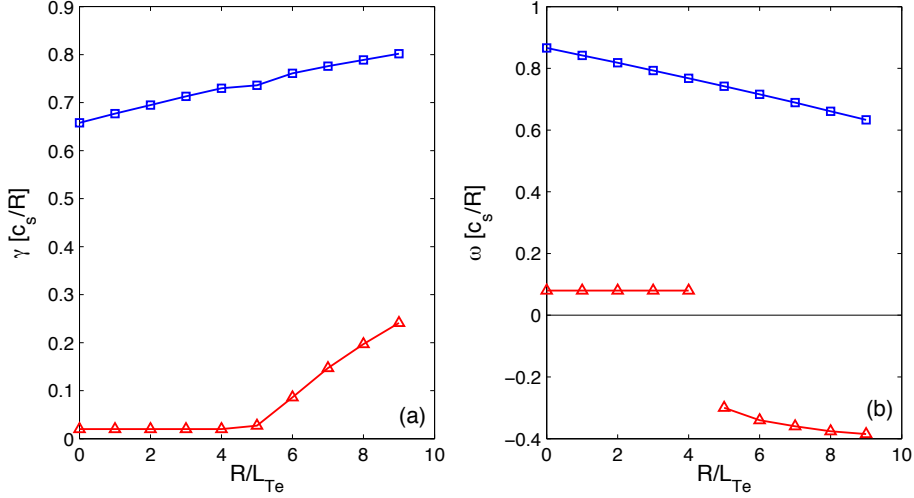


Figure 6.19: Growth rates (a) and frequencies (b) for the 2 dominant modes in a R/L_{Te} scan for the kinetic electron CBC with $R/L_{Ti} = 8.75$.

linearly has an unstable electron mode, had both ion and electron fluxes that matched the $R/L_{Te} = 4$ case within the statistical fluctuations of the simulation. In summary, in spite of the seeming breaking of the sub-critical turbulence paradigm due to the existence of sub-dominant electron modes when including kinetic electrons at high R/L_{Te} , the impact of this mode is minimal. For the single non-linear case examined, the sub-critical turbulence conclusion derived from adiabatic electron studies remain pertinent. Further study in more extended regions of parameter space are necessary to gain increased confidence in this statement.

6.5.2 Novel growth-rate calculation method

In the cases with rotation discussed above, the growth rates were calculated from an average of the fluctuating (due to flow shear) growth rate. However, the timescale of this averaging is much greater than the non-linear decorrelation time, which raises doubts whether this averaging leads to a physically relevant quantity. In Ref. [16], an alternative method was proposed whereby the effective growth rate is calculated over the time during which the mode amplitude is increased by a predefined amplification factor (100 was suggested). In this work, we propose an additional physics-based method for effective growth rate calculation. The underlying assumption is that the relevant timescale for growth rate calculations is the non-linear decorrelation time. We then make the further assumption that the non-linear decorrelation time at each spatial scale is $1/\gamma_k$, the inverse linear growth rate of the most unstable mode at that spatial scale. From analysis of frequency broadening from previous non-linear simulations, this assumption has shown

to hold in many cases at low, transport relevant k_y values [33]. The proposed method is thus to iteratively calculate the growth rate using an adaptive time window until the width of the time window converges to the inverse growth rate calculated. This is illustrated by an example given in Fig.6.20, where a mode amplitude timetrace for the CBC kinetic electron $R/L_T = 8.75$ case with $\gamma_E = 0.3$ is shown. A diagnostic was written in which a time window scans over the amplitude timetrace. At each point in the scan $\gamma_k(t_1, \Delta t)$ is defined as $\gamma_k(t_1, \Delta t) = \ln \left(\frac{n(t_1 + \Delta t)}{n(t_1)} \right) / (\Delta t)$. t_1 is the starting point of the time window, Δt is the time window width, and n is the density fluctuation level. For a given Δt , $\gamma_k(\Delta t)$ is then defined as an average over the $\gamma_k(t_1, \Delta t)$ peaks in the t_1 scan over the timetrace, which smooths out any variations in the peaks which may arise due to the discrete Δk_x shifts present in the implementation of the flow shear in GENE [50]. The time window displayed in Fig.6.20 is at a position corresponding to one of the $\gamma_k(t_1, \Delta t)$ peaks in the t_1 scan for a given Δt . γ_k is then obtained by iterating this procedure and adapting Δt , until convergence is achieved when $|1 - (\Delta t) \cdot \gamma_k| < \delta$. The convergence criteria δ has been chosen as 0.02 for the particular examples shown in this work. We will from henceforth refer to this growth rate calculation method as the ‘ τ_{ac} method’.

Growth rate calculations using the τ_{ac} method are displayed in Fig.6.21 for the Cyclone Base Case at $R/L_{Ti} = 8.75$ and for both adiabatic and kinetic electrons. In the kinetic electron case, $R/L_{Te} = 4$ such that we avoid the sub-dominant electron mode which masks the ITG quenching at high γ_E as discussed in section 6.5.1. For both adiabatic and kinetic electrons, the fundamental quench behaviour is very similar, with the quench occurring at $\gamma_E \approx 2\gamma_0$, where γ_0 is the static growth rate. However, for low γ_E

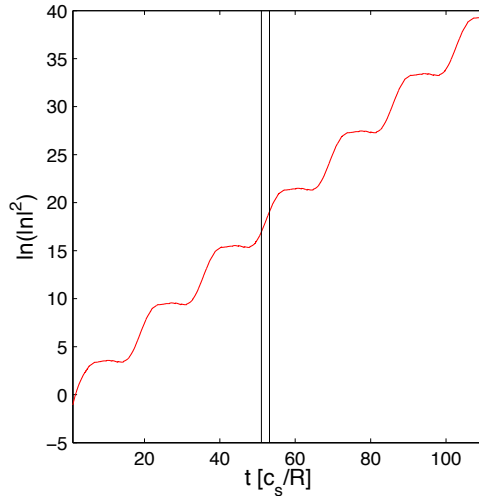


Figure 6.20: Mode amplitude timetrace for the CBC kinetic electron $R/L_T = 8.75$ case with $\gamma_E = 0.3$. The displayed time window is set at one of the $\gamma_k(t_1, \Delta t)$ peaks.

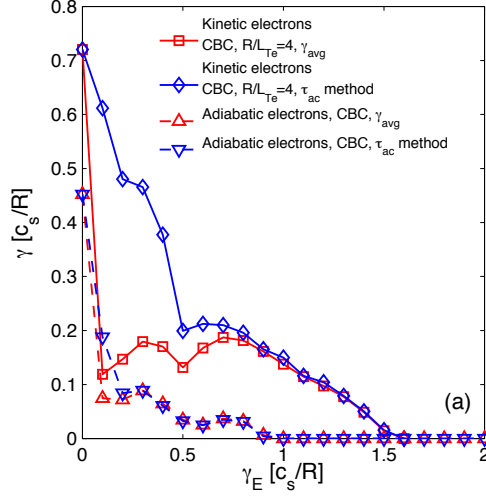


Figure 6.21: Comparison of growth rate calculations with long time-scale averaging and the new τ_{ac} method for CBC parameters with $R/L_{Ti} = 8.75$ for both adiabatic and kinetic electrons.

the initial sharp drop in growth rate previously seen is now mitigated, and much smoother profiles result. At higher γ_E , the growth rates are sufficiently low that the time window in the τ_{ac} method averages over a number of cycles, and is effectively equivalent to the previous long time-scale averaging method.

In reduced transport models, the growth rate quenching due to flow shear may be modelled through an effective growth-rate in a mixing length rule. However, it is vital that simultaneously the PVG destabilisation is included in the linear model itself, to not overestimate the transport reducing effect of flow shear. The parametric dependencies of both the flow shear quenching and PVG destabilisation can be explored in large-scale linear scans with codes such as GENE, and the new τ_{ac} growth-rate calculation method may offer higher fidelity with physical growth-rate values. In future work, GENE linear growth rate calculations as presented here are to be applied for validation of the gyrokinetic quasilinear model QuaLiKiz [51]. Comparison with non-linear results can be carried out in selected locations in parameter space.

6.6 Conclusions

Observations at JET have shown evidence of reduced ion temperature profile stiffness correlated with low magnetic shear and increased flow shear. This has motivated extensive non-linear gyrokinetic simulations, using the GENE code, with parameters based on a subset of these JET discharges. Transport sensitivity scans of various parameters that

differed between the discharges - aside from rotation - were carried out, to assess potential mechanisms that may lead to the observed decreased stiffness regime. Full simulations including electromagnetic effects, numerical geometry, Z_{eff} , experimental T_e/T_i , and rotation were then performed at $x = 0.33$ (in the low stiffness zone) and $x = 0.64$ for the discharges studied, and the predictions were compared with experiment. Finally, a discussion of differences between adiabatic and kinetic electron formulations of flow shear quenching of linear modes was presented. A novel physics-motivated method of growth rate calculation in the presence of flow shear was introduced. The conclusions can be summarised as follows:

- (1) According to the gyrokinetic simulations, the measured values of toroidal flow shear are insufficient to explain the transition to the low stiffness regime. While the competition between parallel velocity gradient (PVG) destabilisation and $E \times B$ stabilisation can reduce the stiffness in the vicinity of the turbulence threshold, the predicted flux levels themselves are still significantly higher than the experimental values. Improved agreement between the simulations and observation is however obtained when ignoring PVG destabilisation, and assuming γ_E values above the measured values. These rotation settings are more consistent with poloidal rotation, which we have assumed to be negligible due to neoclassical damping. However, poloidal rotation values significantly above neoclassical values have been observed within internal transport barriers (ITBs) [9]. While highly unlikely that in our regime any significant poloidal rotation could be maintained in the presence of the neoclassical damping, it would still be of great interest to measure the poloidal rotation in the low-stiffness-regime discharges to examine whether nonetheless any anomalous poloidal rotation is observed.
- (2) The predicted Dimits shift for the discharges simulated is $\Delta(R/L_{Ti}) \approx 0.5$. A significant departure from the Dimits shift paradigm is thus not experimentally observable with great certainty due to the experimental error in extrapolating to the instability thresholds.
- (3) The transport sensitivity to R/L_n variations, fast particle content, and the effect of rotation on the equilibrium, were all examined. It was established that none of the above factors are mechanisms for the transition to the reduced stiffness regime.
- (4) The sensitivity of the transport to β_e was examined. It was established that even for the relatively low β_e values present in these discharges, the non-linear electromagnetic ITG stabilisation is significant. This stabilisation, at least for $\beta_e < 0.48\%$, is a stiffness reduction as opposed to a threshold shift. The non-linear stabilisation is significantly greater than the linear β_e stabilisation, and may be related to an increased relative amplitude of zonal modes. Further investigations of the parameterisation of this effect is important for incorporation into the ‘mixing length rule’ of quasilinear transport formulations. It is expected that this effect would, using such formulations, lead to more optimistic predictions for the energy confinement in future devices such as ITER and DEMO.

- (5) The gyrokinetic predictions and experimental fluxes were also compared at $x = 0.64$ for the three discharges. The experimental variation in flow shear between the discharges is not predicted to be sufficient to lead to a discernible difference in R/L_{Ti} . While the comparison for the high rotation discharges 66404 and 66130 agreed within the experimental uncertainties, it was not possible to reconcile the prediction and observation for the low rotation discharge 70084. The situation is thus the opposite of the comparisons at $x = 0.33$, where only the 70084 comparison agreed within the experimental uncertainties.
- (6) A comparison of flow shear quenching of linear modes assuming either adiabatic or kinetic electrons was carried out for Cyclone Base Case (CBC) parameters. Above an R/L_{Te} threshold, a sub-dominant electron mode can arise which is not quenched by flow shear due to the mode being widely extended in ballooning space. However, this mode drives negligible ion heat flux, and a limited non-linear exploration has shown that the contribution of this mode to the electron heat flux is minimal. For the case examined, the predictions of the onset of sub-critical ion heat flux driving turbulence in the presence of high flow shear are maintained with kinetic electrons.
- (7) A new method of growth rate calculation in the presence of flow shear has been presented. This method is based on the assumptions that the relevant time-scale for growth-rate calculation is the non-linear decorrelation time, and that this time can be represented by $1/\gamma_k$ at each length-scale. γ_k can thus be calculated iteratively with an adaptive time window. It is planned to apply this method for aiding in the validation of effective growth rates in quasilinear transport models.

Acknowledgements

This work, supported by the European Communities under the contract of Association between EURATOM/FOM and EURATOM/CEA, was carried out within the framework of the European Fusion Programme with financial support from NWO. The views and opinions expressed herein do not necessarily reflect those of the European Commission. This work is supported by NWO-RFBR Centre-of-Excellence on Fusion Physics and Technology (Grant nr. 047.018.002). The authors would like to thank: D.R. Hatch, H. Doerk, M.J. Pueschel, A. Schekochihin, and E. Highcock for stimulating discussions. This research used resources of the HPC-FF in Juelich, and the National Research Scientific Computing Center, which is supported by the Office of Science of the U.S. Department of Energy under Contract No. DE-AC02-05CH11231. The authors are extremely grateful to D.R. Mikkelsen for having provided computational resources.

References

- [1] E.J. Doyle *et al.*, Progress in the ITER Physics Basis Chapter 2: Plasma confinement and transport, 2007 *Nucl. Fusion* **47** S18.
- [2] F. Romanelli, 1989 *Phys. Fluids B* **1** 1018.
- [3] H. Biglari, P.H. Diamond and M.N. Rosenbluth, 1989 *Phys. Fluids B* **1** 109.
- [4] X. Garbet, 1992 *Phys. Fluids B* **1** 136.
- [5] S.C. Guo and F. Romanelli, 1993 *Physics of Fluids B* **5** 520.
- [6] P. Diamond, S.-I. Itoh, K. Itoh and T.S. Hahm, 2005 *Plasma Phys. Control. Fusion* **47** R31.
- [7] K.H. Burrell, 1997 *Phys. Plasmas* **4** 1499.
- [8] P.W. Terry, 2000 *Rev. Mod. Phys.* **72** 109.
- [9] K. Cromb   *et al.*, 2005 *Phys. Rev. Lett.* **95** 155003.
- [10] P.C. de Vries *et al.*, 2009 *Nucl. Fusion* **49** 075007.
- [11] P.A. Politzer *et al.*, 2008 *Nucl. Fusion* **48** 075001.
- [12] R.E. Waltz, G.D. Kerbel and J. Milovich, 1994 *Phys. Plasmas* **1** 2229.
- [13] R.E. Waltz, G.D. Kerbel, J. Milovich and G.W. Hammett, 1995 *Phys. Plasmas* **2** 2408.
- [14] R.E. Waltz, J.M. Candy and M.N. Rosenbluth, 2002 *Phys. Plasmas* **9** 1938.
- [15] J.E. Kinsey *et al.*, 2005 *Phys. Plasmas* **12** 062302.
- [16] C.M. Roach *et al.*, 2009 *Plasma Phys. Control. Fusion* **13** 124020.
- [17] R.E. Waltz *et al.*, 1997 *Phys. Plasmas* **7** 2482.
- [18] J.E. Kinsey *et al.*, 2008 *Phys. Plasmas* **15** 055908.
- [19] P.J. Catto, M.N. Rosenbluth and C.S. Liu, 1973 *Phys. Fluids* **16** 1719.
- [20] S.L. Newton, S.C. Cowley and N.F. Loureiro, 2010 *Plasma Phys. Control. Fusion* **52** 125001.
- [21] A.M. Dimits, B.I. Cohen, W.M. Nevins and D.E. Shumaker, 2001 *Nucl. Fusion* **40** 1725.
- [22] P. Mantica *et al.*, 2009 *Phys. Rev. Lett.* **102** 175002.
- [23] P. Mantica *et al.*, 2011 *Phys. Rev. Lett.* **107** 135004.
- [24] F. Jenko, W. Dorland, M. Kotschenreuther and B.N. Rogers 2000 *Phys. Plasmas* **7** 1904, and <http://gene.rzg.mpg.de>.
- [25] J.F. Artaud *et al.*, 2010 *Nucl. Fusion* **50** 043001.
- [26] A.J. Brizard and T.S. Hahm, 2007 *Rev. Mod. Phys.* **79** 421  468.
- [27] X. Lapillonne *et al.*, 2009 *Phys. Plasmas* **16** 032308.
- [28] A.J.C. Beli  n, M.A. Botchev, J.P. Goedbloed, B. van der Holst and R. Keppens, 2002 *J. Comp. Phys.* **11** 91.
- [29] F. Merz, C. Kowitz, E. Romero, J.E. Roman and F. Jenko, 2012 *Comput. Phys. Commun.* **183** 922.

-
- [30] J. Citrin *et al.*, 2012 *Plasma Phys. Control. Fusion* **54** 065008.
 - [31] J. Candy and R.E. Waltz, 2003 *Phys. Rev. Lett.* **91** 045001.
 - [32] F. Jenko *et al.*, 2001 *Phys. Plasmas* **8** 4096.
 - [33] J. Citrin *et al.*, 2012 *Phys. Plasmas* **19** 062305.
 - [34] J.E. Kinsey, R.E. Waltz and J. Candy, 2006 *Phys. Plasmas* **13** 022305.
 - [35] E.G. Highcock *et al.*, 2010 *Phys. Rev. Lett.* **105** 215003.
 - [36] G.T.A. Huysmans, J.P. Goedbloed and W. Kerner, 1991 *CP90 Conf. on Comp. Physics (Singapore: Word Scientific)* p 371.
 - [37] E.G. Highcock *et al.*, 2012 *Submitted to Phys. Rev. Lett.*
 - [38] A.M. Dimits *et al.*, 2000 *Phys. Plasmas* **7** 969.
 - [39] D.R. Mikkelsen and W. Dorland, 2008 *Phys. Rev. Lett.* **101** 135003.
 - [40] F. Merz and F. Jenko, 2010 *Nucl. Fusion* **50** 054005.
 - [41] J. Weiland and A. Hirose, 1992 *Nucl. Fusion* **32** 151.
 - [42] M.J. Pueschel, M. Kammerer and F. Jenko, 2008 *Phys. Plasmas* **15** 102310.
 - [43] C.F. Maggi *et al.*, 2010, *Nucl. Fusion* **50** 025023.
 - [44] M.J. Pueschel and F. Jenko 2010, *Phys. Plasmas* **17** 062307.
 - [45] F. Militello, M. Romanelli, J.W. Connor and R.J. Hastie, 2011 *Nucl. Fusion* **51** 033006.
 - [46] G. Tardini *et al.*, 2007 *Nucl. Fusion* **47** 280.
 - [47] M. Schneider *et al.*, 2011 *Nucl Fusion* **51** 063019.
 - [48] C. Holland *et al.*, 2011 *Phys. Plasmas* **18** 056113.
 - [49] M. Barnes *et al.*, 2010 *Phys. Rev. Lett.* **106** 175004.
 - [50] G.W. Hammett, W. Dorland, N.F. Loureiro, and T. Tatsuno. Implementation of Large Scale ExB Shear Flow in the GS2 Gyrokinetic Turbulence Code. *APS Meeting Abstracts*, pages 1136PŨ+, October 2006.
 - [51] C. Bourdelle *et al.*, 2007 *Phys. Plasmas* **47** 14 112501.

7 Evaluation and future prospects

In this section we revisit our original research questions and evaluate the progress made in addressing them. The underlying motivation behind the research was to increase the understanding of the turbulent regime typical of tokamak hybrid scenarios, which have the potential to extrapolate to a long-pulse reactor scenario. We have focused primarily on the effect of the characteristic hybrid scenario q -profile and magnetic shear (derived from the current profile) on ITG turbulence. In section 7.1, the specific research sub-questions posed in section 1.3 are answered. In section 7.2, the outlook for follow-up work and new potential research directions is surveyed.

7.1 Conclusions

What is the optimum application of external current drive in the ITER hybrid scenario for obtaining the current profile shape that minimises turbulent transport? (Chap.3 and Ref. [1])

The CRONOS suite of integrated modelling codes [2] coupled to the GLF23 transport model [3] was applied for optimising the current drive application in the ITER hybrid scenario under certain constraints. These constraints were the maintenance of $q > 1$, achieving $P_{fus} \sim 350 \text{ MW}$, and reaching $Q > 5$. The primary instability which leads to turbulent transport in the scenario was the ITG mode. In GLF23 the critical threshold of the instability has a dependence on the current profile in line with the \hat{s}/q parametrisation in analytical formulations [4]. This led to a clear correlation between the volume averaged $\langle \hat{s}/q \rangle$ and P_{fus} in the simulated discharges.

Maximising $\langle \hat{s}/q \rangle$ by application of current drive, while still satisfying the $q > 1$ constraint, was shown to be key to optimising the scenario, according to the GLF23 transport model. The ideal current drive combination for optimum q -profile shaping was seen to be the combination of off-axis neutral beam injection (NBI) and electron cyclotron current drive (ECCD). NBI provides high current drive efficiency (defined as $[MA]/[MW]$), increasing the non-inductive current fraction necessary for $q > 1$. While the NBI current deposition shape is not flexible, the general position of the off-axis NBI deposition is beneficial for the desired q -profile shaping. ECCD has reduced current drive efficiency compared with NBI, but the ECCD current profiles are focused and tunable, allowing for more flexibility in q -profile shaping. Strong sensitivity of the fusion power to the precise ECCD settings was observed, with up to 20% difference of P_{fus} when adjusting the simulated ECCD launcher mirror angles by only a few degrees. The application of ion cyclotron resonance heating (ICRH) was not predicted to be beneficial to the scenario due to the stiffness of the GLF23 transport model and the lack of ICRH current drive. The application of lower hybrid current drive (LHCD) was predicted to be detrimental due its high current drive efficiency combined with an unfavourable deposition radius.

The current deposition location of LHCD is too far off-axis, which strongly decreases $\langle \hat{s}/q \rangle$, and is predicted to lead to reduced fusion power.

The importance of current profile shaping during the ramp-up phase of the discharge was stressed. Current diffusion following current ramp-up tends to increase $\langle \hat{s}/q \rangle$. Thus to maximize the average Q gain factor during a discharge, the q -profile should reach its final stationary-state optimum shape immediately after the L-H transition.

What are the limits for defining an ITER hybrid scenario operational window given the scenario constraints? (Chap.3 and Ref. [1])

One of the strongest sensitivities of the ITER hybrid scenario predictions was the pedestal height assumption. The optimisation exercise was carried out for $T_{ped} = 3, 4, 5$ keV. For $T_{ped} = 3$ keV no satisfactory scenario was found for any current drive mix, with $x(q = 1) = 0.44$ at 1200 s. For $T_{ped} = 4$ keV a satisfactory hybrid scenario was predicted. This scenario however demands an available ECCD power of up to 37 MW, more than the ITER baseline level of 20 MW. This strongly informs the considerations for potential ITER heating and current drive system (H/CD) upgrades for advanced scenario operation. For $T_{ped} = 5$ keV, the operational margins are much wider, and a satisfactory ITER hybrid scenario is predicted within the bounds of the ITER baseline H/CD system.

The strong sensitivity of the pedestal height in setting the operational windows of the scenario suggests that integrated modelling including self-consistent pedestal predictions is vital. Nevertheless, the simulations carried out do show that for $T_{ped} \geq 4$ keV a scenario is predicted that satisfies the primary ITER hybrid scenario goal of $Q > 5$ for $t > 1000$ s. Furthermore, the trends predicted for the scenario improvement with q -profile shaping hold regardless of the various modelling assumptions.

Is the predicted q -profile impact on the turbulent transport validated by present-day experimental discharges? (Chap.4 and Ref. [5])

This impact of increased \hat{s}/q on core confinement was assessed on JET and ASDEX Upgrade (AUG) hybrid scenario discharges. This was carried out by integrated modelling with CRONOS coupled to the GLF23 transport model as in the ITER hybrid scenario study. For both machines, discharge pairs were analysed displaying similar pedestal confinement yet significant differences in core confinement and q -profiles.

For the JET pair, it was found that isolating the effect of the q -profile could explain $\sim 60\%$ of the observed confinement difference. The bulk of the remaining difference could be explained by the variations in the experimental edge values serving as the GLF23 boundary conditions.

For the AUG pair, the isolated impact of the \hat{s}/q effect in explaining the confinement difference was $\sim 35\%$ - still significant but not the dominating factor. A further $\sim 25\%$ of the confinement difference could be explained by the experimental edge condition variations between the pair. Two possible factors were identified in the reduced confinement AUG discharge which may play a role in setting the remaining 40% confinement difference: the existence of an NTM, and a flattened core rotation profile. These differences hamper the isolation of the \hat{s}/q effect in AUG pair compared to the JET pair.

The absolute predictions of the core energy content in all discharges depend on the degree of rotational flow shear turbulence suppression assumed. When including the full GLF23 flow shear suppression model with $\alpha_{ExB} = 1.35$, significant overprediction of the core energy content was obtained for all discharges. With $\alpha_{ExB} = 0$, satisfactory agreement with the experimental values was obtained. A number of suggestions can be raised as to why this core energy content overprediction occurs. Firstly, the inclusion of real geometry, which is not taken into account in GLF23, is predicted to reduce the ITG critical thresholds [6]. This would diminish the degree of overprediction. This was also observed with QuaLiKiz [7] critical threshold modelling of these discharges. Furthermore, $\alpha_{ExB} = 1.35$ may be an unrealistically high value. More recent non-linear gyrokinetic simulations point towards appropriate values of $\alpha_{ExB} \sim 0.5$ [8–10]. Additionally, parallel velocity gradient (PVG) destabilisation may play a role in reducing the effectiveness of the flow shear destabilisation [9, 11, 12]. It is important to validate the PVG destabilisation of quasilinear models against more complete physical models. Nevertheless, the \hat{s}/q effect on core confinement is independent of the flow shear suppression model. The encouraging results regarding the validation of the importance of q -profile shaping for increasing ITG critical thresholds in hybrid scenarios hold, regardless of the absolute predictions.

While the work in Chap.3-4 concentrated on the beneficial effect of high \hat{s}/q at outer radii on the ITG critical thresholds, Chap.5-6 concentrated on the beneficial effect of low magnetic shear at inner radii on the stiffness. The following questions were asked:

What is the non-linear physics at low magnetic shear (\hat{s}) that leads to reduced stiffness in ITG turbulence? (Chap.5 and Ref. [13])

From extensive simulations with the non-linear gyrokinetic code GENE [14], it was found that the changes in the spatio-temporal scales of ITG turbulence at low- \hat{s} results in flux reduction compared to high- \hat{s} , in spite of the linear critical threshold *not* decreasing at low- \hat{s} . This constitutes a stiffness reduction.

It was shown that at low- \hat{s} the turbulence radial correlation length decreases compared to high- \hat{s} . This was postulated to be due to the observed increased zonal flow activity at low- \hat{s} , which leads to increased eddy shearing. The increased zonal flows are possibly due to the increased poloidal symmetry of the linear ITG modes at low- \hat{s} , which facilitates non-linear mode-coupling between the drift waves and the zonal flows.

This effect is combined with increased non-linear frequency broadening around the linear ITG frequencies at the spatial scale of each k_y mode at low- \hat{s} . This led to a tendency of the autocorrelation time to decrease at low- \hat{s} . Since the Kubo numbers are below (although close to) unity in the system, this is also expected to lead to a reduction in diffusivity [15]. The frequency broadening may also be a signature of increased coupling to damped linear modes in the system, which would reduce the flux. It was postulated that the increased zonal flows at low- \hat{s} may facilitate the coupling to damped linear modes.

Can the QuaLiKiz model be improved such that increased agreement with non-linear ITG turbulence predictions is obtained at low magnetic shear? (Chap.5 and Ref. [13])

The knowledge acquired from the non-linear simulations was applied for improving the QuaLiKiz gyrokinetic quasilinear transport model. It was first established that the discrepancy between QuaLiKiz and non-linear simulations at low- \hat{s} resulted from the mixing length rule, and not from other fundamental approximations in the QuaLiKiz model. It was, however, seen that for negative- \hat{s} the QuaLiKiz growth rate predictions are not accurate, most probably due to the eigenmode width ansatz made in the model. This has repercussions for using QuaLiKiz for steady-state scenario modelling.

The QuaLiKiz mixing length rule was improved by introducing a new formula for capturing the non-linear $\langle k_x \rangle$ values at each k_y scale-length, based on the non-linear observations. This improved the accuracy of the assumption made for reproducing the non-linear flux spectrum maxima in the QuaLiKiz model, and also more accurately captures the non-linear correlation length trends. The increased frequency broadening effect was captured in an *ad-hoc* manner by simply dividing the QuaLiKiz predicted fluxes by a \hat{s} dependent factor corresponding to the average degree of frequency broadening observed in the non-linear simulations at each \hat{s} . This roughly captures the effect of decreased correlation time in the diffusivities.

The combined effect of these two improvements led to significantly improved agreement between QuaLiKiz and a database of non-linear \hat{s} -scans. This increases our confidence in applying QuaLiKiz for hybrid scenario modelling in the future.

Can the observed reduced stiffness observed in JET discharges at low- \hat{s} and high rotational flow shear be understood through non-linear simulations? (Chap.6 and Ref. [16])

Gyrokinetic simulations with GENE were carried out based on specific JET discharges where reduced ion temperature stiffness was observed at combined low- \hat{s} and high rotational flow shear [17]. It was found that, according to the simulations, the measured values of toroidal flow shear cannot explain the transition to the low stiffness regime. For the low radii cases where lowered stiffness was observed, the heat flux value from a low rotation, low flux discharge was successfully predicted by the simulations. However, the simulations for the high rotation discharges produced flux values ~ 4 times higher than the experimental values. The competition between stabilising $E \times B$ shear and destabilising parallel velocity gradient (PVG) destabilisation did lead to decreased stiffness with rotation, but significantly less than the experimental observation.

However, many additional insights were gained from the simulations. The sensitivity to the stiffness to the various parameters varying between the discharges was assessed. The sensitivity was found to be low for all cases apart from β_e (the ratio between electron and magnetic pressure). The non-linear ITG stabilisation with β_e was seen to be significantly higher than the linear stabilisation, and is manifested as stiffness reduction as opposed to a critical threshold shift. This was correlated with an increase in zonal flow activity. While the degree of stiffness reduction is not sufficient to fully explain the experimental observation, it does play a significant role and cannot be ignored. With regard to hybrid scenarios, linear β_e stabilisation has already been invoked to partially explain improved core confinement [18]. Since the non-linear stabilisation is stronger, the future investigation of this effect is highly desirable.

Finally, it was possible for the simulations to reach the experimental flux values for the high rotation cases when simultaneously assuming a flow shear level higher than the experiment, and ignoring the PVG drive. This may be consistent with significant poloidal rotation, even though it is commonly considered to be negligible due to neoclassical damping. This stimulates the experimental investigation of the poloidal rotation in this class of discharges.

7.2 Outlook

Many avenues for continued research based on the work covered in this research remain open. These consist both of the generalisation and completion of the research carried out, as well as new potential fruitful research directions that can be taken. These ideas are listed below, sorted by the chapter in which the original research was expounded.

7.2.1 Chap.3

Given the sensitivity of the results to the pedestal assumption, it would clearly be of great benefit to self-consistently include a prediction for the pedestal height in the integrated modelling. Initial work in this direction has already been carried out [19], where ITER hybrid scenario predictions with CRONOS were carried out with pedestal heights consistent with predictions from the EPED1 pedestal model [20], based on the work carried out in Chap.3. The next step would be to fully integrate the EPED1 model into CRONOS, for fully self-consistent simulations. Additional steps for increased modelling self-consistency could be to include particle and angular momentum modelling. The application of advanced transport models such as TGLF [21] and QuaLiKiz would be advantageous in this regard, since they incorporate improved formulations for trapped electrons compared to GLF23, which is important for particle transport. TGLF also has dependence on plasma shaping, as opposed to GLF23, which could be important for more accurate predictions of the scenario.

While the inclusion of ICRH was not predicted to be beneficial for the hybrid scenario due to a lack of current drive, it would be interesting to examine direct ion heating with He3 minority heating. While both the lack of current drive for q -profile shaping, and the dilution of the main D and T species by He3 may reduce the fusion power, this could be offset by a strong effect of direct ion heating, depending on the stiffness of the transport model used. This question has not yet been addressed by integrated modelling.

It was shown that to maximise the average fusion gain $\langle Q \rangle$ in the discharge, it is important to optimise the q -profile shaping during the ramp-up phase of the discharge. In this work the ramp-up phase was not fully optimised. Additional work has been started in this direction [22]. Additional optimisation work is projected to continue with a fast current profile solver [23].

We have insisted on maintaining the constraint $q > 1$ for a ‘satisfactory’ hybrid scenario. This constraint was based on the avoidance of deleterious NTMs seeded by sawteeth. However, there is empirical evidence that the β value for NTM triggering by

sawteeth depends on the sawtooth period [24]. We can thus envisage a hybrid scenario with sufficiently low β where the sawtooth period is reduced by maintaining a small $x(q = 1)$ radius and applying ECCD and ICRH for sawtooth control [25, 26]. A hybrid scenario with a small region of allowed $q < 1$ would greatly increase the operational window of the scenario, since the current profile tends to be peaked due to neoclassical resistivity and it is quite difficult to maintain $q > 1$ completely. Future work in this direction is highly recommended.

Finally, the sensitivity of the fusion power to the precise ECCD deposition opens up the opportunity for closed loop control of the hybrid scenario. In this work, the ideal location of the ECCD deposition was found by open loop optimisation, which is inefficient. It is envisioned that this can be carried out in a closed loop manner, optimising a cost function based on the ideal q -profile shape subject to constraints in the input power and $q > 1$. Initial work in this direction has already been carried out [27, 28], and continued work is recommended.

7.2.2 Chap.4

The main challenge of this work was the relatively small differences in q -profile between the discharges in each pair, which hampered achieving a high degree of certainty in the conclusions. Further q -profile shaping experiments aiming for larger differences would be extremely helpful for continued study. In addition, studies of recent JET hybrid scenarios with the ITER-like-wall (ILW) would be extremely beneficial for increased confidence in ITER extrapolations. It has been observed that with the ILW, impurity transport can play an important role in setting the electron temperature and resistivity during the rampup, which affects the q -profile evolution [29]. It would thus be important to improve the impurity transport capabilities of the integrated modelling codes to take this into account.

In addition, it was seen that the experimentally measured q -profiles were not always reproducible by current diffusion modelling. This discrepancy is particularly acute during the ramp-up phase. It has been suggested that the accuracy of the calculated neoclassical resistivity in the integrated modelling codes is dependent on the collisionality, and that the accuracy may be compromised at low collisionality [30]. It has also been suggested that using a free boundary solver for the equilibrium is important for the correct evaluation of the q -profile evolution during the ramp-up phase [31]. This matter should be investigated more carefully, since the scenario extrapolations depend strongly on the predicted q -profile evolution during the ramp-up phase.

7.2.3 Chap.5

Multiple improvements can still be made to the QuaLiKiz model. For increased efficiency in routine use as a transport model within the integrated modelling framework, the code itself can still be numerically optimised. In addition, plasma shaping should be taken into account in the model, which is seen to be important for calculation of ITG linear

thresholds [6]. Additionally, incorporation into the model of parallel flow shear destabilisation and $E \times B$ shear stabilisation - validated against non-linear simulations - would then allow for the modelling of discharges with rotation, important for hybrid scenario modelling.

Further improvement in incorporating the effect of the increased non-linear frequency broadening at low- \hat{s} can be made, beyond the *ad-hoc* normalisation factor currently applied. It may be possible to develop a relatively simple model for zonal flow generation, guided by non-linear simulations. The linear response could then possibly be renormalised based on the zonal flow mode amplitudes. A simpler improvement would be to incorporate the low- \hat{s} parameterisation of the increased frequency broadening into the Lorentzian inserted into the frequency integration in the QuaLiKiz flux calculation itself.

7.2.4 Chap.6

The inclusion of rotation was only predicted to lead to ion heat fluxes close to the experimental values when PVG destabilisation was ignored, and when γ_E was taken higher than the experimental values. This would be consistent with non-negligible poloidal rotation. The simulations assumed fully toroidal rotation. Experimental measurements of poloidal rotation for this class of discharges is thus recommended, in spite of the expectation of strong neo-classical damping.

Another possibility for obtaining reduced flux in the simulations, previously not taken into account, is α -stabilisation due to the fast particle pressure [32]. While dilution due to the fast particles was ruled out as an important stabilising factor, self-consistent equilibria including the increased Shafranov shift due to fast particle pressure was *not* included in the calculations. This still needs to be examined.

The observed high degree of non-linear β_e stabilisation is extremely interesting and deserves further study. Since this stabilisation is correlated with increased zonal flow activity, it would be interesting to examine in deeper detail any possible mechanisms for increased non-linear mode coupling to zonal flows. As a first step, any changes in the ITG mode structure which develop at finite β_e should be studied, since this could facilitate coupling to zonal flows.

References

- [1] J. Citrin *et al.*, 2010 *Nucl. Fusion* **50** 115007.
- [2] J.F. Artaud *et al.*, 2010 *Nucl. Fusion* **50** 043001.
- [3] R.E. Waltz *et al.*, 1997 *Phys. Plasmas* **7** 2482.
- [4] S.C. Guo and F. Romanelli, 1993 *Physics of Fluids B* **5** 520.
- [5] J. Citrin *et al.*, 2012 *Plasma Phys. Control. Fusion* **54** 065008.
- [6] F. Jenko *et al.*, 2001 *Phys. Plasmas* **8** 4096.
- [7] C. Bourdelle *et al.*, 2007 *Phys. Plasmas* **47** 14 112501.
- [8] R.E. Waltz, J.M. Candy and M.N. Rosenbluth, 2002 *Phys. Plasmas* **9** 1938.
- [9] J.E. Kinsey *et al.*, 2005 *Phys. Plasmas* **12** 062302.
- [10] C.M. Roach *et al.*, 2009 *Plasma Phys. Control. Fusion* **13** 124020.
- [11] R.E. Waltz, G.D. Kerbel and J. Milovich, 1994 *Phys. Plasmas* **1** 2229.
- [12] A.M. Dimits, B.I. Cohen, W.M. Nevins and D.E. Shumaker, 2001 *Nucl. Fusion* **40** 1725.
- [13] J. Citrin *et al.*, 2012 *Phys. Plasmas* **19** 062305.
- [14] F. Jenko, W. Dorland, M. Kotschenreuther and B.N. Rogers 2000 *Phys. Plasmas* **7** 1904, and <http://gene.rzg.mpg.de>.
- [15] T. Hauff, 2009, PhD Thesis, Universität Ulm.
- [16] J. Citrin *et al.*, Ion temperature profile stiffness: non-linear gyrokinetic simulations and comparison with experiment. *Submitted to Nucl. Fusion* (2012).
- [17] P. Mantica *et al.*, 2011 *Phys. Rev. Lett.* **107** 135004.
- [18] C.F. Maggi *et al.*, 2010, *Nucl. Fusion* **50** 025023.
- [19] X. Litaudon *et al.*, *24rd IAEA Fusion Energy Conference, San Diego, USA* (2012).
- [20] P.B. Snyder *et al.*, *Nucl. Fusion* **51** 103016 (2011) and *Phys. Plasmas* **19** 056115 (2012).
- [21] J.E. Kinsey *et al.*, 2008 *Phys. Plasmas* **15** 055908.
- [22] G.M.D. Hogewij *et al.*, *Accepted by Nucl. Fusion*, (2012).
- [23] F. Felici *et al.*, 2011 *Nucl. Fusion* **51** 083052.
- [24] I.T. Chapman *et al.*, 2010 *Nucl. Fusion* **50** 102001.
- [25] I.T. Chapman *et al.*, 2012 *Nucl. Fusion* **52** 063006.
- [26] J.P. Graves *et al.*, 2012 *Nat Commun.* **3** 624.
- [27] S. Djordjevic, M.R. de Baar, M. Steinbuch, J. Citrin, G.M.D. Hogewij, *38th EPS Conference on Plasma Physics, Strasbourg, France* (2011) and *Proc. 50th IEEE-CDC, Orlando, USA* (2011).
- [28] E. Maljaars, 2012, MSc thesis, Eindhoven University of Technology.
- [29] E. Joffrin *et al.*, 2012 *24th Int. Conf. on Fusion Energy 2012 (San Diego, USA)* (Vienna IAEA).
- [30] I. Jenkins *et al.*, 2010 *Proc. 37nd EPS Conf. on Plasma Physics (Dublin, 2010)*.

- [31] E. Fable, *private communication* (2012).
- [32] C. Bourdelle *et al.*, 2005 *Nucl. Fusion* **45** 110.

Summary

Title: Turbulent transport in tokamak advanced scenarios

Nuclear fusion has the potential of providing a high baseline, environmentally friendly, and sustainable source of energy. A plasma consisting of the hydrogen isotopes deuterium and tritium, heated to temperatures of $\sim 10^8$ K, can sustain fusion reactions at a sufficiently high rate for energy production. In a reactor the plasma must be confined and insulated from the walls. The leading confinement concept is the tokamak, where the plasma is trapped in a toroidal chamber by helical magnetic fields. The confinement is then limited by turbulent transport, which leads to leakage of heat and particles at a rate higher than expected from collisional transport.

The poloidal component of the helical field is produced by toroidal current in the plasma itself. This current is in standard operation induced by a transformer in the centre of torus, where the plasma loop acts as the secondary circuit. The use of a transformer is not ideal for reactor operation; the discharge pulse times are limited since the transformer current cannot be infinitely ramped. The underlying question motivating the work in this thesis is thus: can an achievable tokamak operational scenario be developed which allows for significantly longer pulses, compatible with reactor requirements?

One such scenario developed in present-day tokamaks is the ‘hybrid-scenario’. The scenario operates at reduced plasma current compared with fully inductive scenarios, and has an increased non-inductive current fraction through increased external current drive. Importantly, hybrid scenarios display better confinement than expected from empirical scaling laws, which can compensate the confinement lost due to the reduced plasma current. This holds great promise for the extrapolation of this scenario to future machines, and may even pave the way towards a long-pulse reactor scenario. This thesis focuses on an a particular factor which may partially explain the improved confinement - the impact of the broad current profile which characterises hybrid scenarios, on the turbulent transport which limits plasma confinement. The particular instabilities studied are those driven by the ion temperature gradient (ITG). This the dominant source of turbulence in the tokamak regimes studied.

The current profile characteristics are represented by the following quantities derived thereof: the q -profile and magnetic shear (\hat{s}). Hybrid scenario q -profiles are characterised by high \hat{s}/q at high radii and low- \hat{s} at low radii. The beneficial effects of increased \hat{s}/q at high radii for increasing ITG critical gradient thresholds are quantified in an extrapolation of the hybrid scenario to the ITER tokamak (currently under construction) by integrated modelling with the CRONOS suite of codes coupled to the GLF23 transport model for predicted heat transport. The confinement is optimised by tailoring the q -profile with external current drive sources. It is predicted that for a mix of off-axis neutral beam injection (NBI) and electron cyclotron current drive (ECCD), an ITER hybrid scenario satisfying $q > 1$, $Q = 5$, and $t > 3000$ s can be achieved for an edge transport barrier (pedestal) temperature of $T_{ped} > 4$ keV. The fusion gain factor is defined as $Q = \frac{P_{fus}}{P_{input}}$.

It is also predicted that ion cyclotron resonance heating (ICRH) and lower hybrid current drive (LHCD) are not beneficial for the ITER hybrid scenario main burn phase, since they do not provide beneficial q -profile shaping.

These results are validated versus experimental discharges. Two pairs of hybrid scenario discharges from both the JET and ASDEX-Upgrade tokamaks are analysed. Each pair is characterised by similar pedestal heights but differences in q -profile and core confinement. The degree to which the differences in core confinement can be attributed to the \hat{s}/q effect is studied. CRONOS and GLF23 are used for predictive simulations of the discharges, as in the ITER extrapolation. These predictions are then compared to the actual experimental data. The effect of \hat{s}/q can be isolated in the simulations since all the various parameters and profiles in the simulations can be interchanged independently. Particularly for the JET pair, it is found that \hat{s}/q can indeed explain a major component of the core confinement difference. However, including the rotational flow shear turbulence suppression model in GLF23 leads to significant overprediction of the ion temperatures for all discharges studied. This raises questions regarding the importance of plasma shaping effects, and the validity of the parallel velocity gradient (PVG) destabilisation in the model.

The beneficial effect of reduced temperature profile stiffness at low- \hat{s} in inner radii is assessed with non-linear modelling using the GENE gyrokinetic code. It is found that at low- \hat{s} the turbulence correlation lengths are decreased and the non-linear frequency broadening increases compared to high- \hat{s} cases. Both these effects may be related to the observed increase in zonal flow activity, and leads to a reduction in the predicted flux compared to the high- \hat{s} cases. With these results, the validity of an advanced quasilinear transport model, QuaLiKiz, was extended to low- \hat{s} parameter space. The underlying assumptions of the model are examined, and the mixing length rule improved with guidance from the non-linear simulations. This work improves the confidence in using the QuaLiKiz transport model in the future for hybrid scenario predictions.

Finally, the experimentally observed stiffness reduction at low- \hat{s} and high flow shear was investigated with non-linear modelling. This topic is also of importance to hybrid scenarios, to further understand the relative importance of the various factors contributing to improved confinement. Hybrid scenarios on present-day machines also tend to be associated with high levels of flow shear. The simulations do not predict the degree of reduced stiffness as experimentally observed, and this question is thus still open. Experimental measurements of the poloidal rotation profile in this class of discharge may shed more light on the matter, as we assumed that the rotation is purely toroidal due to the expected neoclassical poloidal damping. Nevertheless, additional insights were gained into the non-linear nature of ITG turbulence. From electromagnetic simulations, the non-linear β_e (ratio of electron pressure to magnetic pressure) stabilisation of ITG turbulence is observed to be significantly greater than the well-known linear β_e stabilisation. This may be related to the observed increase in zonal flow activity within the β_e range studied. Beyond the increase in fundamental understanding, this effect could also be important for furthering the interpretation of transport in hybrid scenarios, which tend to operate at higher β_e than in inductive scenarios.

Acknowledgements

Ever since the beginning of my physics studies, it has been my desire to join the ranks of those tackling the grand challenge of fusion energy development. The publication of this thesis represents a significant personal milestone towards that goal. However, the road has not been walked on alone. Over the last four years, both here in my adopted home in the Netherlands and during work trips to France, Germany, and the United Kingdom, I have had the fortune to meet and work with many wonderful people and scientists who have been more than instrumental in helping me begin to turn this desire into reality. While these few lines cannot be sufficient to convey the depth of my gratitude, I hope here to nevertheless try and express my deep thanks to all those who have made it possible – and enjoyable – to set forth on this adventure.

First, I would like to thank my daily supervisor, Dick Hogeweij, for his constant guidance, advice, knowledge, encouragement, organisation, and kindness, which have all been indispensable for a successful ‘PhD campaign’. Thank you Dick for your trust and flexibility when the direction of the work began to veer away from the original plan, for helping me gain confidence in my abilities, and for your consistently positive attitude which is an inspiration in itself.

I would like to thank my first promotor, Wim Goedheer, for the continuous oversight and support of my work, especially during these last few months when I needed the push to actually finish! I would also like to thank my second promotor, Niek Lopes Cardozo, particularly for the constructive advice on how to best introduce the ideas and goals presented in this thesis, and also for the vital aid in shifting the defense to TU/e on such short notice.

I owe a great deal to Yitzhak Maron and Ramy Doron at the Weizmann Institute of Science in Israel, whose excellent guidance, support, and travel opportunities provided during my MSc research period made my transition abroad to a tokamak related PhD topic possible. Thank you both very much. The scientific culture you have instilled in me then still remains fixed today.

Thank you Marco de Baar, for our first enthusiastic communication at the Carolus Magnus Summer School 2007 which helped sow the seeds of my Rijnhuizen position, for the continuous support and further application of our work in your group, and also for the careful reading of the thesis.

Many thanks to Egbert Westerhof, whose continuous input, discussion, and encouragement has been highly valued. Thank you Tony Donné for your constant encouragement, kindness, and good spirit. Thank you Hugo de Blank, for always having an open door and the patience to answer basic theory questions. Thanks also to the DIFFER management team, for showing so much support and flexibility during the difficult times that arose within the period of this PhD.

Special thanks to Clarisse Bourdelle, whose initial suggestion at a conference in Riga spawned a collaboration that has unleashed the floodwaters of gyrokinetics into my scientific career, enriching my experience greatly. Thank you Clarisse for your infectious en-

ergy, warmth, support, patience, and knowledge which has made the many weeks worth of visits to Cadarache a true pleasure. Thanks also to Luca Giovanelli for his legendary pasta - it provided strong motivation to keep coming back to Aix!

Special thanks also to Frank Jenko. I have had the great privilege of to have been introduced to the GENE code by him and his group, an incredible opportunity which I am extremely grateful for. Thank you Frank for the numerous periods spent visiting you and your remarkable group at Garching and for the time you set aside for me then. Those periods were among the most productive, interesting, and beneficial weeks of work which helped lead to this thesis.

I would also like to thank Frédéric Imbeaux, Jeronimo Garcia, and Jean-François Artaud at CEA Cadarache, for their patience and efficiency in teaching me the CRONOS code and promptly answering any questions or requests related to its use. Thank you also Yves Buravand and Hélène Parrat for always being so quick and helpful when solving issues on the Saturne cluster.

Thanks also to the rest of the GENE team at IPP Garching, particularly Tobias Görler, M.J. Pueschel, Daniel Told, David Hatch, Hauke Doerk, Florian Merz, and Mirjam Schneller, for their fantastic support in teaching me GENE, for the quick modifications made in the code and diagnostics to further the research, for being so quick and eager to help, and also for being such good company during my visits to the group.

I would also like to note my great appreciation to the members of the ITER Scenario Modelling Working Group – in particular to Vassili Parail, Xavier Litaudon, Irina Voitsekhovitch, and Florian Koechl – for the many productive and enjoyable working sessions we have had together. Thank you also Jörg Hobirk for your expert input and patience in enlightening me on the experimental aspects of our field.

I owe a debt of gratitude to everyone who has contributed in making Rijnhuizen/DIFFER such a special place to work in and making me feel so much at home in the Netherlands. Thank you Rob, Federico, Wouter, Wolf, Rianne, Thijs, Merlijn, Gillis, Gieljan, Irene, Joeri, Amy, Dagmar, Jan-Willem, Kirill, Tom, Kuba, Bircan, Hans, and so many others. Rob, you have been the ultimate office-mate, connoisseur and provider of liquids of various forms, pillar of support, and gracious Mölkky champion. One of the most enjoyable and memorable periods at Rijnhuizen was the glory months of fusion's finest rock band, The Wrong Assumptions, and our headline gig at Rijnhuizen's 50th birthday bash. Thanks Wouter, Joeri, Jeff, and Erik for the music and laughs. Thanks also to the football group, who really provided something to look forward to on Tuesdays and Thursdays, and for tolerating my meager skills. Also thanks to my colleagues on the OR, particularly for their patience and understanding during my long absences and language difficulties.

Finally, to my family. You have provided unbounded love and support and have always pushed me and encouraged me to follow my dreams, wherever they may take me. These past couple of years have been exceedingly difficult for us all. This thesis is dedicated to the memory of my father David and sister Galit, who are always in our hearts. It is also dedicated to my brother Ilan and to my mother Katia, foundation stones of love and support throughout my life. I love you both. Dafna, without you Team Jonda would just be Jon, and that isn't very special. Thanks for absolutely everything. I love you.

Curriculum vitae

I was born on December 15 1980, in Hong Kong. At age 14 I moved with my family to Israel. My initial education in Hong Kong was based on the British curriculum. In Israel I graduated in 1998 from the ‘Ort Yad-Giora’ high-school in Herzliya, having matriculated to the physics and computer science stream. Following a three-year compulsory national service stint in the Armoured Corps of the Israeli Defense Forces between 1999-2002, I began studying towards a B.Sc. degree in physics at Tel Aviv University in 2003. From the summer of 2005, I combined my studies with a research internship at the plasma physics laboratory at the Weizmann Institute of Science in Rehovot, Israel. Following my B.Sc. degree (graduated with Distinction), I was awarded with a Feinberg Graduate School Fellowship to attend graduate studies at the Weizmann Institute. I was conferred with a M.Sc. degree (awarded with the Dean’s Prize) in December 2008. The M.Sc. research, which resulted in a thesis entitled “High resolution measurements of a nearly collisionless plasma”, investigated the propagation of a magnetic shock on nanosecond timescales in a plasma-operating-switch (POS) device, using visible/UV spectroscopy.

In January 2009, I began my Ph.D. research with the high temperature computational plasma physics group at the FOM Institute DIFFER (formerly the FOM Institute for Plasma Physics “Rijnhuizen”) in Nieuwegein, the Netherlands. The work concentrated on the integrated modelling and gyrokinetic modelling of tokamak core plasma turbulence in regimes relevant for ‘hybrid’ tokamak operational scenarios. The work was mostly carried out at FOM DIFFER, together with multiple visits under EURATOM mobility to collaborators at CEA Cadarache in France, the Max Planck Institute for Plasma Physics in Germany, and to the Joint European Torus (JET) in the United Kingdom. The results of the work are presented in this thesis.